IndiaTrib-2022

December 12-14, 2022
New Delhi, India

**Tribology for
Energy, Environment and Society**

www.indiatrib.org

**Extended
Abstract Book**

Microstructural and tribological characteristics of HVOF sprayed CrMnFeCoNi high entropy coatings for extreme environments

Payank Patel[1,2*], Navid Sharifi[1], Amit Roy[1,2], Mary Makowiec[3], Pantcho Stoyanov[4],
Richard R. Chromik[2], Christian Moreau[1]

1.Department of Mechanical, Industrial and Aerospace Engineering, Concordia University, Canada
2.Department of Mining and Materials Engineering, McGill University, Canada
3.Pratt & Whitney, 400 Main Street, East Hartford, CT 06118
4.Department of Chemical and Materials Engineering, Concordia University, Canada
Corresponding author: Payank Patel (ppayank13196@gmail.com)

Abstract

High-entropy alloys (HEAs) are characterized as alloys containing five or more principal elements in equal or close to equal atomic percentage. Because of the high configurational entropy compared to conventional alloys, HEAs are usually composed of a simple solid solution phase instead of a complex, brittle structure. HEAs as bulk materials and coatings are considered potential candidate for high-temperature applications owing to their superior combination of mechanical and thermal properties. However, limited studies have focused on the tribological behavior of HEAs fabricated by means of High Velocity Oxy-Fuel (HVOF) process. In the present study, the CrMnFeCoNi HEA coatings with different Al content were developed using high-velocity oxygen fuel (HVOF) process. The high velocity of the particles and low process temperature allows for the formation of a dense coating with limited porosity and oxide content. The microstructure, mechanical properties and tribological behavior of the as sprayed HEA coatings were systematically evaluated. The wear behavior of these HEA coatings against alumina (Al2O3) ball was tested under the dry sliding conditions at room and elevated temperatures. Ex situ characterization was performed using X-ray diffraction (XRD) and XPS for phase analysis, FE-SEM for cross-section microscopy and surface morphology identification. In addition, EDS analysis was performed to evaluate the phase compositions of the HEA coatings. The powder particle size distribution, microstructural changes, phase compositions, microhardness, and wear performance of the various HEA coatings are discussed further in the paper. A strong emphasis is placed on the correlation between the interfacial processes and wear behavior of the HEA coatings.

Introduction

Conventional Ni- and Co-based alloys (binary and ternary), being widely used in the aerospace industry, have shown some limitations when operating in demanding conditions. Yeh et al. [1], Cantor et al. [2] and Ranganathan et al.[3] introduced the concept of high entropy alloys (HEAs), which have shown to be promising candidates for such harsh conditions. Indeed, the development of HEA coatings with excellent tribological properties can address several issues under demanding service conditions. More recently, several authors have suggested four core effects behind the unique behavior of HEAs and described the influence on the properties of HEAs: (1) high entropy effects, (2) severe lattice distortion, (3) sluggish diffusion, and (4) cocktail effects. More details can be found in the review article by Patel et al. [4], who explored and summarized the different aspects of HEA coatings in terms of feedstock preparation, different HEA coating systems, and their properties. Among the newly developed HEA systems, the CrMnFeCoNi HEA has been extensively investigated in bulk form and reported some interesting results such as the good balance of ductility and strength, low stacking fault energy, high tensile strength and fracture toughness [5–7]. However, the investigation of the CrMnFeCoNi HEA coating and its tribological characteristics has gained much less attention compared to other HEA systems.

In this research study, CrMnFeCoNi (with a variation of Al content) HEA coatings were developed using HVOF, and their room temperature and high temperature tribological behavior was critically evaluated. Ex situ analysis was performed on the worn surfaces to provide a better understanding of the interfacial processes, including tribo-layer formation, material transfer, and debris particle formation.

Experimental Details

Materials

Commercially available CrMnFeCoNi HEA powder (Eutectic Powders, Canada) with a particle size range of 15–53 μm was used as feedstock. The prepared CrMnFeCoNi HEA powder with equal molar ratio (1:1:1:1:1) was sprayed on 304L stainless steel substrates.

Coating Preparation

The CrMnFeCoNi HEA powder was used as a feedstock material to develop the coating by High Velocity Oxy-Fuel (HVOF) using a Oerlikon-Metco Diamond JetTM 2700 Gun. The HVOF processing parameters and schematic diagram are shown in Table 1. Similarly, different spraying condition have been investigated to optimize the coatings for improved tribological behavior.

Table 1: Spray process parameters of HVOF for developing the HEA coatings.

Gun used	Diamond Jet™ 2700
Feed rate	23 gm/min
Oxygen	303.5 L/min
Propylene	78.8 L/min
Air	421.8 L/min
Transverse Speed	1 m/s
Spraying Distance	150 mm

Characterization

The CrMnFeCoNi feedstock and coatings were characterized using X-ray Diffraction (XRD) and Raman spectroscopy for phase analysis, Scanning Electron Microscope (SEM) for cross-sectional microstructure and surface topography, energy dispersive spectroscopy (EDS) for elemental analysis and Vickers microhardness test for hardness measurement.

The wear test of the coatings was conducted using a ball-on-disk tribometer in a reciprocating motion (Model: Anton Paar TriTec SA, Switzerland), where alumina balls (Φ 6.35 mm) were used as counter surface and tested against pre-polished surfaces. The testing parameters can be found in Table 2. The characterization of the wear tack was carried out with SEM and EDS to analyze the tribo film formation, materials transfer, debris removal and to understand the wear mechanism.

Table 2: Friction test parameters performed on ball-on-disk tribometer.

Tribometer type	Ball-on-Disk
Load	5N
Frequency	1 Hz
Amplitude	10mm
Velocity	3.14 cm/s
Cycles	5000
Counter ball	Alumina
Diameter	6.35 mm
Total sliding distance	100 m

Results and discussion

Feedstock

Figure 2 represents the microstructure of as received feedstock material (CrMnFeCoNi HEA powder).
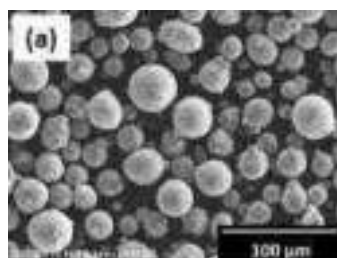

Figure 2: SEM images of (a) CrMnFeCoNi HEA powder (b) single powder particle (c) cross-section of the HEA powder particle

Figure 3 shows the XRD pattern of the CrMnFeCoNi HEA powder (feedstock) and coatings.
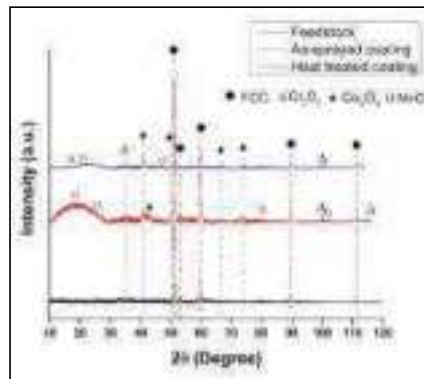

Figure 3: XRD pattern of the feedstock powder, AS and HT coatings

Table 3 also shows other characteristics of the coatings such as porosity, oxide content, surface roughness and microhardness.
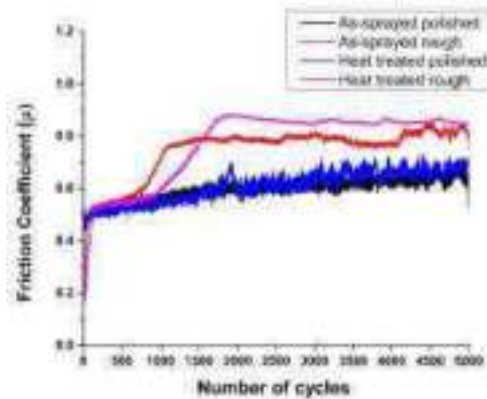
3.2 Friction and wear behavior of coatings

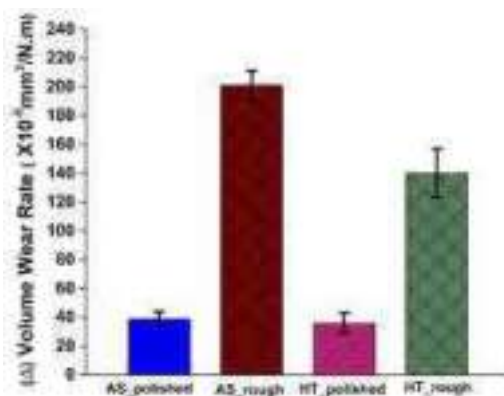Figure 8: Friction coefficients of the AS_polished, AS_rough, HT_polished and HT_rough coatings.

Figure 10: Volume wear rate measurements of the AS_polished, AS_rough, HT_polished and HT_rough coatings.

Conclusions

In this study, CrMnFeCoNi HEA coatings were developed by means of HVOF with subsequent annealing heat treatment. The coefficient of friction and wear rate of AS polished and HT polished coatings are almost equivalent, which indicates that there was no significant influence of annealing on the wear performance of the CrMnFeCoNi HEA coatings. However, just negligible effect can be observed in the friction coefficient result which were almost similar after some 2000 cycles. The rough surfaces of AS and HT coatings showed high wear rate relative to polished surfaces due to higher initial maximum contact stress and formation higher amount of debris particles with

potentially large size. The dominant wear mechanism was adhesive for polished surfaces whereas third body abrasion wear mechanism played vital role for rough surfaces.

References

○ Yeh J, Chen S, Lin S, Gan J, Chin T, Shun T, Tsau C and Chang S 2004 Nanostructured high-entropy alloys with multiple principal elements: novel alloy design concepts and outcomes Adv. Eng. Mater. 6 299–303

○ Cantor B, Chang I T H, Knight P and Vincent A J B 2004 Microstructural development in equiatomic multicomponent alloys Mater. Sci. Eng. A 375 213–8

○ Ranganathan S 2003 Alloyed pleasures: multimetallic cocktails Curr. Sci. 85 1404–6

○ Patel P, Roy A, Sharifi N, Stoyanov P, Chromik R R and Moreau C 2022 Tribological Performance of High-Entropy Coatings (HECs): A Review Materials (Basel). 15 3699

○ Haglund A, Koehler M, Catoor D, George E P and Keppens V 2015 Polycrystalline elastic moduli of a high-entropy alloy at cryogenic temperatures Intermetallics 58 62–4

○ Zhu Z G, Nguyen Q B, Ng F L, An X H, Liao X Z, Liaw P K, Nai S M L and Wei J 2018 Hierarchical microstructure and strengthening mechanisms of a CoCrFeNiMn high entropy alloy additively manufactured by selective laser melting Scr. Mater. 154 20–4

○ Sun S J, Tian Y Z, Lin H R, Dong X G, Wang Y H, Zhang Z J and Zhang Z F 2017 Enhanced strength and ductility of bulk CoCrFeMnNi high entropy alloy having fully recrystallized ultrafine-grained structure Mater. Des. 133 122–7

Effect of the alkyl chain length on the tribological performance of two organic lubricant additives

Sukdeb Mandal[1,2,] Sanjukta Zamindar[1,2,] Manilal Murmu[1,2,] Naresh Chandra Murmu[1,2,] Harish Hirani[3,] and Priyabrata Banerjee[1,2,*]

1Surface Engineering and Tribology Group, CSIR-Central Mechanical Engineering Research Institute, Mahatma Gandhi Avenue, Durgapur 713209, West Bengal, India
2Academy of Scientific and Innovative Research (AcSIR), AcSIR Headquarters CSIR-HRDC Campus, Sector-19, Kamla Nehru Nagar, Ghaziabad, 201002, India
3Department of Mechanical Engineering, Indian Institute of Technology Delhi, New Delhi, 110016, India
Email (First Author): sukdeb.cmeri19j@acsir.res.in

Abstract

It has been established that the performance of a lubricant blend depends upon the judicious choice and the optimized concentration of the lubricant additive(s). From the literature data, it has been revealed that various organic molecules, complexes, etc. are used as proficient lubricant additives. In order to develop cost-effective, efficient surface protective and eco-friendly lubricant additive azomethine functionalized, different alkyl chain containing two organic molecules namely (3E)-N-((E)-2-(octadecylimino)ethylidene)octadecane-1-amine (ODE) and (3E)-N-((E)-2-(dodecylimino)ethy lidene)dodecane-1-amine (DDE) have been synthesized. The performances of these two additives have been explored in paraffin oil (base oil) using a four-ball tester instrument according to ASTM D4172 test method. The experimental outcome shows that ODE exhibited a better reduction in friction coefficient (~62%) and the amount of wear (~23%) than DDE. The existence of an additional alkyl chain in the ODE is mainly responsible for reducing friction and wear. Extra alkyl chain length helps to cover up a large surface area by forming a protective tribofilm on the surface and subsequently friction as well as wear amount decreases. Surface morphology has been characterized using a field emission scanning electron microscope and a non-contact optical three-dimensional surface profilometer. Furthermore, to explore the adsorption mechanism and tribofilm forming ability of the lubricant additives on the metal surface theoretical approaches like density functional theory (DFT) and molecular dynamics (MD) simulation have been performed.

Introduction

In the present scenario, it has been found that tribological interactions lead to around 23% of global energy consumption [1]. Lubricants play a vital role to minimize as well as optimize several tribological properties like wear, friction etc by forming a protective layer in between the sliding surfaces which are in contact [2-4]. To date, several lubricant additives have been synthesized and used. But the presence of Zn, S, P etc. creates an adverse environment for surviving the emission system of an engine. In this regard, the development of eco-friendly, cost-effective, and highly-efficient lubricant additives is in urgent need. From the literature survey, it has been found that there are limited numbers of organic lubricant additives [5-7].

In the present study, two organic lubricant additives namely, (3E)-N-((E)-2-(octadecylimino)e thylidene)octadecan-1-amine (ODE) and (3E)-N-((E)-2-(dodecylimino)ethylidene)dodecan-1-amine (DDE) have been synthesized and their anti-frictional property were evaluated in paraffin oil (PO). Furthermore, theoretical calculations have also been performed to corroborate the experimental findings.

Experimental Detail

ODE and DDE were synthesized via single-step condensation of amine (octadecan-1-amine and dodecan-1-amine for ODE and DDE respectively) and oxaldehyde in a 2:1 ratio, (Vide Fig. 1). FT-IR spectroscopy, ESI mass spectroscopy and Nuclear Magnetic Resonance (NMR) spectroscopy were performed for characterization of these molecules. Dynamic light scattering (DLS) study was carried out to find out the average dimension of the particles.
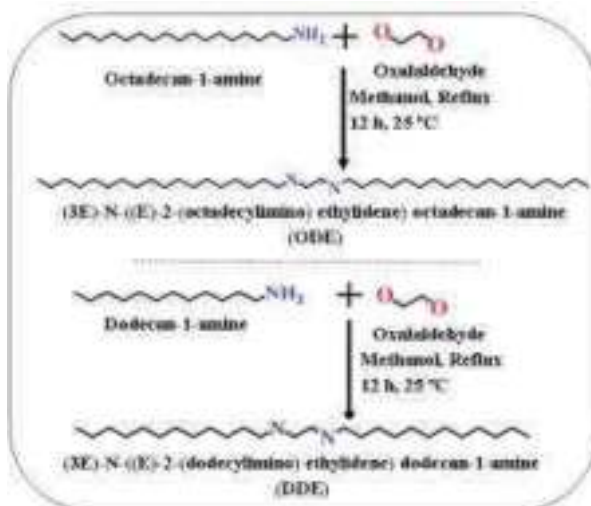
Fig. 1 Scheme for the synthesis of ODE and DDE

Tribological tests were accomplished in a four-ball tester with four different concentrations i.e., 0.016, 0.023, 0.035 and 0.042 w/v% of ODE and DDE in PO according to ASTM D4172 standard procedure [8].

For further confirmation of the experimental findings, molecular dynamic (MD) simulation was performed. MD simulation has been proven to be one of the significant tools for understanding the interaction between molecules and interactive metallic surfaces [9]. Forcite module was used to visualise the interaction of the additive molecules, ODE and DDE and a ten-layered Fe (1 1 0) surface at 348 K temperature. NVT ensemble, Nosé thermostat and COMPASS II forcefield have been utilised to perform quench tasks for having the minimum global energy [10, 11].

Result And Discussion

The change in COF with varying the concentration of the additive blends was analyzed and the result obtained has been graphically represented in Fig. 2. The concentration of the additive plays a pivotal role in the anti-wear property of the lubricant. The optimal concentration for ODE and DDE in PO was found to be 0.035 w/v %. It has been revealed that at optimum concentration ODE in PO reduces the COF value in much amount than DDE in PO.
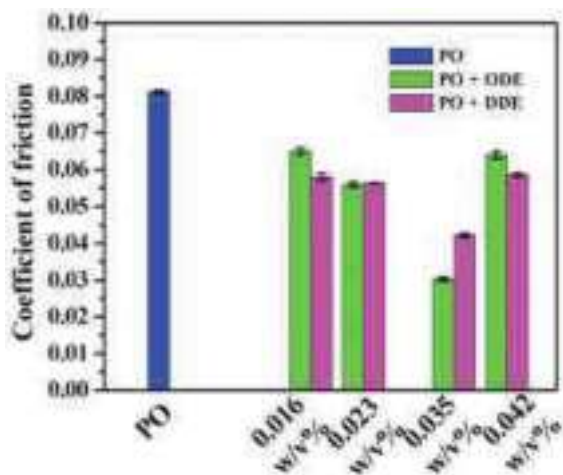
Fig. 2 Variation of COF value with varying concentrations of the additive blends

From the theoretical study, the interaction energy of the ODE and DDE with Fe (1 1 0) surface were found to be -1385.95 KJ mol-1 and -1144.87 KJ mol-1 respectively. These findings also corroborate the experimental outcomes that ODE acts as a better and more efficient lubricant additive than DDE.

Conclusion

A nutshell conclusion is that the addition of ODE to the PO remarkably reduced the COF value to 0.030, showing better results than DDE alone. The spontaneous diminution of COF and wear can be attributed to its unique geometrical structure, chain length, and electronic property of the synthesized ODE additive.

Acknowledgement

References

- K. Holmberg, et al. Tribol Int. 2019; 135: 389–396.
- S. Mandal et al. J. Adhes. Sci. Technol. 2022, 1-27.
- M. Murmu, et al. RSC Advances, 2020, 10, 33401-33416.
- Q Zeng et al. J Adhes. Sci. Technol. 2018; 32 (17):1911–1924.
- Q. Zeng, et al. J. Adhes. Sci. Technol. 2019; 33(9): 1001–1018.
- R. K. Singh, ACS Sustainable Chem. Eng. 2014; 2(8): 1959–1967.
- D. Zheng et al. Tribol. Int. 2019; 130: 324–333.
- ASTM International. D4172-20, West Conshohocken, PA, 2020.
- Y. Ma et al. J. Mol. Model. 2020; 26(4): 81.
- S. Meng et al. RSC Adv. 2021; 11(50): 31693–31711.

Investigating The Antiwear Characteristics Of Castor Oil Based Ionano Lubricant Using Four Ball Tester

Gitesh Kumar[1*] and H.C. Garg[2]

[1,2]Department of Mechanical Engineering, Guru Jambheshwar University of Science and Technology, Hisar, Haryana, INDIA
*Corresponding author E-mail: giteshgju@gmail.com

Key Words: Tribology, Wear, Materials, Lubrication

Abstract

Environmental issues due to excessive use of mineral and synthetic oil have forced us to develop environmentally acceptable lubricants. Non-edible vegetable oils are the most suitable alternative to the base oil. The present study aims to investigate the synergistic effect of copper oxide (CuO) nanoparticles and halogen-free ionic liquid (IL) trihexyltetradecyl phosphonium bis (2,4,4 trimethylpentyl) phosphate [P66614] [BTMPP] in castor oil as hybrid additives. Antiwear properties of ionano lubricant has compared with castor oil containing ZDDP (common antiwear additive). The shape morphology and particle size of CuO nanoparticles (<80nm) were investigated using FESEM. Three samples were formulated with castor oil containing 0.02 volume fraction CuO, 0.1 vol/vol% [P66614] [BTMPP] IL and 2% ZDDP, respectively. Three other samples were formulated by varying the concentration of CuO in 0.02, 0.04, and 0.06 volume fraction and IL in 0.1, 0.2, 0.3 vol/vol%, respectively. Antiwear characteristics of formulated ionano lubricants have been investigated using Four ball tester under ASTM D 4172 B. The worn-out surfaces of steel balls were investigated using optical microscopy. Average wear scar diameter (AWSD) of 0.589 mm was found at an optimum concentration of 0.02 volume fraction CuO and 0.1 vol/vol% IL. AWSD has increased with increase in concentration of both additives. The steel balls show smoother surfaces at optimum concentration of additives. The lowest AWSD of 0.514 mm was found for castor oil containing 2% ZDDP. This study shows that formulated castor oil based ionano lubricant is environmentally acceptable and provides better antiwear properties.

Introduction

Lubricants are applied between two moving parts to prevent wear between them. In the ancient time, Environment friendly lubricants were used as lubricant such as water, vegetable oil and animal oils. Nowadays, mineral and synthetic are commonly used as lubricants. Although, the mineral or synthetic oils are dangerous to environment. Environmental protection has forced us to reduce the uses of petroleum dependent lubricants. Today, lubricant industries are more ecologically focused on manufacturing a new class of environmentally acceptable lubricants (EALs) or bio-lubricants. The bio-lubricants are suitable alternative to mineral and synthetic oils. Bio-lubricant are composed of base oil and additives. The non-edible vegetable oils are suitable alternatives of base oil. Colloidal suspension of solid nanoparticles in base oil is termed as nanolubricant. IL and nanoparticles are selected as lubricant additives in base oil and denoted as ionano lubricant. Generally, vegetable oils have superior properties such as high viscosity index, high flash point, high biodegradability and low toxicity. The major disadvantage of vegetable oils low and high temperature stability. The aim of the present study is to formulae a castor oil based EAL containing oil miscible IL and nanoparticles. ILs are thermally stable compound and they have a large operating temperature up to 300˚C where they maintain their fluidity. Jiang et al. investigated the friction and wear properties of rapeseed oil with ILs 1-methyl-3-hexylimidazolium tetrafluoroborate and 1-methyl-3-hexylimidazolium hexafluorophosphate in 1,2, and 3 wt.% using optical SRV oscillating friction and wear tester. Results revealed that at 1 wt.% IL concentration, the lowest value of CoF and wear volume was observed for steel surfaces under different loads [1]. Grace et al. investigated the tribological properties of coffee bean oil with trihexyltetradecylphosphonium decanoate,trihexyl-tetradecyl phosphonium, bis(trifluoromethylsulfonyl) amide in 1,2.5,5 wt.% using block-on-flat reciprocating tribometer.

The wear volume was decreased with addition of IL to coffee bean oil. Also, the obtained value of wear volume was comparable to conventional lubricant [2]. Bhaumik et al. investigated the antiwear and extreme pressure properties of castor oil containing ZnO nanopartilces in different concentration using four ball tester. At optimum concentration of 0.1% of ZnO nanoparticles shows better antiwear and extreme pressure properties [3]. Kumar et al. investigated the tribological characteristics of refined soybean oil (RSBO) based lubricant containing 0.04, 0.05, 0.1 and 0.2 wt.% CuO nanoparticles and ZDDP using ball on disc tribotester. Friction and wear was decreased by the increment in the concentration of CuO and ZDDP in RSBO.

The optimum concentration of CuO nanoparticles was found 0.5 wt.% [4]. Al kaisy et al. investigated the tribological properties of six low viscosity, hydrophobic, halogen-sulfur-phosphorous free ILs as neat lubricant using a four ball tribotester. A significant friction reduction up to 28-65% was observed in comparison to polyalphaolefin lube base oil [5]. Shafi and charoo investigated the antiwear pressure properties of hazelnut oil containing ZDDP using four ball tester. Antiwear properties of hazelnut oil was improved to 43.7% and 45.7% at 1 nas 3 wt.% respectively. Load wear index was increased from 29 to 73.1 at 3 wt.% of ZDDP [6]. Kumar and garg investigated the rheological and tribological characteristics of canola oil-based lubricant containing [EMIM][DCN] IL. Friction and wear effects of bio-ionic lubricants was investigated using ball on disc tribotester at different speed and loads. The rheological properties of canola oil were improved significantly with

Figure 1 FESEM of CuO nanoparticles

addition of IL. Minimum CoF and wear was observed at an optimum concentration of 2 wt.% of IL [7]. Kumar et al. investigated the the lubrication efficiency of blended oil (rice bran: sunflower oil) containing CuO nanoparticles in 0.01, 0.02, 0.03 and 0.04 % volume fraction using four ball tester. The result showed that better dispersion stability was found at optimum nanoparticles to surfactant ratio of 1:3. The minimum CoF and WSD was observed at 0.04 % volume fraction of CuO nanoparticles [8].
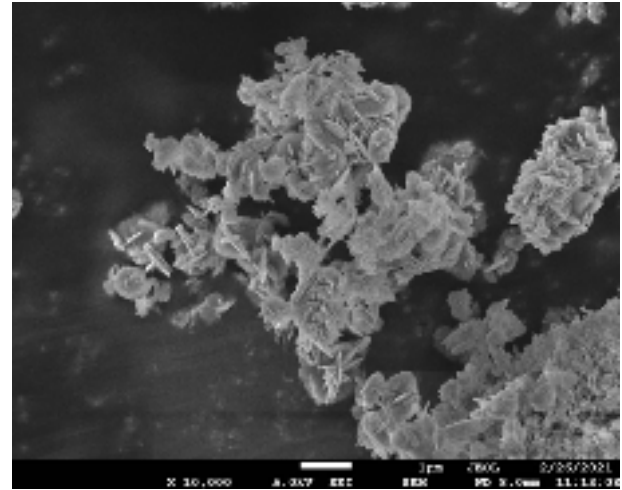
The literature review showed that castor oil has been studied as lubricant with different additives like nanoparticles and ionic liquids. However, no study was found with castor oil containing IL and nanoparticles as hybrid additives. The aim of this study was to investigate the antiwear characteristics of castor oil with hybrid additives. Additionally, compared with castor oil containing 2% ZDDP.

Experiment Details

The castor oil and CuO nanopartilces are purchased from HPLC Pvt. Ltd. Phosphonium based IL trihexyltetradecylphosphonium bis (2,4,4-trimethylpentyl) [P66614][BTMPP] is purchased from sigma Aldrich. To ensure the dispersion stability of CuO in castor oil Tween 20 (1:1) is used as surfactant and purchased from loba chemie pvt. Ltd. To investigate the antiwear properties six ionano lubricant samples have been formulated. Three samples have been formulated with castor oil containing 0.02 volume fraction CuO, 0.1 vol/vol % [P66614][BTMPP] IL and 2% ZDDP, respectively and denoted as CN1, CIL and CZ. Three other samples have been formulated by varying the concentration of CuO in 0.02, 0.04, and 0.06 volume fraction and IL in 0.1, 0.2, 0.3 vol/vol%, respectively and denoted as CNIL1, CNIL2, CNIL3.

Calculated amount of each additive has been mixed in castor oil by magnetic stirring for 90 minutes and followed by bath ultrasonication for 30 minutes. Antiwear properties of ionano lubricant has compared with castor oil containing 2 % ZDDP (common antiwear additive). Steel balls of AISI 52100 of 12.7 mm diameter are used. The dispersion stability of CuO nanoparticles in castor oil have been investigated by visual inspection. [P66614][BTMPP] IL has good miscibility in non-polar base oil reported by [9]. The representative images of castor oil based ionano lubricant and castor oil containing ZDDP are presented in Figure 2. Figure 2 (a) shows the freshly prepared ionano lubricants and 2(b) shows the ionano lubricant after 30 days. Castor oil based ionano lubricants have been successfully formulated. Antiwear characteristics of formulated ionano-lubricant has been investigated using four ball tester according to ASTM D 4172B. The operating condition are as follow; load:392N, speed:1200 rpm, temperature:75℃, time: one hour.
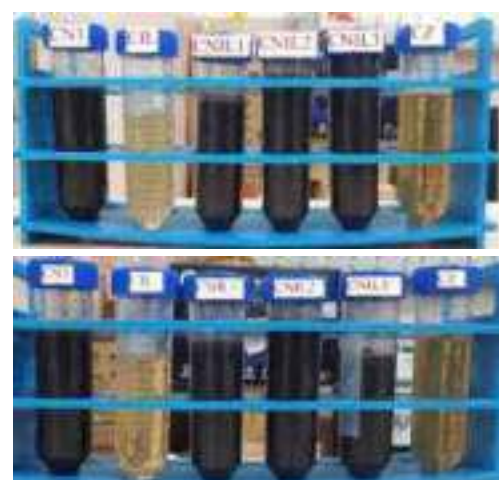

Figure 2 (a) Freshly prepared ionano lubricants and castor oil containing ZDDP and 2(b) after 30 days.

Results & Discussion

The shape morphology and particle size of CuO nanoparticles

(<80nm) were investigated using FESEM as shown in figure 1. CuO nanoparticles are lamellar in structure and particles size are <80 nm as shown in figure1. It has been confirmed from figures 2(a) and (b) that formulated ionano lubricant are stable for 30 days. Figure 3(a) shows the average wear scar diameter (AWSD) and average CoF for formulated castor oil based ionano lubricants and castor oil containing ZDDP. The AWSD for CN, CIL, CNIL1, CNIL2, CNIL3 are 0.828, 0.749, 0.589, 0.805, and 0.758 respectively. The Average CoF are 0.327, 0.3335, 0.3384, 0.3327, and 0.348 respectively. AWSD has increased with increase in concentration of both additives. Castor oil containing CuO nanoparticles show highest AWSD of 0.828 mm. AWSD of 0.589 mm was found at an optimum concentration of 0.02 volume fraction CuO and 0.1 vol/vol% IL.

The lowest AWSD of 0.514 mm was found for castor oil containing 2% ZDDP. Figure 3(b) shows the evolution of CoF with time for formulated castor oil based ionano lubricants and castor oil containing ZDDP. Formulated ionano lubricants shows approximately similar average CoF. Castor oil containing ZDDP has lowest WSD and highest average CoF because ZDDP form a tribofilm on the mating surfaces. The wear scar diameter of worn-out surface of steel balls have been evaluated using image acquisition system attached with four ball tester. The steel balls show smoother surfaces at optimum concentration of additives.
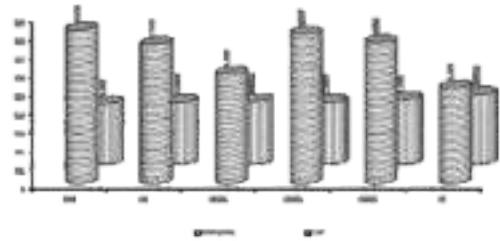
Conclusions

Castor oil based ionano lubricant containing IL and CuO nanoparticles were successfully formulated. From visual inspection it has been confirmed that formulated ionano lubricant is stable for 30 days. Among formulated ionano lubricant, lowest AWSD of 0.589 mm was found for castor oil containing an optimum concentration of 0.02 volume fraction CuO and 0.1 vol/vol% IL. Castor oil containing 2% ZDDP shows lowest WSD of 0.514 mm and highest CoF, Because of tribofilm formation capacity of ZDDP. This study shows that castor oil based ionano lubricants provides better antiwear properties. This study helps in the formulation of environmentally acceptable lubricant. Ionano lubricant containing lowest concentration of additives and castor oil containing 2% ZDDP shows comparable results.
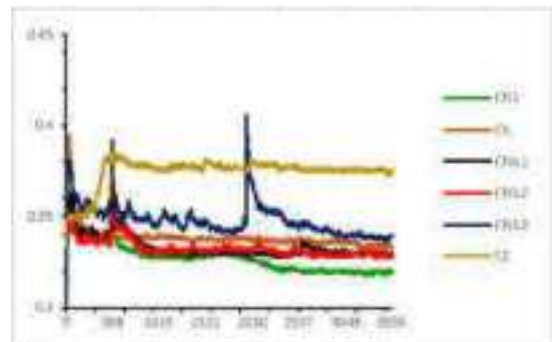

Figure 3(b) Evolution of friction with time

References

- Jiang, D. Hu, L. and Feng, D. Tribological properties of crown-type phosphate ionic liquids as lubricating additives in rapeseed oils: ionic liquids as a lubricating additive, Lubrication. Science, Apr. 2013, vol. 25, no. 3, pp. 195–207.
- Grace, J. Vysochanska, S. Lodge, J. and Iglesias, P. Ionic liquids as additives of coffee bean oil in steel-steel contacts, Lubricants, 2015, p. 13.
- Bhaumik, S. Maggirwar, R. Datta, S.and Pathak, S. D. Analyses of anti-wear and extreme pressure properties of castor oil with zinc oxide nano friction modifiers, Applied Surface Science, Aug. 2018, vol. 449, pp. 277–286.
- Kumar, G. Garg, H. C. and Gijawara, A. Experimental investigation of tribological effect on vegetable oil with CuO nanoparticles and ZDDP additives, Industrial Lubrication Tribology, Apr. 2019, vol. 71, no. 3, pp. 499–508.
- Al Kaisy, G. M. J. Mutalib, M. I. A Rao, T. V. V. L. N. and Senatore, A. Tribological performance of low viscosity halogen-free ammonium based protic ionic liquids with carboxylate anions as neat lubricants, Tribology International, Aug. 2021, vol. 160, p. 107058.
- Shafi W. K. and Charoo, M. S. Antiwear and extreme pressure properties of hazelnut oil blended with ZDDP, Industrial Lubrication Tribology, Mar. 2021, vol. 73, no. 2, pp. 297–307.
- Kumar G. and Garg, H. C. Influence of a halogen free ionic liquid on the rheological and tribological characteristics of canola oil, Industrial Lubrication Tribology, Jun. 2022, doi: 10.1108/ILT-12-2021-0487.
- Sunil Kumar D., Garg H. C., and Kumar G., Tribological analysis of blended vegetable oils containing CuO nanoparticles as an additive," Materials. Today, Proceeding, 2022, vol. 51, pp. 1259–1265.
- Qu J. et al., "Antiwear Performance and Mechanism of an Oil-Miscible Ionic Liquid as a Lubricant Additive," ACS Applied Material. Interfaces, Feb. 2012, vol. 4, no. 2, pp. 997–1002.

Vibration Analysis Of Hydrodynamic Conical Journal Bearing and Fault Prediction Using Machine Learning

Harshal S. Bhat[1*], Rahul K. Yadav[2], Sarang V. Bhudhar[3*], Sagar Nikam[4],
Avinash Mandarha5 and Vikas M. Phalle6

[1] PG Machine Vibration Dynamics Lab, Department of Mechanical Engineering,
Veermata Jijabai Technological Institute (VJTI), India
Email: hsbhat_b18@me.vjti.ac.in

Abstract

In industry 4.0, condition monitoring is gaining significant importance due to its capability for early diagnosis of the symptoms of the faults that result in severe damage in the rotating machinery. Conical journal bearings (CJB) are used in heavy rotating machinery due to their high radial and axial load carrying capacity and need to be adequately monitored during the operation. Thus an experimental study is carried out on a healthy and faulty CJB, which is scratched due to frequent start and stop machine operation, i.e. worn out internal surface material of bearing. Therefore, the dynamic response of a journal changes significantly due to wear. The vibration response of bearing in the time domain was acquired and transformed into the frequency domain and a comparative analysis is carried out. The experimental results demonstrate the unique vibration characteristic of worn-out bearing at the 4th multiple of operating frequency. Recently different machine learning techniques have been used as fault diagnosis approaches. An efficient method for fault diagnosis i.e., support vector machine (SVM), is employed in this study. Five statistical features are extracted from the vibration data, and these are fed to the SVM model, and the later data are trained and tested. The trained SVM model is capable of differentiating the faulty bearing with a testing accuracy of more than 85%.

Introduction

A journal bearing is a conventional type of hydrodynamic bearing employed in rotary machinery. A circular shaft called a journal is allowed to rotate inside a fixed sleeve called the bearing which forms its primary construction. It supports high loads due to the wedging action between the journal and bearing because of considerable relative motion [1]. In our case, full lubrication occurs, resulting in no contact between the bearing and the journal because of high relative motions. This type of bearing finds application in IC engines for supporting the crankshaft, rotor assemblies, and turbochargers. [2].

The proposed Conical hydrodynamic journal bearing is capable of sustaining high radial loads and mitigating the effects of axial load on rotating elements. Journal and thrust hydrodynamic bearings are being replaced by conical bearings due to their compact size, low cost, and radial and axial load conditions and are used in supporting precision spindle of rotating types of equipment [3]. When a journal bearing is in use, the surface asperities of the bearing lining and the steel shaft interact & the mating surfaces wear out since bearing material is softer than journal material, its wear rate is higher and it is generally defined as abrasive wear or scratching[4]. Wedge action refers to the pressure created by the lubricating film & requires a certain minimum speed to occur. At the start and shutdown sessions, this criterion is not met and a bearing slowly accelerates to the operating speed before decelerating to zero. During these two instances, the journal and bearing rub against each other, causing wear on the surfaces [5]. Eccentricity, film thickness, and load-carrying capacity are affected due to wear [6]. The most common wear observed in lubricated machinery is abrasive wear or scratching, which occurs due to particle contamination [7]. Hence scratched bearing is used as a faulty bearing for recording the vibration signals on the CJBTR (Conical Journal Bearing Test Rig).

To allow preventive action against catastrophic severe failures and decrease the probable loss of production due to the breakdown of the machine, early detection of fault symptoms is important & it is detected by the condition monitoring of the bearing and thus mitigates the downtime during running, and leads to the economic operation of systems. Hence, monitoring techniques can be employed in the early wear regime such as vibration and vibro-acoustic analysis. Moreover, bearing performance analysis and lubricating oil analysis (fluid contamination and wear debris analysis) can also be employed for monitoring journal bearings [9]. The vibration is a result of geometrical imperfections on the separate bearing components caused while manufacturing and due to wear and tear during operation [10]. Vibration analysis is one of the extensively used condition monitoring techniques that can produce

useful quantitative data and be controlled remotely in real time. Alarm limits can be pre-set and automatically activated based on observed signals [11].

To increase fault identification performance, signal processing and AI technologies are combined by extracting characteristics from the vibration signals. Thus, the raw vibration signals supplement features for fault classification in the time-frequency domain and their subsequent time and frequency domains are then passed to high fidelity artificial intelligence methods such as random forest, support vector machine (SVM), and artificial neural network (ANN) [12-16]. The GA-based[17] strategy was used to improve the input feature selection and the relevant classifier parameters. Samanta et al. [18] focused on a genetic algorithm-based bearing fault detection using SVM and ANN. SVM performed substantially better than ANN with the entire feature set.

SVM is a novel computational and statistical learning theory that may be used as an Expert system [19]. With finite samples, and estimating (learning) dependencies, this theory incorporates essential ideas and Learning principles, well-defined formulation, and self-contained mathematical theory. SVMs have been used in machine learning, computer vision & pattern recognition for their high accuracy and good generalization capabilities [20]. Hence, we deployed the SVM algorithm for fault classification and detection of the CJB.

We have used a healthy & scratched (faulty) bearing for collecting vibration signals on the CJBTR. Based on the aforementioned research, it is viable to infer that combining the approach of signal processing with the AI method improves CJB fault classification performance. The different features derived from vibration signals are fed into the SVM model for bearing classification. Thus, we propose an efficient SVM-based conditional monitoring of hydrodynamic conical journal bearing for fault detection.

Experimental Setup & Procedure

The below figure shows the system arrangement of CJBTR consisting of a machine control unit for adjusting the running & loading conditions, an air supply system for actuating the cylinders for applying the radial load, a lubricant re-circulating unit having water cooled heat exchanger in-line used during high speed & load conditions & DAQ system for recording the vibration signals at a sampling rate of 512 Hz collected by the trial-axial accelerometer mounted on the CJB having x, y & z faces aligned along the lateral, longitudinal & radial directions of the bearing resp.
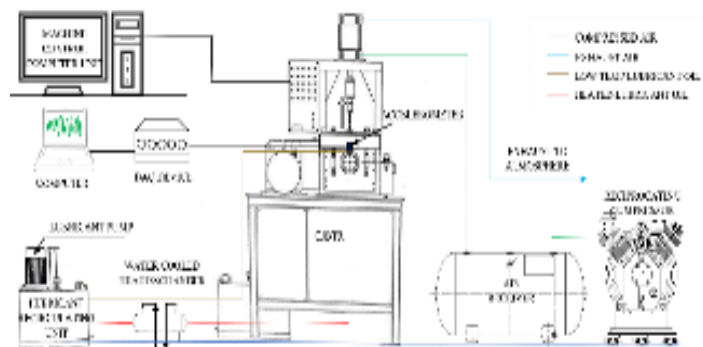

Figure 1: System Arrangement of JBTR

The machine is allowed to run at 500 RPM constantly& radial load is increased from 250-1050 N with a span of 100N & signals are recorded for each condition with HB mounted on the test rig having perfectly machined internal conical surfaces, the same is followed for constant load 350 N & speeds increasing from 200-1500 RPM with a span of 100 RPM. The same loading & running conditions are followed in the case of a scratched bearing (SB) having 12-20 μm radial & longitudinal scratches on the internal surface of the bearing.

Svm Methodology

The recorded dataset (122x5x2) consists of 5 normalized features with 122 sample cases and 2 classes (healthy & faulty bearing) which are split into two subsets for testing and training the SVM algorithm. The recorded vibration signals calculate statistical features of mean, skewness, kurtosis, standard deviation, and RMS. For this algorithm, the Gaussian radial basis function (RBF) kernel is used since it is a general-purpose kernel and when used with appropriate regularization parameters, the estimation and approximation errors are minimized. While using SVM with Gaussian RBF, a trade-off has to be made between two parameters i.e. C and γ, where C is the inverse of regularization parameter λ, where λ is used in linear regression to address the problem of overfitting. Increasing or decreasing the value of C and γ results in overfitting or underfitting of the dataset. A set of combinations of these hyper-parameters are fed to the algorithm and an average score is calculated to select the best hyperparameters. 1 and 0.1 were found to be hyperparameters for C and γ, giving the highest average score of 81.09%.

Results & Discussion

4.1 Comparison between HB & SB:

Figure 4 shows the comparison of the acceleration amplitudes in the Y-direction (longitudinal), which indicates amplitudes ranging from 3.29 to -2.67 m/s2 in case of healthy bearing & 1.83 to -1.72 m/s2 in case of scratched bearing, both bearing operates at 1500 RPM & 350 N radial load. The signals are further processed using FFT & amplitude spectrums are obtained for the corresponding signals of HB & SB. Figure 5 shows the comparison of the amplitude spectrums between HB & SB, in which peak values are 0.344 m/s2 at 49.95 Hz & 0.8773 m/s2 at 99.99 Hz in the case of HB & SB respectively.
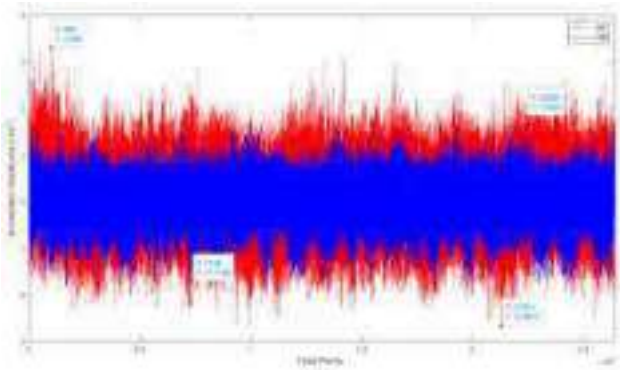

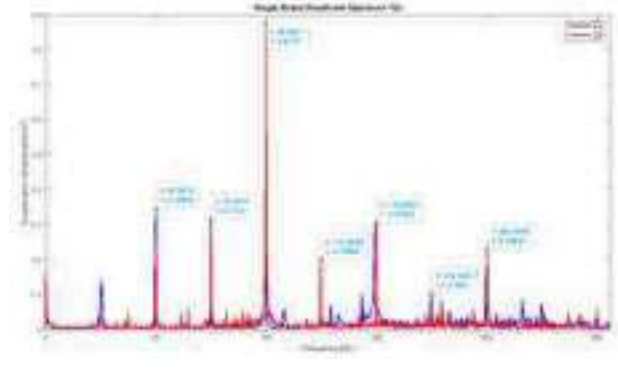*Figure 2: Acceleration Amplitudes comparison between HB & SB at 1500 RPM & 350 N*

Figure 3: Amplitude Spectrum comparison between HB & SB at 1500 RPM & 350 N

4.2 SVM Results:

The Results of the SVM model are obtained in terms of the Confusion Matrix. It allows us to visualize the performance of the algorithm in machine learning, especially in the case of classification problems. A 2x2 confusion matrix is obtained which predicts for classification between two classes i.e. 'Healthy Bearing' and 'Faulty Bearing'. For the training set, out of 101 cases, the algorithm predicts the right decision in 85 cases which gives an accuracy of 84.16% whereas in the test set, out of 21 examples right prediction is made for 18 examples which provide a validation accuracy value of 85.71%. The precision value is 85.45%, Recall is 85.45% and the F1 score is 85.43%.
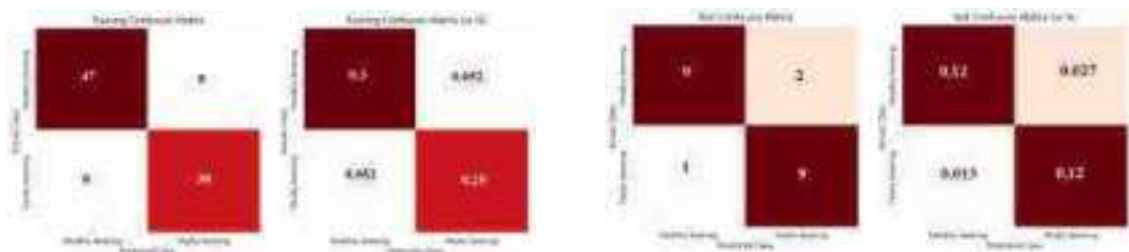

Figure 4: Training & Test Confusion Matrix

Conclusion

The experimental study focuses on a comparison between healthy and scratched hydrodynamic conical journal bearing based on acceleration amplitudes & spectrum, and SVM-based fault classification. From the study, the following conclusions can be drawn:

(1) Higher acceleration amplitudes are observed in the case of the internally scratched bearing during constant load & variable speed conditions along the longitudinal direction. It is primarily due to the lubrication mixing caused by the scratches present which alter the damping capacity of the fluid film in the scratched regions & it also affects the pressure distribution hence excitation forces acting on bearing increase. The maximum amplitude observed is 3.29 m/s2 when bearing running at 1500 RPM with 350N radial load.

(2) Maximum peak has occurred at 2nd & 4th multiple of operating frequency i.e. 25Hz (1500 RPM) in case of healthy & internally scratched bearing respectively. The peak frequency has been shifted from 49.95 Hz to 99.99 Hz due to scratches in the bearing.

(3) Peaks have occurred at the consequent multiples of the operating frequency in scratched bearing, showing a definite pattern on the spectrum.

(4) Training & validation accuracy obtained in the SVM algorithm are commendable. Hence we propose an SVM-based vibration analysis of an HCJB which will help in condition monitoring of the bearing.

References

- Tiwari, P., & Kumar, V. (2012). Analysis of hydrodynamic journal bearing: A review. International Journal of Engineering Research & Technology, 1-7.
- Childs, P. R. (2013). Mechanical design engineering handbook. Butterworth-Heinemann.
- Gangrade, A. K., Phalle, V. M., & Mantha, S. S. (2019). Performance analysis of a conical hydrodynamic journal bearing. Iranian Journal of Science and Technology, Transactions of Mechanical Engineering, 43(3), 559-573. Fig.4 Acceleration Amplitudes comparison between HB & SB at 1500 RPM & 350 N Fig.5 Amplitude Spectrum comparison between HB & SB at 1500 RPM & 350 N
- Singh, H., & Sen, S. S. (2014). Wear in hydrodynamic journal bearings: a review. International Journal Of Modern Engineering Research (IJMER), 4, 45-57.
- Harnoy, A. (2002). Bearing design in machinery: engineering tribology and lubrication. CRC press.
- Rozeanu, L., & Kennedy, F. E. (2001). Wear hydrodynamic journal bearings. In Tribology Series (Vol. 39, pp. 161-166). Elsevier.
- Scott, R. (2008). Basic wear modes in lubricated systems. Mach. Lubr, 7.
- Samanta, B. I. S. W. A. J. I. T., Al-Balushi, K. R., & Al-Araimi, S. A. (2003). Artificial neural networks and support vector machines with genetic algorithm for bearing fault detection. Engineering applications of artificial intelligence, 16(7-8), 657-665.
- Poley, J. A. C. K., & Murphy, M. I. C. H. E. L. (2007). The history of oil analysis. Machinery Lubrication.
- Kankar, P. K., Sharma, S. C., & Harsha, S. P. (2011). Fault diagnosis of ball bearings using machine learning methods. Expert Systems with Applications, 38(3), 1876-1886.
- Roylance, B.J. (2003). Machine failure and its avoidance—what is tribology's contribution to effective maintenance of critical machinery? Proceedings of the Institution of Mechanical Engineers, Part J: Journal of Engineering Tribology, 217, 349 - 364.
- Cerrada, M., Sánchez, R. V., Li, C., Pacheco, F., Cabrera, D., de Oliveira, J. V., & Vásquez, R. E. (2018). A review on data-driven fault severity assessment in rolling bearings. Mechanical Systems and Signal Processing, 99, 169-196.
- El-Thalji, I., & Jantunen, E. (2015). A summary of fault modelling and predictive health monitoring of rolling element bearings. Mechanical systems and signal processing, 60, 252-272.
- Bellini, A., Filippetti, F., Tassoni, C., & Capolino, G. A. (2008). Advances in diagnostic techniques for induction machines. IEEE Transactions on industrial electronics, 55(12), 4109-4126.
- Dai, X., & Gao, Z. (2013). From the model, signal to knowledge: A data-driven perspective of fault detection and diagnosis. IEEE Transactions on Industrial Informatics, 9(4), 2226-2238.
- Henriquez, P., Alonso, J. B., Ferrer, M. A., & Travieso, C. M. (2013). Review of automatic fault diagnosis systems using audio and vibration signals. IEEE Transactions on systems, man, and cybernetics: Systems, 44(5), 642-652.
- Chen, W., & Yuan, H. M. (2014, June). An improved GA-SVM algorithm. In 2014 9th IEEE Conference on Industrial Electronics and Applications (pp. 2137-2141). IEEE.
- Samanta, B. I. S. W. A. J. I. T., Al-Balushi, K. R., & Al-Araimi, S. A. (2003). Artificial neural networks and support vector machines with genetic algorithm for bearing fault detection. Engineering applications of artificial intelligence, 16(7-8), 657-665.
- Vapnik, V. N. (1995). The nature of statistical learning. Theory.
- Gunn, S. R. (1998). Support vector machines for classification and regression. ISIS technical report, 14(1), 5-

Needle Roller Bearing Performance, Issues and Mitigation

Preeti Banzare[1*], Harpreet Singh[2] & Jeremy J. Wagner[3]

[1]John Deere Ltd., India
Email: banzarepreeti@johndeere.com

Abstract

Bearings being basic components of every transmission, are the enablers of the required relative motion. An optimized transmission needs optimally selected and assembled bearings. Needle Roller Bearings have a trait of being capable of taking high radial loads, however, they must be assembled with an optimum radial internal clearance and have a distributed contact zone over the rollers under load. In the current study, NRB failure in a transmission was observed. Investigation of the failed parts pointed towards the possibility of radial internal clearance and misalignment being a concern, as the failure zone on the physical parts was running off the edge. A system level simulation was performed to figure out the root cause of the failure. Simulation results agreed with the condition of the failed bearings, which showed the stress contour falling off the edges of the roller – which alluded to off-cantered contact caused by misalignment under load. To mitigate the problem, Radial internal clearance and Roller micro-geometry were optimized. Roller micro-geometry was corrected in a way that the load should be distributed over the roller length rather than being concentrated on a side and falling off the edge, under load. Redesigned bearing with optimum assembly, met the design goal in physical testing.

Introduction

Selection of bearing in the concept design phase and obtaining required bearing rating life is of the prime considerations of a Drivetrain system. Bearing life depends on various parameters viz. misalignment, vibration of the system, its load carrying capacity, equivalent loads on the bearings, field application, space constraint and system stiffness [1]. A needle roller bearing design must satisfy various constraints, e.g., geometrical, kinematics and the strength, while delivering high reliability, excellent performance, and long life. Misalignment above the allowable limit in Needle roller bearing can cause edge loading on the bearing rollers, which may lead to failure. This invokes a need of an optimal radial internal clearance into the bearing to minimize misalignment and achieve an optimized roller micro-geometry for a distributed contact stress pattern on rollers.

This paper presents a study performed for a transmission system to identify root cause of a Needle Roller bearing failure in a lab test and provide solution to mitigate the problem. To achieve the bearing target life goal, a comprehensive analysis was performed, with a focus on optimizing roller microgeometry, along with tuning the bearing internal clearance to eliminate roller edge loading to achieve even stress distribution. Simulation results correlated well with the lab testing.

ISSUE AND MITIGATION APPROACH

For the problem area under investigation, a Gear is mounted on a set of two Needle roller bearings, on Differential Drive Shaft. Lab test outcomes showed that the bearing is damaged over the roller edges and discrete loading marks are evident. To understand the system behavior, the transmission system was modeled and analyzed in simulation software (A). For simulation outcomes, bearing lives and contact stress patches were observed and were compared to the physical test results. A >80% correlation was observed between the outcomes from physical and simulation domains – edge loading on Needle Bearing Rollers, pointing towards high misalignment (Fig.1, 2 and 3).

In the contact stress plots "S" indicates the highest stress value in Mpa.

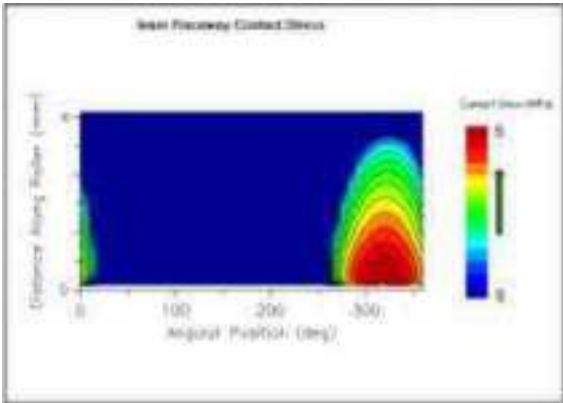

Figure:1- Tested bearings in Lab.

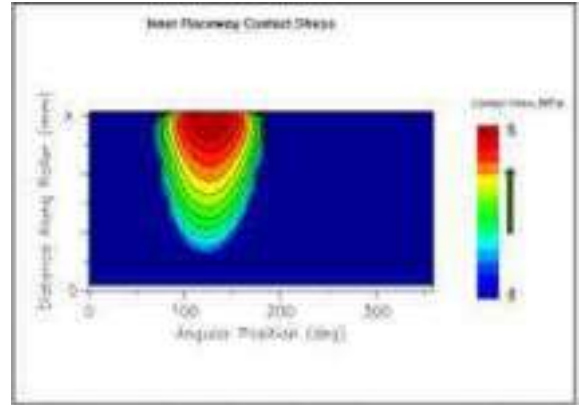*Figure:2 – Roller Contact Stress patterns
(LH Side - Bearing.)*

*Figure:3 - Roller Contact Stress patterns
(RH Side -Bearing.)*

To mitigate the issue as an initial measure, radial internal clearance was iterated, which helped the cause, however, not to the extent desired. It did not move the contact patch completely off the edge. Geometric, assembly and manufacturing constraints did not allow significant changes to the gears and shafts, leaving only option to optimize the roller micro-geometry (Fig. 4). Based on the simulation results, an optimal bearing size, radial internal clearance and micro-geometry was recommended for the optimal system performance.

Figure:4 - Optimized Roller Crowning

Results & Discussion

As per the provided design recommendations, next set of analysis was performed to evaluate bearing lives and contact stress patches. (Fig. 5, 6). Contact Stress was taken off the edge, hence, relieving the needles from edge loading.
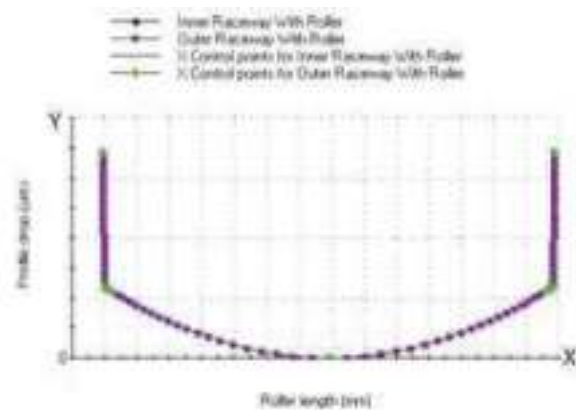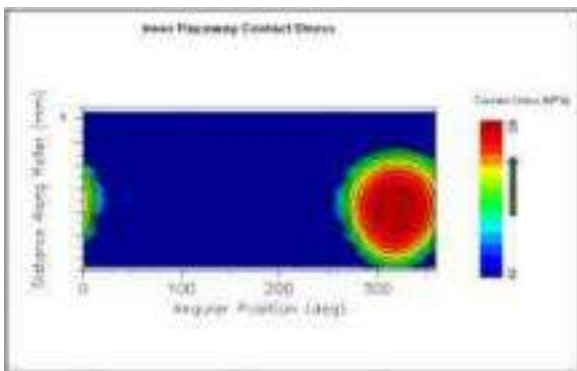

*Figure:5 - Optimized contact stress patterns on
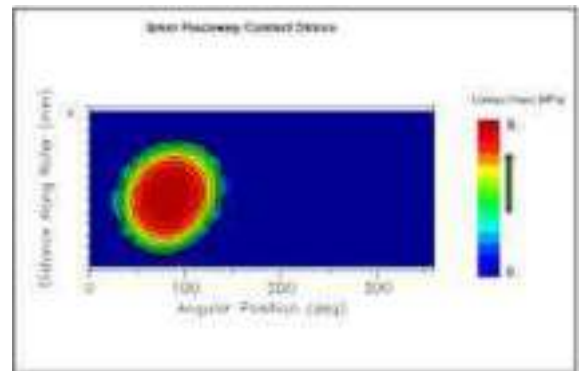Rollers (LH side Bearing)*

*Figure:6 - Optimized contact stress patterns on
Rollers (RH side Bearing)*

Eventually, the new needle roller bearings made as per the recommended specifications met the target life in physical testing (Fig. 7, 8).

Figure: 7 - Post Test picture of NRBs made as per recommended specifications.

Figure: 8 - Tested gear bore with new Needle Roller Bearings

Conclusion
- Needle roller bearings are very sensitive to misalignments.
- Optimum radial internal clearance must be ensured during the assembly to achieve optimum performance.
- Distributed stress over the roller length is key to the bearing performance. For misaligned bearings, this can be achieved by optimizing microgeometry.
- It is highly recommended to perform a system simulation during the design stage. An upfront simulation can detect design and performance issues and can increase the chances of first pass yield to multifold.

References
- Prashant M. Jundale Department of Mechanical Engineering, PG Student, SKN Sinhgad college of Engg. "Optimization of Needle Roller Bearing System by using Finite Element Analysis", International Journal of Engineering Research & Technology (IJERT) IJERT ISSN: 2278-0181 Vol. 3 Issue 5, May – 2014
- https://www.sciencedirect.com/topics/engineering/needle-roller-bearings - ScienceDirect
- https://www.bearing-news.com/the-importance-of-bearing-selection-on-gearbox-performance/ - Bearing News.com

Development of highly durable self-regenerative superhydrophobic coatings through flame spraying

Aaishwarika Sharma, Harpreet Arora, and Harpreet Singh Grewal
Surface Science and Tribology Lab, Department of Mechanical Engineering, Shiv Nadar University, India
Email: harpreet.grewal@snu.edu.in

Key Words: Tribology, Wear, Materials, Lubrication

Abstract

Superhydrophobic surfaces with excellent water repellency helps in attaining multi-dimensional features such as self-cleaning, anti-icing, anti-fogging. However, poor tribological properties of these eminent surfaces results in reduced durability. In present work, fabrication of self-regenerating superhydrophobic coatings is demonstrated using economical flame spraying technique. The self-regenerative behavior helps circumvent the durability issue, hindering the use of superhydrophobic surfaces. Different coatings of aluminum were developed on the mild steel substrates through systematic variation of standoff distance and air pressure. The developed aluminum coatings showed formation of a multi-order hierarchal roughness from nano to microscale with in-situ formation of nano alumina particles. The variation in spraying parameters showed significant influence on the morphology and wetting behavior. All coatings showed superhydrophilic behavior with transition to superhydrophobicity after surface modification using 1H,1H,2H,2H-Perfluorooctyltriethoxysilane. The coatings were able to achieve high advancing angles in excess of 155 ° and receding angles more than 150 ° exhibiting low contact angle hysteresis. All the coatings also showed excellent water droplet rolling with sliding angles less than 5°. Similar to many natural superhydrophobic surfaces, the coated samples also showed very low adhesion to the water droplet (< 50 μN). The self-regenerative behavior of the coating was investigated using abrasion test performed at 100 mN load for more than two hours against 2000 SiC abrasive paper as counter surface. The coating developed at larger standoff distance showed high durability illustrated through regained surface morphology and chemistry after mechanical abrasion and consistent de-wetting characteristics. The coating also exhibited excellent self-cleaning properties against different types of contaminants. Developed coating through flame spraying provides a cost effective and facile approach for generation of robust self-cleaning superhydrophobic coatings for various outdoor applications.

Introduction

Bio-inspired superhydrophobic surfaces, with unique properties such as self-cleaning, anti-corrosion, drag reduction and anti-freezing properties, are of increasing interest to researchers due to their applicability to real-world problems [1]. The focus is on developing robust and durable superhydrophobic surfaces to improve poor tribological behavior. There are different methods like hydrothermal [2], etching [3], sol-gel [4], electrospinning [5], and electro-deposition [6] for fabrication of superhydrophobic coatings. The Cassie state achieved due to entrapped air in cavities created by enhanced surface roughness is less stable for such coatings. The coatings fabricated using these methods are less resistant towards abrasion and have low durability. In this study a new route for fabrication of superhydrophobic surface using inexpensive flame spray technique is developed. The coatings developed by flame spray method generates multi-order hierarchal surface roughness, which is essential for a superhydrophobic surface. The flame spray coating is an inexpensive method and have ability to produce nano-porous coatings which act as a texture of surface and promotes wetting behavior.

EXPERIMENTAL DETAILS

The aluminum powder is purchased from MEC, India. The aluminum coatings are deposited on 10 x 10 x 5 mm mild steel substrates coupons. The oxy-acetylene flame at 1.1 bar and 2.2 bar respective pressure are used to melt the powder. Prior to flame spraying the substrate are chemically etched in in 5 % HNO3 solution for 2 minutes to generate roughened surface for better coating-substrate adhesion. The air pressure of cooling jet assembly and stand-off distance are varied from 0.5 to 2 bar and 2.5'' and 4.5'' respectively. The surface chemistry of surface is modified by depositing 1H,1H,2H,2H-Perfluorooctyltriethoxysilane (FOTES) coating using vapor deposition technique at 150 °C for 90 minutes. The morphological examination and elemental chemical distribution are conducted via field emission scanning electron microscope, FESEM (JEOL, JSM-7610FPlus, Japan) with 15 kV accelerating voltage equipped with energy dispersive spectroscopy, EDS. The contact angle measurements were performed on Goniometer (Apex, India). The adhesion force was measured using the force tensiometer (Sigma 701, Sweden). The Atomic force microscopy, AFM (Park systems, XE7, Korea) on a scan area of 2 x 2 μm2 with 0.5 Hz scan rate was used for three-dimensional surface morphology examination. The mechanical durability was performed on

Tribometer (Rtec, USA), using 2000 abrasive sheet as counter surface. The rain impact durability was evaluated in rain simulator at 0.25 kg/cm2 at 300 mm distance. The corrosion studies were performed in in 3.5 % NaCl in potentiostat (Gamry, 100E) in a three- electrode system. The potentiodynamic polarization and electrochemical impedance spectroscopy (EIS) test were performed on coatings to evaluate the corrosion behavior. The self-cleaning behavior of superhydrophobic surface was evaluated using different types of contaminants.

RESULTS & DISCUSSION

The multi-order hierarchal structures were seen in FESEM with micropores at splat boundaries as shown in Fig.1. The oxidation was promoted with increase in stand-off distance resulting in sponge like nanostructures as seen in Fig.1(b) inset. These nanostructures appeared as a texture on the surface and increased the surface roughness. Whereas in Fig. 1 (a) at low stand-off distance the nanostructures are absent due to low tendency of oxidation. The accelerated molten/semi-molten particles in the flame impact the substrate surface and rapid cooling of particles leads splat formation with splashing. The generated morphology led to enhanced wetting behavior. The high oxygen content was witnessed in EDS analysis for samples with high stand-off distance. The coatings at high stand-off distance developed nano-composite coatings with in-situ formation of nano alumina particles which is clearly visible in cross-sectional analysis of coating in Fig.1(c). The coatings achieved advancing angles greater than 153 ° and receding angles greater than 150 ° with sliding angle less than 5 °.The coatings were able to achieve very low adhesion even for some samples adhesion was less than that of lotus [7]. The samples have shown high resistance to abrasion and rain impact. Also, after mechanical abrasion coatings were able to regenerate the similar morphology and surface chemistry which proclaim the self-regeneration behavior. The evaluation for self-regenerative behavior was done by contact angle measurements after each abrasion cycles as shown in Table 1. The superhydrophobic samples retained the de-wetting behavior for more than one hour after abrasion. The self-cleaning behavior of superhydrophobic coatings were revealed using different contaminants like chalk dust, sand, muddy water, coca-cola, and milk. The coatings were able to clean all the contaminants. The coatings exhibited high corrosion resistance in comparison to substrate for both potentiodynamic polarization and EIS test. The coatings deposited at high stand-off distance displayed lower corrosion current density. The sample at high stand-off distance improvised corrosion resistance by
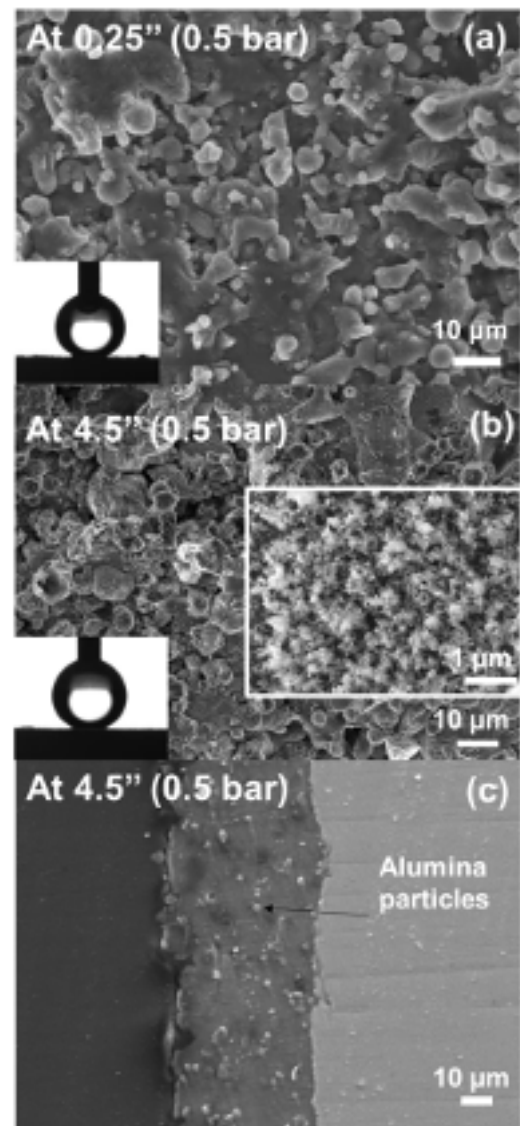

Fig. 1: Surface morphology using FESEM (a) Microstructural analysis of superhydrophobic coating at 2.5 inch stand-off distance and 0.5 bar air pressure, (b) Microstructure analysis for superhydrophobic coating at 4.5 inch stand-off distance and 0.5 bar air pressure with inset of sponge like nanostructures (c) Cross-sectional analysis for coating at 4.5 inch at 0.5 bar depicting the in-situ formation of alumina particles in aluminum coating

1.8 times compared to mild steel. The similar coating has shown highest polarization resistance of 1.47×10^3 $\Omega.cm^2$ whereas, polarization resistance for mild steel was 207.3 $\Omega.cm^2$. The coated samples were able to retain the superhydrophobicity even for more than 48 hours in immersed conditions

Table 1: Analysis of self-regenerative behavior based on contact angle measurement at 0.5bar air pressure at 4.5'' stand-off distance

Time (min)	Advancing angle (°)	Receding Angle (°)
0	154 °	152 °
15	154 °	152 °
30	153 °	151 °
45	150 °	147 °
60	148 °	143 °

CONCLUSIONS

The self-regenerative, robust, and mechanically durable superhydrophobic surfaces were fabricated through economical flame spray technique. The aluminum coatings with multi-order hierarchal surface roughness on mild steel substrate resulted in enhanced de-wetting behavior. The coatings have achieved high advancing and receding angles with low contact angle hysteresis. The sliding angles less than 5 ° enhanced the self-cleaning behavior. At high stand-off distance the in-situ development of alumina particles resulted in formation of nano-composite coatings, enhancing the mechanical durability. The superhydrophobic coatings improved the tribological behavior. The corrosion resistance was improved at most by 1.8 times in comparison to substrate. The improved polarization resistance in EIS scan also proved better corrosion performance of superhydrophobic samples.

References

○ J. Lin, Y. Cai, X. Wang, B. Ding, J. Yu, M. Wang, Fabrication of biomimetic superhydrophobic surfaces inspired by lotus leaf and silver ragwort leaf, Nanoscale 3(3) (2011) 1258-1262.J. Ivvala, H.S. Arora, H.S. Grewal, Development of superhydrophobic metallic surfaces with tuned morphology through microwave processing, Materials Chemistry and Physics 275 (2022) 125310.

○ Z. Wei, D. Jiang, J. Chen, X. Guo, Combination of chemical etching and electrophoretic deposition for the fabrication of multi-scale superhydrophobic Al films, Materials Letters 196 (2017) 115-118.

○ Y. Fan, C. Li, Z. Chen, H. Chen, Study on fabrication of the superhydrophobic sol–gel films based on copper wafer and its anti-corrosive properties, Applied Surface Science 258(17) (2012) 6531-6536.

○ V.A. Ganesh, A.S. Nair, H.K. Raut, T.T. Yuan Tan, C. He, S. Ramakrishna, J. Xu, Superhydrophobic fluorinated POSS–PVDF-HFP nanocomposite coating on glass by electrospinning, Journal of Materials Chemistry 22(35) (2012) 18479-18485.

○ S. Bai, X. Liu, L. Xu, J. Xuan, Y. Liu, Y. Shao, Y. Xin, X. Li, L. Fan, Enhancement of corrosion resistance and lubricating performance of electrodeposited Ni-Co coating composited with mesoporous silica nanoparticles and silicone oil impregnation, Materials Chemistry and Physics 282 (2022) 125929.

○ H.J. Ensikat, P. Ditsche-Kuru, C. Neinhuis, W. Barthlott, Superhydrophobicity in perfection: the outstanding properties of the lotus leaf, Beilstein journal of nanotechnology 2 (2011) 152-61.

Augmenting The Performance of Eco-friendly Greases Using Synergistic Natural Resources

Ankit Saxena[1], Deepak Kumar[1*], Naresh Tandon[1]

[1] Centre for Automotive Research and Tribology, Indian Institute of Technology Delhi, India
*Corresponding author (E-mail: dkumar@iitd.ac.in)

Keywords: Grease, Vegetable Oil, Polysaccharide Gum, Tribology

Abstract

The grease industry extensively uses non-renewable, non-biodegradable, and toxic entities as ingredients that collectively achieve the desired performance, however, at the cost of environmental health. Several eco-friendly ingredients have been tried to formulate environmentally benign greases; however, a potential alternative is not yet reached. The present study explores a maiden effort to enhance the performance of eco-friendly greases (based on vegetable oil and organoclay) using polysaccharide gums as additives. Two different series of greases containing 0 - 10 %w/w of gum acacia (GA) and guar gum (GG) are developed, characterized, and evaluated for tribology, i.e., anti-wear (AW) and extreme-pressure (EP) tests as per ASTM standards. GG-based greases displayed superior AW (up to $\approx$ 22% enhancement), frictional (up to $\approx$ 42% enhancement), and EP response (up to $\approx$ 60% enhancement). Whereas GA-based greases displayed superior EP characteristics (up to $\approx$ 60% enhancement), however, inferior AW response.

Introduction

Lubricating oils and greases are widely used in industry to mitigate energy losses and prevent machine damage or failure. Greases are semi-solid lubricants made of two primary ingredients: base oils and thickeners. Apart from these, various additives are blended frequently to grease to tailor their characteristics. The grease industry extensively uses harmful entities as ingredients that satisfy the performance goals and jeopardize the environment simultaneously. A potential, sustainable, and economical, eco-friendly alternative to harmful petroleum-based lubricants is, therefore, a big challenge for the 21st-century lubricant industry. The present study explores, for the very first time, an effort to enhance the performance of eco-friendly greases (based on vegetable oil and organoclay) using biopolymers (like polysaccharide gums) as additives. Polymers have shown enormous potential as a lubricant additive in the past. However, their environmentally friendly counterparts, i.e., biopolymers, have never been explored as a lubricant additive. Polysaccharide gums are biopolymers that have shown tremendous prospects [1-3] in various tribological applications involved in cosmetics, pharmaceuticals, printing, adhesives, textile, oil drilling, food, etc. Their superior tribology is due to numerous reactive functional groups (carboxyl, hydroxyl, amino) in the structure that facilitates easy anchoring over metallic surfaces to form protective films [4]. Besides better tribology, polysaccharide gums are biodegradable, renewable, non-toxic, economical, and widely available.

Experimental Details

Two different series of greases containing 0.5 - 10 %w/w of the gums, i.e., gum acacia (GA) and guar gum (GG), are developed and evaluated for antiwear (AW) and extreme-pressure (EP) tests as per the ASTM standards. The proportion of ingredients was decided to develop greases with bearing grade consistency (i.e., NLGI 2) as greases are used most frequently in the rolling bearings. The maximum doping was constrained to 10 % w/w as consistency appeared to change beyond that. An all-purpose mineral oil-based commercial grease was used for benchmarking purpose (the name is not disclosed because of copyright issues).

A Four-ball tester (Ducom Instruments, India) was utilized to record the AW and EP characteristics of greases as per ASTM D2266 and ASTM D2596 standards. The instrument configuration comprises a three-point sliding contact of steel balls in which an upper ball rotates over the lower three stationary balls clamped in a ball pot. The pot is filled with sufficient grease to cover the contacting points completely. In the AW test, a load of 392 N, a rotating speed of 1200 RPM, and an operating temperature of 75 °C were applied for a 1-hour duration. The variation of frictional torque (FT) with time and overall coefficient of friction (c.o.f.) were recorded for each experiment to evaluate the frictional performances of greases. The size of the wear scars on the lower stationary balls was measured using an optical microscope (accuracy = $\pm$ 0.01 mm), and the average wear scar diameter (WSD) of three balls was recorded for each experiment. Triplicate experiments were performed for each grease, and the average response was reported. In the EP test, the upper ball is rotated at a speed of 1770 $\pm$ 60 RPM, a temperature of 27 $\pm$ 8 °C, and for a duration of 10s under an applied load, and welding of balls is observed. Load is increased progressively in steps till welding is

confirmed. Triplicate runs were performed on each load for the determination of weld load (WL) and pre-weld load (PWL). The WL is the lowest applied load at which the sliding surfaces seize and then weld, whereas the PWL is the highest applied load at which the surfaces slide without seizure or welding.

After AW and EP tests, worn surfaces were investigated using a scanning electron microscope (SEM), energy dispersive spectroscopy (EDS), FTIR spectroscopy, and 3D optical profilometry to understand the interfacial lubrication mechanisms.
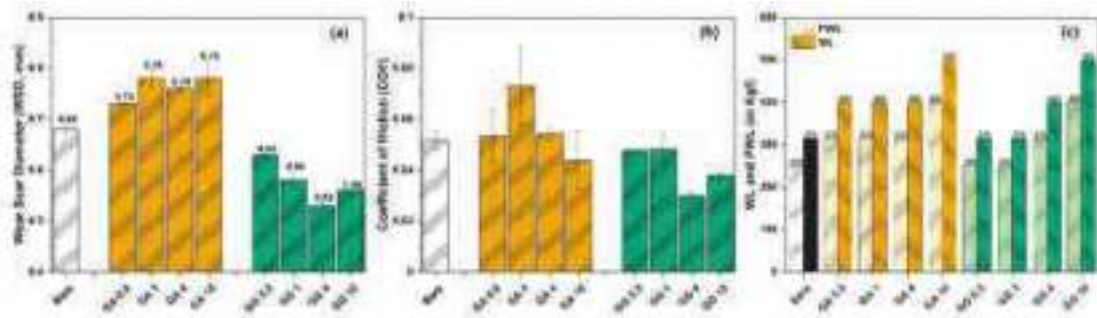
Results & Discussion

Figure 1. Grease tribological characteristics - (a) Wear scar diameter (WSD), (b) Coefficient of friction (COF), and (c) weld load (WL) and pre-weld load (PWL)

Figure 1a and 1b show the antiwear characteristics of different greases in terms of wear scar diameter (WSD) and coefficient of friction (c.o.f). Figure 1c shows the weld loads (WLs) and pre-weld loads (PWLs) for different greases (extreme-pressure characteristics).

In the case of GA-based greases, compared to the bare grease, the WSD increases on adding GA to grease at all concentrations (figure 1a). However, no clear trend is observed between GA's concentration and WSD. From the comparison of c.o.f, it is clear that, except for GA-10 grease, none of the formulations showed lower c.o.f. than that of the bare grease (figure 1b).

In the case of GG-based greases, compared to the bare grease, the addition of GG results in lower WSDs at all concentrations (figure 1a). The WSD decreases progressively with an increase in GG concentration from 0.5% to 4% and then increases with further addition (for GG-10). This suggests an optimum concentration of GG for the maximum reduction in WSD. The GG-4 registers the most impressive AW characteristics among all greases ($\approx$ 22% reduction in WSD compared to bare grease). The optimal performance of GG-4 is almost equivalent to that of commercial grease. All the GG-based formulations display better frictional coefficients than bare grease (figure 1b), with GG-4 registering the most significant reduction of $\approx$ 42% (lower c.o.f than commercial grease).

The contradictory AW behavior of polysaccharide gums is attributed to their different interfacial interaction tendencies (synergistic for GG and antagonistic for GA) with organoclay. The attraction between the lone pair of electrons of oxygen (of GG) and the metal surface facilitates the formation of a physisorbed tribofilm (thereby reducing wear) in GG-based greases. The dendritic polymer architecture of GG stimulates the formation of a thicker film with freely moving polymer arms acting as molecular brushes assisting smooth shearing (thereby reducing friction).

Unlike AW characteristics, both the series of polysaccharide gums-based greases display impressive EP performances compared to the bare grease and the commercial grease. For GA-based greases, even at the slightest addition of 0.5%, GA is activated and registers a $\approx$ 26% increment in PWL compared to the bare grease. Increased concentration from 0.5% to 10% further enhances the EP performance; however, an apparent increment is registered by GA-10 ($\approx$ 60% increment). For GG-based greases, an enhancement in the EP performance is not observed at lower concentrations up to 1%. With a further increase in GG concentration, a $\approx$ 26% increment and a $\approx$ 60% increment are registered by GG-4 and GG-10, respectively.

The superior EP performance is attributed to an in-situ formed polymer-layered silicate nanocomposite tribofilm at the interface via chemisorption (GA) or physisorption (GG) based upon the results of microscopic and spectroscopic explorations.

Conclusions

Organoclay-polymer synergism is exploited to develop novel, high-performance greases that can serve as a possible eco-friendly alternative for harmful mineral oil-based greases ($\approx$ 60% better in terms of EP characteristics and equivalent in lubricity). Guar gum (GG) enhances the AW response ($\approx$ 22% reduction in WSD) and frictional response ($\approx$ 42% reduction in c.o.f.) when added to greases in the concentration range 0.5 – 10 %w/w. On the contrary, the addition of gum acacia (GA) leads to inferior tribological responses. Optimal lubricity performance (equivalent to the commercial grease) is achieved by adding 4 %w/w GG in greases. Polysaccharide gums have immense potential as EP additive for greases based on vegetable oil and organoclay. Adding GA or GG to such greases enhances EP performance by up to $\approx$ 60%, and the performance ameliorates with gum's concentration.

This research is a step ahead in pursuing a potential, economical, and sustainable solution of providing an eco-friendly alternative to long-established harmful mineral oil-based greases. The study explores and recommends polysaccharide gums as performance additives to greases based on vegetable oil and organoclay.

References

❍   Methacanon P, Gamonpilas C, Kongjaroen A, Buathongjan C. Food polysaccharides and roles of rheology and tribology in rational design of thickened liquids for oropharyngeal dysphagia: A review. Compr Rev Food Sci Food Saf 2021;20:4101–19. https://doi.org/10.1111/1541-4337.12791.

❍   Zafar R, Zia KM, Tabasum S, Jabeen F, Noreen A, Zuber M. Polysaccharide based bionanocomposites, properties and applications: A review. Int J Biol Macromol 2016;92:1012–24. https://doi.org/10.1016/j.ijbiomac.2016.07.102.

❍   Yu Y, Shen M, Song Q, Xie J. Biological activities and pharmaceutical applications of polysaccharide from natural resources: A review. Carbohydr Polym 2018;183:91–101. https://doi.org/10.1016/j.carbpol.2017.12.009.

❍   Singh Lodhi AP, Kumar D, Kaur T, Singh N. Development of lubricious, non-toxic, and corrosion-resistant metalworking fluid: A possible replacement for mineral oil-based fluids. J Clean Prod 2021;323:129173. https://doi.org/10.1016/j.jclepro.2021.129173.

A Comparative Study Of Rolling Bearing Fault Classification Using Cwt-cnn and Stft-cnn Methods

Thomas Joseph[1*], Keerthi Krishnan K[2] and Sudeep U[3]

[1]Research Scholar Department of Mechanical Engineering NSS college of Engineering Palakkad, APJ Abdul Kalam Technological University Trivandrum 695019, India

[2]Department of Electronics and Communication Engineering NSS college of Engineering Palakkad 678008, India

[3]Department of Mechanical Engineering NSS college of Engineering Palakkad 678008

tjk4411@gmail.com, keerthikrishnank@nssce.ac.in, sudeep@nssce.ac.in

Abstract

Early fault detection (EFD) of rolling bearing is critical for healthy and long operation of the rotating machinery. In addition to EFD, fault classification is also important in overall diagnosis of rolling bearing condition. Many researchers have focused on time and frequency-domain based approaches for EFD. Very recently, machine learning based methods are gaining priority in automatic fault feature extraction and fault classification. This work is focused on the effectiveness of two different methods for EFD and fault classification. The first method comprises of combining Continuous Wavelet Transform (CWT) and Convolutional Neural Network (CNN) for fault diagnosis and classification whereas, the second method uses a combination of Short-Term Fourier Transform (STFT) and CNN. Alexnet is a widely used CNN for image classification which provides superior results. In this work Alexnet is used for the classification of images of vibration signals. Initially vibration data is acquired from healthy bearing as well as bearings having various seeded defects on the races and balls. The CWT and STFT images are generated from the vibration data and the image data is used for training and testing in CNN. An accuracy of 95.8% is obtained for CWT and CNN combination while 92.2% for STFT and CNN combination.

Introduction

Rolling bearing is an important component of all rotating machinery. The faults in rolling bearing can lead to catastrophic failure of the rotating machinery. Rolling bearing defects are categorized as local defects and distributed defects. Local defects involve defects in inner race, outer race and in rolling elements i.e. the ball. The distributed defects are mostly waviness and misalignment.

Early fault detection of rolling bearing helps to avoid many issues and especially important in critical applications. Various early fault detection methods are classified as vibration-based, sound based, current based and torque based. Among these methods vibration based early fault detection methods have prime importance due to high sensitivity. The vibration-based fault detection methods are classified broadly as fault frequency identifiation methods and automated early fault detction using machine learning methods. The most commonly used fault frequency identification methods are Fourier transform, wavelet transforms (WT), decomposition methods. WT methods are further classified as continuous wavelet transform (CWT), discrete wavelet transform (DWT) and wavelet packet transform (WPT). Similarly decompsotion methods are research include empirical mode decomposition (EMD), ensemble empirical mode decomposition (EEMD), local mean decomposition (LMD) and variational mode decomposition (VMD). Artificial Neural network (ANN), SVM, KNN and deep learning networks are some of the machne learning methods [1,2].

Modal decomposition methods like EMD, VMD along with classification using ANN and KNN exhibits better accuracy since fault features are predominant after decomposition [3]. Ensemble empirical mode decomposition (EEMD) along with CNN can classify the faults, but the selection of modes of the fault feature is difficult [4]. Few researchers introduced short term Fourier transform (STFT) and CWT for fault frequency analysis [5], but these two techniques do not give an accurate prediction about the bearing faults due to the presence of noise. Thus, noise removal is an important parameter while predicting the condition of the bearing. A method for fault diagnosis of ball bearing by Hilbert- Huang Transform (HHT) to classify bearing fault pattern is described [6]. A one-dimensional CNN for fault detection and identification of rolling bearings is proposed [7] which can provide better classification accuracy. However [8] proposed a CNN network for bearing fault diagnosis under noisy operations. CNN is the most used Deep learning algorithm that identify the feature automatically [9]. Meanwhile it is very difficult to classify the

faults accurately. A deep convolutional network based and the domain adaptation is used to classify the faults accurately which can give better classification accuracy when the data available is large [10]. However, it consumes more time for the training and validation of data. CWT and CNN in diagnosis of aero-engine control system with a classification accuracy of 97% has also been reported [11]. But the application of this method is not observed for fault detection and classification of defects in rolling bearings. Alexnet network is found to be used for detecting and classifying bearing fault, where the bearing signal is decomposed by using EEMD improving the fault feature classification [12].

Compared to conventional methods, deep learning methods have distinct advantages in fault detection and classification. Conventional methods require a complex computational procedure for feature extraction while deep learning methods like CNN, feature extraction is achieved by including different layers. In this paper a comparative study of CWT – CNN and STFT-CNN for early fault detection of rolling bearing are implemented and compared with classification accuracy. The AlexNet is used as the CNN for classification.

Experimental Details
A rolling bearing test rig is shown in figure 1. An ICP type accelerometer is attached at the load zone of the test bearing and is connected to a 2-channel ,102.4 kS/s/ch Simultaneous, ±5V, C Series Sound and Vibration Input module provided by National Instruments. With the help of LabVIEW software, raw vibration signals under different conditions are taken for testing and validation.

In this study SKF 6007 deep groove ball bearings are used. The defects are seeded at different sizes in the races of the bearings using electric discharge machining. The various defects are seeded in ball inner race, outer race and in combination at inner and outer races and balls are shown in figure 2. Thousand vibration data sets are taken from a healthy bearing and bearings under different fault conditions under a load of 100N and operating speed of 1000 rpm so that to get fairly large amount of experimental data for training and testing.

After acquiring data using experimental setup detailed above, CWT as well as STFT of the signal is computed and plotted. Thus, the time frequency plot obtained from CWT and STFT are reshape into images of size 227 x 227 x 3. The reshaping helps in implementing transfer learning approach for training as the input layer of AlexNet is of size 227 x 227 x 3. CWT and STFT images of the signals are obtained with the help of MATLAB.

The AlexNet is trained and validated using the CWT-image and STFT-image of the vibration signals separately. Figure 3 shows the flow diagram for the methodology adopted.

While training initially the learning rate is set to a small value and later increased the leaning rate.   Out of the acquired data, 80% data is used for training and 20% for testing. In CWT-CNN initially the learning rate is set to 0.01 for training of CWT images using Alex net network.

Training accuracy of 100% and validation accuracy of 50% is obtained while on further changing the learning rate to 0.001 it is found that the validation accuracy changes to 92% while training rate validation accuracy
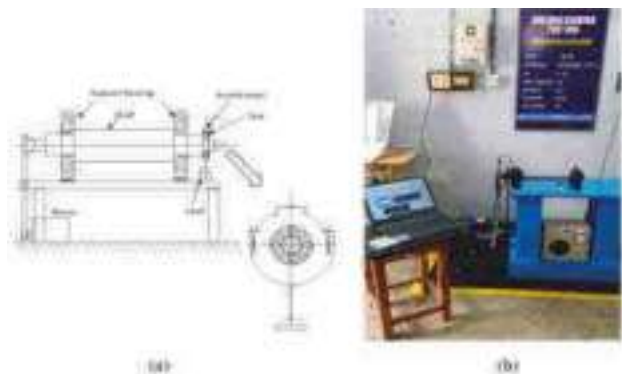

Figure 1: Rolling bearing test rig
(a) Schematic diagram (b) Experimental setup

Figure 2: Defects in
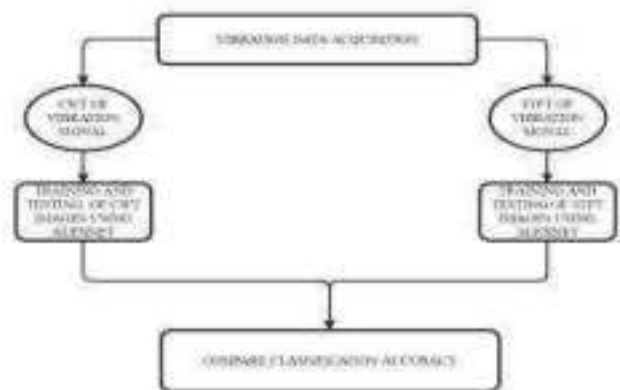*(a)Inner race (b) Outer race in SKF ball bearing*

Figure 3: Flow diagram of CNN in Bearing fault Classification using both CWT and STFT images

reaches a saturation of 95.8%. For a training rate of 0.0001 the training accuracy remains unchanged as 100%. For a training rate of 0.01 STFT+ CNN method shows an accuracy of 100% during training and 50% during testing on further decreasing the training rate up to 0.0001. This combination shows an accuracy of 92.8 % in validation and 100 percentage in training.
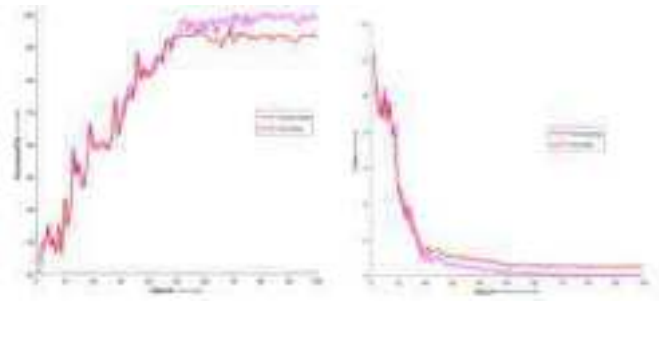
Results & Discussion

Figure 4 shows the accuracy and loss plots of CWT-CNN method. From accuracy evaluation plot, it is observed that with an epoch rate of 100 the accuracy is 95.8% in testing and 100% in training.
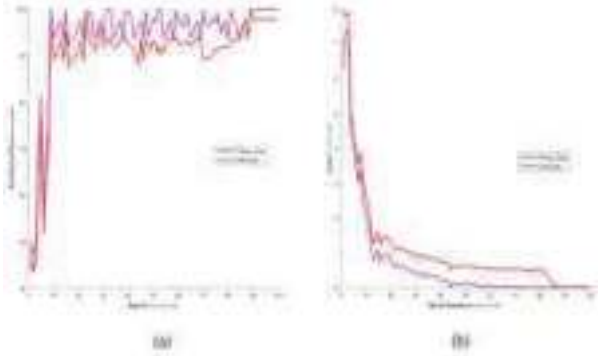
Figure 4: 2CWT+CNN
(a)Accuracy evaluation plot (b)Loss evaluation plot

Figure 5: STFT+CNN
(a) Accuracy Evaluation plot (b)Loss Evaluation plot

Figure 5 shows the accuracy evaluation plot and loss evaluation plot of STFT-CNN from accuracy evaluation plot analyzed that with in an epoch of 100 we can get an accuracy of 92.8% for validation and almost 100% accuracy on training.

Conclusions

A comparative study of CWT-CNN and STFT-CNN has been conducted. These methods show a superior classification accuracy than conventional methos. Transfer learning plays an important role in fault detection and classification. From the graphs we can find out that classification accuracy of images obtained by CWT will give more validation accuracy than the images from STFT. Accuracy evaluation plots for both the methods show that an epoch of 100 saturation level is obtained. Classification accuracy of CWT-CNN method is 95.8 and STFT-CNN method is 92.8. It is concluded that CWT-CNN is a better classification method for early fault identification in rolling bearing in comparison with STFT-CNN.

References

○ Wei. Y, Li. Y, Xu. M., and Huang. W, "A review of early fault diagnosis approaches and their applications in rotating machinery," Entropy,2019, vol. 21, pp-4

○ Kankar.P.K., Satish C. Sharma, Harsha S.P, "Fault diagnosis of ball bearings using machine learning methods", Expert Systems with Applications,2011, vol.38, pp.1876-1886.

○ Ben Ali. J, Fnaiech N, Saidi L, Chebel-Morello B, and Fnaiech F, "Application of empirical mode decomposition and artificial neural network for automatic bearing fault diagnosis based on vibration signals," Applied Acoustics,2015, vol. 89, pp. 16–27.

○ Toma R. N, Kim C. H, and Kim J. M, "Bearing fault classification using ensemble empirical mode decomposition and convolutional neural network," Electronics (Switzerland), 2021, vol. 10, pp 11

○ Saxena M., Bannet. O, Gupta M, and Rajoria R. P, "Bearing Fault Monitoring Using CWT Based Vibration Signature," in Procedia Engineering, 2016, vol.144, pp.234–241.

○ Kabla A. and Mokrani K, "Bearing fault diagnosis using Hilbert-Huang Transform (HHT) and support vector machine (SVM)," Mechanics and Industry, 2016, vol. 17, pp-3

○ Eren L., "Bearing fault detection by one-dimensional convolutional neural networks," Mathematical Problems in Engineering,2017.

○ Zhang W, Li C, Peng G, Chen Y, and Zhang Z, "A deep convolutional neural network with new training methods for bearing fault diagnosis under noisy environment and different working load," Mechanical Systems and Signal Processing, 2018 vol. 100, pp. 439–453.

○ Alzubaidi L "Review of deep learning: concepts, CNN architectures, challenges, applications, future directions," Journal of Big Data,2021 vol. 8, pp-1.

○ Xu J, Huang J, Zhao Y, and Zhou L., "A robust intelligent fault diagnosis method for rolling bearings based on Deep convolutional neural network and Domain Adaptation," in Procedia Computer Science, 2020, vol. 174, pp. 400–405.

○ Gou L, Li H, Zheng H and Pei X., "Aeroengine Control System Sensor Fault Diagnosis Based on CWT and CNN," Mathematical Problems in Engineering,2020.

○ Shi X, Cheng Y, Zhang B, and Zhang H, "Intelligent fault diagnosis of bearings based on feature model and Alexnet neural network," in Proceedings of the Annual Conference of the Prognostics and Health Management Society, PHM, 2020.

Influence of Indian Footwear Tread Wear on Friction at the Shoe-floor Interface During Slips

Shubham Gupta[1], Subhodip Chatterjee[1] and Arnab Chanda[1,2,*]

[1]Centre for Biomedical Engineering, Indian Institute of Technology (IIT) Delhi, India
[2]Department of Biomedical Engineering, All India Medical Institute of Medical Sciences (AIIMS), Delhi, India
*Corresponding Author (E-mail: arnab.chanda@cbme.iitd.ac.in)

Abstract

Accidental injuries sustained due to slipping and falling incidents are very common in the workplaces. The major reason for these accidents is the inadequate friction available at the shoe-floor interface. Furthermore, the presence of slippery contaminants (i.e., water or oil) over the flooring significantly increases the slipping hazards. In addition to the existence of slippery pollutants, wearing of outsole treads over time is one of the key reasons that can lead to a large reduction in the friction. Although footwear-based slip risk assessment has been performed extensively on a variety of floorings and pollutants, limited studies have examined the influence of worn shoes on slipping. In the current work, four high selling footwear from popular Indian brands were considered to study their slip severity in new and worn conditions. The topographical features of the outsoles were modelled, progressively worn, and slip tested using a customized tribometer (i.e., British pendulum skid tester) across three types of contaminant situations (i.e., dry, water, and canola oil) and three different floorings (i.e., laminate, ceramic, and anti-skid). Reduction in the ACOF values ranged from 40% to 90% as the outsoles were worn progressively. Outsoles consisting oblique tread design were found to produce high friction as compared to other tread geometries. Increase in worn area was found to strongly correlate ($R2=0.86$) with the decrease in friction. The economical modelling methods and the study results are anticipated to provide guidelines for footwear manufacturers in the selection of appropriate tread designs and suggesting the replacement thresholds.

Introduction

Accidental occurrences like slips and falls are frequent, resulting in numerous severe injuries [1] .Additionally, slip-and-fall incidents are a common occurrence in India [2] which accounts for around 80% total cases across the world [3]. Slips and falls happen when there is a sudden decrease in the amount of friction that is available between the floor and the footwear [4]. The significance of footwear in reducing these risks is often overlooked since there is little understanding of the causes of these incidents. Therefore, it is crucial to evaluate how well Indian footwear grips common slick surfaces. These situations frequently result from a quick decrease in friction during a variety of gait activities (such as walking, running, and recreational activities)[5]. By calculating the available coefficient of friction (ACOF) at the contact between the floor and the shoe, these changes can be measured[6]. The outsole tread pattern, material hardness, progressive wear, kind of flooring, and existence of slippery materials on these floorings are vital aspects that influence a shoe's ACOF [7]. Therefore, taking these aspects into account is necessary to assess the performance of the footwear. Four pairs of formal Indian shoes from well-known brands were chosen for this study, and the tread characteristics of each pair were examined using a British Pendulum slip testing instrument. Three flooring types—laminated, ceramic, and anti-skid—were tested for slip resistance under three different situations (i.e., dry, water, and canola oil). In order to evaluate the frictional capabilities of the shoe outsoles, they were also gradually worn through various wear cycles and slip tested. The outcomes are anticipated to help understand the impact of various tread patterns and wear cycles on footwear slip risk across floorings and contaminants.

Experimental Details

Four pairs of shoes from brands with significant sales in India were examined in this study. In a sophisticated 3D modelling software, the tread orientations and geometries were imported and traced. After being fully mixed in a ratio of 100:40, a two-part polyurethane polymer was poured into the 3D-printed moulds and allowed to cure for five hours. The created outsoles were taken from the corresponding moulds after curation, and their dimensions were measured (i.e., tread widths, gaps, depth, etc.). It was observed that outsoles matched the real tread geometrical specifications. Three wear cycles were utilized to further wear the outsoles. A British Pendulum slip risk measuring device was used to evaluate the frictional performance of these outsoles. The part-shoe was attached to the device via a customized 3D printed connector, underneath which the outsoles were fastened. The tests were performed across three types of contaminant situations i.e., dry, water, and canola oil on three different floorings i.e., laminate,

ceramic, and anti-skid which had peak-to-valley surface roughness of 1.2 μm, 1.8 μm, and 2.6 μm respectively. Figure 1 depicts the slide testing apparatus and Figure 2 depicts the shoe outsoles fabricated for this study. Five trials were run for each flooring-contaminant condition, and the average ACOF was reported.

Figure 1: British Pendulum skid tester with modified shoe outsole arrangement
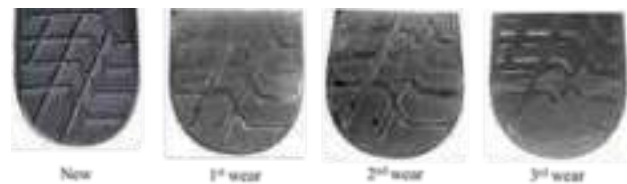

Figure 2: Shoe Outsoles

Figure 3: Outsoles after successive wear cycles

Results & Discussion

The new outsoles' ACOF values varied from 0.352 to 0.380 while they were dry, from 0.251 to 0.270 when they were contaminated with water, and from 0.144 to 0.164 when they were contaminated with Canola oil. Outsoles with horizontal or intricate tread patterns in the heel area (i.e., S2 and S4) performed exceptionally well in terms of friction in dry conditions. S1 and S3's high frictional performance in the presence of water demonstrated the capacity of the tread designs to efficiently channel the flow. High ACOF for S1 and S3 were made possible by the flow channelling, but overall, generalised values were reported because of the viscous oil contamination.

All of the outsoles saw significant decreases in the ACOF values after the first progressive wear cycle. The worn outsoles' ACOF values varied from 0.301 to 0.334 when they were dry, 0.212 to 0.246 when they were contaminated with water, and 0.139 to 0.147 when they were contaminated with Canola oil. Few tread designs (S1 and S3) were nevertheless proven to be useful in this situation for preserving the overall frictional performance under all circumstances.

All of the outsoles saw significant decreases in ACOF values after the second progressive wear cycle as compared to the initial test settings. The fully worn outsoles' ACOF values ranged from 0.265 to 0.295 when they were dry, 0.195 to 0.214 when they were contaminated with water, and 0.121 to 0.138 when they

Figure 4: Variation of ACOF across outsoles in Unworn Condition

Figure 5: Variation of ACOF after 1st wear cycle

were contaminated with Canola oil. Few tread designs (S2 and S4) in this situation were proven to be inefficient at preserving the overall frictional performance. In comparison to earlier test settings, all the outsoles exhibited significant reductions in ACOF values after the third progressive wear cycle.
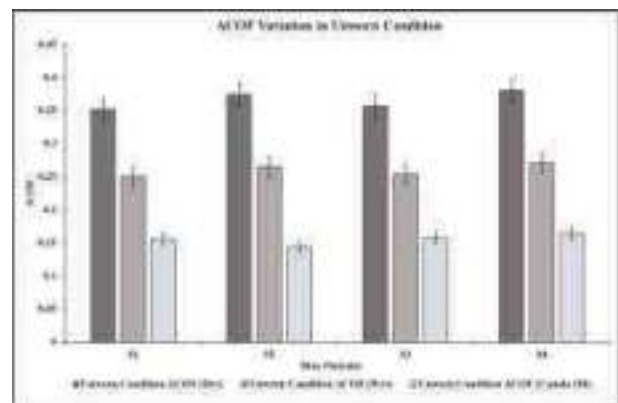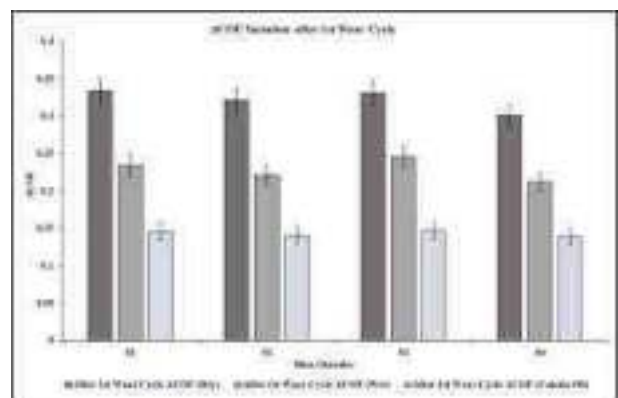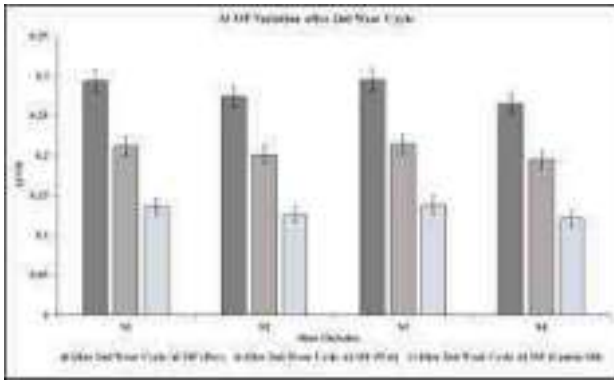
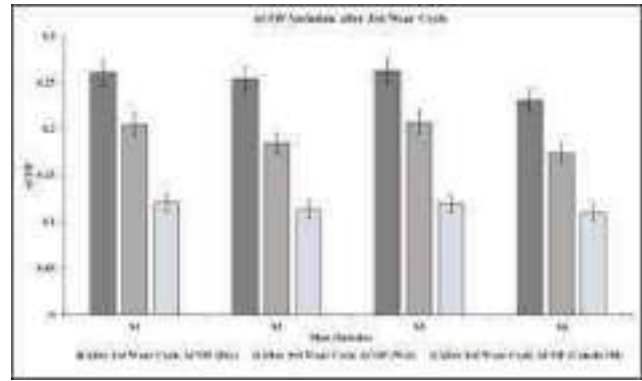*Figure 6: Variation of ACOF after 2nd wear cycle*

Figure 7: Variation of ACOF after 3rd wear cycle

The fully worn outsoles' ACOF values varied from 0.231 to 0.263 when they were dry, from 0.174 to 0.207 when they were contaminated with water, and from 0.110 to 0.121 when they were contaminated with Canola oil. In this instance, outsoles that were entirely worn out performed similarly to the base material. Thus we were able to observe how the ACOF decreased with each wear cycle and as high viscosity contaminants were implemented for slip testing, a similar and generalizable trend in the ACOF values were also observed.

Conclusions

This present work focuses on understanding the effect of wear on different patterned footwear outsoles. Reduction in the ACOF values ranged from 40% to 90% as the outsoles were worn progressively. Outsoles consisting oblique tread design were found to produce high friction as compared to other tread geometries. Increase in worn area was found to strongly correlate ($R^2 = 0.86$) with the decrease in friction. The economical modelling methods and the study results are anticipated to provide guidelines for footwear manufacturers in the selection of appropriate tread designs and suggesting the replacement thresholds.

References

○ 2017 Liberty Mutual Workplace Safety Index. n.d.

○ Sharma PK, Bunker CH, Singh T, Ganguly E, Reddy PS, Newman AB, et al. Burden and Correlates of Falls among Rural Elders of South India: Mobility and Independent Living in Elders Study. Curr Gerontol Geriatr Res 2017;2017. https://doi.org/10.1155/2017/1290936.

○ (WHO) WHO. Falls n.d. https://www.who.int/news-room/fact-sheets/detail/falls (accessed August 17, 2022).

○ Strandberg L, Lanshammar H. The dynamics of slipping accidents. J Occup Accid 1981;3:153–62. https://doi.org/10.1016/0376-6349(81)90009-2.

○ Redfern MS, Cham R, Gielo-Perczak K, Grönqvist R, Hirvonen M, Lanshammar H, et al. Biomechanics of slips. Ergonomics 2001;44:1138–66. https://doi.org/10.1080/00140130110085547.

○ Chanda A, Jones TG, Beschorner KE. Generalizability of Footwear Traction Performance across Flooring and Contaminant Conditions. Https://DoiOrg/101080/2472583820181517702 2018;6:98–108. https://doi.org/10.1080/24725838.2018.1517702.

○ Chanda A, Reuter A, Beschorner KE. Vinyl Composite Tile Surrogate for Mechanical Slip Testing. Https://DoiOrg/101080/2472583820191637381 2019;7:132–41. https://doi.org/10.1080/24725838.2019.1637381.

Barefoot Traction Testing In Indian Bathrooms:
A Novel Experimental Framework

Subhodip Chatterjee[1], Shubham Gupta[1] and Arnab Chanda[1,2,*]

[1]Centre for Biomedical Engineering, Indian Institute of Technology (IIT) Delhi, India
[2]Department of Biomedical Engineering, All India Medical Institute of Medical Sciences (AIIMS), Delhi, India
*Corresponding Author (E-mail: arnab.chanda@cbme.iitd.ac.in)

Abstract

Barefoot slips and falls are common in Indian bathrooms. However, to date, there has been limited experimental works to understand barefoot traction on slippery bathroom floorings. This is majorly due to the lack of any barefoot simulant, which is structurally, materially, or tribologically like the human foot. In context, this pioneering work consisted of designing and fabricating a human foot simulant for barefoot slip testing, and a novel experimental framework was developed for slip testing of this simulant on realistic dry and wet surfaces. Imaging and additive manufacturing was employed to fabricate the simulant and tune its structural and mechanical properties with the foot. The coefficient of friction (COF) was measured using the simulants for short and medium length slips, on eight glazed porcelain tiles commonly found in Indian bathrooms. The COF was observed to decrease moderately from dry to wet flooring condition, and drastically with the use of highly viscosity shampoo. Generalizable ACOF was measured across floorings for soap and shower gel contaminated conditions. High repeatability and low intra tile variations were also recorded for the traction tests with the simulant. The results from this study are anticipated to provide important guidelines for barefoot slip risk assessment in bathrooms, and also assist in selection of suitable anti-slip bathroom floorings in the future.

Introduction

With 1.21 billion people and rising, India is a nation with a significant population density. Consequently, a rise in the elderly population could result in a higher overall potential for falls and slips [1]. In accordance to the Center for Disease Control and Prevention, approximately one-third of all Indians encounter a fall event each year, either in the bathroom or kitchen of a residential building [2]. Bathroom barefoot slips have been linked to wet and slippery flooring as a major contributing cause [3]–[5].

In this study, a unique barefoot heel surrogate was used to estimate the risk of barefoot slips on bathroom floor tiles fabricated from porcelain in the presence of contaminants including water, shower gel, and shampoo.

Experimental Details

The anatomical characteristics of the human foot were recorded using a 3D scanner in order to recreate the motion of barefoot slipping. Using the 3D Sense application, the initial data points collected post scanning were converted into a foot model. The heel portion of the scanned whole foot model was split using the Mesh mixer software. According to reports, the typical human slip angle (between the heel and the ground) was found to be 17 degrees. The Voxelab Aquila 3D printer was used to generate the heel mold's design. A support mould was also 3D printed in order to link the barefoot surrogate to the skid tester. Polylactic Acid (PLA) filament with 1.75 mm diameter was the substance used to create the moulds. A two-part material composition was created that had the same shore A hardness (i.e., 30A) as the plantar foot skin.

The measurements were taken utilizing a weight measuring device, and the combination mixture was stirred for 120 seconds before being transferred into the moulds of the 3D-printed heel and adaptor, where it was allowed to cure for 5 hours. The surrogate mould was covered with the partially-cured adaptor during the curing process so that it could finish curing and adherently bond to each other. Two heel surrogates namely Surrogate A and Surrogate B were fabricated and their repeatability was also examined. The British pendulum skid tester was utilised for the current slip testing investigations. The skid tester's level placement was adjusted so that the spirit level indicator displayed a level position. As part of the calibration procedure, the skid tester's zero reading during free swinging was confirmed. The rubber slider was attached to the two barefoot surrogates (Surrogate A and Surrogate B) utilizing the adapter. The angle at which the barefoot surrogate would make contact with the flooring tile surface was fixed at 17°, which is the most typical foot-flooring tile angle seen during human slips.

For the slip testing study, eight standard glazed porcelain bathroom flooring tiles were chosen. These flooring tiles were procured from the same business proprietor (Orient Bell, India). These tiles were selected based on reviews and feedback of the customers and also on the business and sales statistics of the major outlets selling these flooring tiles. Using a digital scale profilometer, the surface roughness measurements were performed. Realistic slip risk evaluation was performed on wet, shower gel, and shampoo spill conditions. Five trials were run for each flooring-contaminant condition, and the mean ACOF was reported. On all of the flooring tiles, repeatability tests utilizing both barefoot surrogates were also carried out.
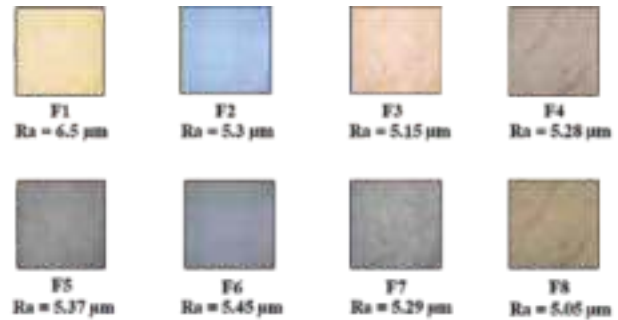

Figure 1: British Pendulum Skid Tester

Figure 2: Flooring Tiles Used in Study

Results & Discussion

Considering the situation of wet slip testing among the eight different porcelain bathroom flooring tiles, the ACOF values ranged from 0.202 to 0.298. The ACOF variation decreased in the event when shower gel was implemented as the contaminant, the ACOF values in this scenario ranged from 0.168 to 0.225. The contaminant scenario which had exhibited the lowest ACOF values were that of the shampoo spill condition in which the ACOF values ranged from 0.101 to 0.151. Repeatable nature were observed in all the contaminant scenarios also. Generalizable trends and higher correlation in the frictional performance among the different bathroom flooring tiles were observed to increase from wet to shampoo spill condition. Another important observation which was also made was that in the scenario when the ACOF values and the surface roughness of the flooring tiles were compared, the effect of surface roughness on the ACOF values decreased with the increasing viscosity of the bathroom contaminants that is this trend was the most observed when shower gel and shampoo spill were used during slip risk assessment.
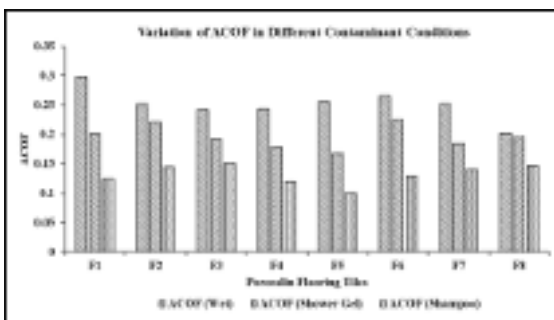

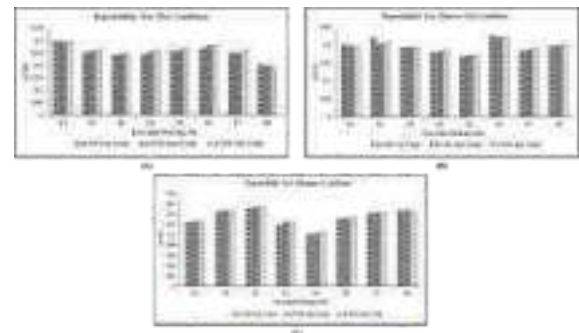Figure 3: Variation of ACOF in different conditions

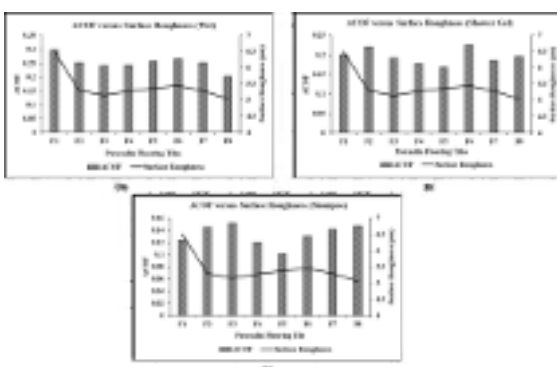Figure 4: Repeatability Test in Different Conditions

Figure 5: ACOF versus Surface Roughness

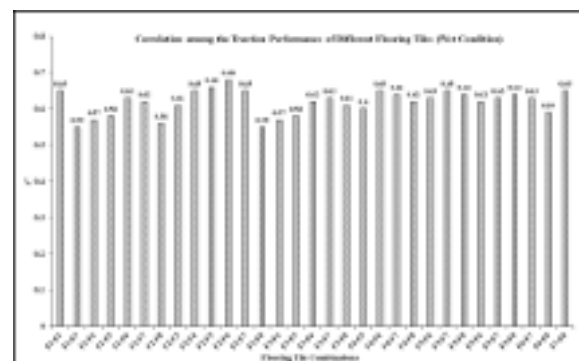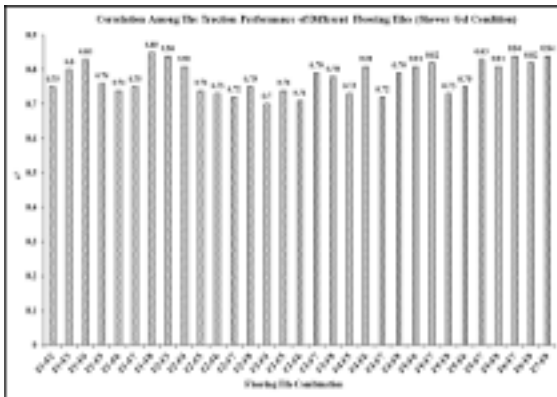Figure 6: Correlation (Wet Slip Test)

Figure 7: Correlation (Shower Gel Slip Test)

Figure 8: Correlation (Shampoo Test)

Conclusions

This present work focuses on understanding the variation in ACOF when the slip testing was performed in dry state and when liquid contaminants such as water, shower gel and shampoo were used. The predominance of the shower gel and shampoo contaminants over the surface roughness of the flooring tiles helps to a substantial amount in understanding the effect of the high viscosity film formation on the flooring and its effect on barefoot traction performance. Generalizable trend in the barefoot traction performance in the different flooring tiles in the presence of high viscosity contaminants were also recorded. This study will aid in the proper selection of bathroom flooring tiles in households from the tribological view point which will ultimately lead to lower risk of slip related accidents and related injuries.

References

○ P. Pitchai, H. B. Dedhia, N. Bhandari, D. Krishnan, N. R. J. D'Souza, and J. M. Bellara, "Prevalence, risk factors, circumstances for falls and level of functional independence among geriatric population - A descriptive study," Indian J. Public Health, vol. 63, no. 1, pp. 21–26, 2019.

○ R. Agarwalla, A. M. Saikia, R. Pathak, F. Is-Lam, M. Borah, and M. Parashar, "A Cross Sectional Study on Assessment of Falls in Community Dwelling Elderly of As-sam," Ntl J Community Med, vol. 7, no. 5, pp. 368–371, 2016.

○ A. C. Scheffer, M. J. Schuurmans, N. Van dijk, T. Van der hooft, and S. E. De rooij, "Fear of falling: Measurement strategy, prevalence, risk factors and consequences among older persons," Age Ageing, vol. 37, no. 1, pp. 19–24, 2008.

○ B. J. Vellas et al., "Activity restriction induced by fear of falling and objective and subjective measures of physical function: A prospective cohort study," J. Am. Geriatr. Soc., vol. 26, no. 3, pp. 1805–1810, 2011.

○ J. Howland, M. E. Lachman, E. W. Peterson, J. Cote, L. Kasten, and A. Jette, "Covariates of fear of falling and associated activity curtailment," Gerontologist, vol. 38, no. 5, pp. 549–555, 1998.

Study of Tribological Properties of Disc Surface of Mr Disc Brake

Rakesh Kumar Singh[1*] Chiranjit Sarkar[1]

1Department of Mechanical Engineering, Indian Institute of Technology, Patna, India
*Corresponding author Email: rakesh_2121me12@iitp.ac.in

Abstract

The magnetorheological (MR) disc brake has MR fluid between the rotating disc and stationary housing. In the off state, there is no magnetic force (normal force) on iron particles of MR fluid, but in the on state, magnetic forces act on iron particles which help to make contact between particles and the disc surface. The tribological characteristics of MR fluid on the disc surface of MR brake indirectly affect MR thickness with time, which is a brake performance parameter. In the present work, a mathematical relationship is derived for surface roughness of disc surface using conventional theories. The tribological characteristics of the disc surface are studied experimentally using FESEM and a surface profilometer. The small-sized disc has been used to measure the surface tribological properties. These discs are placed on the disc of MR brake and applied for brake cycles on the designed test rig. The surface properties of small discs are measured before and after the experiment. The effect of MR fluid on the tribological properties of the disc surface is observed by comparing the measured surface properties. The surface roughness for the small disc is measured experimentally and compared with the mathematical model result.

Introduction

Introduction

MR fluids are suspension of micro-sized carbonyl iron particles, base fluid, and additives. Iron particles form fibrous chain-like structures whenever a magnetic field is applied in the fluid domain [1]. These chains like structure reversibly generate remarkable change in the rheological properties such as viscosity, shear yield stress, storage and loss modulus etc. of MR fluid. Some applications of MR fluid in the automotive field are dampers [2], clutches [3], brakes [4] and valves. The MR fluid in these machineries operated in shear, squeeze and flow modes. In shear mode, iron particles of MR fluid directly contact to the rotating or sliding magnetic pole and stationary magnetic pole. Due to this cause, wear problem is severe in shear mode [5]. In the previous few decades, the tribological properties of MR fluid have been investigated using pin-on-disc apparatus [6], block-on-ring apparatus [7], four-ball tester [8], etc.

MR brakes belong to the category of the electro-mechanical brake. MR brakes have disc type [9], drum type [10], and hybrid type [11] geometry, in which MR fluid is used as a working medium, which provides braking torque to the rotor when electromagnet activates. In MR brakes, MR fluid operates in shear mode. Wear is serious in shear mode and indirectly affects the MR fluid gap in MR disc brake, which is one of the performance parameters. The tribological study of disc surface of MR disc brake is very few as per the author knowledge. In the present study, the action of MR fluid on the disc of MR disc brake is investigated using FESEM and surface profilometer. Due to large size of disc, it isn't easy to study its surface properties. Hence, small blind holes are drilled on disc surface and small discs are placed on disc and used for the tribological study. In addition with the experimental study, a mathematical model is represented to measure the surface roughness of small discs. The results of the experimental study and mathematical model are compared.

Methodology

To study the action of MR fluid on disc surface of MR disc brake, the blind holes of 6mm diameter and 2mm depth are drilled on the disc surface, and small discs of 5mm diameter and 2mm thickness are glued in the blind holes. Before placing inside the holes, the surface properties, such as morphology and roughness of small discs, are measured using FESEM and surface profilometer. The MR fluid for MR brake is prepared using 80% fraction of carbonyl iron, 0.5 % fraction of oleic acid, and 19.5% fraction of silicone oil. To get the MR fluid, the mixture of these three is stirred in a mechanical stirrer for two hours at 400 rpm. The MR fluid is filled in the fabricated MR disc brake, whose inner diameter in MR zone was 150mm and outer radius was 220mm. The MR fluid is filled in the gap between disc and housing, which was 1mm.

The fabricated MR disc brake has an electromagnet with 290 copper coils of SWG22. The test rig is prepared for MR brake operation using a motor, torque-speed sensor, MR brake, DAQ system, speed controller, DC current source, and laptop see figure 1. For the tribological study, 120 numbers of brake cycles are utilized. Each cycle consists of 5 minutes of mean speed rotation (500 rpm) in the off state and 30-second rotation in the on state, i.e., the brake is applied for 30 seconds after 5 minutes of disc rotation in off state (see figure 2). On state indicates that the electromagnet is "on," which means MR fluid is in magnetic field, while off state indicates the electromagnet is "off", meaning there is no magnetic field in MR fluid. For brake actuation, 2A current is utilized for electromagnet. One hundred twenty brake cycles are equivalent to 60 minutes on-state operation of MR disc brake. After the experiment, small discs are removed from the disc, and their surface properties are again measured and compared with the results before.
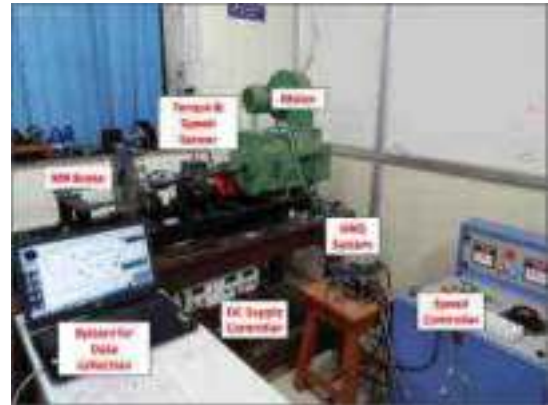

Figure 1- Test rig for MR disc brake testing

MATHEMATICAL MODEL FOR INCREASE IN SURFACE ROUGHNESS

For mathematical modeling, the following assumptions are made

- ❍ No wear of disc surface in the off state.
- ❍ No slip of iron particle on the disc surface.
- ❍ Initial roughness is assumed to be zero..

Magnetic force along the direction of magnetic field which will act as normal force on iron particle in MR zone [12]

$$F_N = F_B = \frac{\pi (R_i)^2 B^2}{2\mu} \qquad (1)$$

Figure 2- Brake cycles used for tribology testing of the disc surface

Where B = magnetic field intensity on the disc surface
    Ri = average radius of iron particle
    μ = relative permeability of MR region

Magnetic field intensity will be the function of MR gap. It will be

BHN = Brinell hardness of disc material in (N/m2)
RPM = rotation during braking
Time = total on-state time
NP = Number of iron particles will pass through a point in one rotation of disc

NP = 2πr (particle fraction)/diameter of particle   (4)

$$B = \frac{\mu_0 \times I \times (R-r) \times R}{2 \times ((R-r)^2 + x^2)^{3/2}} \qquad (2)$$

$$(R_a)_f = \frac{1}{2}\left[R_i - \sqrt{(R_i)^2 - \frac{F_N \times RPM \times N_p \times time}{\pi \times BHN}}\right] \qquad (3)$$

Results & Discussion

Experimental Measurement Of Surface Roughness

The surface roughness of small disc is measured using interferometric surface profilometer (zygo-ZeGage). The measured surface roughness values before the experiment is shown in figure 3(a) and 3(c) and while figure 3(b) and 3(c) indicate after experiment roughness for disc1 and disc2. From figure 3, it can be concluded that surface roughness value is grown. It is attributed to the hardening of soft iron particles due to the deformation of bunches of particles on the contact zone [13]. The hardened particles behave as abrasive particles and two body abrasion of the disc surface occur in the contact zone. The roughness before the experiment was 0.062µm and 0.052µm
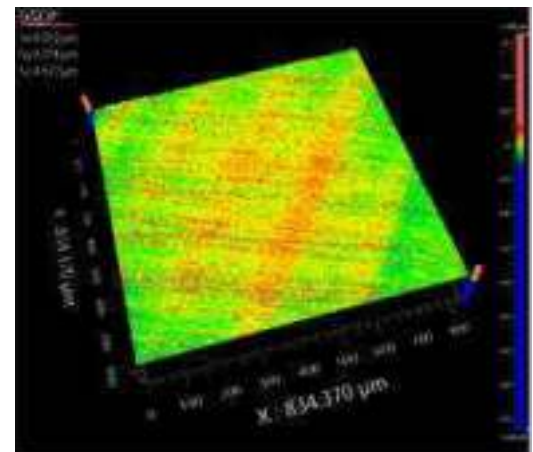

Figure 3. Surface roughness of friction disc (a) before experiment for disc 1 (b) after the experiment for disc 1 (c) before experiment for disc 2 (d) after the experiment for disc 2

respectively for disc1 and disc2, while after the experiment was 0.223µm and 0.251µm respectively for disc1 and disc 2. Effective roughness generated by iron particles is 0.161µm (0.223-0.062) for disc1 and 0.199µm for disc2. The scratches in figure 3(d) may be due to misalignment of the shaft axis with coupling.

Analytical Measurement Of Surface Roughness

The required data for mathematical modeling is given in table 1. Equations (1), (2), (5), and (6) are utilized for the measurement of surface roughness generation.

Table 1. Parameters for mathematical measurement

Parameters	Value
Relative permeability of MR zone 'I'	$10I_r$
Supplied current to electromagnet 'I'	2A
Number of coil turns in electromagnet 'N'	290
Mean coil radius of electromagnet 'R'	127.5mm
Radial distance of small disc 'r'	92.5mm
Axial distance 'x'	4mm
Mean iron particle radius 'r_i'	3.5 µm
BHN for disc material	585 MPa
Mean RPM during on state	300 RPM
On state time	60 min

Roughness generated due to iron particles in MR disc brake at one point
$$Ra = 0.1472547 \mu m$$

Error in experimental and mathematical results is
$$Error\% = \frac{(R_a)_{Exp} - (R_a)_M}{(R_a)_{Exp}} \times 100$$

For disc 1   Error% = 8.53%
For disc 2   Error% = 26.00%

More error in disc2 may be due to scratches caused by misalignment. These error values are within acceptable limits. It means the mathematical model satisfied the experimental results successfully.

Surface Characteristics Of Disc Surface

To observe the surface characteristics of the disc surface before and after experiment scanning electron microscopy (Gemini SEM 500) is utilized. Two small discs are used for SEM analysis. Figure 4 shows the surface characteristics of small discs before and after the experiment. The more deep grooves and wear marks can be observed on disc1 surface after the experiment see figure 4. This confirms the wear and increase in surface roughness of disc surface because of the abrasive behavior of hardened iron particles. The disc surface of figure 5 has more wear marks than that of disc1, which may be attributed to rubbing of the disc surface due to misalignment.

The chemical characterization of the disc2 surface is investigated using energy-dispersive spectroscopy (EDS), as illustrated in figure 5. It has been discovered that the percentages of carbon and oxygen enhanced more after the experiment, which confirms the wear and damage of the surface.
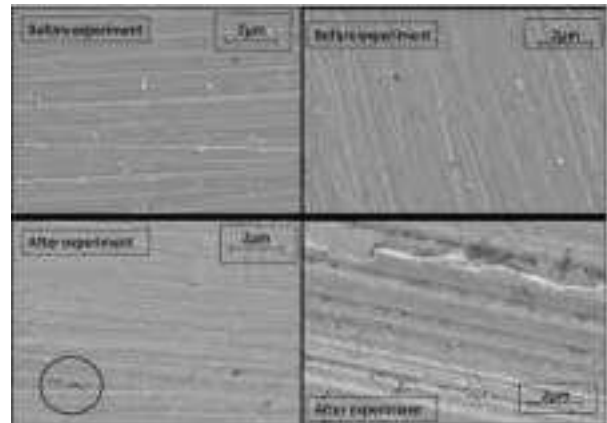

Figure 4. FESEM images (a) & (c) for disc 1and (b) and (d) for disc 2

Conclusions

In this work, the action of iron particles of MR fluid on the surface properties of the rotor of MR disc brake is studied. To perform experimental observations, small discs are placed in blind holes on the disc surface of brake and operated for 120 cycles, equivalent to one hour on-state operation of MR disc brake. The brake operation is performed on the established test rig. The surface properties of small discs are measured before and after the test using surface profilometer and FESEM. A mathematical relationship for enhancement in surface roughness is established using conventional theories. It is observed that wear and surface roughness of the disc surface are increased after brake operation due to the abrasive action of hardened iron particles. The experimental results are compared with the analytical results. It is observed that analytical results satisfactorily followed the experimental results with acceptable errors.
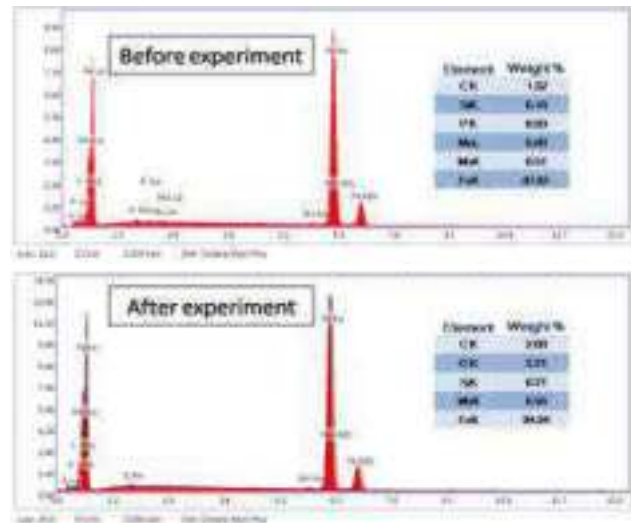
Figure 5. EDS results of small disc2 surface

References

○ Sarkar, C. and Hirani, H., 2015. Effect of particle size on shear stress of magnetorheological fluids. Smart Science, 3(2), pp.65-73.

○ Ashfak, A., Saheed, A., Rasheed, K.A. and Jaleel, J.A., 2011. Design, fabrication and evaluation of MR damper. International Journal of Aerospace and Mechanical Engineering, 1, pp.27-33.

○ Wu, J., Deng, B., Huang, Y., Zhang, H. and Tang, S., 2022. A multi-pole magnetorheological clutch powered by permanent magnets and excitation coils. Journal of Intelligent Material Systems and Structures, p.1045389X221103493.

○ Shiao, Y. and Kantipudi, M.B., 2022. High torque density magnetorheological brake with multipole dual disc construction. Smart Materials and Structures, 31(4), p.045022.

○ Choi, S.B. and Han, Y.M., 2012. Magnetorheological fluid technology: applications in vehicle systems. CRC press.

○ Song, W.L., Choi, S.B., Choi, J.Y. and Lee, C.H., 2011. Wear and friction characteristics of magnetorheological fluid under magnetic field activation. Tribology Transactions, 54(4), pp.616-624.

○ Wong, P.L., Bullough, W.A., Feng, C. and Lingard, S., 2001. Tribological performance of a magneto-rheological suspension. Wear, 247(1), pp.33-40.

○ Hu, Z.D., Yan, H., Qiu, H.Z., Zhang, P. and Liu, Q., 2012. Friction and wear of magnetorheological fluid under magnetic field. Wear, 278, pp.48-52.

○ Sarkar, C. and Hirani, H., 2015. Development of a magnetorheological brake with a slotted disc. Proceedings of the Institution of Mechanical Engineers, Part D: Journal of Automobile Engineering, 229(14), pp.1907-1924.

○ Qin, H., Song, A. and Mo, Y., 2019. Performance evaluation of a hollowed multi-drum magnetorheological brake based on finite element analysis considering hollow casing radius. IEEE Access, 7, pp.96070-96078.

○ Nguyen, Q.H. and Choi, S.B., 2012. Optimal design of a novel hybrid MR brake for motorcycles considering axial and radial magnetic flux. Smart Materials and Structures, 21(5), p.055003.

○ Kala, P., Sharma, V. and Pandey, P.M., 2017. Surface roughness modelling for double disk magnetic abrasive finishing process. Journal of Manufacturing Processes, 25, pp.37-48.

○ Wong, P.L., Bullough, W.A., Feng, C. and Lingard, S., 2001. Tribological performance of a magneto-rheological suspension. Wear, 247(1), pp.33-40.

Precise Friction Measurement of Adsorbed Additive Layer In Lubricant by Combined Use Of Atomic Force Microscopy and Metal Line Patterning

Naoki Yamashita[1*] and Tomoko Hirayama[1]

1Department of Mechanical Engineering and Science, Kyoto University, Japan
*Corresponding author Email: naoki@me.kyoto-u.ac.jp

Keywords: Lubrication, Atomic force microscopy, Line patterning, film thickness

Abstract

In this study, the thickness and friction property of adsorbed layer formed by lubricant additives were precisely measured under boundary lubrication by atomic force microscope (AFM), which can simultaneously measure topography and friction. A specimen with line and space pattern of thin Cu films was prepared by microfabrication technology on a Si chip and friction measurements were carried out using AFM. Lubrication additives are less likely to be adsorbed on Si surface, and wear of Si is also less likely to occur due to its high hardness. The thickness of the adsorbed layer formed by additive during friction in lubricant can be estimated by measuring the combined height of the Cu film and adsorbed layer from the Si surface and subtracting the thickness of the Cu film previously measured in base oil without additive. In this study, Cu line pattern, which has about 3 μm width and 15 nm thickness, was prepared as a specimen and stearic acid was used as a lubrication additive. In measurements using stearic acid, friction coefficient on Cu line pattern became smaller while that on Si surface showed constant value. The thickness of adsorbed layer of stearic acid on Cu was about 1 nm at the actual contact part during friction. In addition, the thickness of adsorbed layer was unstable and varied widely after many cycle frictions, indicating the possibility of generation of metallic soap layer and the cantilever tip trace inside as well as on top of it.

Introduction

Introduction

Additives in lubricants form adsorbed layers on the metal surface and protect the surface of sliding parts from damages. The adsorbed layer plays an important role as the dominant factor in determining the magnitude of friction and wear. In the contact area of the two surfaces during friction, the adsorbed layer is considered to be deformed under compressive and shear stresses. The thickness of the adsorption layer is generally in nanometer-scale, but it often dramatically changes the friction coefficient. It has been reported that the frictional properties of the adsorbed layer vary depending on the type of additive, but detailed verification focusing on the state of the adsorbed layer in the actual contact part under boundary lubrication has not been conducted.

To understand the friction properties exhibited by the adsorbed layer, it is necessary to obtain information on the thickness of the adsorbed layer simultaneously with friction coefficient. In this study, Si was selected as a substrate that does not easily adsorb additives, and Cu line pattern was fabricated on it. This specimen was used for friction measurement by AFM. The friction coefficient and thickness of the adsorbed layer formed on Cu line pattern were evaluated by setting a base line on the height of Si surface between Cu lines.

Experimental Details

The specimen fabrication process is shown in Fig. 1. First, a 4-inch Si (100) wafer was cleaned by sulfuric acid-hydrogen peroxide mixture and ultrasonic jet water in a cleaning system (KSC-150CBU, Kanamex). Then, native oxide layer on Si surface was removed by diluted buffered hydrofluoric acid solution. Subsequently, a photo resist (PMGI-SF5S) with a film thickness of 240 nm was deposited as 1st layer resist using a spin coater and baked on a hot plate at 180°C for 5 minutes. Then, 2nd layer resist (TDMR-AR80) with a film thickness of 0.95um was deposited by using a spin-coater and baked at 90°C for 90 seconds. The resist layers were exposed to UV laser by direct laser writing system (DWL2000, Heiderberg Instruments) for making 3 μm line-and-space pattern, and then baked on a hot plate at 110°C for 90 seconds. The Si wafer was immersed it in 2.38 wt% TMAH aqueous solution for 70 seconds to develop the pattern. Finally, the Si wafer was rinsed with pure water for 60 seconds and dried with N2 blow. All the process described above was carried out in the clean room with yellow light.

Next, a vacuum evaporation system (RD-1400, SANVAC) was used to deposit a 5 nm Cr as an adhesion layer and 10 nm Cu film on it. The deposition rates for both metals were adjusted to be approximately 0.05~0.10 nm/sec. The Si wafer was stored in vacuum desiccator until friction measurements. Before measurement, the Si wafer was cut for making small chips. Then, the chips were immersed in 1-Methyl-2-pyrrolidinone (NMP) at room temperature for 60 minutes as a lift-off process, and immersed in second NMP heated on hot plate at 80°C for 60 minutes to clean the resists more intensively. Finally, the Si chip was then ultrasonically cleaned for 5 minutes, transferred to isopropyl alcohol and further

ultrasonically cleaned for 1 minutes, finally rinsed with ultrapure water and dried with N2 blow. In some cases, the unintentionally formed native oxide layer on Si chip was removed again by using a special hydrofluoric acid solution that does not corrode Cu film.

Simultaneous measurement of topography and friction were carried in 50 μL hexadecane on the specimen and observing 15 times at a load of 200 nN using an AFM (SPM-9700HT, Shimadzu). A round probe type cantilever made of Si, which has a typically 150 nm tip curvature radius, was used for evaluations. The same measurements were carried out after adding 50 μL lubricant containing stearic acid in hexadecane at a concentration of 0.2 wt% to make 0.1 wt% lubricant on Si chip.

The observed AFM images were analyzed by a free software Gwyddion. The height distribution of substrate (Si base line and Cu film) was calculated, and the mean heights were found from the peaks of the curves obtained by Gaussian fitting. The friction coefficient was calculated from the combined load of the pushing force calculated from the cantilever deflection and the adhesion force detected in the force curve measurement, and the friction force mechanically calculated by detected cantilever torsion.

Results & Discussion
A microscopic image of the prepared specimen surface is shown in Fig. 2(a), and an observed image in the dynamic mode of AFM is shown in Fig. 2(b). From these images, it was confirmed that there were no resist or metal residues on the specimen surface and that the line-and-space was fabricated successfully.

Next, continuous friction was performed on the Si using AFM under 200 nN load. The results showed that the amount of wear of the Si in the area subjected to friction was around 0.3 nm. This result shows the possibility that Si surface can be used as a base line for the height measurement in this study.

‡@Si cleaning   ‡DLaser beam drawing

‡ASiO$_2$ removing   ‡EResist developing

‡B1st resist coating   ‡F Cr/Cu depositing
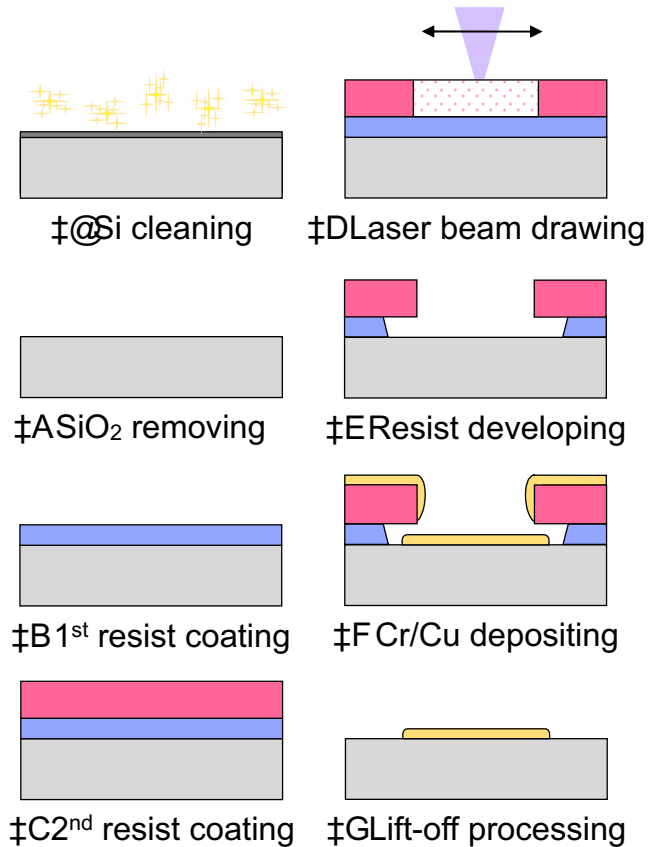
‡C2nd resist coating   ‡GLift-off processing

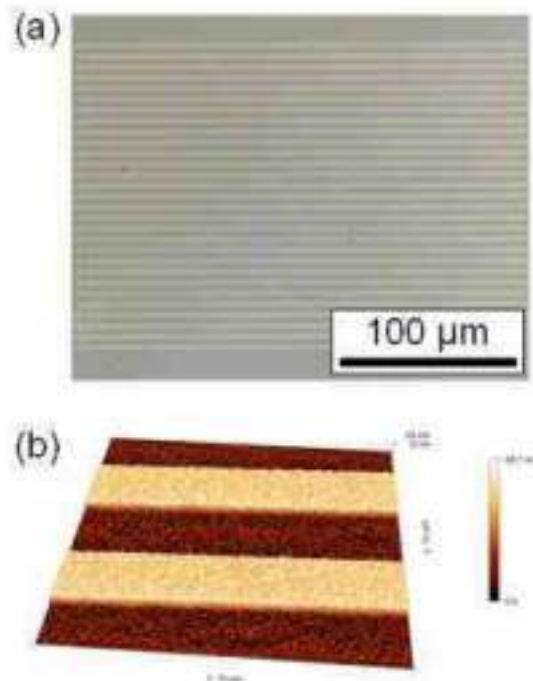*Figure 1: Process for fabricating line pattern specimen*

Figure 2: Microscope image (a) and AFM image (b) of the line pattern after the lift-off process.

38

The results of the experiments with stearic acid are shown in Figs. 3(a)-©. According to the results of friction measurements shown in Fig. 3(a), there was no significant difference in the friction coefficient on Si surface before and after adding the lubricant with stearic acid. This result indicates that stearic acid is most likely not adsorbed on the Si surface. On the other hand, friction coefficient on Cu was reduced by using the lubricant with stearic acid, indicating the formation of adsorbed layer on Cu surface.

The results of the height measurements of the Cu line pattern under each load are shown in Fig. 3(b). Although no clear load dependence was identified because the error magnitude was approximately ±0.5 nm, it was found that the height on the Cu line pattern was 0.7-1.4 nm larger in lubricant containing stearic acid. This value is corresponding to the thickness of the adsorbed layer of stearic acid at the actual contact part.

The results of height measurements under 200 nN load (Fig. 3©) show that there was no significant difference in the friction coefficient in the 1st and 15th scan in hexadecane, whereas the variation was greater in lubricants containing stearic acid. It is generally reported that fatty acids like stearic acid are chemisorbed on Cu surface and a metallic soap layer grows when continuous friction is applied [1]. The variation in the combined height of the Cu film and adsorbed layer observed in this experiment indicates that the growth of metallic soap and the chemical wear of the Cu surface may have an effect. Since a metallic soap layer formed by chemical corrosion is softer than a densely packed adsorbed layer, the AFM cantilever tip may have sometimes traced inside as well as on top of the metallic soap layer and make the measured height unstable.

Conclusions
In this study, Cu line pattern was fabricated on Si substrate and evaluated the friction coefficient and the thickness of the adsorbed layer simultaneously by

AFM. Stearic acid form adsorbed layer on Cu surface and kept 0.7-1.4 nm thick layer at the contact point, realizing lower friction.
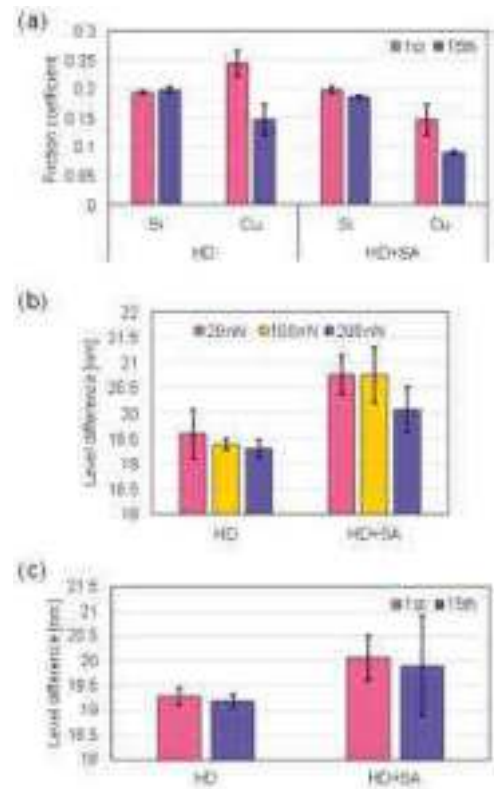

Figure 3: Friction measurement under 200 nN load (a), height measurements under various loading conditions (b), height measurements under continuous friction (c).

References
○ T. Hirayama, et al., Cross-sectional imaging of boundary lubrication layer formed by fatty acid by means of frequency-modulation atomic force microscopy, Langmuir, 2017, Vol. 33 (40), pp. 10492-10500.

The Effects of Nano-friction Stimulation On The Wear of The Endothelial Glycocalyx Layer

H. Gato[1*], K. Sato[1] and S. Sasaki[2]

[1]Graduate school of Mechanical Engineering, Tokyo University of Science, Japan
[2]Department of Mechanical Engineering, Tokyo University of Science, Japan
*Corresponding author
Email: 4522515@ed.tus.ac.jp

Keywords: EGL, EC, AFM, Mechanotrandaction.

Abstract

The endothelial glycocalyx layer (EGL) has an important role in maintaining vascular homeostasis. In catheter surgery, friction is applied to EGL and considered to affect its functioning. However, detailed studies focusing on the effects of friction on the functioning of the EGL are not conducted at the nanoscale because of the difficulty of direct in-situ observation. In this study, we performed friction tests varying load and sliding cycles, in addition, force curve measurements on bovine aortic endothelial cells were acquired to investigate the changes in the cell surface layer before and after the friction tests. As a result, it was found that EGL wear was promoted by increasing vertical load and the number of cycles, and EGL wear was suppressed at the vertical load of 0.7 nN. In addition, EGL wear could be prevented by decreasing the load and the number of friction cycles.

Introduction

Catheter surgery is becoming popular as a less invasive treatment for serious diseases, such as brain aneurysms or cardioembolic diseases. However, complications after surgery sometimes occur and can lead to the death of patients; therefore, a method of minimizing the risk of complications is necessary. In catheter surgery, frictional stimulation is applied to the vascular wall and can influence the structure and mechanical properties of the ECs and/or EGL directly contacting the catheter. Therefore, friction by direct contact can be a major cause of complications. However, detailed research on the effects of friction has not yet been conducted because in-situ observation is difficult.

Endothelial cells (ECs) are a layer of spindle-shaped cells that line the lumen of blood vessels and are present at the interface between the blood and blood vessels. On the interface, ECs have a glycan structure called the endothelial glycocalyx layer (EGL). On the aspects of physiological functions of EC and EGL, it is known that the EC regulates vascular contraction and dilation[1], and the EGL regulates thrombus formation[2]. Currently, some researchers have focused on the relationship between the structure and functions of ECs and EGL. Levesque et al. reported that the shape of ECs in the longitudinal direction became longer by static fluid shear stress[3]. Sato et al. found that elastic modulus locally increases at the location of high shear stress[4]. These previous researches showed that the effects of stress influence the structure and mechanical properties of EC and EGL. Therefore, the topic of elucidating functions at the cellular level has attracted attention to maintain proper functioning and reduce organ diseases.
In this experiment, we focused on the change in elastic modulus and cell surface layer before and after friction test, so we performed nano friction test and the measurement of elastic modulus using atomic force microscopy (AFM). Using contact mode AFM, we applied frictional stimulation on cultured bovine aorta endothelial cells, and, using force curve mapping, investigated the elastic modulus and the thickness of the cell surface layer before and after friction.

Materials and Methods
Bovine aortic vascular ECs were used for EC sample, and the growth medium used was DMES (Life Technologies, Carlsbad, CA) containing 10% FBS (Life Technologies, Carlsbad, CA) and 5% antibiotics (Life Technologies, Carlsbad, CA). EC samples were incubated at 37 °C and 5% CO_2 to reach confluence, seeded onto a polystyrene Petri dish (VWR, Pennsylvania, USA), and used for AFM measurements.

In AFM measurements, we used AFM (SPM-8100FM, Shimadzu, JP) and a tipless cantilever attached to a φ6 μm polystyle bead (Thermo Fisher Scientific, Massachusetts, USA). The cantilever's spring constant was 0.06 N/m calculated by dimensional methods [5]. To investigate the effects of friction stimulation, we performed two types of measurements: contact mode measurements and force curve mapping. Contact mode measurement was utilized as

nano-friction tests, and force curve mapping was used for acquiring the shape, the cell surface layer, and elastic modulus of ECs before and after contact mode measurement. The cell surface layer was examined under three different conditions varying the vertical load and number of friction cycles. Table 1 shows the contact mode measurement's condition before surface thickness measurements.

Table 1 Friction tests conditions

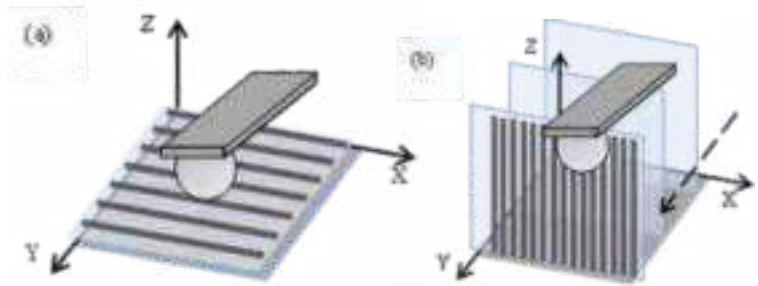| Temperature	37		℃	
Vertical load	1.2	0.7	1.2	nN
Cycle number	5	5	15	-
Scan speed	15		Hz	

Figure 1: Scheme of AFM measurements:
(a) contact mode and (b) force curve mapping.

Results

Figure 2 shows the shapes of the ECs before and after friction. We obtained the shape images, which show the height equivalent to the same repulsive force at each XY point. In addition, the elastic modulus mapping was calculated using the JKR 2-point method [6] from the force curve of each XY point. As shown in Figure 2, the cell is spindle-shaped and matches the ordinal shape of bovine aorta ECs, it is known that EC has an ordinal shape[7], therefore, we can measure the shape of the cell using force curve mapping. In addition, EC's shape after the nanofriction test became longer than that before the nanofriction test.
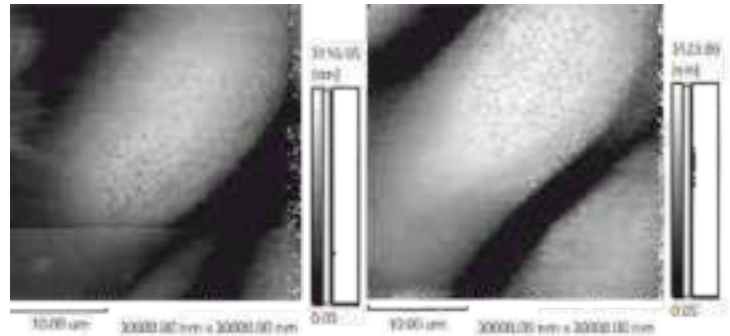

Figure 2: Shape of the cell (a) before and (b) after friction

Figure 3 shows the elastic modulus mapping of the endothelial cells before and after nanofriction tests. Before the nanofriction test, the elastic modulus of the cells was uniformly distributed, regardless of the place However, after friction, we observed a significant increase in the elastic modulus of the center of the cell. The elastic modulus of the EC's center increased from 0.8 to 1.8 kPa, and that of the edge increased from 0.35 to 0.6 kPa. Therefore, we found that the elastic modulus was affected by friction and increased after friction.
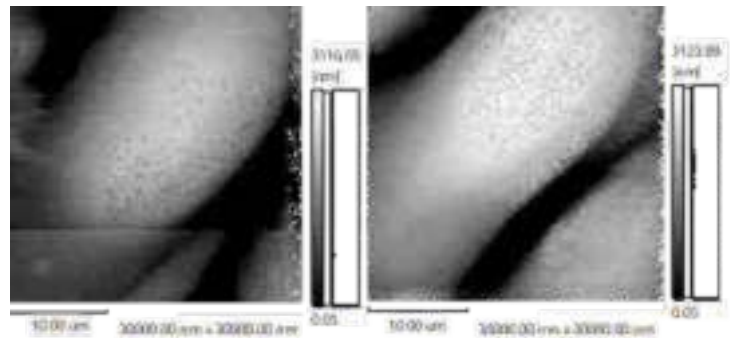
Figure 3: Elastic modulus mapping
(a) before and (b) after friction

Figures 4 and 5 show the ZX images before and after friction stimulation at vertical loads of 1.2 nN and 0.7 nN. In this experiment, we evaluated the thickness of the cell surface layer as the distance indented until the constant repulsive force. The distance between two red lines in figures 4 and 5 shows the thickness of the cell surface layer. At a vertical load of 1.2 nN, the thickness changed from 558 nm to 320 nm, while at a vertical load of 0.7 nN, it only changed from 621 nm to 558 nm. The decrease in the thickness at a vertical load of 1.2 nN /0.7 nN was 158 nm/63 nm, respectively. These results show that the surface layer is soft and worn corresponding to the magnitude of vertical load.
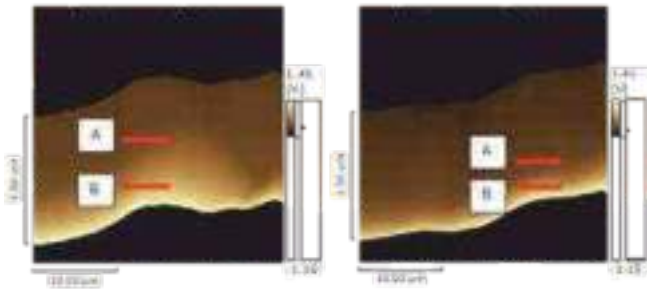
Figure 4: ZX image of the cell (a) before and (B) after friction test at load of 1.2 nN

Figure 5: ZX image of the cell (a) before and (b) after friction test at load of 0.7 nN

Figure 6 shows the surface thickness with respect to sliding cycles. The results show that a decrease of approximately 150 nm was observed for cycles 0 to 5 and 5 to 10, respectively. On the other hand, no significant decrease was observed for cycles 10 to 15. This result showed that the EC's film under the soft layer has high resistance to wear. Additionally, a total reduction of 400 nm was observed for the 15 cycles.

Discussion
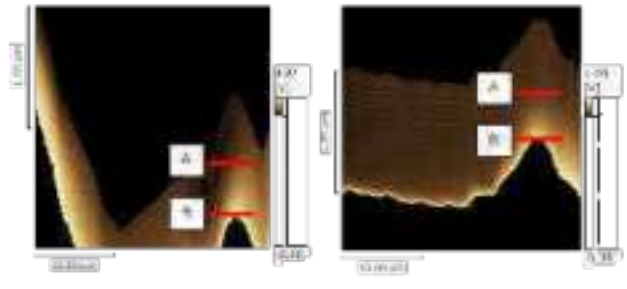
Ke et al. degraded heparin acid in human umbilical vein endothelial cells, the main component of EGL, by enzymatic treatment with heparinase and investigated the subsequent changes in elastic modulus over time. They confirmed a change of the elastic modulus from 1.20/2.93 to 0.33 kPa when EGL was recovered [8]. In addition, the elastic modulus before friction was equivalent to that after EGL recovery, whereas the value of the elastic modulus after friction was reasonable for cells after enzymatic treatment. In addition, the EGL is a layer with a thickness of 20 to 1000 nm [9], which is consistent with the reduction in the cell surface layer in the experimental results shown in Figure 6.
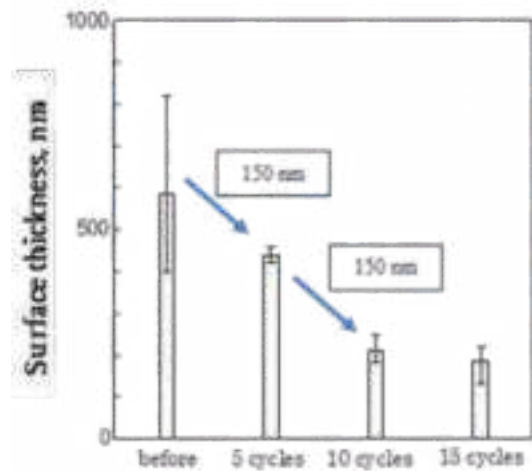
Figure 6: The thickness of cell surface layer per sliding cycle

From these results, as shown in Figure 7, this wear phenomenon can be assumed to occur on the outermost surface of ECs subjected to frictional stimulation. First, before friction, the cell surface was covered by the EGL, and a low elastic modulus was measured by force curve mapping. Subsequently, EGL wear was caused by frictional stimulation and the cell membrane was exposed. Although EGL is so soft that even slight frictional forces can cause them to wear away, cell membranes do not.

Besides that, the decrease in surface thickness after friction at 0.7 nN is suppressed compared to that at 1.2 nN. Since EGL has an important role of keeping vascular homeostasis, EGL wear may lead to the decline of vascular functioning and vascular disease.

Therefore, this result can provide design guidelines considering EGL wear for the prevention of the occurrence of complications after catheter surgery.

Conclusions

To investigate the effects of frictional stimulation on the interfacial structure of vascular endothelial cell surfaces, we investigated the changes in the surface structure in the height direction before and after frictional stimulation using AFM and obtained the following findings.

(1)   Friction tests were conducted using the AFM contact

Figure 7: Scheme of EGL wear in the experiment

mode, and the changes in the elastic modulus distribution before and after friction were confirmed using force-curve mapping measurements.

(2)　　The elastic modulus was significantly increased at the center of the cell by frictional stimulation. This may be due to the removal of the soft EGL from the cell surface by friction.

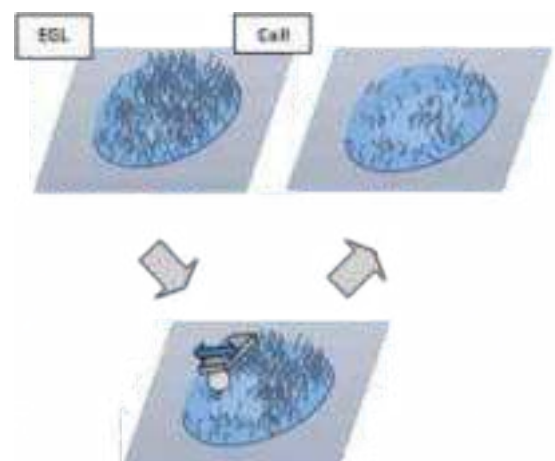(3)　　Using AFM and investigating the surface thickness of the cell, we found that the surface thickness decreased with increasing load

(4)　　A significant decrease in the surface thickness was observed in the initial period from 1 to 10 cycles, while after a decrease of 400 nm, no decrease in the surface thickness was observed even with more friction test.

References

○　Deguchi, S., Function of vascular endothelium in hemostasis and methods for the estimate of them, Vol. 19, (1988), pp.111-121

○　Iba, T., Levy, J. H., Derangement of the endothelial glycocalyx in sepsis, Journal of Thrombosis and Haemostasis, Vol 17, (2019), pp.283-294.

○　Levesque, M. J., Nerem, R. M., The elongation and orientation of cultured endothelial cells in response to shear stress, Journal of Biomedical Engineering, (1985), pp.341-347

○　Nagayama, K., Kataoka, N., Sasaki, M., Hane, H., Local mechanical properties measured by atomic force microscopy for cultured bovine endothelial cells exposed to shear stress, Journal of Biomechanics, Vol. 33, (2000), pp.127-135.

○　Waren C. Y., "Roark's Formulas for Stress and Strain", McGraw Hill, (January 1, 1989)

○　Nakajima, K., Development of quantitative evaluation method for the elastic modulus of soft- materials by atomic force microscopy, Journal of the Vacuum Society of Japan, Vol. 56, (2013), pp.258-266

○　Tokunaga O., Watanabe T., Morphological Characteristics of Human Aortic Endothelium,

○　Arteriosclerosis, Vol. 16, (1988), p903 – 910.

○　Ke B., Wen W., Spatio-temporal development of the endothelial glycocalyx layer and its mechanical property in vitro, Journal of the royal society interface, Vol. 9, (2012), pp.2290-2298

○　Nakajima, Y., Glycocalyx and its protection in the vascular endothelium, Clinical Anaesthesia, Vol. 40, (2016), pp.711-720

Effect of Er Lubrication on Annular Hybrid Thrust Pad Bearing Compensated With CFV Restrictor

Narendra Kumar[1*], Satish C. Sharma[2]
Research Scholar[1*], Professor[2]

[1,2]Department of Mechanical and Industrial Engineering, Tribology Laboratory, Indian Institute of Technology, Roorkee, 247667, India
*Corresponding author Email: narendra_k@me.iitr.ac.in

Abstract

The performance characteristic of the hybrid thrust pad bearings is significantly influenced by the rheological behavior of the lubricants. Smart lubricants such as electro-rheological lubricants have made a great impact on the performance of tribo-pairs. The present paper studies the non-Newtonian behavior of electro-rheological lubricant on the performance of the hybrid annular thrust pad bearing compensated with a constant flow valve. The modified Reynolds equation for the hybrid annular thrust pad bearing has been solved using the Finite Element Method (FEM). The rheological behavior of electro-rheological lubricant has been analyzed considering the continuous Bingham fluid model. The numerically simulated results reveal that for electro-rheological lubricant operated hybrid annular thrust pad bearing, the value of load-carrying capacity and fluid film stiffness coefficient gets affected as compared to bearing operating under Newtonian lubricant.

Introduction

Hydrostatic thrust pad bearing configurations are currently widely used in various applications in industries. The load-carrying capacity of thrust pad bearing is limited because of the lack of a physical wedge between the flat surfaces. This restricts their application to simple axial positing of the rotor in machines such as electric motors, crankshafts, household electrical appliances, etc. The use of an external lubricant supply pump effectively enhances the load-carrying capacity of flat land thrust pad bearings and widens their range of application from small precision equipment to supporting enormous structures/machines.

Osman et al. 1 scrutinized the experimental study of hydrostatic thrust pad bearing and computed the performance parameters of bearing in terms of fluid film thickness, pressure distribution, and oil flow rate. Further, it was reported that pocket size and shape have a significant influence on the behavior of hydrostatic thrust pad bearings. Yu et al. 2-4 studied the pressure distribution of hydrostatic thrust pad bearing for different pocket shapes (sector, rectangular, elliptical, and I-shaped pockets) using CFD (Computational fluid dynamic) and Finite Volume technique. They revealed that rectangular-shaped recess provides a larger pocket pressure value as compared to other geometric shapes of pockets.

Nowadays, the use of smart lubricants such as Electrorheological fluids has emerged as new technology to enhance the performance of the tribological system. Electrorheological fluids are materials that change from a liquid to a solid when applied to an electric field. Kollias and Dimarogonas 5 were the first to propose the ER fluid design, applying it to a low-speed partial journal bearing and computing the hydrodynamic pressure. Their conclusions were found to be in good agreement with Wada et al. 6 theoretical Bingham model. Peng and Zhu 7 used the CFD technique to analyze the lubricating behavior of ER lubricant in a hydrodynamic circular journal bearing. They observed that the ER lubricant significantly affects the lubricating behavior of the fluid film bearings.

Numerical Formulation

The governing modified Reynolds equation for non-Newtonian and incompressible lubricant domain in the clearance space is expressed as:[8]

$$\frac{\partial}{\partial \alpha}\left(h^3 F_2 \frac{\partial p}{\partial \alpha}\right) + \frac{\partial}{\partial \beta}\left(h^3 F_2 \frac{\partial p}{\partial \beta}\right) = \frac{\partial h}{\partial \alpha}\bar{U}\left(1 - \frac{F_1}{F_0}\right) + \frac{\partial h}{\partial \beta}\bar{V}\left(1 - \frac{F_1}{F_0}\right) + \frac{\partial h}{\partial t} \quad (1)$$

where, $\bar{U} = -r\bar{\Omega}\sin\theta$ and $\bar{V} = r\bar{\Omega}\cos\theta$

F_0, F_1 and F_2 refers to cross film viscosity integrals, these are used for non-Newtonian lubricants and computed as

$$F_0 = \int_0^1 \frac{1}{\bar{\mu}} d\bar{z}, \quad F_1 = \int_0^1 \frac{\bar{z}}{\bar{\mu}} d\bar{z}, \quad F_2 = \int_0^1 \frac{\bar{z}}{\bar{\mu}}\left(\bar{z} - \frac{F_1}{F_0}\right) d\bar{z}$$

Finite Element Formulation

By using FEM numerical technique to solve Eq.1, the performance characteristics of the hydrostatic thrust pad bearing system are computed. A 4-noded isoparametric element is used to discretize the non-Newtonian fluid film domain. Approximated fluid film pressure over an element is as follows [8];

$$\bar{p} = \sum_{j=1}^{n^e} N_j \bar{P}_j \qquad (2)$$

Applying Galerkin's technique for orthogonality conditions the following elemental algebraic equation is obtained as:

$$[F_{ij}]^e \{\bar{P}_j\}^e = \{\bar{Q}_i\}^e + \{\bar{R}_{xu}\}^e + \bar{h}_i \{\bar{R}_i\}^e \qquad (3)$$

Table 1:
Bearing operating and geometric parameters.

S.No	Geometric parameters	Value
1	Inner radius of recess	0.5
2	Outer radius of recess	1.0
3	Annular radius of recess	0.707
4	Type of compensating element	Constant flow valve (CFV)
5	Restrictor design parameter ($\bar{C}_{s2}$)	0.2,0.4,0.6,0.8,1.0
6	Applied voltage, (V)	0 , 800,1200
7	ER fluid parameter,(A)	6.619×10^{-33}
8	ER fluid parameter,(B)	2.185
9	ER fluid viscosity,μ	0.0816

2.2. Bearing Performance Characterestic

The hydrostatic performance characteristics of constant flow valve compensated hydrostatic circular thrust pad bearing are expressed as:

2.2.1 Load Carrying Capacity

$$\bar{F}_o = \bar{F}_{o|land\,area} + \bar{F}_{o|pocket\,area}$$

$$\bar{F}_o = \sum_{e=1}^{n_e} \left\{ \int_{-1}^{1} \int_{-1}^{1} \left(\sum_{i=1}^{n_{l=4}} \bar{p}_i N_i \right) |J| d\xi d\eta \right\} + \sum_{i=1}^{i=n_p} \bar{A}_c \bar{p}_c \qquad (4)$$

2.2.2 FLUID FILM STIFFNESS COEFFICIENT

$$\bar{S} = -\frac{\partial \bar{F}_o}{\partial \bar{h}} = \sum_{e=1}^{n_e} \left\{ \int_{-1}^{1} \int_{-1}^{1} \left(\sum_{i=1}^{n_{l=4}} \frac{\partial \bar{p}_i}{\partial \bar{h}} N_i \right) |J| d\xi d\eta \right\} + \sum_{i=1}^{i=n_p} \bar{A}_c \frac{\partial \bar{p}_c}{\partial \bar{h}} \qquad (5)$$

2.2.3 Fluid Film Damping Coefficient
$$\bar{C} = \sum_{e=1}^{n_e} \left\{ \int_{-1}^{1} \int_{-1}^{1} \left(\sum_{i=1}^{n_{l=4}} \frac{\partial \bar{p}_i}{\partial \dot{\bar{h}}} N_i \right) |J| d\xi d\eta \right\} + \sum_{i=1}^{i=n_p} \bar{A}_c \frac{\partial \bar{p}_c}{\partial \dot{\bar{h}}} \qquad (6)$$

3. Results And Discussion

The geometric and operating parameters of the bearing system is shown in Table 1. The performance characteristics of constant flow valve compensated annular recess hydrostatic thrust pad bearings are numerically simulated as shown in Fig. (1-4). The bearing characteristics have been presented for a Newtonian lubricant (V=0) and ER lubricant (V=800 and 1200 Voltes). These results are discussed below.

3.1. Pocket Pressure

The pocket pressure ($\bar{p}\_c$) distribution over the fluid film domain versus restrictor design parameter ($\bar{C}\_{s2}$) of annular hybrid thrust pad bearings are illustrated in Fig. 1. It can be seen that the pocket pressure ($\bar{p}\_c$) increases with an increase in the value of ($\bar{C}\_{s2}$). It can also be seen that the pocket pressure ($\bar{p}\_c$) for ER lubricant is higher as compared to the Newtonian lubricant (V=0).

3.2. Load Carrying Capacity

From the Fig. 2, it can be seen that the load-carrying capacity ($\bar{F}\_o$) increases with an increase in the value of ($\bar{C}_{s2}$). It can also be observed that the load-carrying capacity ($\bar{F}\_o$) for ER lubricant is enhanced as compared to the Newtonian lubricant (V=0).
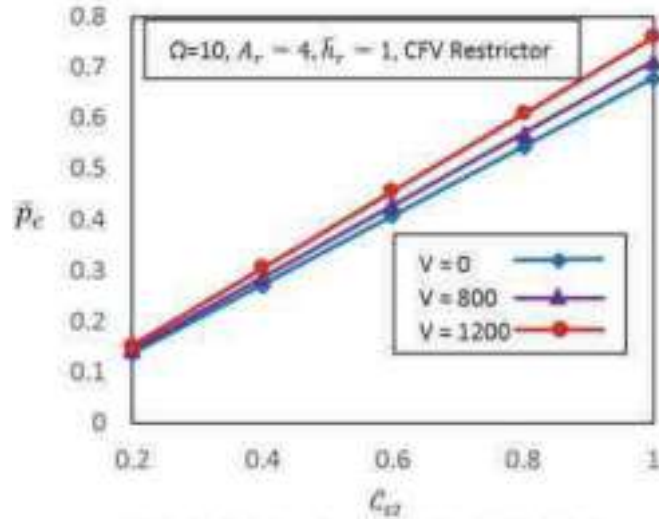
Fig. 1. Pocket Pressure ($\bar{p}_c$) Vs ($\bar{C}_{s2}$)

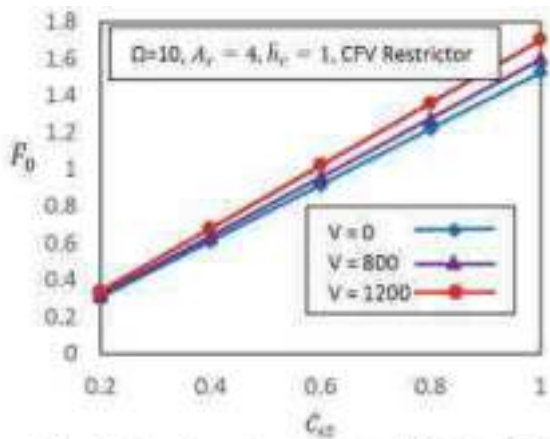### 3.3. Fluid Film Stiffness Coefficient

From the Fig. 3, it can be seen that the fluid film stiffness coefficient ($\bar{S}$) increases with an increase in the value of ($\bar{C}_{s2}$). It can also be seen that the fluid film stiffness coefficient for ER lubricant is improved as compared to the Newtonian lubricant ($V=0$).

Fig. 2. Load carrying capacity ($\bar{F}_0$) Vs ($\bar{C}_{s2}$)
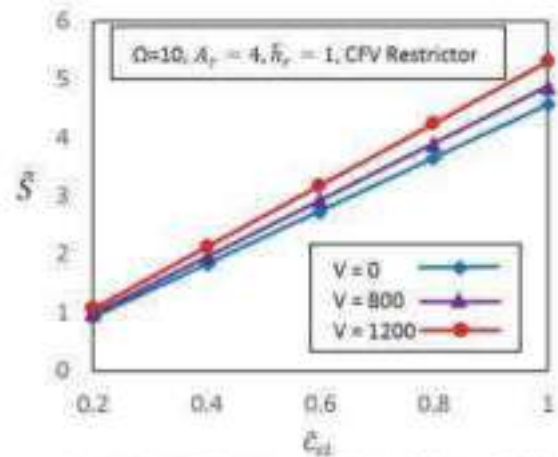
Fig. 3. Stiffness coefficient (S) Vs ($\bar{C}_{s2}$)

3.4. Fluid Film Damping Coefficient

From Fig. 4, it can be seen that the fluid film damping coefficient ($\bar{C}$) slightly increases with an increase in the value of ($\bar{C}_{s2}$). It can also be seen that the fluid film damping coefficient for ER lubricant is higher as compared to the Newtonian lubricant ($V=0$).

4. Conclusion

The above study shows the effect of the ER lubricant on the performance of constant flow valve compensated annular recess hybrid thrust pad bearing. The conclusion has been drawn from the numerical computation result are as follows:

It has been found that the use of ER lubricant increases the pocket pressure, load-carrying capacity, fluid film stiffness and dampind coefficient the of the bearing system as compared to the Newtonian lubricant ($V=0$).
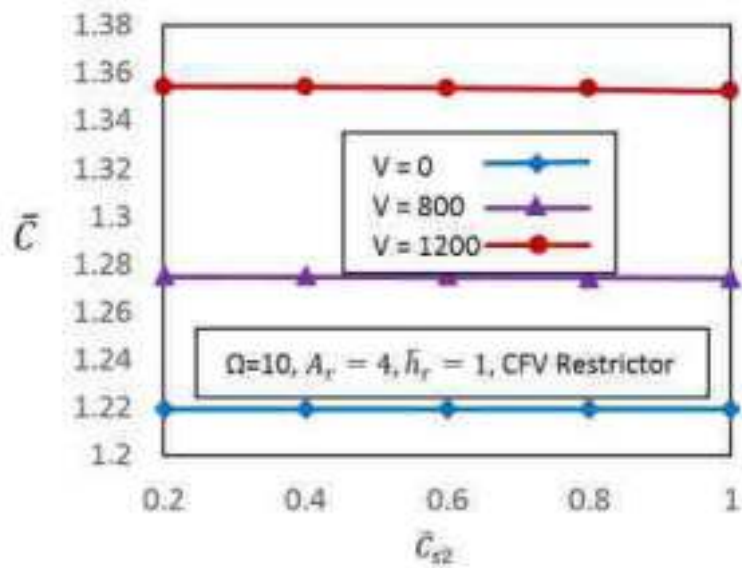
Fig. 4. Damping coefficient $(\bar{C})$ Vs $(\bar{C}_{s2})$

References

○ Osman T, Dorid M, Safar Z, Mokhtar M. Experimental assessment of hydrostatic thrust bearing performance. Tribology international. 1996; 29: 233-9.

○ Yu XD, Li ZG, Zhou DF, et al. Influence Research of Recess Shape on Dynamic Effect of Hydrostatic Thrust Bearing. Applied Mechanics and Materials: Trans Tech Publ, 2013, p. 57-60.

○ Yu M, Yu X, Zheng X, Qu H, Yuan T, Li D. Influence of recess shape on comprehensive lubrication performance of high speed and heavy load hydrostatic thrust bearing. Industrial Lubrication and Tribology. 2018; 71: 301-8.

○ Yu X, Wang Z, Meng X, et al. Research on dynamic pressure of hydrostatic thrust bearing under the different recess depth and rotating velocity. International Journal of Control and Automation. 2014; 7: 439-46.

○ Kollias A, Dimarogonas A. Electrorheological fluid flow in partial journal bearings. ASME-Publications-Fed. 1994; 205: 69-.

○ WADA S, HAYASHI H, HAGA K. Behavior of a Bingham solid in hydrodynamic lubrication: part 1, general theory. Bulletin of JSME. 1973; 16: 422-31.

○ Peng J, Zhu K-Q. Effects of electric field on hydrodynamic characteristics of finite-length ER journal bearings. Tribology international. 2006; 39: 533-40.

○ Sharma SC, Yadav SK. Performance analysis of a fully textured hybrid circular thrust pad bearing system operating with non-Newtonian lubricant. Tribology International. 2014; 77: 50-64.

Mechanical and Tribological Studies of Structalit™/ Uhmwpe Composites for Hip Joint Application

Jaswant Kumar Hirwani* and Sujeet Kumar Sinha

Department of Mechanical Engineering, Indian Institute of Technology Delhi, India
*Corresponding author (E-mail: jaswant.hirwani@gmail.com)

Keywords: Tribology, Wear, Materials, Structalit, UHMWPE

Abstract

Structalit/UHMWPE composites were tested for biotribological performance and results were compared with UHMPWE samples. Experiments were conducted under serum lubrication with a contact stress and sliding speed of 2 MPa and 20.73 mm/s. Ploughing and burnishing were the major wear mechanism found in the case of UHMWPE with a specific wear rate of $2.8 \times 10\text{-}6$ mm3/Nm whereas structalit/UHMWPE composites had no sign of plastic deformation and abrasive wear marks, which is due to the higher yield strength and hardness of the composite and low shear interface provided by the presence of UHMWPE. Specific wear rate of the optimized composite was $1.35 \times 10\text{-}6$ mm3/Nm which is found to be marginally significant than UHMWPE data in student-t test.

Introduction

Ultra-high molecular weight polyethylene (UHMWPE) is a widely accepted gold standard liner material for total hip arthroplasty (THA). However aseptic loosening and dislocations are the most significant reasons for implant failure. One of the studies presented that 65.9 % implants failed due to aseptic loosening and dislocation [1]. These conditions require a revision surgery which poses the increased risk of health complications and chances of second revision increases five times [2]. Therefore, longevity of these implants is of the utmost importance.

The primary reason for aseptic loosening is osteolysis which occurs due to the adverse tissue reaction of wear debris generated from sliding of UHMWPE [3]. Therefore, it is well understood that the specific wear rate of newly formulated materials should be lower than the existing one. Dislocation is termed as the complete separation of femoral head out of the acetabular cavity, which can be avoided by selecting a larger head diameter and increasing the range of motion [4]. A study observed that increasing the head diameter from 52 to 54 mm increases the global ROM by 56.1° [5]. This concept is briefly discussed in supporting information S1. General practice is to use a thicker UHMWPE cup to provide enough strength during gait movement and avoid radial cup deformation after press-fit implantation [6]. This implies that the head diameter should decrease which reduces the range of motion and increases the probability of dislocation [4]. In another study conducted with older patients with a mean age of 71 years, the authors observed that every 1° loss of spinal pelvic motion is associated with 0.9° compensatory increase in femoral motion [7]. It is therefore necessary to improve mechanical strength of cup material to allow lower thickness to be coupled with larger head diameter. In short, the range of motion criteria should always be kept alongside with wear criteria for improved mechanical stability and increased longevity to target both younger and older patients. Considering all the above issues, research continues to improve both mechanical as well as tribological properties of the cup material. In this work we investigate an epoxy based composites for hip implant application due to their higher mechanical strength and biocompatibility.

Experimental Details

Structalit with grade number 8801 has been selected as a commercially available biocompatible epoxy (certified according to ISO 10993-5, Biological evaluation of medical devices Part 5: Tests for in vitro cytotoxicity) for composite preparation. It is a product of Panacol-Elosol GmbH, Germany. Micrometer sized UHMWPE particles were used as a filler material for structalit/UHMWPE fabrication. S04 composites represents the structalit composite with 4 wt.% of UHMWPE particles and so for the other composites. Mechanical properties were evaluated based on the compression behavior and Vickers hardness. For friction measurement a unidirectional pin on disc device was used. Wear screening of samples were conducted on a lab fabricated multi-station prosthetic biotribometer. UHMWPE and structalit/UHMWPE composites were fabricated in the form of pin and a polished CoCrMo was used as a disc material. Stress and sliding velocity were kept at 2 MPa and 20.73 mm/s. The diluted bovine serum which had a

protein concertation of 20 mg/ml was used as lubricant and replaced after 48 hours in the total test run of 96 hours. Wear was measured using precision balance with an accuracy of 0.01 mg. Surface analysis were conducted using scanning electron microscope and optical microscope.

Results & Discussion

Structural analysis
Figure 1 indicates a firmly attached UHMWPE particle using a fibrillar structure. The UHMWPE particle was confirmed from its original size before mixing and the absence of calcium from the structalit.

Mechanical Behavior
The reduction in mechanical properties of composites is due the presence of softer UHMWPE phase. Although the overall mechanical strength of composites was found to be higher than the UHMWPE as shown in Figure 2. The Young's modulus, yield strength, and Vickers hardness of S24 were 82%, 268%, and 189% higher than the UHMWPE.
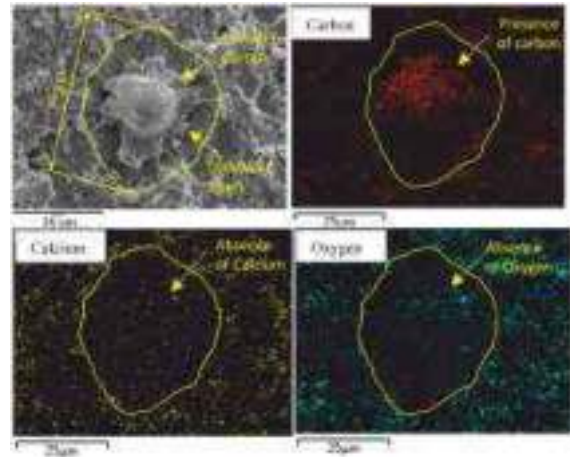
Figure 1: Image on the top left is SEM image of structalit/UHMWPE composite and other images represent and EDS spectra of different elements

Tribological Behavior
Friction analysis under unidirectional sliding revealed a ploughing wear mechanism in case of UHMWPE with a coefficient of friction (COF) of 0.11 (Figure 3 and 5). The low COF is due to the lower shear strength of UHMWPE, whereas lower yield strength increases the depth of abrasion. In case of multidirectional sliding both abrasion and burnishing were found as the dominant wear mechanism. Protuberances were also found which were formed due to continuous changes in the direction of friction vector during cross-shear sliding. There was no transfer film formation on counterface disc. The specific wear rate was $2.8 \times 10\text{-}6$ mm3/Nm which is presented in Figure 4.

Figure 2: Compression modulus, yield strength and Vickers hardness of strcutlait/UHMWPE composite and UHMWPE sample.

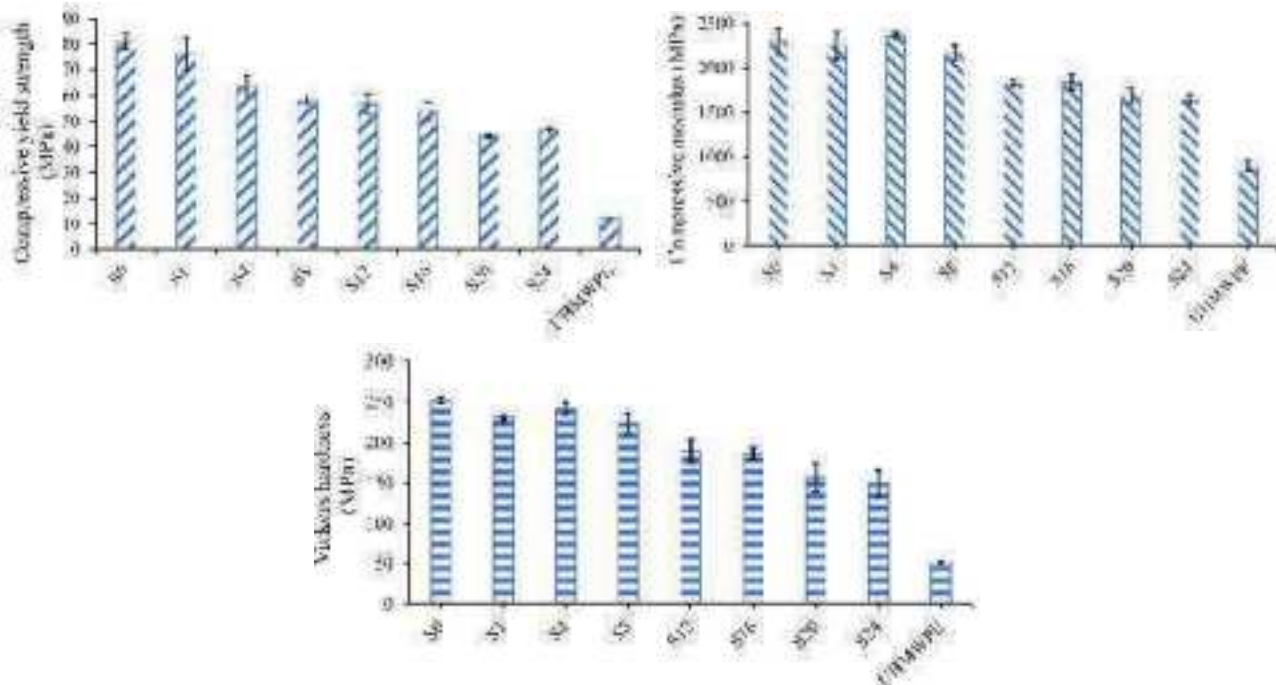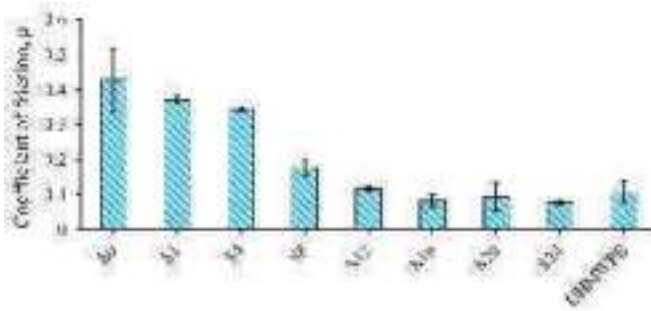*Figure 3: Friction coefficient of the pin samples tested in serum lubrication under unidirectional sliding condition.*
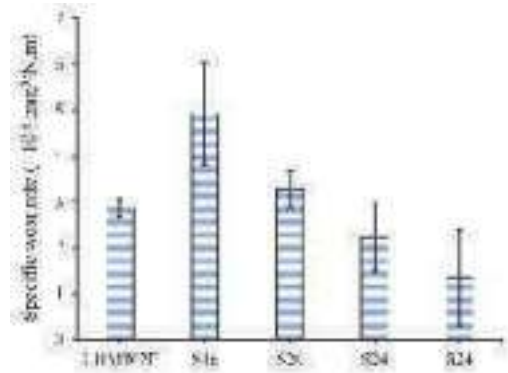

Figure 4: Specific wear rate of pin samples tested in serum lubrication under multi-directional sliding condition.

In case of structalit, higher COF value reveals higher shear strength of the material. Some cracks were also observed on the surface which indicates lower fatigue strength of the matrix.

In case of composites addition of UHMWPE particles reduced the interfacial shear strength and therefore lower friction force was obtained and the absence of cracks on the surface is an indicative of higher toughness and fatigue strength. Elongation of UHMWPE particles on the surface of composites provide low shear resistance and therefore friction reduces as the percentage of filler loading increases. Based on the mechanical properties and friction coefficient three composites S16, S20 and S24 were selected for wear test. Lower specific wear rate of S24 (1.35×10-6 mm3/Nm) in comparison to UHMWPE supports the above mentioned hypothesis.
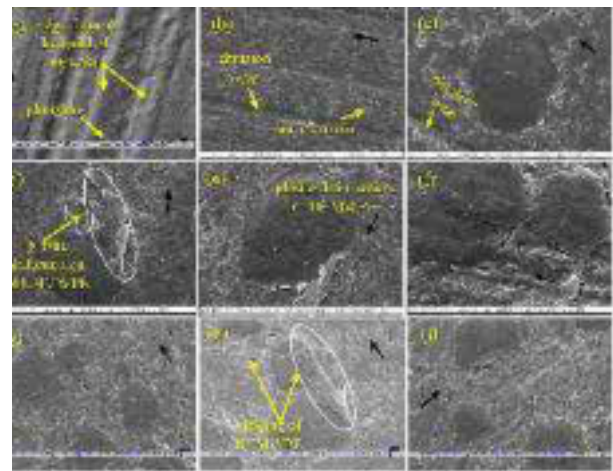

Figure 5: SEM analysis of pin samples after friction test in serum lubrication in unidirectional sliding condition.

Conclusions

A composite with higher mechanical and tribological properties were developed for hip joint application. Higher yield strength and hardness of the composite provided a resistance against the abrasion during sliding as compared to UHMWPE. The low friction interface of composite provided the coefficient of friction close to UHMWPE. These combined bulk and surface properties of composites resulted in lower specific wear rate of 1.35×10-6 mm3/Nm for S24 compared to higher value of 2.8×10-6 mm3/Nm for UHMWPE. Therefore structalit/UHMWPE composites have potential for implant applications.

References

○ Burger NDL, de Vaal PL, Meyer JP. Failure analysis on retrieved ultra-high molecular weight polyethylene (UHMWPE) acetabular cups. Eng Fail Anal. 2007, 14(7):1329.

○ Ong KL, Lau E, Suggs J, Kurtz SM, Manley MT. Risk of subsequent revision after primary and revision total joint arthroplasty. Clin Orthop Relat Res. 2010, 468(11):3070.

○ Cooper RA, McAllister CM, Borden LS, Bauer TW. Polyethylene debris-induced osteolysis and loosening in uncemented total hip arthroplasty. A cause of late failure. J Arthroplasty. 1992, 7(3):285.

○ Yoshimine F, Ginbayashi K. A mathematical formula to calculate the theoretical range of motion for total hip replacement. J Biomech. 2002, 35(7):989.

○ Vendittoli PA, Ganapathi M, Nuño N, Plamondon D, Lavigne M. Factors affecting hip range of motion in surface replacement arthroplasty. Clin Biomech. 2007, 22(9):1004.

○ Goebel P, Kluess D, Wieding J, Souffrant R, Heyer H, Sander M, et al. The influence of head diameter and wall thickness on deformations of metallic acetabular press-fit cups and UHMWPE liners: A finite element analysis. J Orthop Sci. 2013, 18(2):264.

○ Cunningham R, Beck D, Peterson C. Dislocation Following Total Hip Arthroplasty. JBJS J Orthop Physician Assist. 2017, 5(1): e8.

Ferromagnetic Particles Removal From Bearings –
a Micro-piv and Computational Fluid Dynamics Approach

Chiranjit Sarkar[1*]

[1]Department of Mechanical Engineering, Indian Institute of Technology Patna, India
[*]Corresponding author Email: csarkar@iitp.ac.in

Keywords: Ferromagnetic Particles, Bearings, Magnetic Field, Particle Tracing, CFD

Abstract

In this paper, numerical simulations of ferromagnetic particles removal in lubricating grease flow from bearings are presented. The rheology of three lithium greases with NLGI (National Lubricating Grease Institute) grades 00, 1 and 2 respectively are considered. The grease is modeled as a single-phase Herschel–Bulkley fluid. The particle tracing in the presence of magnetic field has been considered in grease pockets formed between ball and bearing races where the inner race is rotating and driving the flow. The main principle presented in this paper is a development of computational model for grease flow in bearings to remove magnetic particles from a lubrication channel using permanent magnets located at the inner ring of bearing. It was found that the change in the flow characteristics and particle migration due to the influence of different magnetic field. This computational method predicts the position of magnets which can remove particles without needing to remove the grease and stop normal use of the bearing.

Introduction

Introduction

Wind Turbine Blade pitching systems, which actively rotate blades along their longitudinal axes, are used in active-pitch and active-stall controlled wind turbine systems. The pitching motion is typically driven by hydraulic actuators [1] or electric motors. The pitch control system is critical for utility-scale turbines, as it allows the system to optimize power extraction and minimize unnecessary loads. Above all else, the pitching system is employed as a fail-safe aerodynamic brake to stop the turbine when wind speeds become excessive [2], thus making the pitching system critical for preventing catastrophic failure of the whole turbine [3]. The use of a pitching system necessitates that the blades be exclusively supported by rolling element bearings at their roots. The bearings themselves are subject to large static loads as well as centrifugal and cyclic bending loads when the turbine is in operation. Most modern turbines use four-point contact bearings or ball bearing slewing rings for pitch operation. Pitch bearings are generally lubricated using grease with a high-viscosity base oil. Similar to drivetrain bearings, the grease in pitch bearings should maintain the thickest lubricant film possible to prevent premature damage. Because pitch bearings operate under slight oscillatory motion, fretting wear and/or false brinnelling can occur when the lubricant film is insufficient. Additionally, a report by the National Renewable Energy Laboratory (NREL) suggested the pitch bearing be periodically (i.e., once per day) rotated through a large amplitude oscillation cycle in order to redistribute grease that has been previously displaced [4]. Most wind turbines are intended for operating lifetimes of 20 years or longer; however, field reports [5] have shown that drivetrain bearings tend to fail much earlier than 20 years. These added maintenance and repair costs contribute significantly to the total cost of wind energy [6]. According to industry averages [7] 10 to 20 percent of the up tower time involved in servicing a turbine is spent on re-lubrication (technicians crawling around in the cramped nacelle and hub to grease lubrication points numbering from 10 to more than 80 with several different greases in each turbine). And, in the case of conventional manual lubrication methods, over- or under-greasing (leading to potential failure) always is an unwanted possibility; lubrication intervals may be sporadic or ill timed; contaminants can inadvertently be introduced, and equipment performance may be compromised.

Methodology

The purpose of the proposed project is to show how the rheology of the grease can be varied and thus how the flow dynamics of the flow can be altered. In this project, the practical implementation of a MR flow system in a bearing is presented together with a concrete practical example of how a MR grease can enhance the lubrication. The main principle presented in this project is a development of the ideas by Andauga et al. [8] who developed a device for large wind turbine bearings to remove magnetic particles from a lubrication channel using permanent magnets located at the inner ring bearing. This is a static solution, meaning the dynamic control of the fluid by the use of MR technology not is considered. The idea presented here is based on the MR flow technology using electromagnets rather than permanent magnets. Combining the ability to active control the activity of electromagnets together with the MR flow

response to magnetic fields, a method to increase the lubrication at the maximum Hertz contact in a wind turbine bearing/gear with permanent magnet is presented by Raj et al. [9]. Considering the pitch angle gear and bearings in the gear box, there is a limited region in the angular direction of the bearing in which the maximum loads occur. This condition is due to the limited pitch motion of the turbine blade. The main idea is based on the physical property that magnetic particles are attracted by magnetic fields, considering the analogous physics enabling wear particles to gather on the magnet as in the solution by Andauga et al. [8]. Before moving ahead, we reflect on the intricacy in this physical problem. Modeling the motion of magnetized particles is in detail a very difficult problem as it cover both electromagnetics (particle electrical- and magnetic properties) and fluid mechanics (particle shape, particle number density effect on the flow etc.). The ambition in this project is by no means to resolve these details with experimental and numerical approach.
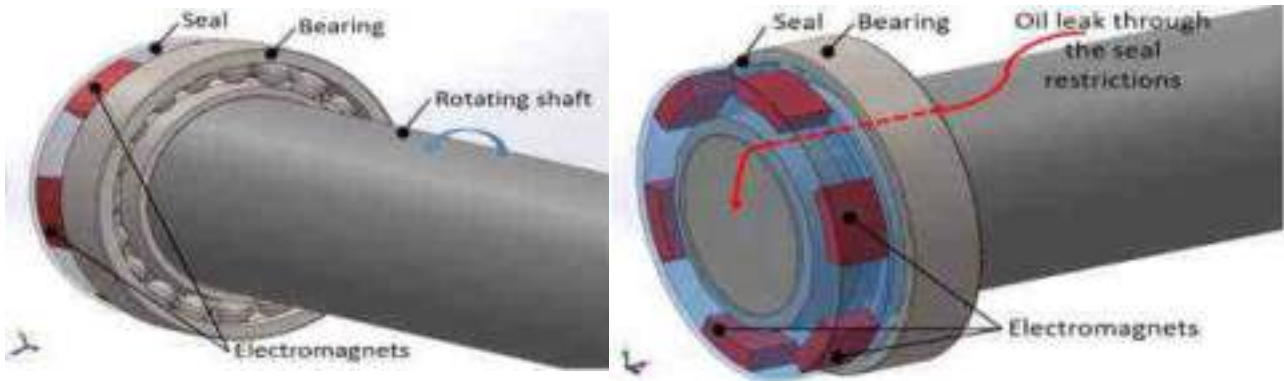
Figure 1: Schematic 3D drawing of the proposed seal geometry applied to a bearing system. Here six electromagnets are placed in the seal to attract the magnetic particles and control the yield stress and the dynamic viscosity of MR grease.

Results & Discussion

The influence of magnetic field on the flow of grease suspended with iron particles is visualized with the help of mPIV. The raw images, as shown in Figure 2 illustrate the behavior of iron particles in the dense grease medium in the incidence of magnetic field. The images are caught away from the shaft. Ferromagnetic iron particles line up themselves in the direction of magnetic field, thus increasing the apparent viscosity of the grease medium.

The magnetic field circulation at two different planes is analyzed in this study. The XY- plane is the radial plane of visualization for mPIV experiments. The YZ plane represents the axial plane. Since the camera position could not be changed in the magnetic seal system experimental set-up, flow visualizations could only be carried out in the radial plane. The grey scale zone in Figure 8 represents the annular grease domain. These are taken after carrying out a magnetic field study numerically to evaluate the maximum magnetic field generated in the grease medium.

Figure 2: Raw images extracted from mPIV at (a) B = 0 T (b) B = 0.6 T

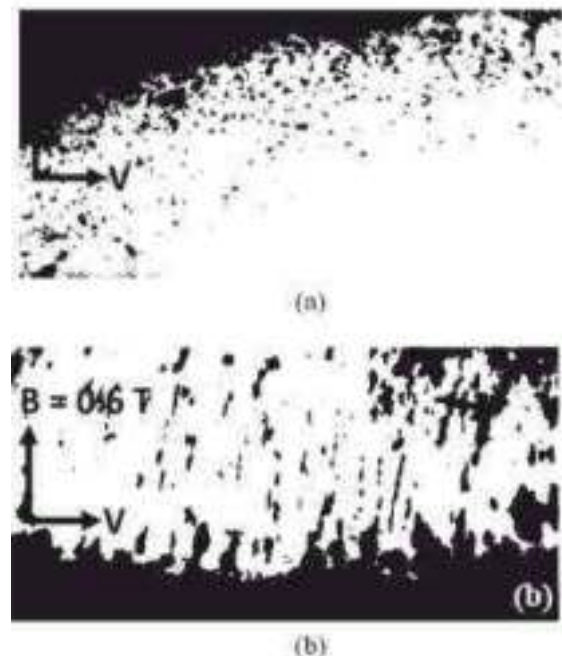As can be seen from Figures 3(a) and (b), the magnetic field strength is least in the locality of the shaft. It gradually upsurges towards the periphery of the PMMA housing. The field strength at different locations obtained from numerical study can help us to predict the actual field strength in the magnetic seal grease set-up.

Conclusions

This work accounts an experimental and numerical flow study of grease suspended by dispersing iron particles into a lithium based grease. The flow investigation is passed out in a magnetic seal grease medium for different magnetic field strengths i.e., on-state as well as off-state conditions. The rotational speed of the shaft disturbs the grease (suspended with iron particles) flow characteristics. The maximum momentum transfer to the locality of the shaft is confirmed by reduced velocities as we move away from the shaft. This is attributed to strong magnetic chains formed as a result of the magnetic field. Near the rotating shaft, there are competing effects of momentum transfer from the motion of the shaft as well as the resistance offered to the flow by the field-induced chains.
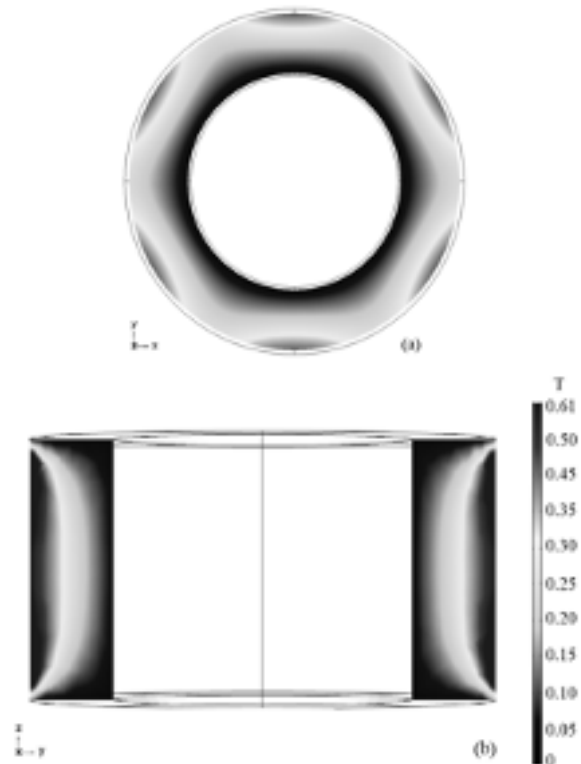
Figure 3: Magnetic field distribution on (a) radial plane (XY plane) and (b) axial plane (YZ plane)

References

○ Senjyu, T., Sakamoto, R., Urasaki, N., Funabashi, T., Fujita, H., and Sekine, H., 2006, "Output power leveling of wind turbine generator for all operating regions by pitch angle control," IEEE Trans. Energy Convers, 21: 2, pp 467–475.

○ Hau, E., 2006, Wind Turbines (Springer-Verlag, Berlin, 2006).

○ 20% Wind Energy by 2030, U.S. Department of Energy Technical Report, 2008.

○ Harris, T.A., Rumbarger, J.H., and Butterfield, C.P., 2009, "Wind turbine design guideline DG03: yaw and pitch rolling bearing life," NREL Technical Report No. NREL/TP-500-42362, 2009.

○ Ribrant, J., Bertling, L., 2007, "Survey of failures in wind power systems with focus on Swedish wind power plants during 1997–2005," IEEE Power Engineering Society General Meeting, 2007.

○ Terrell, E.J., Needelman, W.M., and Kyle, J.K., 2009, "Current and future tribological challenges in wind turbine power systems," in STLE/ASME international joint tribology conference, ASME IJTC2009-15220.

○ https://www.windsystemsmag.com/lubrication-technologies-for-the-wind-farm/ (Accessed on July 16, 2022)

○ International Patent WO2017/174832 [2017], "device for cleaning ferromagnetic particles from bearings and cleaning method," Laulagun Bearing, Spain.

○ Raj, A., Sarkar., C., Kumar, P., and Pathak, M., 2022, "Investigation of magnetorheological grease flow under the influence of a magnetic field," Journal of Molecular Liquids, 361, Article No. 119682.

Tactile Friction Under Boundary Lubrication:
Effect of Molecules on Human Skin

Suyash Gairola[1*] Sanjeev Kumar[1] and M.S. Bobji[2]

[1]Department of Chemical Engineering, Indian Institute of Science (IISc Bangalore), India
[2]Department of Mechanical Engineering, Indian Institute of Science (IISc Bangalore), India
*Corresponding author Email: suyashg@iisc.ac.in

Abstract

The "feel" of products with which we interact via the sense of touch is an essential aspect of product design. Tactile perception is complex, taking elements from mechanics, interfacial sciences, psychology, and many more fields. While holding any object, there is an active interaction between our fingertips and the object's surface. In such cases, sliding commences between the human finger and the counter substrate, where the contact might be intermediated by materials that can act as a lubricant. Tactile friction becomes a critical force in examining and quantifying tactile perception. The goal is to study friction between a deformable patterned soft substrate sliding on a stiffer substrate under boundary lubrication. Coefficient of friction (COF) values were calculated from tactile measurements for different lubricating solutions on various substrates. The measurements have been done on an in-house developed strain gauge based force sensor. The results highlight the fall in COF values after adding a drop of lubricant (water/sodium dodecyl sulphate (SDS)), with SDS giving a more significant reduction. SDS masks the effect of textures and wetting properties across the different substrates as an effective boundary lubricant giving similar COF values for all substrates. Also, water on smooth silicon gave a higher COF value than other substrates. The observations highlight that specific interactions between different molecular species and a given substrate influences tactile friction.

Introduction

Understanding and quantification of tactile perception is something that still alludes us. The advances made in the study of friction based tactile perception can be used in designing haptics, prosthetics, clothes and detergents. Tactile perception can be quantified using the coefficient of friction (COF) [1]. Hence, understanding tactile friction might be the key to grasping tactile perception for tribological systems in sliding contact. Friction between the human finger and a stiff substrate in the presence of a boundary lubricant is a generic framework that encapsulates this motive. The goal is to study friction between a deformable patterned soft substrate and a stiffer substrate under boundary lubrication. Factors like elasticity, surface roughness and surface energy control tactile friction is such systems.

COF values were calculated from tactile measurements for different lubricating solutions. All the measurements were made on an in-house developed force sensor. The results indicate the role of surface properties and the molecular interactions of the lubricant with the substrate in affecting friction, i.e., the interaction between molecules and surfaces influences tactile friction significantly. It can help in distinguishing different tribopairs based on tactile perception.

Experimental Details

Quantifying friction between a human finger and a glass slide in the presence of the boundary lubricant of choice was done using a strain gauge based force sensor. Measured COF values can be correlated with tactile data [2]. The experiments discussed here are for preliminary investigation, helping us to build upon this challenging pursuit.

The instantaneous ratio of the tangential and normal load, both of which are picked up independently by the sensor gives the COF. The values are plotted throughout cycles in Figure 1. to see how COF varies during a measurement. The variability observed pertains to one user. Every experiment has 15 cycles, where speed and normal load are manually controlled. Cleaning of substrate afterwards with water and alcohol is recommended. The operating conditions, the instrument schematics and the output are as follows:

Table I: Operating conditions

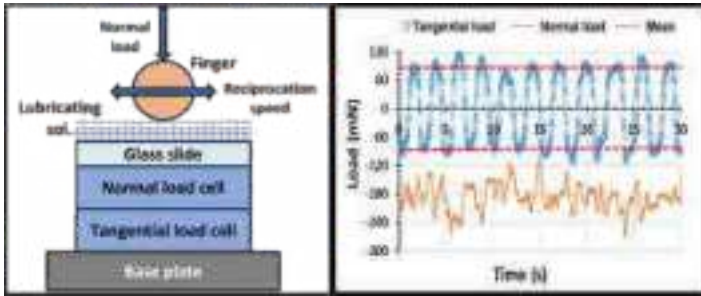|	
Normal load (N)	0.2-0.3
Reciprocating speed (m/s)	0.02-0.03
Stroke length (m)	0.03
Time of one cycle (s)	30

Figure 1: The Finger friction sensor developed
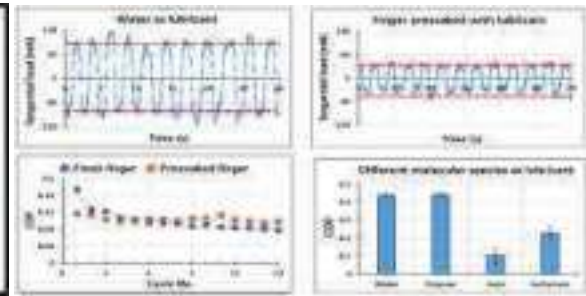in-house, and the tangential load measured by it

Figure 2: Effect of surface features and
different kinds of molecules on COF

Results & Discussion

Different lubricants produce distinct COF values for varying surface conditions. The tangential load decreases for a surfactant solution as compared to plain water. Modifying the finger surface by presoaking it in the lubricating solution leads to lower COF, as shown in Figure 2. COF throughout an experiment reaches an asymptote after decreasing from the higher initial value. However, with a presoaked finger the COF trend is flat. Also, species like polymers (SCMC) don't show the gradual decreasing trend in COF. This corroborates well with the hypothesis that only the surface-active components dynamically adsorb onto the substrate and provide a better lubricating film over time. So, a change in either of the substrate affects the adsorption dynamics of the molecules, hence affecting friction.

It is also observed that different molecular species give different COF values. Apart from adsorption characteristics, molecular effects like stearic hindrance and double layer effects might be responsible for a change in the COF values. Water and SCMC aren't surface active and hence give relatively higher COF values. Sodium carbonate (Washing soda) is reactive with skin and produces 'oily' products, thereby giving significantly lower COF values. Whereas Sodium dodecyl sulphate provides a molecularly adsorbing film that facilitates boundary lubrication and hence a low COF.

In this case, the interplay between the molecules and the surface properties controls friction, which can be used to quantify tactile perception in a tribological context. The interaction of surfactant molecules on a patterned deformable surface needs to be investigated in more detail.

Conclusions

Tactile friction against a glass slide depends on the properties of both the substrate and the lubricant under boundary lubrication. COF can be used to quantify tactile friction using a strain gauge based sensor. Surface active molecules show a dynamic change in COF, which might be attributed to the adsorption of molecules onto the finger surface. A flat COF trend was observed if the finger is presoaked in these molecules or inert molecules like water or SCMC are used as lubricants. Therefore, factors like the conditioning of the finger with the surface-active component play an essential role in this system. Controlling either the surface properties or the intermediary molecular constituent affects friction.

References

◯ Zhang, S. et al., "Finger pad friction and tactile perception of laser treated, stamped and cold rolled micro-structured stainless steel sheet surfaces," Friction 5, 2, 2017, 207–218.
◯ Nacht, S. et al., "Skin friction coefficient: changes induced by skin hydration and emollient application and correlation with perceived skin feel," J. Soc. Cosmet. Chem, 32, 1981, 55-6

Evaluation of Lubrication Properties of Polyethylene Wax Emulsion

Harshadkumar s. Pandit[1*], K. Venkatesh[2], Chaitali Keni[3]
[1] Hindalco Industries Limited, HIC Semi Fab, Taloja, India
[2] Hindalco Industries Limited, HIC Semi Fab, Taloja, India
[3] Hindalco Industries Limited, HIC Semi Fab, Taloja, India
Email: harshadkumar.p@adityabirla.com

Keywords: Tribology, Wear, Lubrication, Polyethylene Wax Emulsion, Extreme Pressure Property

Abstract

In this research polyethylene wax emulsions were studied for their lubrication properties. Five blends of lubricants were prepared. Three blends of polyethylene wax emulsions, one of conventional soluble oil & one with conventional neat oil. Four ball tester is used to characterize the lubricating properties. The Anti-wear test and Extreme Pressure property test are used to determine the average wear scar diameter (WSD), coefficient of friction (COF), last non-seizure load, and weld load (EP). Surface morphology of ball scares from wear preventive test was observed optically. Results from the tribological test indicate that polyethylene wax emulsions have better Antiwear & Extreme Pressure properties compared to conventional soluble oils. Conventional neat oil has better Anti-wear properties but poor Extreme Pressure properties as compared to polyethylene wax emulsions.

Introduction

Introduction

Wax is one of the oldest materials used by humans. Waxes are organic substances that are solid at ambient temperature but become free-flowing liquids at slightly higher temperatures. The chemical composition of waxes is complex, but normal alkanes are always present in high proportion. Waxes are categorized based on their sources like waxes from Plants, Animals, or naturally occurring Petroleum. Waxes are used mostly as additives and active substances & the use of waxes is expected to increase in the future because of their generally favourable toxicological and ecological properties.

Waxes are used in various forms, Emulsion is an important form in which waxes find application in coatings, inks, OPVs, textile and leather treatments, polishes, paper, and cardboard coatings, etc. Wax emulsions like polyethylene waxes are well known for their abrasion resistance property, Anti-sagging property, Anti-settling property, Mar resistance property, and reducing the coefficient of friction and scuff resistance properties. These properties are important for lubricants as well. In literature, we find the use of waxes as a lubricating additive1 & as a direct lubricants2,3, however, nobody studied the wax emulsions as a lubricant. In this research, we have studied polyethylene wax emulsions lubrication properties along with neat and soluble cutting oils. Five blends of lubricants were prepared. Three blends of polyethylene wax emulsions, one of conventional soluble oil & one with neat oil. Four ball tester is used to characterize the lubricating properties. The Anti-wear test and Extreme Pressure property test are used to determine the average wear scar diameter (WSD), coefficient of friction (COF), last non-seizure load, and weld load (EP).

Experimental Details

Materials: Three Wax emulsion samples along with one soluble oil and one neat oil are selected for study. All the samples diluted to 20% with DM water except neat oil. pH of the samples adjusted to 6 - 7.5 with 5% acetic acid solution (Ref. Table 1).

	Material	Concentration	pH at 25 °C
1	Soluble Oil	20%	7.3
2	Neat Oil	100%	N.A.
3	PE Wax Emulsion - 1	20%	6.14
4	PE Wax Emulsion - 2	20%	7.29
5	PE Wax Emulsion - 3	20%	6.33

Table 1: Formulation for Study

Experimental design: An experimental design is done with five samples (see Table 1), three samples of PE wax emulsions, one of neat oil, and one of soluble oil. Wear scare diameter (WSD), Non-sizer load (EP), Coefficient of Friction (COF) & Emulsion Particle Size are used as response variables for the study.

Anti-Wear test: Test is performed according to ASTM D 4172-21[4]. Parameters: load (392 N), rotation speed (1200 rpm), temperature (75 ºC), time (1 hour). Chrome alloys balls were used, reference AISI 52100 (12.7 mm of diameter, hardness 60-66 HRC). The WSD of balls is measured using an optical microscope and ruler. The coefficient of friction (COF) is determined according to ASTM D5183-21a[5].

Extreme Pressure test: Test is used to determine the last non-seizure load and weld point according to the ASTM D2783-21[6]. Parameters: load (variable), rotation speed (1760 rpm), temperature (25 ºC), time (10 seconds). Anti-Wear and Extreme Pressure tests are performed in a four-ball tribometer, the scheme of testing is shown in Fig. 1[7].
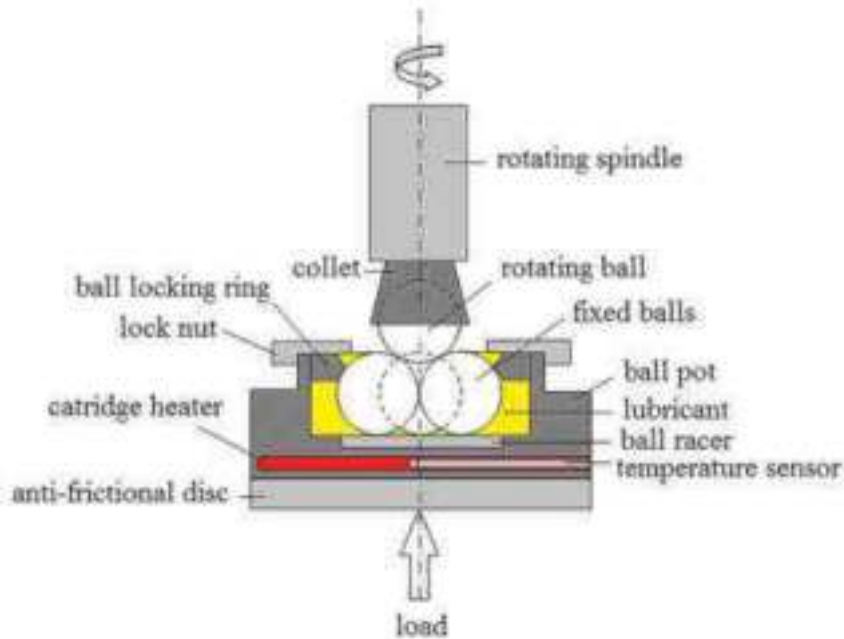

Figure 1: Schematic diagram of four ball tribometer.

Particle Size test: Particle size analysis is used to determine the particle size distribution of soluble oil and emulsions with X-ray diffraction method. Parameters: particles RI (1.550), absorption (1), dispersant (water), dispersant RI (1.330).

Results & Discussion

Anti-Wear & COF Test Performance: The antiwear test is measured in terms of the average wear scare diameter (WSD), higher WSD means lower lubrication. The statistical summary and one-way analysis of variance (ANOVA) for the WSD and COF with 95% confidence level are shown in Tables 2 and 3 respectively. From One way ANOVA, p-value for WSD was 3.82E-22 and p-value for COF was 0.025, therefore the null hypothesis H0 was rejected, all population means are not equal (Tables 2 and 3). The ANOVA analysis of Anti-Wear test indicate that all five samples do not have same average WSD. Neat Oil have WSD of 506 μm, that of PE Emulsion - 3, 2, 1 is 549 μm, 690 um, 917 μm respectively and soluble oil has highest WSD of 1187 μm.

Groups	Count	Sum	Average	Variance
Soluble Oil	12	14245	1187	4877
Neat Oil	12	6077	506	8198
PE Emulsion - 1	12	11006	917	14905
PE Emulsion - 2	12	8279	690	24469
PE Emulsion - 3	12	6590	549	8317

Source of Variation	SS	df	MS	F	P-value
Between Groups	3843489	4	960872	79	3.82E-22
Within Groups	668425	55	12153		
Total	4511914	59			

Table 2: One-way ANOVA of WSD

COF of PE wax emulsions in between 0.074-0.078, that of neat oil is 0.082 & that of soluble oil is 0.095.

Groups	Count	Sum	Average	Variance
Soluble Oil	5	0.477	0.095	6.35E-05
Neat Oil	5	0.408	0.082	9.51E-05
PE Emulsion - 1	5	0.382	0.076	8.72E-05
PE Emulsion - 2	5	0.390	0.078	0.000151
PE Emulsion - 3	5	0.370	0.074	0.00011

Source of Variation	SS	df	MS	F	P-value
Between Groups	0.0014	4	0.00036	3.50	0.025
Within Groups	0.0020	20	0.00010		
Total	0.0034	24			

Table 3: One-way ANOVA of COF

Extreme Pressure Test Performance: Extreme Pressure test is performed to determine the last non-seizure load and weld point of PE wax emulsions, soluble oil, and neat oil (Figs. 4 and 5). When EP test is performed with normal loading as per ASTM D2783-215, all the samples have shown same last non seizure load 100kg (980 N) & same weld point 126 Kg (1234.8N). Whereas when loading is done stepwise on the same chrome alloys balls, interesting results were observed (see fig. 5). PE Wax Emulsion- 1 has 315 Kg (3087 N) last non seizure load & 400 Kg (3920 N) weld point. PE Wax Emulsion- 2 has 250 Kg (3087 N) last non seizure load & 315 Kg (3087 N) weld point. PE Wax Emulsion- 3 has 126 Kg (1234.8 N) last non seizure load & 160 Kg (1568 N) weld point. Soluble oil performance is the worst, 80 Kg (784 N) last non seizure load & 100 Kg (980 N) weld point. In the step loading neat oil has 126 Kg (1234.8 N) last non seizure load & 160 Kg (1568 N) weld point.
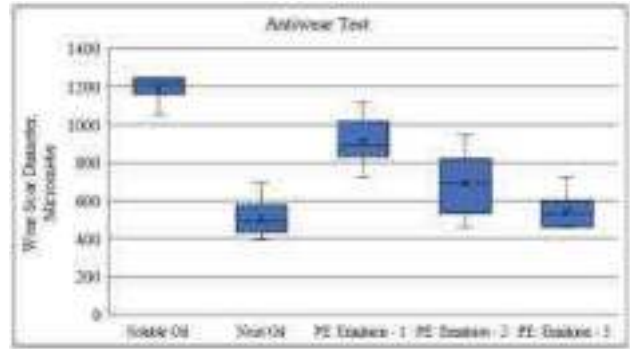

Figure 2: Box plot WSD.
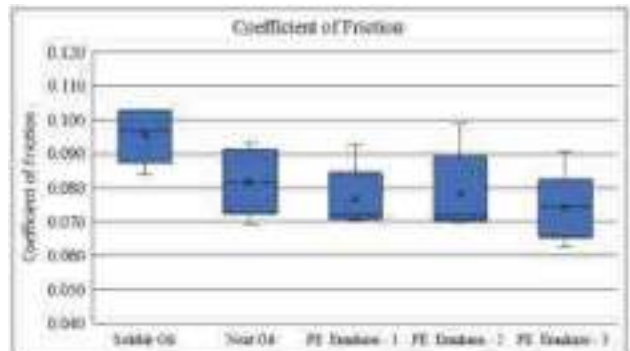
Figure 3: Box plot COF.
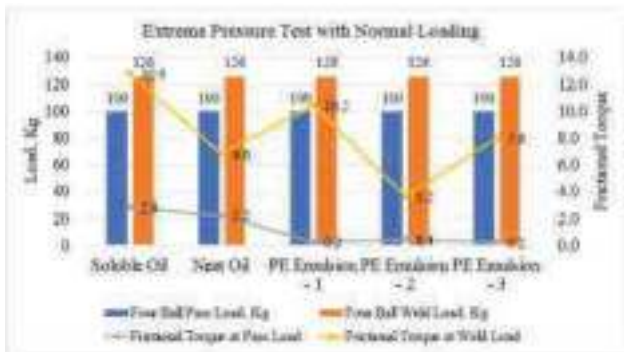
Figure 4: EP test with Normal Loading.

Figure 5: EP test with Step Loading

Particle Size Test Results: Particle size is done to determine the particle size distribution of samples. This test is performed to understand the variation in lubrication properties (AW, COF & EP) w.r.t. Particle size distribution. Higher particle size gives better separation of oil from water which results into high lubricant availability at bite as compared to lower particle size. Thus, Higher particle size emulsion provides better lubrication as compared to lower particles size emulsion.

	Material	Vol. Weighted Mean D[4,3], μm	D(0.5), μm
1	Soluble Oil	0.155	0.147
2	Neat Oil	N.A.	N.A.
3	PE Wax Emulsion - 1	68.728	64.021
4	PE Wax Emulsion - 2	32.670	23.226
5	PE Wax Emulsion - 3	3.008	0.797

Table 4: Particle Size Distribution

Conclusions

Results from the tribological test indicate that PE Wax emulsion samples have better Anti-Wear property compared to soluble oil. Wear Scar Dimeter (WSD) of Neat Oil is 506 μm, that of PE Emulsion - 3, 2, 1 is 549 μm, 690 um, 917 μm respectively and soluble oil has highest WSD of 1187 μm. Similarly, PE Wax emulsion samples have better Extreme Pressure properties compared to conventional soluble oil sample & neat oil sample when step load is applied. PE Wax emulsion samples has last non seizure load between 126 – 400 Kg (1234.8 - 3920N), as compared to 80 Kg (784 N) of soluble oil and 126 Kg (1234.8 N) of neat oil. Tribological properties of PE emulsion samples varied within group. Particle size distribution gives justification for the same. Particle size distribution is important property w.r.t tribology. Higher particle size gives better separation of oil from water which results into high lubricant availability at bite as compared to lower particle size. PE Wax Emulsion – 1 has highest particle size D[4,3], μm 68.728 and thus highest non seizure load 315 Kg (3087 N), as compared to PE Wax Emulsion – 3 has particle size D[4,3], μm 3.008 & non seizure load of 126 Kg (1234.8 N). Particle size of Soluble Oil is least among all the samples D[4,3], μm 0.155 and thus lowest non seizure load of 80 Kg (784 N).

References

○ Yetgin, S. (2020). Characterization Of Lubricant Polyethylene Waxes. European Journal of Technique (EJT) , 10 (2) , 489-500 . DOI: 10.36222/ejt.718423

○ Delgado, Arnoldo & Aperador, Willian. (2019). Evaluation of Polyethylene Wax and Paraffin as Anti Wear and Extreme Pressure Additives in Virgin Sesame Base Stock. tecciencia. 14. 21-29. 10.18180/tecciencia.2019.27.3.

○ Yetgin, Senem & Gönen, Mehmet & Savrık, Sevdiye & Balköse, Devrim. (2021). Polyethylene Wax: Uses, Characterization, and Identification. 10.1201/9781003057918-9.

○ ASTM D 4172-21. Standard Test Method for Wear Preventive Characteristics of Lubricating Fluid (Four Ball Method), 2021.

○ ASTM D5183-21a. Standard Test Method for Determination of the Coe cient of Friction of Lubricants Using the Four-Ball Wear Test Machine, 2021.

○ ASTM D2783-21. Standard Test Method for Measurement of Extreme-Pressure Properties of Lubricating Fluids (Four-Ball Method), 2021.

○ Mubashshir, Mohd & Shaukat, Asima. (2019). The Role of Grease Composition and Rheology in Elastohydrodynamic Lubrication. Tribology Letters. 67. 1-20. 10.1007/s11249-019-1218-z.

○ Sayadi, Hamidreza & Mortazavi, Sseed & Pajohan, A. (2017). Polyethylene wax emulsion production by using the stabilizer substances of ionic surface.

○ Nazare, M & Paleu, Viorel & Bhaumik, Shubrajit & Ianus, Gelu & Olaru, Dumitru. (2018). Performances of automotive lubricants – tests on four ball machine. IOP Conference Series: Materials Science and Engineering. 444. 022013. 10.1088/1757-899X/444/2/022013.

○ Perez J. D. Weller, Jr. and J. Duda (1999) "Sequential Four-Ball Study of Some Lubricating Oils," Lubrication Engineering, September, pp 28-3

Investigation of Oil Flow in a Ball Bearing Using Bubble Image Velocimetry and Cfd Modelling

Ujjawal Arya[1*], Wyatt Peterson[1], Farshid Sadeghi[1], Andreas Meinel[2] and Hannes Grillenberger[2]

[1]School of Mechanical Engineering, Purdue University, West Lafayette, IN 47907, USA
[2]Schaeffler Technologies AG & Co. KG, 91074 Herzogenaurach, Germany
*Corresponding author Email: uarya@purdue.edu

Keywords: Lubricant flow visualization, Bubble Image Velocimetry, Computational Fluid Dynamics

Abstract

The objectives of this investigation were to experimentally and analytically study the oil flow inside a ball bearing using Bubble Image Velocimetry (BIV). A counter rotating angular contact ball bearing test rig (CRACTR) was developed such that bearing races can be rotated simultaneously in opposite directions. The oil flow inside the cage and bearing was analyzed using a high-speed camera. BIV was used to track bubbles in the oil and to understand the flow pattern inside the bearing. Ansys Fluent software was used to develop a computational fluid dynamics (CFD) model for the bearing. Results from the CFD model corroborate well with the experimentally observed flow streamlines and demonstrate the influence of operating conditions and cage designs on fluid flow. The CFD model provided details such as oil velocity at different locations in the bearing and fluid drag torque. The quantitative and qualitative validation of CFD results provides a basis for cage design for efficient lubricant flow inside a bearing.

Introduction

Sufficient lubrication is required to ensure the running performance of the bearings and to reduce the risk of starvation [1,2]. At high speeds, it becomes difficult for the oil to enter the contact area between ball and race due to the formation of vortices around the ball, thus affecting the bearing lubrication [3]. Studying the oil flow field helps identify such vortex regions and potential sources of kinetic energy losses inside the bearings [4]. Knowledge of complex flow behavior inside the bearing is therefore critical to understand the lubrication mechanism and also to improve the heat dissipation performance [5], especially for high-speed rolling element bearings (REBs) [3]. Previous investigations of oil flow in bearings employing Particle Image velocimetry (PIV) have limited resolution of experimental flow fields, and are only able to provide qualitative confirmation of CFD results. In this study, BIV was used to track the bubbles in the oil generated due to self-aeration and to visualize the flow streamlines inside an ACBB.

Experimental Details

Figure 1 depicts the close up of the CRACTR [6] that was designed and developed to visualize the oil flow. The CRACTR was additionally equipped with a High-Speed (HS) camera, capable of recording high-quality frames during the steady state operation of the bearing. All the captured videos were analyzed to quantify the oil flow by tracking bubbles using PIVlab [7]. A fiber optic light source was used to illuminate the bearing chamber. A plane mirror was placed just above the bearing housing at an angle of 45° within the line of sight of the camera to record an overhead view of the bearing. SAE 30 motor oil was used for lubrication and the oil fill level during the bearing operation was maintained such that the bearing was completely submerged for all the operating conditions.

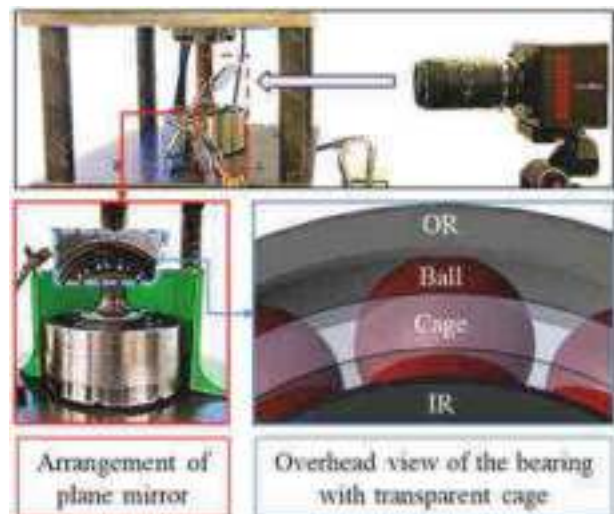Bubbles form in lubricating oils due to the entrained air rising to the surface (known as aeration). Velocity of these bubbles rising to the surface is in the plane normal to the

Figure 1: Close up view of the imaging setup with the CRACTR for oil flow visualization.

viewing angle and thus does not affect the findings. This phenomenon was exploited to perform BIV by tracking these bubbles instead of seeding the oil with tracer particles, as shown in Figure 2. For visualization of oil flow, replicas of common 7311 ACBB cages were fabricated from acrylic and installed in the bearing. The CRACTR was operated in a counter-rotating configuration such that the cage remained stationary during all tests for two cage types.
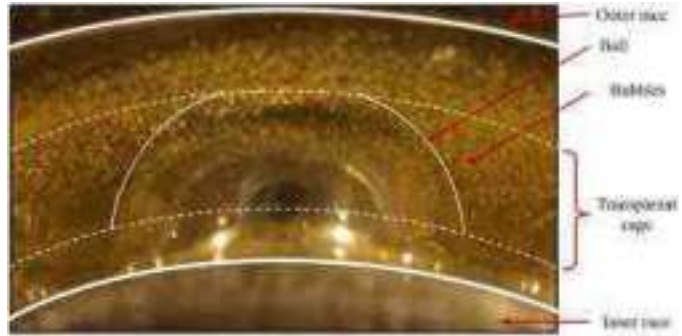
Cfd Model Details

Single phase steady-state oil flow in the 7311 ACBB chamber was modelled using Ansys Fluent software. The cyclical symmetry of the bearing was used to reduce computation time, and only three ball and cage pocket sections were modeled with periodic boundary conditions at the cutting planes [8]. Ansys Mosaic Meshing software was used to develop an efficient polyhedral mesh. Inflation layers were used on the rolling element surface at the raceways and cage pockets. The SST k-ω turbulence model was used in the CFD model to account for turbulent fluid flow inside the bearing.

Figure 2: Snapshot from the High-Speed camera showing bubbles through the transparent cage in CRACTR.

Results & Discussion

The CRACTR was used to visualize the oil flow for two different cage types to study the influence of cage pocket geometry on the oil flow streamlines in an ACBB. Apart from different cage pocket clearances, the two test cages also differ in the pocket shapes which influences the oil flow pattern inside the bearing.

The flow streamlines in Figure 3 (a) with first cage type (cage-B) form a uniform inverted-V (■shaped pattern between each ball across all speeds tested. A growing region of recirculation was observed at the apex of the ■shaped pattern with increasing IR speeds, similar to the observations by Yan et al. [3]. This cage has continuous inner and outer walls and a uniform, spherical cage pocket surface. This results in uninterrupted oil flow around this cage and produces smooth oil streamlines. The velocity of the left ball directs oil toward the cage, where it is deflected toward the OR. The OR directs oil in the clockwise direction, and the right ball acts as an obstacle, directing oil back toward the cage. This results in the formation of ■ shaped oil flow pattern visible in the BIV experiments and from the CFD model.

On the other hand, the second cage type (cage-P) has a non-uniform surface adjacent to the raceways, with angular protrusions on the side wall. These protrusions combined with a larger cage pocket clearance and higher conformity with the ball prevent lubricant from moving throughout the bearing as observed with cage-

Figure 3: BIV results for increasing race speeds with (a) cage-B and (b) cage-P

B. This results in an irregular flow between the cage pockets. This cage also has a slightly larger diameter than cage-B, which results in a smaller space between the cage wall and the outer race. The triangular protrusions on the walls of cage-P adjacent to the outer race obstruct the streamlined flow leaving the ball's surface, creating local recirculation region between each ball, as represented in Figure 3 (b).
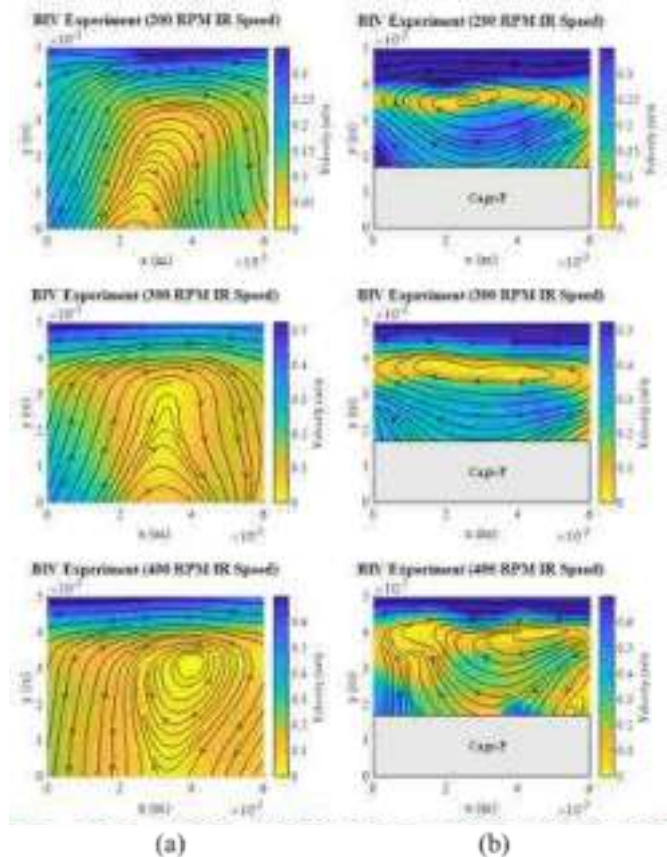
Overall, results obtained from the CFD model are in good agreement with the BIV measurements as illustrated in Figure 4. A selection of points was used to compute the absolute velocity magnitude and direction difference between BIV and CFD results. Velocity vector direction between experimental and analytical results was observed to have a good correlation across the range of speeds tested for both cages. Velocity magnitudes were found to agree well between experimental and analytical results with cage-B, and fair agreement was observed with cage-P.

The CFD model was also utilized to compare the fluid drag torque for both the cage types by integrating the wall shear stress and pressure acting perpendicular to the axis of rotation on the faces of the cage that align with the raceways (neglecting the cage pockets). Figure 5 presents the variation in drag torque with the tangential velocity of the oil flow for both cages from the CFD model in the counter-rotating configuration. The magnitude of fluid drag torque was observed to increase linearly with increasing fluid flow velocity for both cages. Cage-B has nearly equal contributions of IR-driven and OR-driven fluid drag torque due to the similarity in the cage's smooth surfaces facing the raceways. Conversely, cage-P has a higher contribution of IR-driven fluid drag torque compared to OR-driven fluid drag torque. Wall shear concentrations are observed on the protrusions of cage-P near the IR and OR, appearing to be more prominent near the IR. The same fluid velocities will be experienced relative to the cage in a conventional bearing configuration where the OR is fixed and the IR rotates (with no slipping). Thus, the current results from the counter-rotating configuration can be applied generally to ACBBs.

Conclusions

An innovative experimental test rig and measurement technique of Bubble Image Velocimetry (BIV) for studying the oil flow inside the rolling element bearings was presented. The bubbles generated due to self-aeration during bearing operation were captured using high-speed videography, and were used to track the oil flow inside an ACBB. Results from the BIV measurements were used to study oil flow and validate a CFD model of the experimental setup. Following conclusions have been drawn from this investigation:

(i) Experimental and analytical results showed ■-shaped oil flow patterns between rolling elements with the brass cage geometry (cage-B), while recirculating oil vortices formed in the same region with the plastic cage geometry (cage-P) across all speeds tested.

(ii) Results from the single-phase, steady-state CFD models developed in Ansys Fluent corroborated well with the experimental results and were able to predict the oil flow streamlines between the balls for various race speeds. The oil flow streamlines became less uniform with increasing race speeds due to the increase in recirculation, particularly for the cage-B.

Figure 4: Experimental BIV measurements and CFD modelling results for race speeds of IR: 300 RPM and OR: −207 RPM for (a) cage-B and (b) cage-P
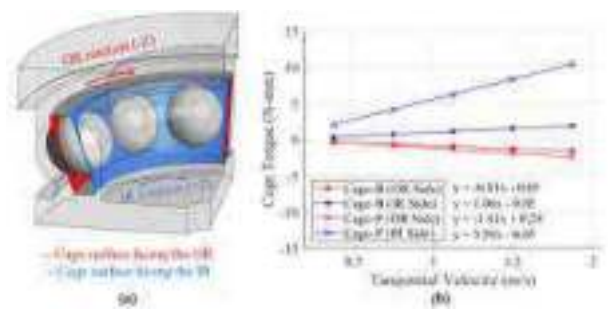

Figure 5: (a) Faces highlighted on the cage to analyze the OR (red) and IR (blue) contributions of fluid torque, and (b) variation of fluid torque on cage-B and cage-P for various flow tangential speeds relative to the stationary cage from the CFD model.

(iii) The CFD model was also used to analyze the flow patterns at different depths into the bearing and highlight the relative fluid drag torques between the two cage types. It was determined that protrusions from cage-P perpendicular to the raceways trapped oil near the cage.
Additionally, cage-P drag torque was dominated by the inner race motion while cage-B drag torque was more evenly influenced by inner and outer race motion relative to the cage.

References

O Fischer, D., von Goeldel, S., Jacobs, G., and Stratmann, A., 2021, "Numerical Investigation of Effects on Replenishment in Rolling Point Contacts Using CFD Simulations," Tribology International, 157, p. 106858.

O Russell, T., and Sadeghi, F., 2022, "The Effects of Lubricant Starvation on Ball Bearing Cage Pocket Friction," Tribology International, 173, p. 107630.

O Yan, K., Dong, L., Zheng, J., Li, B., Wang, D., and Sun, Y., 2018, "Flow Performance Analysis of Different Air Supply Methods for High Speed and Low Friction Ball Bearing," Tribology International, 121, pp. 94–107.

O Zhang, W., Paik, B. G., Jang, Y. G., Lee, S. J., Lee, S. E., and Kim, J. H., 2007, "Particle Image Velocimetry Measurements of the Three-Dimensional Flow in an Exhaust Hood Model of a Low-Pressure Steam Turbine," Journal of Engineering for Gas Turbines and Power, 129(2), pp. 411–419.

O Vasques, J., Ibrahim, A., Hann, D., Simmons, K., and Walsh, M., 2019, "The Effect of Surface Tension on Bubble Generation in Gas-Sheared Liquid Films," Proceedings of the ASME Turbo Expo, 5A-2019.

O Arya, U., Sadeghi, F., Conley, B., Russell, T., Peterson, W., and Meinel, A., 2022, "Experimental Investigation of Cage Dynamics and Ball-Cage Contact Forces in an Angular Contact Ball Bearing," Proceedings of the Institution of Mechanical Engineers, Part J: Journal of Engineering Tribology, p. 135065012210777.

O Thielicke, W., and Sonntag, R., 2021, "Particle Image Velocimetry for MATLAB: Accuracy and Enhanced Algorithms in PIVlab," Journal of Open Research Software, 9.

O Peterson, W., Russell, T., Sadeghi, F., and Berhan, M. T., 2021, "Experimental and Analytical Investigation of Fluid Drag Losses in Rolling Element Bearings," Tribology International, 161, p. 107106.

Synthesis, Rheological Characterization and Tribological Performance of Olive Oil Biolubricant Enhanced With Mos₂ Additive

Rajendra V. Pawar[1*], Dattatray B. Hulwan[2], and Maruti B. Mandale[3]

[1,2]Department of Mechanical Engineering, Vishwakarma Institute of Technology, Pune, Maharashtra, India
[1,3]K. E. Society's Rajarambapu Institute of Technology, Rajaramnagar. Affiliated to Shivaji University Kolhapur, Maharashtra, India
*Corresponding author (Email: rajendra.pawar@ritindia.edu

Keywords: Tribology, Lubrication, Biolubricant, Transesterification

Abstract

The stringent environmental regulations, non-renewability, poor biodegradability, and toxic nature of petroleum oil motivate the researcher to seek eco-friendly biodegradable alternatives synthesized from vegetable oil feedstock. In Industry, Biolubricants synthesized from vegetable oil are gaining more importance because of their renewable, eco-friendly, and less toxic nature and excellent lubrication properties such as high viscosity index, high flash point, high lubricity, and low volatility. In this study, Olive oil biolubricant is synthesized using the transesterification method, and MoS2 additive is blended in biolubricant with 1 wt.%, 2 wt.%, and 3 wt.% concentration. The FTIR technique is used to identify the synthesized biolubricant. The effect of synthetic lubricant SAE20W40 and Olive oil biolubricant enhanced with MoS2 on the tribological performance of journal bearing has been measured using a pin on disc tribometer and four-ball tester under a boundary and thin film lubrication regime. The surface of the pin after the wear test is analyzed using an optical microscope. The rheological, physicochemical, and thermal properties of olive oil with MoS2 are found to be reasonable compared to SAE20W40 oil. Test result reveals that Olive oil with MoS2 has excellent rheological and tribological properties compared to synthetic lubricant. Olive oil blended with 3 wt.% MoS2 could be considered a better sustainable biolubricant oil which would help to reduce the global demand of petroleum and synthetic-based lubricants.

Introduction

The demand for lubricating oil is increasing daily; conventional petroleum-based lubricants are high in cost, depleting rapidly, and would be exhausted in a few decades. Due to availability issues, toxicity, and the non-biodegradable nature of conventional lubricants, researchers moved towards biodegradable lubricants such as vegetable oils [1]. Vegetable oils are the best alternative to conventional lubricants because they are environmentally friendly, renewable, and less toxic. They also have excellent lubricating properties, such as high viscosity index, lubricity, and low volatility. Conventional petroleum-based lubricants are toxic to the environment. A significant portion of used lubricants worldwide is thrown in the environment, which is non-biodegradable and pollutes the surrounding. So, it is necessary to find an alternative for this lubricant.. Bio-lubricants have many advantages over conventionally used lubricants such as having higher lubricating properties, viscosity property, shear stability, high load carrying capacity, and superior dispersencies [2].

Many edible and non-edible vegetable oils are available in the market, such as palm oil, castor oil, canola oil, mustard oil, karanja oil, jatropha oil, coconut oil, sunflower oil, safflower oil, soybean oil, olive oil, groundnut oil, sesame oil, etc. Vegetable oil is obtained from various kinds of seeds, and almost 350 oil-bearing crops are available worldwide. Vegetable oils cannot be used as lubricants directly due to their low thermal oxidation stability, low cloud and pour point, and pour atomization [3]. It can be overcome by using suitable chemical modification methods and proper blending with chemical additives and high oleic vegetable oils. Globally, different kinds of lubricants, such as refined synthetic, mineral, and vegetable oils, are used as lube oil [4]. Olive oil was selected as suitable vegetable oil for the synthesis of biolubricant due to its high oleic acid content, high oxidation stability, and high viscosity index. The presence of a large percentage of monosaturated fatty acids in olive oil results in more resistance to oxidation and stability. Olive acid consists of long-chain fatty acids (more than 20 carbon atoms). Molybdenum disulfide (MoS2) was used as the additive for improving olive oil's wear and friction properties.

Synthesis Of Olive Biolubricant

The two-step transesterification process is used to synthesize the biolubricant from olive oil. In esterification/transesterification, acyl moieties are rearranged to produce new triesters from triglycerides. The

reaction starts with the formation of triglycerides into diglycerides and further into monoglycerides. This process increases the oxidation stability of oil by converting fatty acids into Fatty acid methyl esters (FAME) as it contains fewer allylic methylene positions. In the first step of esterification, oil was converted into FAME and glycerol. KOH was used as a catalyst, and the reaction was carried out at 60 ˚C for 2 hours. In this reaction, 1 mole of triglycerides reacts with 3 moles of alcohol to produce 3 moles of alkyl ester. i.e., biodiesel. Then FAME was treated with silica gel for 30 minutes to remove the soap and filtered. Later it was dried for 12 hours in the oven at 105˚C [5].

In the second transesterification stage, trimethylolpropane was mixed in the FAME at 120˚-130˚C using a magnetic stirrer. Sodium methoxide was used as a catalyst. In this reaction, ester was transformed into another ester through an interchange of the alkyl groups. The product obtained from this reaction is TMP ester which is used as a biolubricant. The reactions are shown in figure 1.
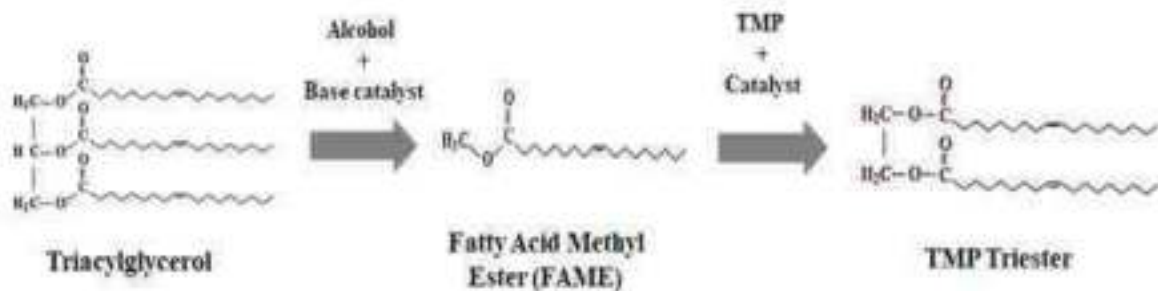

Figure 1: Transesterification Process

Characterization And Properties Of Biolubricant

The Fourier transforms infrared spectroscopy (FTIR) spectrums of the prepared olive TMP ester are presented in figure 2. The FTIR presents that the biolubricant is prepared from the transesterification method. The position and intensity of stretching and bending vibration were analyzed and compared with the spectra of chemical compounds found in olive oil. The yield of produced biolubricant was calculated by Leung and Guo equation given in the literature and found 82.74% yield after washing and moisture removal.

The rheological, physicochemical, and thermal properties of prepared biolubricant and olive oil were measured as per the ASTM standards and compared with synthetic oil. The properties of pure olive oil prepared biolubricant and veedol oil is presented in Table 1. Molybdenum disulfide (MoS2) was selected as the best suitable additive for improving olive oil's wear and friction properties. The MoS2 was blended in olive oil biolubricant with 1 wt.%, 2wt.%, and 3 wt.% concentration.
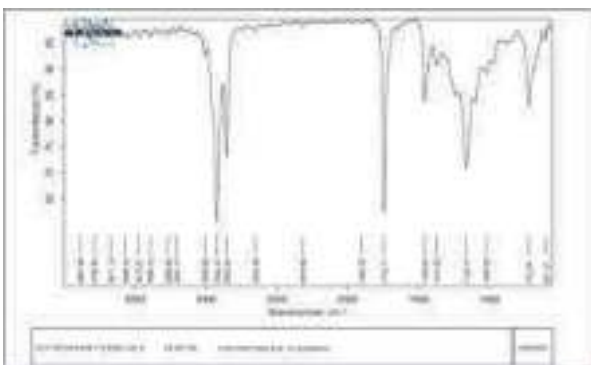

Figure 2: FTIR of produced olive biolubricant

Table 1: Properties of oil

Test description	Ref. Std. ASTM 6751	Unit	Biolubricant (olive oil)	Veedol oil 120W60
Density	D1448	Kg/m³	910	847
Viscosity @ 40°C	D445	Cst	37.04	100
Viscosity @ 100°C	D445	Cst	7.814	14.2
Flash point	D92	°C	265	218
Fire point	D92	°C	273	224
Saponification number	D95	-	168	-
Oxidation stability	D48	Hours	4.5	>3
Cloud point	D2500	°C	<-3	<-5
Pour point	D2500	°C	<-1	<-5

Experimental Details

The application selected for the experimentation is journal-bearing. The pressure and the speed of the journal bearing were measured and converted into test conditions. The test conditions were varied by changing the speed and load conditions. The test was conducted for 6 kN, 10 kN, and 15 kN load and 1000 rpm and 2000 rpm speed conditions. Pin-on-disc tribometer TR20LE was used for experimentation to measure the friction and wear parameters. To minimize the inaccuracy in the experimentation, the same test was carried out three times and the mean average value was considered for analysis. Based on the literature analysis, each test was carried out for 45

minutes to analyze the coefficient of friction and wear rate. The flat and hemispherical pins made of brass material with a length of 30 mm and diameter of 10.2 mm were used for the experiment. A disc is made from EN-31 steel hard material with 165 mm diameter and 8 mm thickness.

Figure 3: Flat and Hemispherical Pin Surface

Results & Discussion

A pin-on-disc tribometer was used to conduct the tests on SAE20W40, olive oil, olive oil with 1% MoS2, olive oil with 2% MoS2, and olive oil with 3% MoS2. The wear rate, coefficient of friction, and frictional force findings are examined.

The coefficient of friction and wear rate of flat pin for various oil under varying load and speed of 2000 rpm is presented in figure 4 and 5, respectively. The coefficient of friction of olive oil was observed low for all load conditions than SAW20W40 and additive blends. The maximum friction force was observed for SAE20W40 oil. The wear rate for olive oil with 3 wt.% MoS2 was observed to be the least between all the oils and olive oil with 2 wt.% MoS2 had maximum wear.

Before and after the test weight of the pin was measured using an electronic weighing balance (accuracy of 0.0001 mg) to check the weight loss. The weight loss for the pin used for olive oil with 1% MoS2 was maximum, and the pins used for synthetic oil had minimum weight loss compared with others. The figure presents the weight loss of pin for various oil blends.

Optical microscopy image analysis was carried out to check the various wear mechanism present on the lubricated surface. The analysis was carried out at 500X magnification. It is observed that the pin used for olive oil with 1% MoS2 had maximum wear, and Olive oil with 3% MoS2 had minimum wear. The wear lines were observed to be more prominent for the pin used for olive oil with 1% MoS2 as compared to other pins used for testing. The wear of the pin used for synthetic lubricant testing is more as compared to the pin used for olive oil-based bio lubricant. The surface roughness is high for a pin used for synthetic lubricant testing as compared to the pin used for olive oil-based bio lubricant testing.
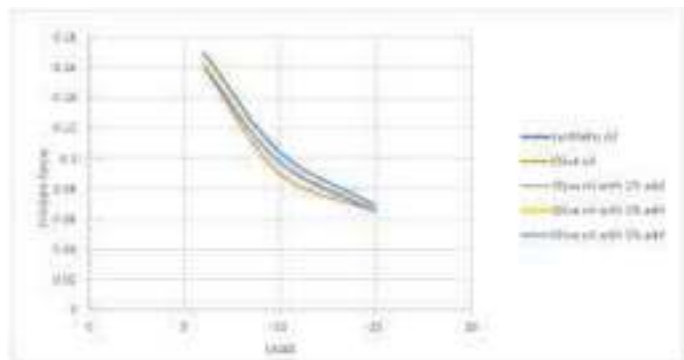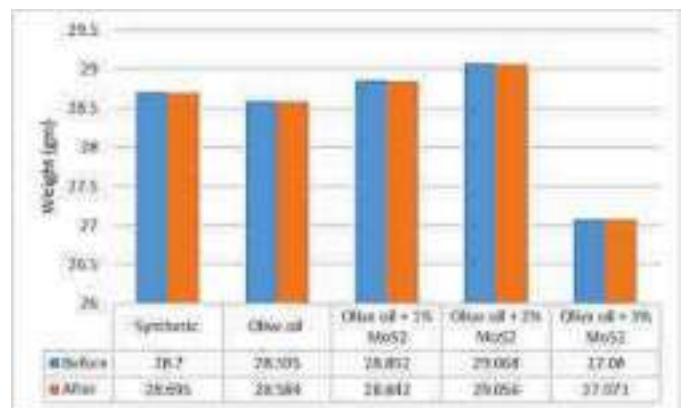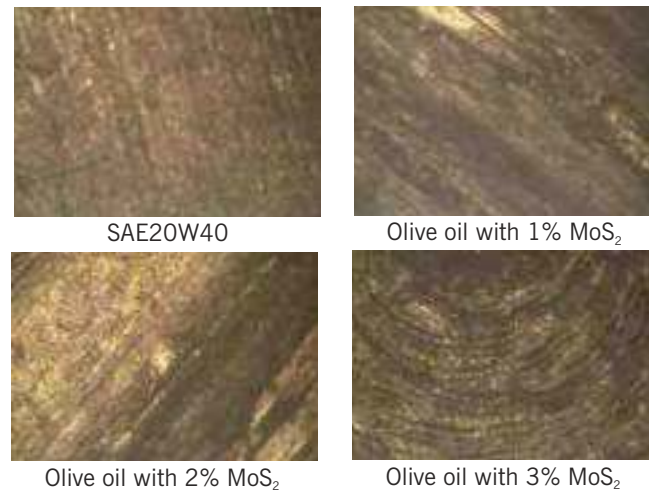

Figure 6: Wear rate of different oils at 2000 RPM

Figure 7: Weight loss of the pin

SAE20W40	Olive oil with 1% MoS$_2$
Olive oil with 2% MoS$_2$	Olive oil with 3% MoS$_2$

Figure 8: Surface analysis of flat pin

Conclusions

Based on the experimental results, the following conclusions are drawn: In this study, the friction and wear behavior of journal-bearing material was evaluated and focused on the effect of the MoS2 additive in olive oil.

    a) The highest friction coefficient was found with an Olive oil bio-lubricant, whereas adding MoS2 to olive oil significantly reduces the friction coefficient.

    b) The journal-bearing material lubricated with olive oil +1wt.% MoS2 has the lowest friction coefficient of 0.106. The frictional coefficient of bearing material lubricated with olive oil is 0.108 and SAE20W40 is 0.111.

The result indicates that olive oil with MoS2 as an anti-wear is the best suitable lubricant for replacing synthetic lubricant, reducing the dependence on petroleum-based products and being environmentally friendly.

References

○ Martín-Alfonso J.E., Valencia C., 2015, Tribological, rheological, and microstructural characterization of oleogels based on EVA copolymer and vegetables oils for lubricant applications, Tribology International, 90, 426–434.

○ Wani Khalid Shafi and M. S. Charoo, 2021, An overall review on the tribological, thermal and rheological properties of nanolubricants, Tribology - Materials, Surfaces & Interfaces, 15, 1, 20-54.

○ Attia N. K., S. A. El-Mekkawi, O. A. Elardy, E. A. Abdelkader, 2020, Chemical and rheological assessment of produced biolubricants from different vegetable oils, Fuel, 271, 117578,

○ Baskar S., Sriram G. and Arumugam S., 2017, Tribological Analysis of a Hydrodynamic Journal Bearing Under the Influence of Synthetic and Biolubricants, Tribology Transactions, 60:3, 428-436.

○ Pantelis G. Nikolakopoulos and Dimitrios A. Bompos, 2015, Experimental Measurements of Journal Bearing Friction Using Mineral, Synthetic, and Bio-Based Lubricants, Lubricants, 3(2), 155-163.

Uncertainty Analysis of Wear and Friction Under Reciprocating Sliding Conditions for Hypereutectic Al-si Cylinder Liner Material

Ajith Kurian Baby[1], P K Rajendrakumar[1] and Deepak Lawrence K[1*]

[1]Department of Mechanical Engineering, National Institute of Technology Calicut, India
[*]Corresponding author Email: deepaklawrence@nitc.ac.in

Keywords: Uncertainty, Wear, Cylinder liner, Hypereutectic Al-Si, Boundary lubrication

Abstract

The service life of an engine is usually determined from wear estimation. Accurate wear prediction is challenging as the wear rate reported in the literature shows a large deviation for similar conditions. Experimental assessment of wear is usually performed using tribometers, and results are often presented with standard deviation, neglecting uncertainties involved in the estimation of wear. This work analyses the various sources of uncertainty as per ISO standards while estimating friction and wear of liner-ring pairs using a linear reciprocating tribometer (LRT). Uncertainty estimation using the Monte Carlo simulation technique was also conducted. The uncertainty analysis was conducted by performing sliding wear experiments using a hypereutectic Al-Si cylinder liner specimen and a chrome-coated piston ring as the counter specimen on the LRT. The experiments were performed to mimic the condition of the engine running under a boundary layer lubrication regime. The various uncertainty components of Type A and Type B related to the tribosystem for this condition were evaluated as per the Guide to the Expression of Uncertainty in Measurement (GUM) approach and the Monte Carlo method, and the results were compared and reported in the study.

Introduction

Introduction
Engineering systems are subjected to different modes of failure like fatigue, fracture, plastic deformation, excess deflection, corrosion and wear [1]. Among the various modes of failure, wear is one of the most complicated and hard-to-predict factors. Bench tests involving tribometers are often used to estimate wear rates. Bench tests remain a practical source for evaluating the friction coefficient for different material pairs under various conditions. The difficulty in accurately estimating friction coefficient also persists, similar to wear rate, as they are influenced by equipment-related uncertainties [2]. This work attempts to estimate the various sources of uncertainty related to the equipment in estimating wear rate and friction. The quantification of wear and friction uncertainty can aid in improving the experimental setup design and help in better assessment and prediction of friction and wear.

Experimental Details
The sliding wear experiments were performed using a linear reciprocating tribometer (Make: Ducom, Model:TR 282) under a boundary lubrication regime to mimic the working of an engine at the top dead centre (TDC). The hypereutectic Al-Si (Si >13%) was used as the specimen, and the chrome-coated piston ring was used as the counter specimen. A finite quantity of lubricating oil (0.2 ml) was added at the contacting interface to achieve the boundary lubrication condition. SAE 15W – 40 (Servo Pride XL) was used as the lubricating oil for all experiments.
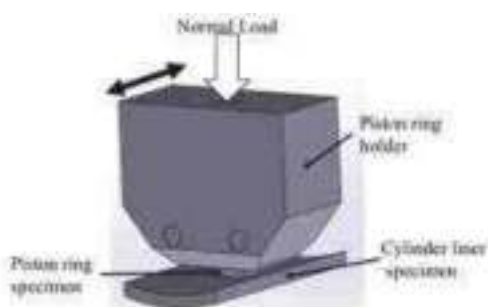

Figure 1: Schematic of contact arrangement of the piston-cylinder liner assembly

A total of 10 experiments were repeated (each for 10,000 cycles) to quantify the wear and friction uncertainty under similar sliding conditions. All the experiments were performed at a constant load of 80 N and at a sliding velocity of 0.2 m/s to mimic the TDC condition [3]. The Al-Si specimen was polished with diamond compound paste and then chemically etched with NaOH for 90 s prior to the test. The main objective of chemical etching was to remove the softer aluminium from the contact interface and to expose the hard silicon particles from the matrix. The silicon particles can act as a load-bearing surface and enhance the wear resistance of the alloy. Chemical etching improves the liner specimen's lubricant retaining property and can entrap debris in the etched region [4–7].

Uncertainty Evaluation by GUM Approach

The wear rate (k) can be quantified as per the following equation [8,9]

$$\kappa = \frac{V^*}{F^* \times D} = \frac{\Delta m\, ltrd\theta}{m_i F^* \times 2Sfx} \quad (1)$$

In Eqn.1, Volume lost $(V^*) = \dfrac{\Delta m}{\rho_{sample}}$ (2)

Total sliding distance, $D = 2Sfx$ (3)

Sample density, $\rho_{sample} = \dfrac{m_i}{V_{sample}}$ (4)

Initial volume, $V_{sample} = ltrd\theta$ where, l, t are the linear dimensions and $rd\theta$ is the length of the curved surface of cylinder liner specimens (mm). Δm - mass loss due to wear (g), m_i – initial mass of specimen (g).

F^* - Average normal force (N), S – stroke length (m), f - frequency (Hz), x - test duration (s)

The instantaneous values of the friction coefficient (μ) can be expressed as the ratio of frictional force (Ff) to normal load. The frictional force was measured using a piezo sensor and normal load (N) with a load cell. The friction coefficient can be mathematically.

expressed as: $\mu = \dfrac{F_f}{F^*}$ (5)

The Guide to the Expression of Uncertainty in Measurement (GUM) describes the guidelines for carrying out uncertainty analysis [10]. The measurand (wear rate and friction coefficient) was determined by measuring individual input quantities like those specified in Eqn.1 and Eqn.5. Even after considering all known systematic errors involved in estimating the measurand, residual uncertainty can persist. This residual uncertainty arises due to uncorrected systematic errors in measurement, like the error in the manufacturer's reported value, uncertainty associated with compensation given for a measurement, uncertainty due to instrument resolution etc. Combined standard uncertainty (uc), which corresponds to the estimated standard deviation (σ) of the measurement result, can be determined from the law of propagation of uncertainty. Combined uncertainty is the function of the standard uncertainty of each input quantity and their sensitivity coefficients (a partial derivative of the measurand concerning each input quantity). The combined standard uncertainty for wear rate can be expressed as Eqn.6 and Eqn.7

$$u_c^2(\kappa) = (\frac{\partial \kappa}{\partial \Delta m})^2 u^2(\Delta m) + (\frac{\partial \kappa}{\partial l})^2 u^2(l) + (\frac{\partial \kappa}{\partial t})^2 u^2(t) +$$
$$(\frac{\partial \kappa}{\partial r})^2 u^2(r) + (\frac{\partial \kappa}{\partial m_i})^2 u^2(m_i) + (\frac{\partial \kappa}{\partial F^*})^2 u^2(F^*) + (\frac{\partial \kappa}{\partial S})^2 u^2(S) \quad (6)$$

$$u_c^2(\kappa) = (\frac{ltrd\theta}{2m_iF^*Sfx})^2 u^2(\Delta m) + (\frac{\Delta m\,trd\theta}{2m_iF^*Sfx})^2 u^2(l) +$$
$$(\frac{\Delta m\,lrd\theta}{2m_iF^*Sfx})^2 u^2(t) + (\frac{\Delta m\,lt}{2m_iF^*Sfx})^2 u^2(r) + (\frac{-\Delta m\,ltrd\theta}{2m_i^2F^*Sfx})^2 u^2(m_i)$$
$$+ (\frac{-\Delta m\,ltrd\theta}{2m_i(F^*)^2Sfx})^2 u^2(F^*) + (\frac{\Delta m\,ltrd\theta}{2m_iF^*S^2fx})^2 u^2(S) \quad (7)$$

Type A or Type B uncertainty analysis can estimate the standard uncertainty for each input quantity in Eqn.6. In Eqn.7, partial derivatives in Eqn.6 were evaluated and expanded. The combined standard uncertainty for the friction coefficient can be expressed as shown in Eqn.8

$$u_c^2(\mu) = (\frac{1}{F^*})^2 u^2(F_f) + (\frac{-F_f}{(F^*)^2})^2 u^2(F^*) \quad (8)$$

vUncertainty Evaluation by Monte Carlo Method The propagation of probability distributions serves as the foundation for evaluating measurement uncertainty. A model of the general form y = f (x1,...,xn) linking input quantities x1,...,xn, about which information is known, and the output quantity y, about which information is required, is developed in order to apply the propagation of probability distributions. A probability distribution for y is provided by an implementation of the propagation of probability distributions, from which the best estimate of y, the standard uncertainty associated with the estimate, and a coverage interval for y corresponding to a specified (coverage) probability can all be calculated [11].

Results & Discussion

The individual standard uncertainty for the wear rate and friction input parameters are evaluated in the following sub-sections.

Uncertainty in Mass Calibration

Mass change ( ) is defined as the difference between the initial and final mass of the cylinder liner specimen ( ). The standard uncertainty of initial and final mass can be assumed to be the same. Hence u( ) = u( ). The mass change was recorded using a precision balance (Sartorius, CP224 S) with a resolution of 0.1mg and a range of 0 - 220 g

$$u_c^2(\Delta m) = u^2(m_{initial}) + u^2(m_{final}) = 2u^2(m_{initial}) \quad (9)$$

The resolution of the instrument was 0.0001 g. Therefore, the type B uncertainty estimated was $0.0001/2\sqrt{3} = 0.00002887$ g. The type A uncertainty was obtained from repeated measurements and the estimated value of uncertainty was 0.0000708 g. Therefore

$$u(m_i) = \sqrt{0.00002887^2 + 0.0000708^2} = 0.00007646 \ \text{g}.$$

From Eqn.9, $u(\Delta m) = \sqrt{2} \times 0.00007646 = 0.0001081\text{g}$

Uncertainty in Linear Measurement (l,t)The length and width of the liner specimen were measured using a digital Vernier caliper (Make: ZHART) with a measuring range of 150 mm and a resolution of 0.01 mm. The standard uncertainty was estimated from the resolution. It was assumed that u(l)

$$= u(t) = 0.01/2\sqrt{3} = 0.002887 \ \text{mm}$$

Uncertainty in Measurement of Radius®

The radius was measured using a 3 D optical profiler (Make: Alicona, Model: Infinite Focus G5). The uncertainty of radius measurement was taken as the one provided by the manufacturer. u(r) = 2 μm.

Uncertainty in Force Measurement (F*)

The normal force was recorded continuously with the help of a load cell during the sliding wear tests. The normal force fluctuates above and below the preset value during the reciprocating motion. The variation of the normal force is bimodal, as shown in Fig.2. The average value of the normal force is estimated by splitting into upper and lower bins, and their average values are calculated separately, as shown in Eqn.9.
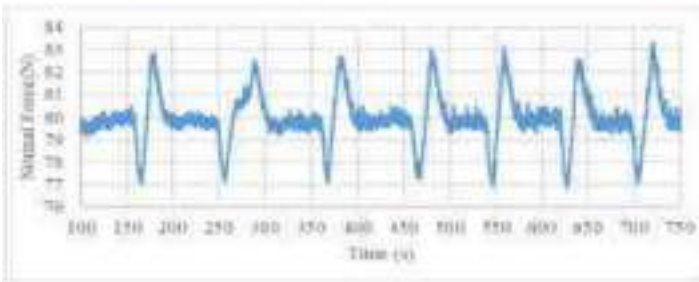

Figure 2: Variation of normal force with time

$$F_{up} = \frac{1}{n_{up}} \sum_{i=1}^{n_{up}} F_{up,i} \ \& F_{low} = \frac{1}{n_{low}} \sum_{i=1}^{n_{low}} F_{low,i} \quad (9)$$

$$u^2(F_{up}) = \frac{\frac{1}{n_{up}-1} \sum_{i=1}^{n_{up}} (F_{up,i} - F_{up})^2}{n_{up}} \quad (10)$$

$$F^* = \frac{F_{up} + F_{low}}{2}, u^2(F^*) = \frac{u^2(F_{up}) + u^2(F_{low})}{4} \quad (11)$$

Eqn.10 shows the standard uncertainty for force in the upper bin, and a similar approach is also applicable to estimate standard uncertainty for the lower bin. The average normal force and the standard uncertainty for the average normal force were evaluated as per Eqn.11 The calculated average normal force was 79.9628 N, and standard uncertainty, u(F*), was 0.01205 N

Uncertainty in Measurement of Stroke Length (S)

The actual displacement of the counter specimen was measured by using a laser displacement sensor (Make: Micro-Epsilon, Model: ILD 1420). The displacement (or commanded distance, Dc) was verified by inputting a value of 10 mm using the tribometer software, and a laser sensor measured corresponding values. The repeated results showed that the values fell within ± 0.3025 mm. Assuming rectangular distribution

$$u(D_c) = 0.3025/2\sqrt{3} = 0.0873 \ \text{mm}.$$

The actual sliding distance could also vary due to the angular misalignment of the specimen. In this case, an angular misalignment (α) of 3° concerning the horizontal was assumed. Hence the actual stroke length due to this misalignment (S) and its standard uncertainty is given by Eqn.12.

$$S = \frac{D_c}{\cos \alpha} = D_c \sec \alpha \quad (12)$$

$$u^2(S) = \sec^2 \alpha u^2(D_c) + \sec^2 \alpha . \tan^2 \alpha D_c^2 u^2(\alpha)$$

where $u(\theta)$ was assumed as $3°(0.05236$ rad), and the calculated value of $u(S)$ was 0.09163 mm. Due to the angular misalignment, the actual sliding distance (S_{act}) will be greater than the commanded motion and is given by, $S_{act} = D.(1 + u^2(\alpha))$ and the reported stroke length, S_{act} was 10.0274 mm

Uncertainty of frictional force (F$_f$)

A piezo sensor measured the frictional force with a least count of 0.1 N. The standard uncertainty $u(F_f) = 0.1/2\sqrt{3} = 0.02887$ N
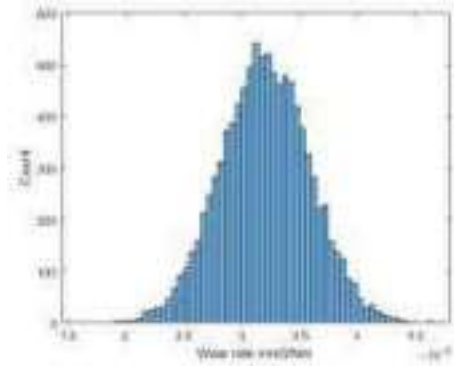

Figure 3: Histogram of Monte Carlo Simulation for wear rate

The Monte Carlo method was also adopted to estimate friction coefficient and wear rate uncertainty. The calculated value of combined standard uncertainty (uc) by the GUM approach (Eqn. 7) for wear rate was 2.554x10-6 mm3/Nm. The expanded uncertainty was analysed by calculating the effective degrees of freedom using Welch-Satterthwaite formula [12]. The effective degrees of freedom for wear rate was 9 and the corresponding value of coverage factor(k) from t-table was 2.262 for 95% coverage interval. The corresponding expanded uncertainty (U = k x uc) obtained was 5.7773x10-6 mm3/Nm. When the Monte Carlo simulations were performed for 10,000 data points, a standard deviation of 5.6788x10-6 mm3/Nm was obtained and Monte Carlo simulation predicted a mean wear rate of 3.2004 x10-5 mm3/Nm. The histogram of simulation is shown in Fig.3. A mean wear rate of 3.1947 x10-5 mm3/Nm was obtained experimentally for 10 repeated experiments with liner-ring pairs, each for 10,000 cycles.
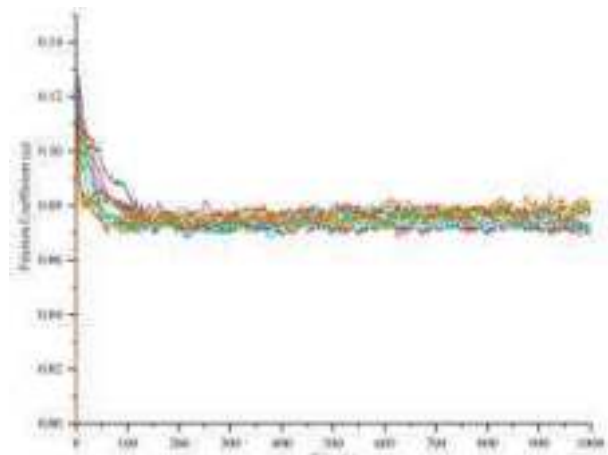

Fig. 4: Variation of friction coefficient with time

Similarly, in the case of uncertainty analysis of friction coefficient, a combined standard uncertainty of 4.6721 x 10-4. The effective degrees of freedom were again determined using Welch-Satterthwaite formula and expanded uncertainty was calculated. The obtained value of expanded uncertainty using GUM approach was 10.568 x 10-4 obtained for an effective degree of freedom of 9. In comparison, the Monte Carlo method predicted a mean friction coefficient of 0.0761 with a standard deviation of 8.897x10-4. Ten repeated experiments with liner-ring pairs showed an average friction coefficient of 0.0762 with a standard deviation of 9.832 x 10-4. Fig.4 shows he variation in friction coefficient for the repeated experiments with time.

The results obtained experimentally fall in the bounds of those obtained by the GUM approach and Monte Carlo simulation, indicating that analysis has taken primary contributors of wear and friction coefficient into consideration. It was observed that the major contributor to uncertainty for wear rate was the mass measurement. Other significant contributors were stroke length measurement and measurement of linear dimension (t). The other factors involved in measurement were negligible. The uncertainty estimate for wear rate is shown in Table 1.

However, in the case of friction coefficient, major contribution was from frictional force measurement. The uncertainty estimate for friction coefficient is shown in Table 2.

Table 1: Uncertainty estimate for wear rate

Input parameter	Mean Value	Standard uncertainty	Sensitivity Coefficient	Percentage contribution (approx.)
Δm (g)	0.0011	0.0006081	2.55x10^{-5}	98.61
l (mm)	35.0113	0.002887	9.37385 x10^{-7}	0
t (mm)	5.0763	0.002887	6.4700 x10^{-6}	0.005
gdθ (mm)	25.4455	2x10^{-3}	1.29088 x10^{-8}	0
F' (N)	79.9628	0.01205	4.1078 x10^{-7}	0
m$_1$ (g)	12.0299	0.00007646	3.73046 x10^{-4}	0
S (µ)	200.548	0.1709	3.27574 x10^{-5}	1.81

Table 2: Uncertainty estimate for friction coefficient

Input parameter	Mean Value	Standard uncertainty	Sensitivity Coefficient	Percentage contribution (approx.)
F$_f$ (N)	6.0862	0.03735	1.2506x10^{-2}	99.94
F' (N)	79.9628	0.01205	9.5185x10^{-4}	0.06

In the present work, other factors that could contribute to uncertainty, like the influence of temperature and angular misalignment of the counter specimen, were neglected. The repeated experiments were performed for a short duration (10,000 cycles each), and all experiments were completed within a closer time span to minimize the effect of temperature variation. Due to the curvature of the liner specimen, it wasn't easy to measure the angular variation of the piston ring while it was in contact with the liner specimen. The size and area of contact of the counter specimen (piston ring) were also very small compared to the cylinder liner; hence, the influence of angular misalignment was assumed to be minimal. However, in practice, it was found that the frictional force measurement was the major contributor to uncertainty and slight variation in contact area could lead to deviation in frictional force values.

Conclusions

The uncertainty evaluation of a linear reciprocating tribometer was performed under a boundary lubrication regime using a chrome-coated piston ring- Al-Si cylinder liner arrangement and an uncertainty estimate was also prepared. This work primarily focused on evaluating various equipment-related sources of uncertainty in the measurement of wear rate and friction coefficient. This work also aims to outline the procedure for uncertainty evaluation of wear rate and friction coefficient measurement. The uncertainty was evaluated based on GUM approach and Monte Carlo method and the results were compared. The key observation was that primary sources of uncertainty for wear rate arise from mass loss measurement, stroke length measurement and measurement of linear dimension (t). The uncertainty predicted by Monte Carlo method and that obtained from GUM approach was very close (1.6% variation). The mean wear rate predicted by Monte Carlo method was almost equal to that obtained experimentally. The major contributor to friction coefficient uncertainty was from the measurement of frictional force. The uncertainty variation in friction coefficient obtained from GUM method and Monte Carlo method were also in close range (17.5 % variation). In the measurement of friction coefficient, angular misalignment could lead to large variations in the values, and hence utmost care has to be ensured in this regard to obtain accurate results.

○ **References**
○ Schmitz TL, Action JE, Burris DL, Ziegert JC, Sawyer WG. Wear-rate uncertainty analysis. J Tribol 2004;126:802–8. https://doi.org/10.1115/1.1792675.
○ Schmitz TL, Action JE, Ziegert JC, Sawyer WG. The difficulty of measuring low friction: Uncertainty analysis for friction coefficient measurements. J Tribol 2005;127:673–8. https://doi.org/10.1115/1.1843853.
○ Mahato A, Sachdev A, Biswas SK. Lubricated tribology of a eutectic aluminium-silicon alloy in the ultra-mild wear and mild wear regimes for long sliding times. ACS Appl Mater Interfaces 2010;2:2870–9. https://doi.org/10.1021/am100550m.
○ Baby AK, Priyaranjan M, Deepak Lawrence K, Rajendrakumar PK. Tribological behaviour of hypereutectic Al-Si automotive cylinder liner material under dry sliding wear condition in severe wear regime. Proc Inst Mech Eng Part J J Eng Tribol 2020. https://doi.org/10.1177/1350650120964616.
○ Dienwiebel M, Pöhlmann K, Scherge M. Origins of the wear resistance of AlSi cylinder bore surfaces studies by surface analytical tools. Tribol Int 2007;40:1597–602. https://doi.org/10.1016/j.triboint.2007.01.015.Chen M, Perry T, Alpas AT. Ultra-mild wear in eutectic Al-Si alloys. Wear 2007;263:552–61. https://doi.org/10.1016/j.wear.2006.12.025.
○ Das S, Perry T, Biswas SK. Effect of surface etching on the lubricated sliding wear of an eutectic aluminium - Silicon alloy. Tribol Lett 2006;21:193–204. https://doi.org/10.1007/s11249-006-9016-9.
○ Kraghelsky IV. Calculation of Wear Rate. J Basic Eng 1965:785–90. https://doi.org/10.1016/b978-1-4832-8422-4.50007-8.
○ Meng HC, Ludema KC. Wear models and predictive equations: their form and content. Wear 1995;181–183:443–57. https://doi.org/10.1016/0043-1648(95)90158-2.
○ International Bureau of Weights and Measures. GUM modeling: Guide to the expression of uncertainty in measurement - Part 6: Developing and using measurement models 2020;JCGM GUM-6:1–103.
○ Esward TJ, De Ginestous A, Harris PM, Hill ID, Salim SGR, Smith IM, et al. A Monte Carlo method for uncertainty evaluation implemented on a distributed computing system. Metrologia 2007;44:319–26. https://doi.org/10.1088/0026-1394/44/5/008.
○ Willink R. A generalization of the Welch-Satterthwaite formula for use with correlated uncertainty components. Metrologia 2007;44:340–9. https://doi.org/10.1088/0026-1394/44/5/010.

An Investigation of The Effects of Dimple and Groove Texture on Frictional Property by In-situ Observation of Lubricant Film Thickness

Y. Yuhara[1*], K. Sato[1] and S. Sasaki[2]

[1]Department of Mechanical Engineering, Graduate School of Tokyo University of Science, Japan
[2]Department of Mechanical Engineering, Tokyo University of Science, Japan
*Corresponding author Email: 4521563@ed.tus.ac.jp

*Keywords: Tribology, Surface texturing, film thickness, in-situ observation*

Abstract

Understanding influence of surface texturing on frictional behavior is one of great importance for industrial applications. However, effects of surface texturing on friction are not fully understood. To elucidate this, we investigated the effects of dimple width (10 μm dimple, 20 μm dimple, 48 μm dimple and 110 μm dimple) and groove direction (parallel groove and vertical groove) on lubricant film thickness and friction coefficient using a laboratory-built tribometer with in-situ film thickness observation. As a results, 10 μm dimple showed lowest friction and highest film thickness in all texture surface. In addition, the effects of groove direction influence the friction coefficient but hardly do film thickness. We considered that the mechanism of the frictional property improvement by surface texturing was the increase of film thickness and decrease the edge contact between texture groove and disk surface.

Introduction

Surface texturing is one of the surface modification technologies controlling frictional properties at sliding surfaces. Understanding influence of surface texturing on frictional behavior is of great importance for industrial applications. However, effects and the mechanism of surface texturing on friction are not fully understood. In addition, the effects of surface texturing on tribological properties differ depending on the surface texture shape and lubrication condition, and the following effects have been known well: texture grooves supply lubricant oil to sliding surfaces and capture wear debris, and the load capacity is improved by generating hydrodynamic pressure in fluid lubrication regime. Many researchs have been conducted on surface texturing with various shapes such as dimple and parallel groove shape from boundary to fluid lubrication regime[1~4]. However, there are many conflicting findings on the effects of surface texturing on frictional properties and the mechanism is still unclear[5]. This is because there are few researchs that observed lubricant film thickness and friction coefficient simultaneously, which are important factor for considering the effects of surface texturing. Therefore it is necessary to develop an in-situ observation technique that can observe lubricant film thickness and friction coefficient accurately in order to clarify the effects of surface texturing on friction properties. In this study, we developed an in-situ observation apparatus that can measure lubricant film thickness and friction coefficient simultaneously with high accuracy and investigated the effects of dimple and groove shape of surface texture on frictional properties.

Experimental Details

Figure 1 shows the developed tribometer. This equipment consists of a ball-on-disk type sliding tester and a white light spectroscopic film thickness measurement system for in-situ observation of lubricant film thickness. The relative sliding speed can be changed in a wide range by controlling the rotation speed of the motor attached to the ball and the disk independently. Friction force and nominal load were measured using a load cell. A bearing steel ball (diameter $\varphi=19.05$ mm; American Iron and Steel Institute (AISI) steel grade: 52100) and an optical glass disk ($\varphi=100$ mm; BK7) coated with the Cr film and the SiO2 film were used as the test specimens. Lubricant film thickness at contact area is observed using a microscope unit (CFI¬60-2/ CFI¬60, Nikon, Japan) equipped with an imaging spectrometer (CLP-50TS, Techno Synergy, Japan) and a high-speed camera (EMRECAM GX-3, Nac Image Technology, Japan). Lubricant film thickness was measured in the line area along rotation axis of the ball.
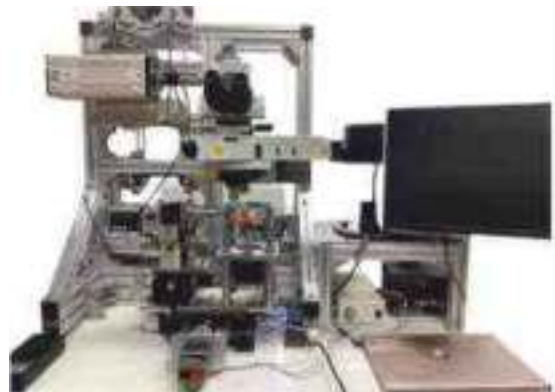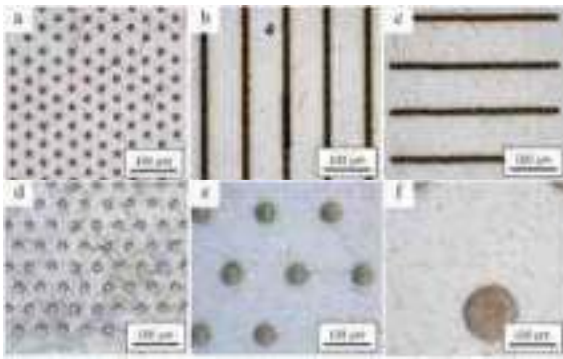

Figure 1: Ball-on-disk tribotester

Figure 2: Schematic diagrams of textured specimen : (a) 10 μm dimple; (b) parallel; (c) vertical; (d) 20 μm dimple; (e) 48 μm dimple; (d) 110 μm dimple.

Table 1: Friction test condition

	a	b	c	d	e	f
Pitch, μm	30	58.6	142	332	100	100
Depth, μm	1.0	1.0	1.0	1.0	1.0	1.0
Width, μm	10	20	48	110	10	10
Area ratio, %	10	10.6	10	9.9	10	10

The oil temperature was room temperature (25.5±0.5℃), the load was 20 N and the sliding speed was 0.01, 0.1, 1, 10, 100, and 1000 mm/s using SRR of 50 %. The lubricant oil used in this study was PAO 4 with a viscosity of 16.8 mm2/s at 40 ℃ and was supplied to the contact area by scraping with ball. Figure 2 and Table 1 show texture patterns and parameters, respectively. The surface texturing was applied to the ball surface.

Results

Figure 3 and Fig. 4 show the friction coefficient and central film thickness against the sliding speed when using the non-texture, 10μm dimple, parallel, and vertical textures, respectively. 10μm dimple, parallel, and vertical textures showed a lower friction coefficient and a larger central film thickness than the non-texture in boundary and mixed lubrication regime where the sliding speed is less than 100 mm/s. On the other hand, parallel and vertical textures showed the highest friction coefficient in fluid lubrication regime where the sliding speed of 1000 mm/s and 100 mm/s. From these results, it is considered that dimple shape is optimal shape for reducing friction coefficient in boundary and mixed lubrication regime. Therefore, we change the dimple diameter and conducted another experiment in order to investigate the effects of dimple texture on friction coefficient more. Figure 5 and Fig.6 show friction coefficient and central film thickness against the sliding speed when using dimple textures with different diameter. It was confirmed that friction coefficient reduced and central film thickness increased as the dimple diameter reduced from 110 μm to 20 μm in boundary, mixed and fluid lubrication regime. However, friction coefficient and central film thickness of 10 μm dimple and 20 μm dimple have few differences especially in boundary and mixed lubrication regime.

Discussion

In boundary and mixed lubrication regime, lubricant oil is not sufficiently supplied by scraping and the lubricant oil is retained on the sliding surfaces by the meniscus. Therefore, the lubricant oil in the textured grooves is pushed out into the sliding surfaces by the elastic deformation of the ball during contact and this caused increasing of lubricant film thickness and then friction reduction.

Focusing on the difference of texture shape, as shown in Fig. 3 and Fig. 4, 10 μm dimple texture was more effective in increasing the lubricant film thickness and reducing friction coefficient in boundary and mixed lubrication regime than the parallel and vertical textures. This is because the lubricant oil flows out of contact area through the grooves in the case of parallel and vertical textures.

As shown in Fig. 5 and Fig. 6, Lubricant film thickness increased and friction coefficient reduced as the diameter of dimple decreased from 110 μm to 20 μm from boundary to fluid lubrication regime. This is because many dimple grooves supplying lubricant oil to the contact surface exist in contact area as dimple diameter is small. In particular, the reason why the 110 μm dimple texture has a lowest lubricant film thickness and highest friction coefficient is outflow of lubricant oil through dimple grooves from contact area same as parallel and vertical textures.

In this way, it is considered that the number of dimple grooves in the contact area is important factor to increase lubricant film thickness and then reduce friction coefficient especially in boundary and mixed lubrication regime. Figure 7 shows the relation between friction coefficient in boundary lubrication regime at 0.01 mm/s and the number

of dimple grooves in the contact area in order to clarify the effects of the number of dimple grooves in the contact area on friction coefficient. The friction coefficient of non-texture has highest friction coefficient and that of dimples reduces as the number of dimple grooves in the contact area increase from 0 to 18.6 until 20 μm dimple. On the other hands, the friction coefficient reduction effects of 10 μm dimple and 20 μm dimple are almost same. From this result, it is considered that the effects of friction coefficient reduction are saturated when the number of dimple grooves is about 18.6 until 20 μm dimple.
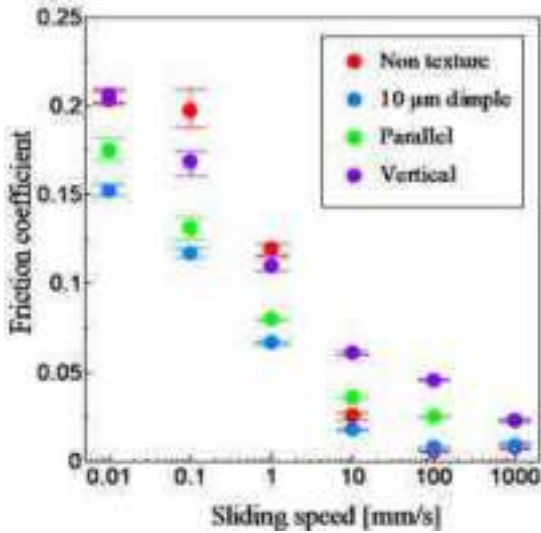

Figure 3: Comparison of friction coefficient
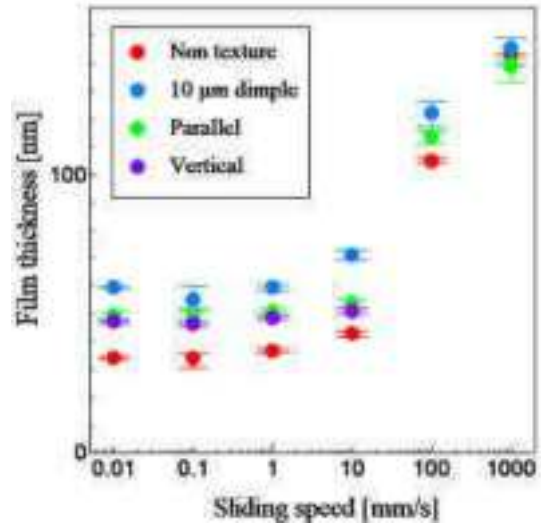as a function of sliding speed

Figure 4: Comparison of central film thickness
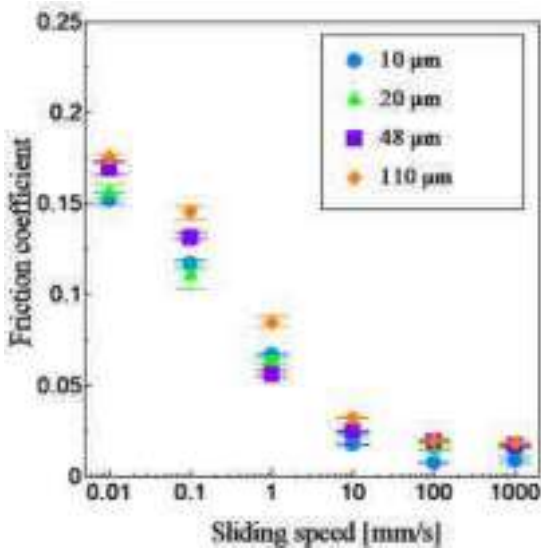as a function of sliding speed

Figure 5: Comparison of friction coefficient of
dimple texture with different diameter
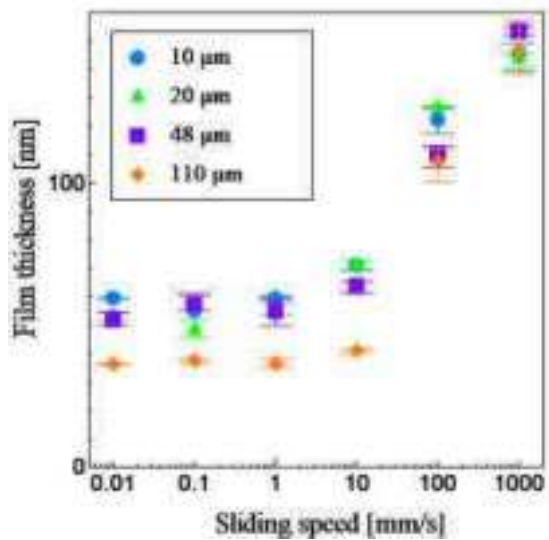as a function of sliding speed

Figure 6: Comparison of central film thickness of
dimple texture with different diameter
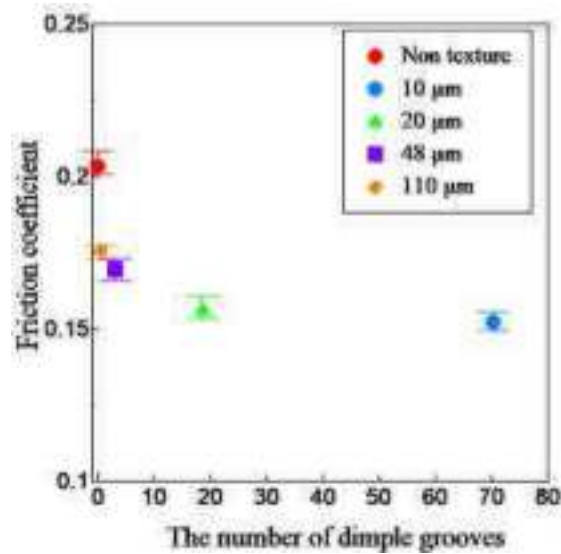as a function of sliding speed

Figure 7: The relation between friction coefficient at 0.01 mm/s and the number of dimple grooves in the contact area

Conclusions

This study aimed to clarify the effects and the mechanism of surface texturing on lubricant film thickness and friction change from boundary lubrication regime to fluid lubrication regime. The balls with different shapes of surface textures were used for in-situ observation of lubricant film thickness and friction measurement. The revealed findings are as follows:

◯ Dimple texture showed a largest lubricant film thickness and lowest friction coefficient compared to non-texture, parallel and vertical surface textures in boundary and mixed lubrication regime.
◯ Vertical surface texture showed highest friction coefficient while non-texture showed lowest friction coefficient in fluid lubrication regime.
◯ Lubricant film thickness increased and friction coefficient reduced as the diameter of dimple decreased.
◯ The effects of dimple texture in boundary lubrication regime are saturated when the number of dimple grooves is 18.6, dimple diameter is 20 μ m.

References

◯ Sorin-Cristian Vladescu, Andrew V. Olver, Ian G. Pegg b, Tom Reddyhoff. The effects of surface texture in reciprocating contacts – An experimental study. Tribology International, 2014, Vol. 82, pp. 28-42
◯ L Mourier1, D Mazuyer1, F-P Ninove1, and A A Lubrecht. Lubrication mechanisms with laser-surface-textured surfaces in elastohydrodynamic regime. SAGA journals, 2010, Vol. 224, pp. 697-711
◯ Chenbo Ma, Hua Zhu. An optimum design model for textured surface with elliptical-shape dimples under hydrodynamic lubrication. Tribology International, 2011, Vol. 44, pp. 987-995
◯ Ulrika Pettersson, Staffan Jacobson. Influence of surface texture on boundary lubricated sliding contacts. Tribology International, 2003, Vol.36, pp. 857-864
◯ C. Gachot, A. Rosenkranz, S.M. Hsu, H.L. Costa. A critical assessment of surface texturing for friction and wear improvement. Wear, 2017 Vol. 372-373, pp. 21-41

Nanoscale friction and wear behavior of CVD-grown aged monolayer Ws₂

Himanshu Rai[1*], Deepa Thakur[2], Ashutosh Pitkar[3], Zhijiang Ye[3], Viswanath Balakrishnan[2], Nitya Nand Gosvami[1]

[1]Department of Materials Science and Engineering, Indian Institute of Technology Delhi, Hauz Khas, New Delhi, India 110016

[2]School of Engineering, Indian Institute of Technology Mandi, Himachal Pradesh, India 175075

[3]Department of Mechanical and Manufacturing Engineering, Miami University, Oxford, OH 45056

Corresponding author*: himanshu.rai@mse.iitd.ac.in

Keywords: Solid lubricant, TMDs, 2D materials, Tribology, Atomic force microscopy

Abstract

Monolayer transition metal dichalcogenides (TMDs) reduce friction; however, wrinkles form on the surface of TMDs due to strain relaxation over time. These wrinkles degrade the tribological properties of the monolayer. In the present work, we discuss the impact of wrinkles on the friction and wear behavior of aged monolayer WS2 grown by chemical vapor deposition (CVD). Load-dependent investigations with atomic force microscopy (AFM) revealed that wear begins at the wrinkles and leads to the removal of the monolayer. Whereas for wrinkle-free regions, wear occurred at higher normal loads similar to the freshly grown WS2, but an increased coefficient of friction (COF) was observed.

Introduction

Friction and wear are a major concern as they result in significant energy loss and removal of materials, and eventually result in mechanical failures. Advanced sensing devices such as micro-electromechanical systems (MEMS) and nano-electromechanical systems (NEMS) has led to the development of various modern devices. For these devices, surface related issues including friction and wear are a crucial concern [1]. Tribological properties of these small-scale devices have an important role in achieving desired lifespan but unfortunately conventional liquid based lubricants can not be used for such small-scale applications [2]. Therefore, ultrathin solid lubricants are suitable for small-scale devices such as MEMS to achieve the desired tribological properties. Solid lubricants are more efficient under harsh conditions to a great extent [3]. Among various solid lubricants, two-dimensional (2D) materials such as graphene and transition metal dichalcogenides (TMDs) are used extensively in tribological applications. But, graphene has poor lubrication behavior under vacuum or dry conditions [4] which provides a strong motivation to explore TMDs including MoS2 and Ws2.

Superior tribological properties are also dependent on the defect-free synthesis of 2D materials; nevertheless, it has been recognized that it is difficult to synthesize a defect-free flat 2D material when the length in one dimension exceeds a threshold value, such as 10 nm for graphene [5]. Self-folding, which results in the production of wrinkles, is one of the flaws that destroys the flatness of two-dimensional materials [6]. In a recent work on graphene, the frictional behavior of wrinkled graphene grown by chemical vapor deposition (CVD) was investigated. On CVD-grown graphene, wrinkles are frequently observed, and their orientation can play a significant role in reducing friction [7].

Therefore, in the present work we have investigated the aged CVD-grown monolayer WS2, which was kept in ambient conditions for one year that lead to the formation of wrinkles over the surface. We demonstrate the onset of wear at the wrinkles, which results in further delamination of the layer from the substrate (SiO2/Si). In wrinkle-free areas, however, wear commenced at higher loads comparable to freshly formed monolayer WS2.

2. Experimental methodology

Atmospheric pressure chemical vapor deposition was used to grow the monolayer WS2 on SiO2/Si substrate (300 nm SiO2 on Si). WO3 nanorods and sulfur powder (99.5% Alfa Aesar) were utilized as precursors and placed in a tube furnace. Further, the synthesis of monolayer WS2 was accomplished at 850 °C (heating rate 8.5 °C/min) for 10 min. To observe the wrinkles on the surface, the samples were kept in a sealed dessicator for around one year. To investigate the tribological properties of aged monolayer WS2, an atomic force microscopy (AFM, Flex Axiom and Drive AFM, Nanosurf, Switzerland) was used. Experiments were performed using a sharp AFM probe (Multi75DLC, Budget-sensors, Bulgaria).

3. Results and discussion

3.1 AFM imaging of the wrinkles

Wrinkles on the CVD-grown aged monolayer WS2 flakes were identified by AFM as shown in Figure 1. Most of the wrinkles do not have any specific orientation and height that can be observed through color contrast in Figure 1a (wrinkles are brighter in contrast). Wrinkles exhibit higher friction (bright contrast in Figure 1b) than the adjacent wrinkle-free region. High magnification topography and friction map of single wrinkle can also be observed in Figure 1c & 1d, respectively.

3.2 Friction and wear behavior of the wrinkled region

To investigate the effect of wrinkles on the nanoscale wear behavior of aged CVD-grown WS2, load-dependent experiments were performed, as shown in Figure 2. Wear of the aged monolayer WS2 was initiated in the wrinkled region at a much lower load, but the tip encountered the underlying substrate (SiO2/Si) at above 300 nN when the normal load was sufficiently high (Figure 2a). Figure 2b shows the zoomed-out friction force mapping of the experimental region (marked as white color dashed square). Figure 2 also depicts the load-dependent topographical changes during the AFM experiment, starting from the upper left and proceeding clockwise around the border. Wear can be seen initiating at wrinkles and advancing as the normal load increases.
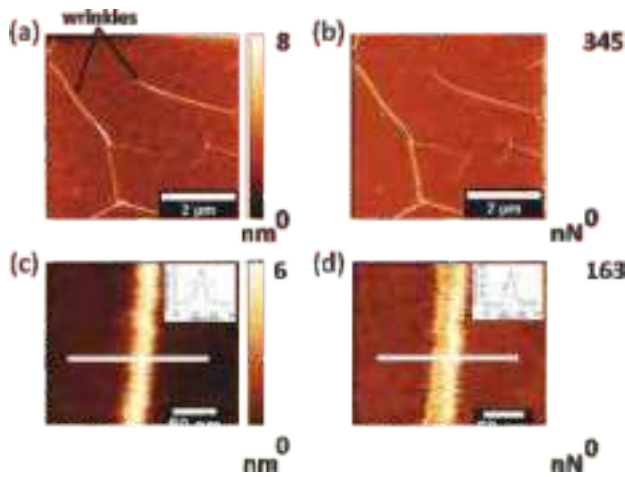

Figure 1. (a) Low magnification AFM topographic and (b) friction force map of the aged monolayer WS2 showing wrinkles. (c) Higher magnification AFM topographic image of a wrinkle showing height profile in the inset, (d) corresponding friction force map of the wrinkle showing higher friction on the wrinkle (line profile is shown in inset).
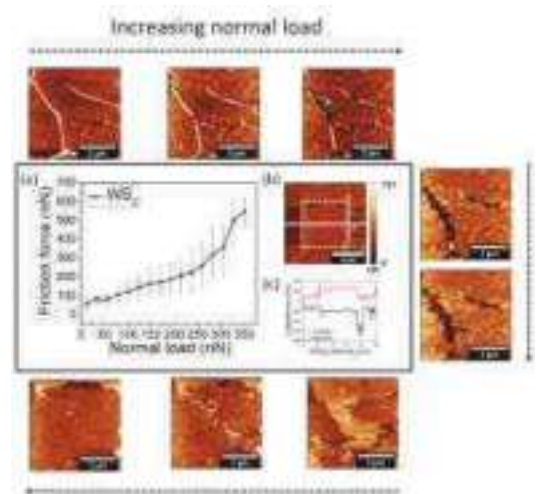

Figure 2. (a) Friction force vs normal load. (b) Zoomed-out friction force map of the experimental region (shown in white color dashed square). (c) The line profile of the friction force map (white color solid line drawn in the middle) shows an abrupt increase in the friction force in the experimental region.

3.3 Friction and wear behavior of the wrinkle-free region

Apart from wrinkles, experiments were also performed in the wrinkle-free region in the aged sample. In Figure 3a, an abrupt increase in the friction force can be observed above ~ 950 nN, that is due to the wear of the monolayer WS2 at a higher normal load when the tip encountered the underlying substrate. An increase in COF was also observed in the wrinkle-free aged monolayer WS2 sample as compared to the fresh sample. This increase in the COF can be due to the adsorbed hydrocarbons on the surface of the aged monolayer which was confirmed using XPS and MD simulations.
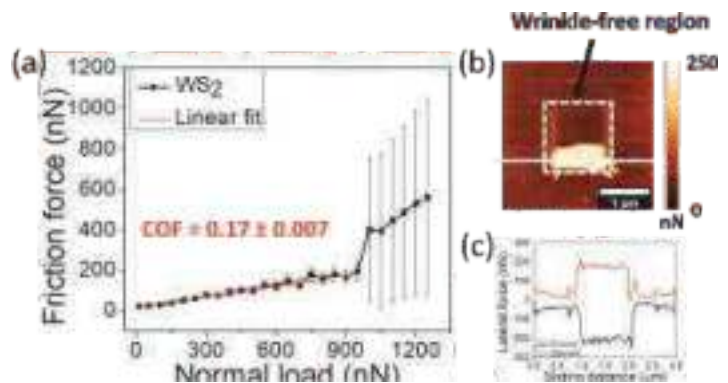

Figure 3. (a) Friction force vs normal load. (b) Zoomed-out friction force map of the experimental region (shown in white color dashed square). (c) The line profile of the friction force map (white color solid line drawn in Figure (b) shows an abrupt increase in the friction force in the removed part of experimental region.

Conclusions

In conclusion, friction and wear behavior of CVD-grown aged monolayer WS2 was investigated, and the significance of wrinkles was investigated using AFM. Systematic experiments were conducted on wrinkled and wrinkle-free regions. In load-dependent AFM tests, the effect of wrinkles on the friction and wear behavior of aged monolayer WS2 was observed. It was discovered that the wrinkles increase friction significantly and wear began around the wrinkleed regions at a significantly lower normal load than the freshly produced monolayer WS2. However, experiments conducted in a region free of wrinkles demonstrate that wear occurs at a higher load, similar to the freshly grown WS2 monolayer. We also observed a higher COF in aged monolayer WS2 due to oxidation and the presence of hydrocarbon groups adsorbed to the surface. In a nutshell, the importance of wrinkles on friction and wear behavior of aged monolayer WS2 and their significance in achieving the desired tribological properties are demonstrated by our findings. This work will undoubtedly assist situations where WS2 is employed as a long-lasting solid lubricant.

References

○ D. Boer, T.M. Mayer, Tribology of MEMS, MRS Bull. 26 (2001) 302–304. http://journals.cambridge.org/action/displayAbstract?fromPage=online&aid=7964492.

○ A. Erdemir, C. Donnet, Tribology of diamond-like carbon films: Recent progress and future prospects, J. Phys. D. Appl. Phys. 39 (2006) R311. https://doi.org/10.1088/0022-3727/39/18/R01.

○ P. Sutor, Solid Lubricants: Overview and Recent Developments, MRS Bull. 16 (1991) 24–30. https://doi.org/10.1557/S0883769400056864.

○ B.K. Yen, Influence of water vapor and oxygen on the tribology of carbon materials with sp2 valence configuration, Wear. 192 (1996) 208–215. https://doi.org/10.1016/0043-1648(95)06807-4.

○ X. Meng, M. Li, Z. Kang, X. Zhang, J. Xiao, Mechanics of self-folding of single-layer graphene, J. Phys. D. Appl. Phys. 46 (2013) 055308. https://doi.org/10.1088/0022-3727/46/5/055308.

○ W. Chen, X. Gui, L. Yang, H. Zhu, Z. Tang, Wrinkling of two-dimensional materials: Methods, properties and applications, Nanoscale Horizons. 4 (2019) 291–320. https://doi.org/10.1039/c8nh00112j.

○ F. Long, P. Yasaei, W. Yao, A. Salehi-Khojin, R. Shahbazian-Yassar, Anisotropic Friction of Wrinkled Graphene Grown by Chemical Vapor Deposition, ACS Appl. Mater. Interfaces. 9 (2017) 20922–20927. https://doi.org/10.1021/acsami.7b00711.

Enhanced output performance of PAN/CNT nanofibrous triboelectric nanogenerator

Shailendra Kumar[1*], Ashish Kakoria[2'3], Rajesh Kumar Jha[1], Chhotrai Soren[1], Sumit Sinha-Ray[3] and Ankur Goswami[1]

[1]Department of Materials Science and Engineering, Indian Institute of Technology Delhi,
Hauz Khas New Delhi-110016, India
[2]School of Engineering, Indian Institute of Technology Mandi, Kamand, Mandi Himachal Pradesh-175075 India
[3]Department of Textile and Fiber Engineering, Indian Institute of Technology Delhi, Hauz Khas New Delhi-110016, India
*Corresponding author E-mail: msz198714@mse.iitd.ac.in, agoswami@mse.iitd.ac.in

Abstract

The increasing demand of green and sustainable energy has piqued the interest of researchers in the field of triboelectricity in the last decade. A triboelectric nanogenerator (TENG) allows one to harvest electrical energy because of the contact separation of two dissimilar material surfaces due to mechanical vibration. This form of energy offers an excellent opportunity to run the power portable, flexible and wearable devices. Although known for the last 3000 centuries, this energy source was merely useful to mankind because of the low output current despite its potential to generate a high output voltage. Power density of TENG devices mainly depend on the contact area, contact force, type of interfaces, and microstructure of materials. Significant efforts have been made in recent years to improve energy generation by employing various combinations of materials to exploit the effect of interfaces. In this proposed work, we investigate the triboelectrification between composites of electrospun polyacrylonitrile (PAN) membrane with different weight fractions of multi-walled carbon nanotube (MWCNT) and a metal surface (copper) using an in-house built triboelectric setup. The short circuit current density (Jsc) and peak-to-peak open circuit voltage (VP-P) were found to be 15.3 nA/cm2 and 25.3 volts with 0.00005 wt.% MWCNT in 10 wt.% PAN mixture. The efficiency of the device and structural figure of merit of the devices is 7.07 % and 0.13. The obtained results are encouraging to use these materials as self-power wearable sensors.

Introduction

With the advancement of technology and as well as rise in the world's population global energy demand also increases [1, 2]. Alternatives to renewable energy sources for energy demand are a major environmental and global issue. As our resources are very miniscule for sustainable civilization. The sole way to complete the demand is fossil fuel derived resources. But this also comes with negative consequences as environmental pollution, climate change, etc.[3]. Here is an alternative to this is Renewable and clean energy. Since the inception of triboelectricity reported by Wang et al, Significant progress has been made in past few decades,[4, 5]. TENG fundamentally works on the principle of triboelectrification coupling effect principle and electrostatic induction and mechanical motion conversion on a small scale are converted into electrical power [6]. TENGs are possibly manufactured from a wide range of materials, as well as waste materials. Various TENG materials are being explored to improve the output performance of TENG devices, In addition to that existing materials also been investigated by changing in its microstructure. [7]. Various materials are discovered with triboelectric effect such as nanotubes, nanofibers, nanowires, and nanoparticles to improve electrostatic induction, permittivity, and surface roughness, as well as electron gaining-losing tendencies, because of high surface-to-volume ratios and higher volumetric porosity for ample charge distribution and transfer [8]. Smart and portable electronic devices are getting more compact day by day and to run these devices using traditional batteries may cause several environmental issues [9]. Here, TENGs appear at this moment as devices that can produce electricity and covers a gap in meeting resources derived from renewable energy. TENGs are most prominent devices these days as electrical converters for fulfilling the power requirement for most of the electronic and wearable devices by using biomechanical energy generated from human body [10]. To scavenge waste mechanical energy, this study designed, and fabricated nanofiber based TENGs with PAN/MWCNT additive composites for high triboelectric performance. The triboelectric effect or tribo-negativity feature can be improved by adding MWCNT into the PAN polymer.

Experimental Details

The polymer polyacrylonitrile (PAN) (mol wt. = 150 kDa) and Multiwall carbon nanotube (MWCNT) were purchased from Sigma-Aldrich. The prerequisite solvent for preparing the polymer and MWCNT solutions using N, N-dimethylformamide (DMF), was obtained from Alfa-Aesar. Both solutions were prepared by blending them in DMF in the ratio 1:0.00005 (Polymer: MWCNT) mentioned below to obtain the final concentration of 10 wt.%. The mixture

was kept at 80 °C on a magnetic stirrer for 8 h. Electrospinning of the above-mentioned solution was carried out at ambient conditions with a new Era syringe pump and a feed rate of 0.7 ml/h and 20-gauge needle in a 10 ml syringe with applied voltage of 12 kV. All the nanofibers were collected on a steel rotating drum at 200 rpm. Figure 1 and 2 shows the actual setup schematic used for the experiment and obtained physical picture of the obtained mat respectively.
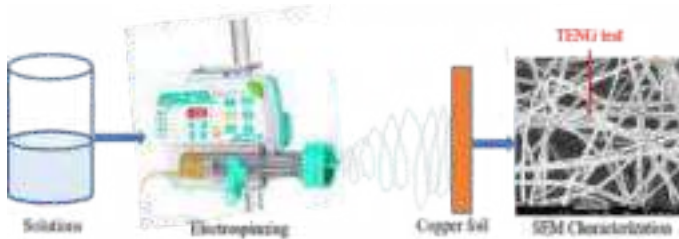

Figure 1: Fabrication and structure of the PAN-based TENG device by electrospinning process.

Figure 2: Image of the polymer/MWCNT composite nanofiber material.

The TENG is designed with dimensions 25*25 mm2 and a thickness of $1\mu m$. Conductive copper was taken as the outer layers of the TENG. As copper has higher conductivity (100 % IACS). PAN nanofiber layer and PAN/MWCNT layers were placed on the copper substrate with the help of highly conductive silver paste with minimum resistivity of (0.001 Ω cm). When samples were prepared paste on the substrate holder (moving plate and stationary plate). On the primary plate, nanofiber was pasted, and a copper sheet was placed on the stationary plate. Two electrical connection was connected with the sample and measured the electrical potential. This PAN/CNT-based nanofiber device works on the contact electrification method. The electrical parameters of the PAN/CNT nanofiber triboelectric nanogenerator peak-to-peak open circuit voltage (VP-P) and short circuit current (ISC) were measured by using a mixed domain oscilloscope (MDO 3024) and a programmable Keithley source meter (2636 B) in real-time. As we know, in the triboelectric nanogenerator the output current is very low in the range of nA-μA, therefore we measure the output current in a self-written python program. The whole electrical measurement was carried out in an air atmosphere and at room temperature.

SEM micrographs were acquired by using field emission scanning electron microscopy. X-ray diffraction patterns of PAN and PAN/MWCNT samples were obtained from X-ray diffractometer (Rigaku Corporation) within 3° to 95°.

Result and Discussion

Figure 3(a) and (b) are the SEM micrographs of PAN-MWCNT nanofibers at a 1 ■m scale with a mean fiber diameter of 1.1 ■m with a standard deviation of 0.31 ■m. Figure 3(c) is the XRD pattern of the pristine PAN and PAN-MWCNT composite nanofibers. Where peaks at 17.2o confirm the presence of PAN polymers and 26.1o confirms the presence of MWCNT in the composite membrane [11, 12].
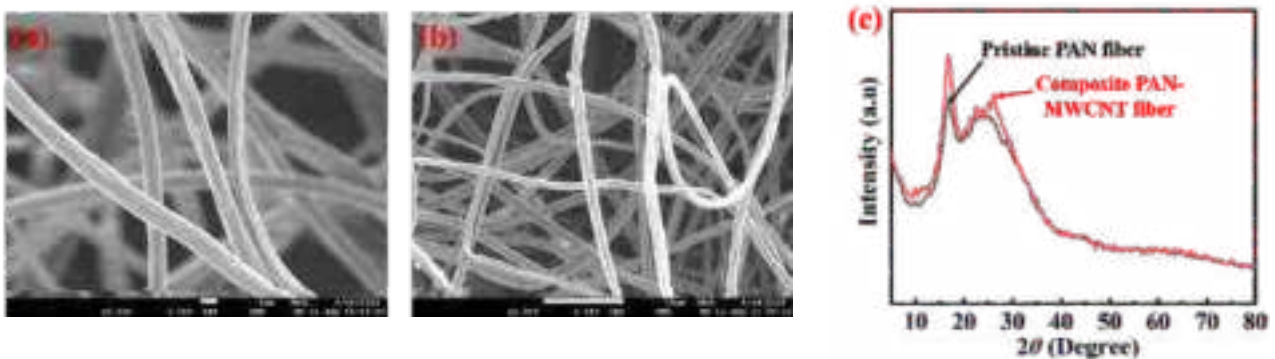

Figure 3: (a) & (b) FESEM image of Polyacrylonitrile (PAN-MWCNT) fiber.
(c) X-Ray diffraction pattern of PAN- (black color) and PAN-MWCNT- (red color).

Electrical parameters such as peak-to-peak voltage and short circuit current were obtained at a constant force of 2.0 N for both Pristine PAN and PAN-MWCNT composite nanofibers. A VP-P of 12.3 V and ISC of 15.6 nA was obtained in the case of pristine PAN nanofibers respectively. Whereas in the case of PAN-MWCNT composite nanofibers both (VP-P) and (ISC) were increased by 25.3 V and 96.1 nA respectively as shown in Figure 4(a-d). Short circuit current density (Jsc) of pristine PAN and PAN-MWCNT composite nanofibers were obtained at 2.14 nA/cm2 and 15.3 nA/cm2 respectively. As, PAN has two typical conformations: planar zigzag and 31-helical. The output voltage and current introduces in pristine PAN nanofibers is due to its all-transform (TTTT) structure and having dipole moment (3.5 Debye) larger than that of β-phase PVDF (2.1 Debye). [13]. Whereas in case of PAN-MWCNT value of (VP-P) and (ISC) as mentioned above has increased. After addition of MWCNT and PAN nanofibers the overall dielectric constant of the composite membrane has increased also the charge transfer regulated because of the high surface-to-volume ratio of MWCNT [14].
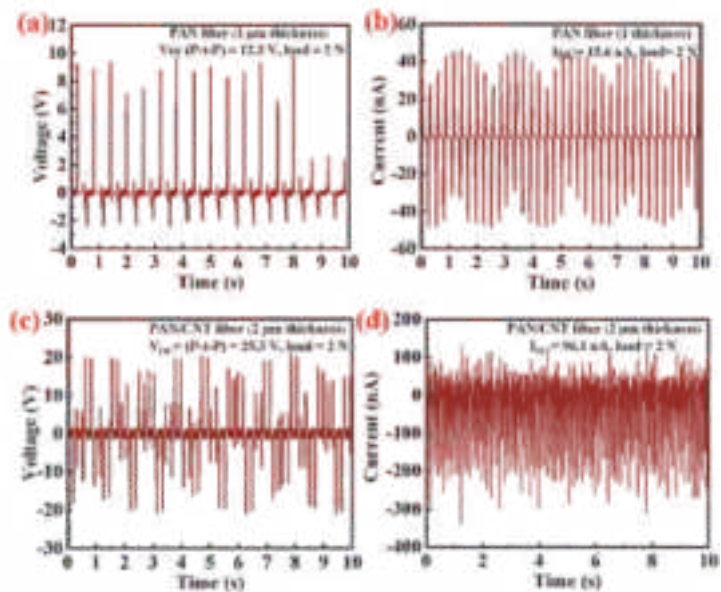

Figure 4: I-V and C-T characterization of Polyacrylonitrile (PAN) and composite PAN and multiwall carbon nanotube (MWCNT).

Conclusions

In this study, fabrication of pristine PAN and PAN-MWCNT nanofibers was demonstrated for triboelectricity generation. Where PAN-MWCNT nanofibers demonstrated higher peak-to-peak voltage (25.3 V), short circuit current density (15.3 nA/cm2) than pristine PAN nanofibers for constant applied force of 2.0 N. The efficiency of the device and structural figure of merit of the devices is 7.07 % and 0.13. In addition, the fabricated PAN-MWCNT composite nanofibers can be a potential material for generating piezoelectricity and pyroelectricity.

Acknowledgement

References

❍ Y. Zi, P. Basset, and J. J. E. Chen, "Triboelectric nanogenerator—Progress and perspectives," vol. 3, no. 5, 2021.
❍ Z. L. J. A. n. Wang, "Triboelectric nanogenerators as new energy technology for self-powered systems and as active mechanical and chemical sensors," vol. 7, no. 11, pp. 9533-9557, 2013.
❍ J. Chen, "Triboelectric nanogenerators," Georgia Institute of Technology, 2016.
❍ Z. L. Wang, "On the first principle theory of nanogenerators from Maxwell's equations," Nano Energy, vol. 68, p. 104272, 2020/02/01/ 2020.
❍ S. Niu and Z. L. J. N. E. Wang, "Theoretical systems of triboelectric nanogenerators," vol. 14, pp. 161-192, 2015.
❍ L. Zhou et al., "Rationally designed dual-mode triboelectric nanogenerator for harvesting mechanical energy by both electrostatic induction and dielectric breakdown effects," vol. 10, no. 24, p. 2000965, 2020.
❍ Z. Zhao et al., "Selection rules of triboelectric materials for direct-current triboelectric nanogenerator," Nature Communications, vol. 12, no. 1, p. 4686, 2021/08/03 2021.
❍ N. Hassan, "Energy-neutral event monitoring for internet of nano things," UNSW Sydney, 2018.
❍ A. Sekretaryova, "Powering wearable bioelectronic devices," in Wearable Bioelectronics: Elsevier, 2020, pp. 89-132.
❍ J. Song et al., "Highly flexible, large-area, and facile textile-based hybrid nanogenerator with cascaded piezoelectric and triboelectric units for mechanical energy harvesting," vol. 3, no. 6, p. 1800016, 2018.
❍ A. Mirmohseni, M. S. S. Dorraji, and M. G. Hosseini, "Influence of metal oxide nanoparticles on pseudocapacitive behavior of wet-spun polyaniline-multiwall carbon nanotube fibers," Electrochimica Acta, vol. 70, pp. 182-192, 2012/05/30/ 2012.
❍ P. S. Saud et al., "Photocatalytic degradation and antibacterial investigation of nano synthesized Ag 3 VO 4 particles@ PAN nanofibers," vol. 18, pp. 30-36, 2016.
❍ L. Yuan et al., "Piezoelectric PAN/BaTiO3 nanofiber membranes sensor for structural health monitoring of real-time damage detection in composite," Composites Communications, vol. 25, p. 100680, 2021/06/01/ 2021.
❍   Z. Kınas et al., "High-performance triboelectric nanogenerator based on carbon nanomaterials functionalized polyacrylonitrile nanofibers," Energy, vol. 239, p. 122369, 2022/01/15/ 2022.
❍

A Study On Hydrodynamic Analysis of Spiral Grooved Thrust Bearing for Locomotive Turbocharger

Hara Prakash Mishra* and Suraj Kumar Behera

National Institute of Technology, Rourkela, Odisha, India, 769008
*Corresponding author Email: haraprakashmishra@gmail.com

Abstract

As a significant component of the turbocharger to support the axial loads of the rotor, generated because of the pressure difference between the turbine and compressor wheel, thrust bearing should be studied and designed accurately. This article presents the design methodology and bearing parameter analysis of an oil-lubricated spiral grooved thrust bearing (SGTB) for a high-speed locomotive turbocharger. By applying Newton's second law, the thrust load acting on the turbocharger rotor is calculated analytically and is found to be 4.54 kN for a design speed of 1,00,000 rpm. To carry the designed load, a numerical hydrodynamic model for SGTB is developed using non-linear Reynold's equation and is solved using the finite volume method and successive over relaxation methodology to determine the static characteristics over the bearing surface. The static characteristics analysis of bearing includes predicting the pressure profile, load-carrying capacity, frictional torque, and power loss. Further, the influence of groove parameters such as spiral angle, groove angle, and film thickness ratio on the static characteristics of the bearing has been investigated. An artificial neural network (ANN) model is developed and trained using numerical analysis input-output data set. The performance of the ANN model is evaluated through the computation of regression coefficient ($R2$). The $R2$ value significantly close to 1 indicates the better performance of the model and accurate result prediction with a low error percentage.

Introduction

Dr. Buechi invented turbocharger (TC) to enhance the efficiency of a naturally aspirated internal combustion engine. Its performance is majorly dominated by bearing stability and rotor dynamics. The radial and axial loads of the rotor are supported by the journal and thrust bearings respectively. The thrust bearing has numerous industrial applications, and different experimental and theoretical studies have been carried out for its performance improvement. In recent years, the grooves and textures over bearing surface have attracted the attention of researchers. Among these, the spiral groove on the thrust bearing surface has shown excellent performance. Spiral grooves provide convergent wedge to generate the fluid pressure, resulting in a variety of advantages, such as low friction, large loading capacity, and good stability [1]. The textured spiral grooves on the surface act as a pump and are very effective at increasing pressure in the bearing clearance. Therefore, the spiral groove thrust bearing (SGTB) is widely used in high-speed and ultra-precision rotating machinery. But the application of the SGTB is still limited to oil lubrication and its application in the locomotive turbocharger rotor.

In the early 1950s, Whipple [2] introduced the idea of spiral groove bearing. Since then, several research is done to analyze flow behavior and pressure profile over the spiral grooved bearing. One of the early contributions by Muijderman [3] and Smalley [4] is narrow groove theory to predict pressure profile over the spiral grooved bearing. Later on, the study of complicated geometries like SGTB has been carried out by various numerical approaches, which include: numerical treatments based on the Reynold's equation and finite difference method [5], finite element method [6], and boundary element method [7]. Many researchers are exploring the influence of the texture parameters, such as texture depth, texture area ratio, texture shape, and so on, on the hydrodynamic characteristics of thrust bearing [8].

The present work targets the design of an SGTB to support the axial load generated in the locomotive turbocharger rotor. The thrust load for the turbocharger rotor is calculated analytically and SGTB hydrodynamic behaviour is studied using Reynold's equation. Then ANN and ANFIS models are generated to optimize and decide the best suitable groove parameters to carry the designed LCC obtained from the analytical calculation.

Thrust Load Calculation

The thrust bearing design for the locomotive turbocharger involves the calculation of thrust load (TL), which is induced by pressure difference acting upon the compressor (CW) and turbine wheels (TW). To calculate the TL on the rotor, Newton's second law is employed to the control volume. The TL, Ftotal acting on the rotor is the net forces acting on the CW and TW as indicated in Fig.1 [9]. On the CW, F1,C is the force due to pressure on the inlet face; F2,C is the force on shroud; F3,C is the impulsive force on CW and F4,C is the force at the back face. Similarly on turbine side, the forces acting are represented as F1T, F2,T, F3,T, and F4,T.

Thrust Load on compressor

For the given geometrical parameters of a compressor, the thrust load acting on the compressor is calculated. Different forces acting on compressor faces are calculated as,

$$F_{1,C} = A_1 P_1 = \frac{\pi D_1^2}{4} P_1 = 394.974\,N$$

$$F_{2,C} = A_{s,C} P_{s,c} = A_{s,c}\left(\frac{P_1 + P_2}{2}\right) = 712.658\,N$$

$$F_{3,C} = \dot{m}_c C_{u,1} = \frac{\dot{m}_c^2 R_a T_1}{P_1 A_1} = 25.717\,N$$

$$F_{4,C} = A_{bf,c} P_2 = 1982.642\,N$$

The net force on the CW,
$$F_{CW} = F_{1,C} + F_{2,C} + F_{3,C} - F_{4,C} = -849.293N$$

Fig. 1 Axial forces on turbocharger rotor

Thrust Load on turbine

Similarly, for a given turbine geometrical parameters, the forces acting on the turbine wheel are calculated as,

$$F_{1,T} = A_1 P_1 = \frac{\pi D_1^2}{4} P_1 = 2447.15N$$

$$F_{2,T} = A_{s,T} P_{s,T} = A_{s,T}\left(\frac{P_1 + P_3}{2}\right) = 1039.512N$$

$$F_{3,T} = \dot{m}_T C_{u,1} = \dot{m}_T \left(\frac{\dot{m}_T}{P_{u,1} A_1}\right) = \frac{\dot{m}_T^2 R_a T_2}{P_3 A_1} = 60.405N$$

$$F_{4,T} = A_{bf,T} P_3 = 1370.308\,N$$

The resulting force acting on the TW,
$$F_{TW} = -F_{1,T} - F_{2,T} - F_{3,T} + F_{4,T} = -2176.759N$$

Thus, resulting force on the rotor,
$$F_{T,ax} = F_{CW} + F_{TW} = -3026.052\,N$$

This value of the thrust load is obtained at the speed of 1,00,000 rpm, which is the designed speed of the locomotive turbocharger. Here negative sign indicates the resultant force will be from turbine to compressor. With the factor of safety (FOS) of 1.6, the designed axial load carrying capacity of thrust bearing is,

$$F_{T,Design} = F_{T,ax} \times FOS \approx -5555N$$

Theoretical Model

The hydrodynamic bearing analysis is carried out by solving the Reynolds equation, steering experiments, or carrying out CFD analysis. The most effective and faster approach among these methods is solving the Reynolds equation numerically.

Spiral Grooved Thrust Bearing

The shape of spiral grooves is a logarithmic spiral, expressed as $r = r_{in}e^{\theta\tan\alpha}$. Where α is spiral angle and (r,θ) is polar coordinates. There are Ng no of grooves, having hg groove depth. The land and groove film thickness are hL and (hL+hg) respectively. The schematic of SGTB is shown in Fig. 2. To improve the accuracy of solution, the bearing geometry has been transformed based on a boundary-fitted coordinate system, and the polar coordinate system (r,θ) is converted in to spiral coordinate system (ξ,η). As a result, the grid lines are aligned with groove boundaries [10]. For this process, the coordinate transformation employed is as follows:

$$\theta = \eta + \frac{\ln\left(\frac{r}{r_{in}}\right)}{\tan\alpha}, \quad r = \xi$$

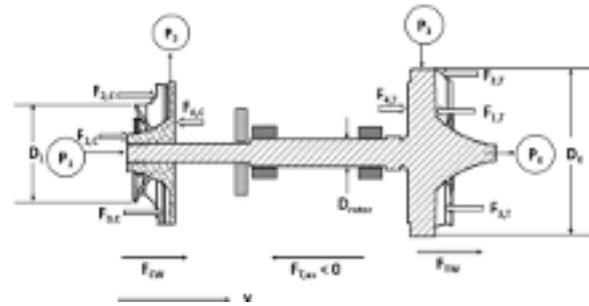After coordinate transformation, the modified Reynold's equation is expressed as,

$$\frac{\partial}{\partial \xi}\left(\frac{\xi h^{3}}{\mu}\left(\frac{\partial P}{\partial \xi}-\frac{1}{\xi}\frac{1}{\tan \alpha}\frac{\partial P}{\partial \eta}\right)\right)+\frac{\partial}{\partial \eta}\left(\frac{h^{3}}{\mu}\left(-\frac{1}{\tan \alpha}\frac{\partial P}{\partial \xi}+\frac{1}{\xi}\frac{1}{\sin^{2}\alpha}\frac{\partial P}{\partial \eta}\right)-6\omega\xi h\right)=0$$
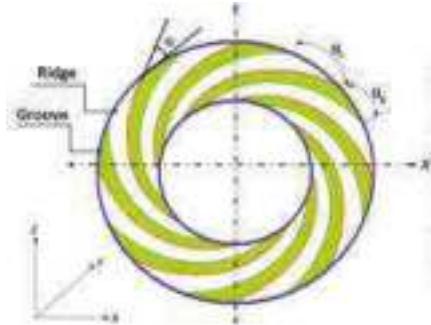

Fig. 2 Schematic of spiral groove thrust bearing

The partial derivative of film thickness at the groove-ridge boundary is discontinuous. Consequently, the partial derivative terms in the modified Reynold's equation could not be solved to calculate the pressure at the groove-ridge boundary. To overcome this, the pressure at these boundaries is calculated by FVM, which is based on conservation of mass. The obtained discrete nodal pressure equation is expressed as,

$$P_{i,j}=\frac{-BP_{i,j+1}-CP_{i,j-1}-DP_{j+1,\xi}-EP_{i-1,j}+F+G}{A}$$

To calculate hydrodynamic pressure, the equation (13) is solved using successive over-relaxation (SOR) algorithm and is expressed as:

$$P^{k}{}_{i,j}=SOR\times P^{k}{}_{i,j}+\left(1-SOR\right)P^{k-1}{}_{i,j}$$

The convergence criteria for the solution of pressure is maintained in order 10^{-6}.

Results & Discussion
The pressure profile over bearing surface was obtained from the numerical solution of Reynold's equation. The periodic profile over bearing surface has been formed along the circumferential direction, and peak pressure of 8MPa has been obtained in the groove region. After the pressure profile plot, Load carrying capacity, Frictional Torque (FT), and Power Loss (PL) for the bearing were evaluated by integrating fluid pressure over the surface and are found to be 4659.67N, 0.0361 N.m, and 0.3446kW, respectively.

Ann And Anfis Methodology
In the current paper, the artificial intelligence(AI) technique, i.e., ANN and ANFIS methodology are used to predict the optimum value of groove variables, which are more influential towards LCC, FT, and PL. The groove parameters considered for ANN and ANFIS analysis are shown in Table 1. The 2-layer feed-forward backpropagation type of multi-layer perceptron(MLP) network is selected for the current analysis. MLP network consists of the input, hidden, and output layers.
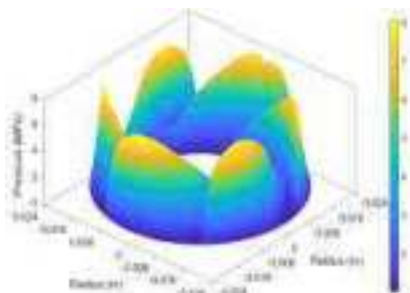

Fig. 3 Spiral grooved thrust bearing pressure profile

Table 1: ANN and ANFIS input Parameters

Parameter	Levels		
	-1	0	+1
Groove angle	12^{0}	15^{0}	18^{0}
Film thickness ratio	0.3	0.5	0.7
Number of grooves	4	6	8

85

From the input and output dataset, the training for the network has been carried out through the feed-forward backpropagation network type, "Levenberg-Marquardt backpropagation algorithm," and TANSIG transfer function. After multiple training of network, the regression curve for LCC obtained from the ANN analysis is shown in Fig. 4. The regression coefficient value close to one signifies the best fit of data.

The development of the ANFIS model involves the selection of appropriate MF from available MFs. For the present study, 'gaussmf' has been considered for input parameters due to the association of lesser training error. After training and testing the ANFIS network, the surface plot obtained for LCC is shown in Fig. 5. The criteria for the prediction of optimum range of groove parameters are LCC should be maximum. For this study, the LCC (thrust load) has been calculated analytically. Thus the optimum bearing parameters need to be determined for this designed LCC. The optimum value of FTR, Ng, and GA for the SGTB design are 0.45, 6, and 16, respectively.

Fig. 4 Regression curve for LCC

Conclusions

The spiral grooved thrust bearing for the locomotive turbocharger has been designed at the rotor speed of 1,00,000 rpm. The investigation begins with the analytical calculation of thrust load for a locomotive turbocharger by applying Newton's second law. The calculated designed thrust load is found to be 4.54 kN, which is to be taken care of by the thrust bearing. Subsequently, a numerical model is developed and solved using FVM and SOR algorithm to predict its hydrodynamic characteristics (pressure profile, LCC, FT, and PL). Then groove parameters influence has been studied using the AI technique (ANN and ANFIS) to determine the optimum range of groove parameters for the designed LCC. The optimum values of FTR, Ng, and GA for the SGTB design are 0.45, 6, and 16, respectively. The present study shows the influence of AI techniques (ANN and ANFIS) in the optimum spiral grooved thrust bearing design for achieving the desired performance.
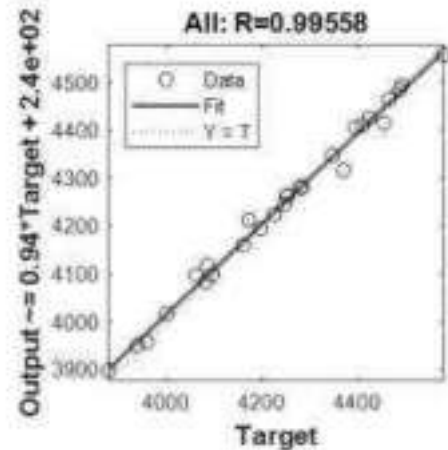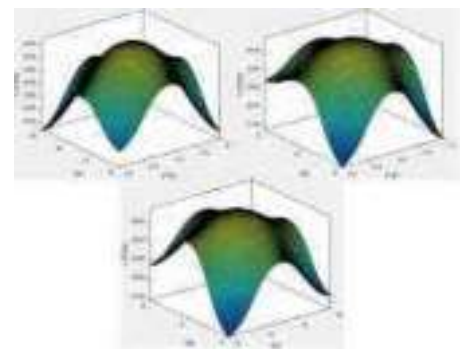

Fig. 5 ANFIS Decision surface for LCC

References

○ Zhang, C., Z. Yi, and Z. Zhang, THD analysis of high speed heavily loaded journal bearings including thermal deformation, mass conserving cavitation, and turbulent effects. J. Trib., 2000. 122(3): p. 597-602.

○ Whipple, R.T., The inclined groove bearing. 1958, United Kingdom Atomic Energy Authority. Research Group. Atomic Energy.

○ Muijderman, E.A., Spiral groove bearings. Industrial Lubrication and Tribology, 1965.

○ Smalley, A. J. (1972), "The Narrow Groove Theory of Spiral Grooved Gas Bearings: Development and Application of a Generalized Formulation for Numerical Solution", Journal of Lubrication Technology, 94, pp 86–92.

○ Lehn A, Schweizer B. Generalized Reynolds equation for fluid film problems with arbitrary boundary conditions: application to double-sided spiral groove thrust bearings. Archive Appl Mech 2016;86(4):743–60.

○ Bonneau D, Huitric J, Tournerie B. Finite-element analysis of groove gas thrustbearings and groove gas face seals. J Tribology-Transactions ASME 1993;115(3): 348–54.

○ Zhu Q, Zhang WJ. A numerical procedure based on the boundary element method analysis of the archimedean spiral grooved thrust oil bearing. J Tribology- Transactions ASME 2000;122(3):565–72.

○ Xu, W. and J. Yang, Spiral-grooved gas face seal for steam turbine shroud tip leakage reduction: performance and feasibility analysis. Tribology International, 2016. 98: p. 242-252.

○ Nguyen-Schäfer, H., Rotordynamics of automotive turbochargers. 2015: Springer.

○ Hu, Y. and Y. Meng, Theoretical and experimental study of transient behavior of spiral-groove thrust bearings during start-up. Tribology Transactions, 2020. 63(1): p. 154-172.

Computational Indentation in Highly Cross-linked Polymer Network

Manjesh Kumar Singh

Department of Mechanical Engineering, Indian Institute of Technology Kanpur, India
*Corresponding author Email: manjesh@iitk.ac.in

Keywords: Molecular simulation, Highly-crosslinked polymer network, Indentation, Contact mechanics

Abstract

Indentation is a common experimental technique to study the mechanics of polymeric materials. The main advantage of using indentation is this provides a direct correlation between the microstructure and the small-scale mechanical response, which is otherwise difficult within the standard tensile testing. The majority of studies have investigated hydrogels, microgels, elastomers, and even soft biomaterials. However, a less investigated system is the indentation in highly cross-linked polymer (HCP) networks, where the complex network structure plays a key role in dictating their physical properties. In this work, we investigate the structure-property relationship in HCP networks using the computational indentation of a generic model. We establish a correlation between the local bond breaking, network rearrangement, and small-scale mechanics. The results are compared with the elastic-plastic deformation model. HCPs harden upon indentation.

Introduction

Polymers are ubiquitous since the early start of life in the form of natural rubber, starch, and cellulose. However, the concept of synthetic polymers is relatively new, which was first proposed in the pioneering work of Hermann Staudinger. Polymers are of particular interest because the relevant energy scale in these materials is about k_BT at the ambient temperature, thus their properties are dictated by the large conformational and compositional fluctuations. Here, k_B is the Boltzmann constant. Therefore, polymers provide a suitable platform for the flexible design of advanced soft materials. For example, polymers are widely used for the lubrication, the confinement mechanics of biological materials, the smart materials, thermoelectric, and in the common daily-use materials, to name a few.

Simulation Details

HCP networks with two different network functionality n are chosen for this study. Here, n defines the maximum number of bonds that a monomer can form with its neighbouring monomers. We have chosen a system of tri-functional (i.e., n = 3) and a tetra-functional (i.e., n = 4) networks. The systems consist of $N = 2.53 \times 10^5$ LJ particles randomly distributed within a cubic box at an initial monomer number density $\rho_m = 0.85\sigma^{-3}$. The simulations are performed using the LAMMPS molecular dynamics package.

We employ a generic molecular dynamics simulation approach. Here, the non-bonded monomers interact with a $6-12$ Lennard-Jones (LJ) potential $U_{non-bonded}(r) = 4\blacksquare[(\sigma/r)^{12} - (\sigma/r)^6] - U_{cut}$ if the distance r between two monomers is less than a cutoff distance $r_c = 2.5\sigma$. $U_{non-bonded}(r) = 0$ for $r > r_c$, and U_{cut} is chosen such that the potential is continuous at r_c. Here, $\blacksquare$ and σ are the LJ energy and the LJ length, respectively. This leads to a unit of time $\tau = \sigma \sqrt{m/\blacksquare}$, with m being the mass of the monomers. The unit of force F is $\blacksquare\sigma$. The values representative of the hydrocarbons are, $\blacksquare = 30$ meV, $\sigma = 0.5$ nm, and $\tau = 3$ ps. The unit of pressure $P_o = 40$ MPa.

The equations of motion are integrated using the velocity Verlet algorithm with a time step 0.005τ and the temperature is set to $T = 1\blacksquare k_B$ that is much higher than the typical glass transition temperatures $T_g \simeq 0.4 \blacksquare k_B$ in these network systems, thus representing an HCP gel phase. The temperature is imposed using a Langevin thermostat with a damping coefficient of $\square =$
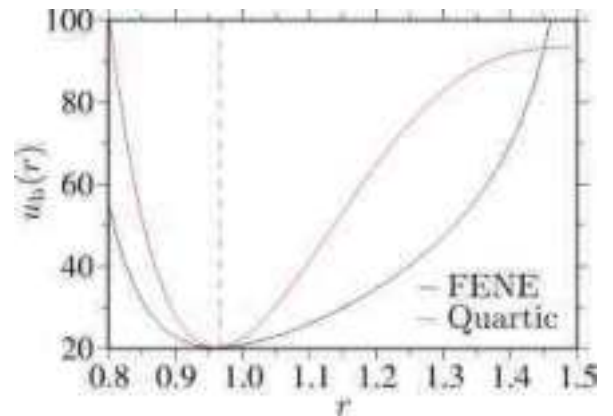

Figure 1: Interaction potentials between the bonded monomers $U_b(r)$ as a function of inter monomer distance r. The equilibrium bond length for these models is around $\ell_b = 0.97\sigma$ represented by the vertical line.

$1.0\square-1$. To model the HCP networks, we have used two different bonded interaction Ubonded(r): namely the finitely extensible nonlinear elastic (FENE) and the quartic potential.

Results & Discussion

We start by discussing the mechanical response of a tetrafunctional HCP network. Fig. 2 shows the typical force (F) versus indentation-depth (d) behavior for two different radius R. Other than the generic behavior, i.e., the increase in F with increasing d, one interesting feature can be seen is the sudden force drop F at various d. Note that we define F only when it magnitude is larger than the percentage of error fluctuation calculated in the elastic regime, i.e., below bond breaking indicated by the black arrows in Fig 1. Such force drop is a well-known phenomenon in the mechanical response of the glassy materials, where the atomic rearrangements during deformation can lead to such force drops. This phenomenon is commonly referred to as the avalanche. In our study, however, we are dealing with a rather rigid cross-linked network that has microscopically different molecular connectivity in comparison to the common glasses.
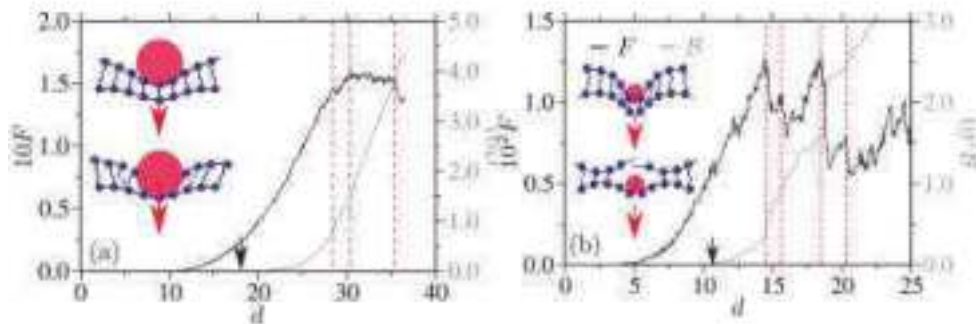

Figure 2: Force F and the percentage of broken bonds B as a function of the indentation depth d. Upper and lower panel show the data for the indenter radius R = 15.0σ and 5.0σ, respectively. The color codes of the data sets are consistent with their corresponding $y-$axes. Data is shown for an indentation velocity of $0.005\sigma/\tau$ and for a tetra-functional network. Vertical lines highlight the major drops in F and the corresponding B. Initial depletion zones below $d < 10.0\sigma$ (in upper panel) and $d < 5.0\sigma$ (in lower panel) are because the lowest part of the indentation tips is certain distance away from the network surface. Arrow indicates at the d values where the bond breaking starts. The insets show different pictorial representations of the indentation tips entering the sample at different d. The upper and the lower panels show the cases just before and after the bond breaking in the samples, respectively.

Figure 3 Same as Fig. 2 (lower panel), however, for two different network functionalities. The inset also includes the percentage of bond breaking B for the trifunctional network. For this network, bond breaking starts at around a depth of $d \simeq 21.0\square$. Data is shown for an indenter radius R = $5.0\square$.
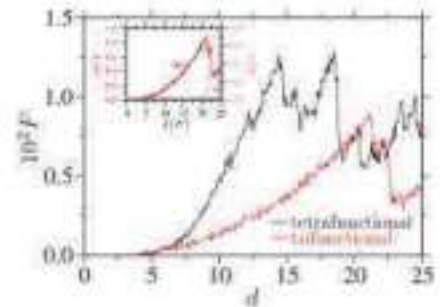

Fig. 3 shows the effect of n on the mechanical response. It can be appreciated that the trifunctional system can withstand almost twice larger indentation depth before the bond breaking happens in a sample. For example, bond breaking starts at $d \simeq 11.0\square$ for a tetrafunctional sample (see lower Fig. 2), while it is about $d \simeq 21.0\square$ for a trifunctional system (see the inset in Fig. 3). This is particularly because the lower bond density of a trifunctional sample, in comparison to a tetrafunctional sample, can withstand a larger elastic deformation. Furthermore, a trifunctional system is twice as ductile as a tetrafunctional sample, while the maximum force these samples can withstand also reduces by about a factor of two for the former (see the main panel in Fig. 3).

Conclusions

Using large scale molecular dynamics simulations of a(mesoscopic) generic model, we investigate the mechanical indentation of different indenter sizes. The use of such method has many advantages over the routinely used tensile deformations. Contrary to the visco-elastic deformations in the standard polymers, the deformations in the HCPs are of elastic-plastic nature. An analysis based on a simple theory of elastic-plastic deformation, suggests that the HCP networks harden upon indentation. This is because the bonds that are pulled or compressed taut and the disruption of the protovoids (collapsed free volume area) that originate within the sample during the network cure.

References
◯ [1] Manoj Kumar Maurya, Céline Ruscher, Debashish Mukherji, and Manjesh Kumar Singh, 2022, Computational Indentation in Highly Crosslinked Polymer Network, Physical Review E, 106, 014501.

Effect of rotational speed and normal load on contact pressure and temperature during pin-on-disc tribotesting

Pooja Verma[1*], Devashish Rajpoot[2] and Rajnesh Tyagi[1]

[1]Department of Mechanical Engineering, Indian Institute of Technology Banaras Hindu University, Varanasi, U.P.-221005, India
[2]Department of Mechanical Engineering, Indian Institute of Technology Bombay, Powai, Mumbai 400076, India
*Corresponding author Email: poojaverma.rs.mec17@itbhu.ac.in

Abstract

The friction and wear in systems pertaining metal to metal contacts govern the product service life, which is owing to material properties as well as operating conditions. When developing tribomaterials, it is important to take contact temperatures and pressures into account, because oxidation of material due to temperature rise leads to wear besides this; additionally, wear increases with an increase in shear stress resulting from a rise in contact pressure. In the present study, tensile experiments on medium carbon steel are performed at various strain rates and notch radii to deduce the Johnson Cook hardening and ductile damage model parameters, respectively. Material hardening and ductile damage parameters are used for finite element analyses to validate the tensile test responses. Pin-on-disc tribotester is modelled in Abaqus; subsequently, simulations are performed at various normal loads, F, (14.7, 19.6, 29.4, 34.3 N) and rotational speeds, N, (275, 550, 825, 1100 RPM). Effects of normal load, F, and rotational speed, N, on temperature, T, and contact pressure, p, are investigated since these are critical parameters for the wear of the material. Maximum temperature increases parabolically with F and saturates at $\sim 130°C$, although maximum p increases linearly with F. Maximum T and p at $F \sim 34.3$ N are $\sim 25\%$ and $\sim 132\%$ higher compared to $F \sim 14.7$ N, respectively. While maximum T increases linearly with N, p remains constant. Maximum T for $N \sim 1100$ RPM is four times than that for $N \sim 275$ RPM. The results suggest that at a constant speed of rotation wear is governed by contact pressure with increasing load since maximum temperature saturates after a critical load and the mechanism of wear is abrasive in nature. However, at a constant load, wear is controlled by temperature rise as the rotational speed increases and adhesive wear is dominant.

Introduction

High strength-to weight ratio, and balanced strength-ductility combination make medium carbon steel an integral part of various automobile components. Some of these components such as pistons, crankshafts and webs experiences sliding contact [1]. Temperature rise caused by frictional heating during sliding causes damage due to plastic deformation, and eventually causes component failure due to wear [2,3]. Pin-on-disc tribotest is the most widely used technique for determining the wear resistance of contacting surfaces. Several researchers[4–7] have conducted experiments and simulations in order to identify the wear mechanism during sliding wear. Bortoleto et al. [4] have conducted a Finite Element (FE) analysis of a pin-on-disc test under various normal loads in order to investigate the stress distribution on the contacting surfaces. Raghavendra et al. [5] carried out a pin-on-disc test to examine the dry sliding friction of A16061 material. They demonstrated that the flow of heat and temperature increases significantly before achieving equilibrium. A comprehensive literature review revealed that the distribution and quantification of temperature and pressure in relation to rotation speed and load is still unclear.

With the motivation to address above mentioned problems FE analyses of pin-on-disc tribotest at various normal loads and rotation speeds have been performed. This paper is organized as follows, tensile experiments and simulations were conducted at various strain rates and notch radii to determine the material hardening and ductile damage parameters. The stress-strain data obtained by FEM has been validated against experiments. Hardening and damage parameters are used for 3D FE analyses of pin on disc tests at various normal loads and rotation speeds. Furthermore, contour plots of temperature and pressure distributions are retrieved and analyzed to provide insights on the wear mechanism.

Experimental And Modelling Details

The uniaxial tensile experiments were performed on medium carbon steel (0.4% C) at various strain rates (10^{-4}, 10^{-2}, 10^{-1}, $\neg\neg$ and 1 s-1) and notch radii (Rnotch = 2, 5, 7.5, ∞ mm) to calculate material hardening and ductile damage model parameters. The obtained Johnson Cook (JC) hardening and ductile damage model parameters

have been used to reproduce uniaxial tensile test results using the FE method (FEM) tool Abaqus. Pin-on-disc tribotester has been modeled to perform wear tests, and a schematic diagram is displayed in Fig. S1. In the pin on disc tribotester, a very fine mesh has been created (Fig. S2). Mesh convergence study was performed, and results obtained were insensitive to element size. Pin and disc have 1116 and 7368 C3D8T elements, respectively. The boundary conditions were set up such that the disc could rotate about its centre and the pin was located at 40 mm from centre of disc and allowed to move in Z axis only. Pin-on-disc tests have been performed at four different loads (14.7, 19.4, 29.4, and 34.3 N) and rotation speeds (275, 550, 825, and 1100 RPM).

Results & Discussion

Calculation of Material Hardening and Ductile Damage Model Parameters

The experimentally obtained stress-strain (σ-ϵ) curves for various strain rates are displayed in Fig. S3. The stress, σ, is found to be increase linearly with ϵ up to yield point, the obtained Young's modulus, E, is ~ 225 GPa. Both yield strength (YS) and ultimate tensile strength (UTS) are found to increase with strain rate. The lowest YS and UTS are observed at quasistatic loading conditions (10-4 s-1), and these are ~ 488 and ~ 720 MPa, respectively. However, YS and UTS for 1 s-1 are ~ 28.6 and ~ 20.4% higher than those for 10-4 s-1. Strain at failure, ϵf, for all the strain rates are very close to each other, whereas maximum ϵf (~ 28.1%) is observed at 10-4 s-1. JC hardening model parameters are calculated using the following equation [8], $\sigma = (A+B\epsilon^n)(1+Cln\epsilon^{\cdot *})(1-T^{*m})$
Where, A, B, n, C, and m are material constant. $\epsilon^{\cdot *}$ and T^* are defined as defined as follows [8],
$\epsilon^{\cdot *} = \epsilon^{\cdot}/\epsilon^{\cdot}\_ref$ and $T^* = (T-T\_ref)/(T\_m-T\_ref)$
Where, $\epsilon^{\cdot}$, $\epsilon^{\cdot}\_ref$, and T_ref are strain rate, reference strain rate, and reference temperature, respectively. Method used by Murugesan et al. [8] is used to calculate material constants, tabulated in Table 1.

Table 1. Johnson-Cook material hardening parameters for medium carbon steel.

Parameters	A (MPa)	B (MPa)	n	C	m
Values	626	1756	0.21	0.006	0.444

The stress-strain curves for various notch radii are displayed in Fig. S4. YS and UTS of medium carbon steel are found to increase with a decrease in notch radii. However, uniform elongation, ϵu, and ϵf decrease with a decrease in notch radii. YS, UTS, ϵu, and ϵf for Rnotch = ∞ are ~ 488 MPa, ~ 720 MPa, ~ 14% and ~ 28%, respectively. YS and UTS of Rnotch = 2 mm are ~ 23 and ~ 11% higher than Rnotch = ∞, respectively. However, ϵu and ϵf of Rnotch = 2 mm are ~ 84 and ~ 85% lower than Rnotch = ∞, respectively.

Ductile damage model parameters are calculated using σ-ϵ curves of various notch radii. Subsequently, these parameters are used in Abaqus to incorporate damage. To examine the commencement of damage owing to nucleation, growth, and coalescence of voids notch sensitivity test is performed using the ductile damage model. Usually, damage in the material typically initiates when the following criteria is satisfied,

$$\omega_D = \int \frac{d\bar{\epsilon}^{pl}}{\bar{\epsilon}_D^{pl}\left(\eta, \dot{\bar{\epsilon}}^{pl}\right)} = 1$$

Where, ω_D, is a damage variable which increases monotonically with plastic deformation, $\bar{\epsilon}^{pl}$ is the equivalent plastic strain, $\bar{\epsilon}\_D^{pl}$ is equivalent plastic strain at the onset of damage which is defined as a function of stress triaxiality factor, η, and equivalent plastic strain rate, $\dot{\bar{\epsilon}}^{pl}$.

Finite Element Analyses of Sliding Wear test

The variations of maximum temperature, T_max, and contact pressure, p_max, with normal load, F, are displayed in Fig. 1. One may observe that T_max increases parabolically with F and saturates at F = 35 N. The lowest value of T_max (~ 104.2°C) is observed at F = 15 N. However, highest value of T_max (~ 130°C) is seen at F = 35 N. The pressure in the pin is not uniformly distributed due to rotation of disc. p_max increases linearly with normal load as seen from Fig.1 and it is lowest (~ 37.23 MPa) at F = 15 N and highest (~ 86.28 MPa) at F = 35 N.

Contour plot of T for various F at 0.3 s are displayed in Fig. 2. It is observed that the region undergoing the temperature rise increases with increase in temperature due to frictional heating although it is not significant. Gaard et al. [9] performed the FE analysis of pin on disc test at various sliding velocities and observed that the temperature rise takes place with an increase in sliding velocity. This results in softening of the contacting surfaces, and eventually, the material fails due to an adhesive wear mechanism. From the contour plots of T, it may be inferred that increase in T with F may lead to adhesion at higher F.
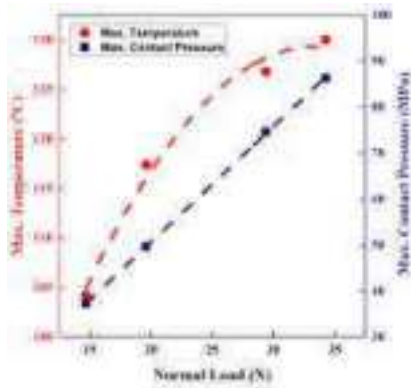

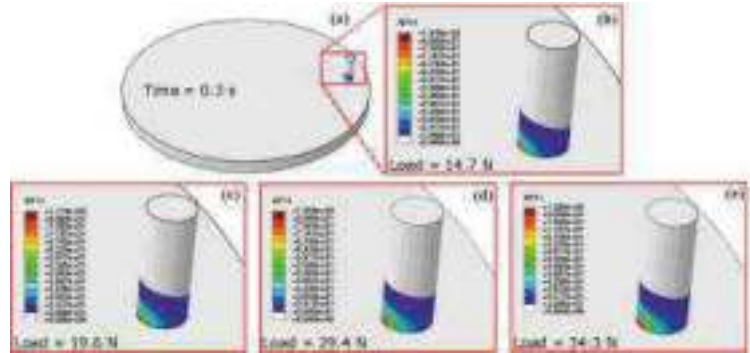*Fig. 1. Variations of maximum temperature and contact pressure with normal load.*

Fig. 2. Contour plots of temperature distribution of the pin and disc assembly at 0.3 s. Magnified view of the region squared in fig. (a) at (b) 14.7, (c) 19.6, (d) 29.4, and (e) 34.3 N normal loads.

Contour plot of p for various values of loads at 0.3 s are displayed in Fig. 3. A non-uniform distribution of pressure is noticed on the disc and pin surfaces due to rotation of disc. It is noticed that the region experiencing pressure rise, the intensity of pressure also increases with increasing normal load. Mao et al. [4] reported that increase in contact pressure causes an increase in abrasive wear. Odabas et al. [5] observed a linear correlation between normal load and wear volume. While the rise in T with an increase in F is not statistically significant ($\sim$ 104.2 N $\rightarrow$ $\sim$ 133.8 N), contact pressure doubles. High p implies high stress that leads to wear of material as a result of the abrasion.
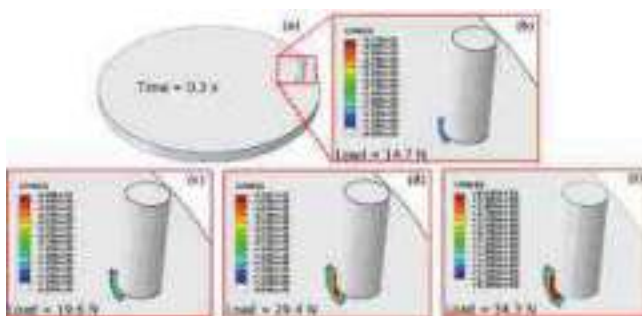

Fig. 3. Contour plots of pressure distribution of the pin and disc assembly at 0.3 s. Magnified view of the region squared in fig. (a) at (b) 14.7, (c) 19.6, (d) 29.4, and (e) 34.3 N normal loads.
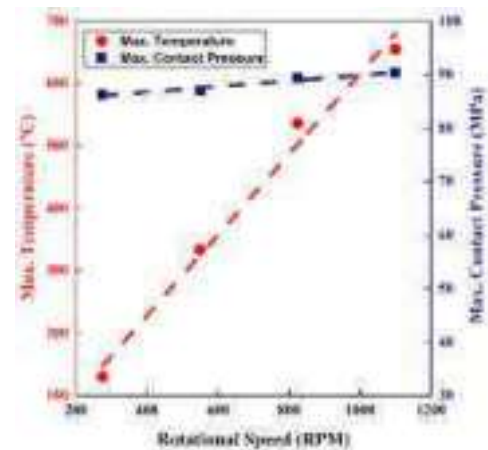

Fig. 4. Variations of maximum temperature and contact pressure with rotational speed.

Contour plots of T and p indicate that the abrasive wear mechanism predominates at high F amongst the adhesive and abrasive wear. T_{max} and p_{max} increase linearly with rotational speed, N, displayed in Fig. 4. Lowest values of T_{max} and p_{max} are observed at N = 275 RPM and these are $\sim$ 130°C, and $\sim$ 86.28 MPa, respectively. However, highest values of T_{max} and p_{max} are observed at N = 1100 RPM, which is $\sim$ 404 and $\sim$ 4.6% higher compared to N = 275 RPM, respectively.

Contour plots of T at 0.3 s for various values of N are displayed in Fig. S5. The area of region in which temperature rise takes place is found to increase with increasing N. Apart from this, the intensity of T is also observed to increase with

N. It is worth mentioning that at higher N, traces of raised temperature on disc surface are observed. Contour plots of p at 0.3 s for various N are displayed in Fig. S6. Region undergoing the pressure rise, the intensity of pressure also increases with increasing rotational speed. Contour plots indicate that dominating wear mechanism is adhesive wear at high rotational speed due to high rate of temperature rise.

Conclusion

Finite element analyses of a pin-on-disc tribotest for medium carbon steel at various normal loads, indicate that increase in maximum temperature, and region experiencing the temperature rise with increasing normal load is insignificant and it saturates beyond a load of 35 N. However, maximum pressure increases significantly with load, with abrasive wear being the dominant mechanism at higher loads. The maximum temperature increases by ~ 404% and maximum pressure increases by ~ 4.6% with increase in rotational speed and the dominating mechanism is adhesive wear at higher rotational speeds.

References

○ Ikpeseni, S. C., 2021, "Review of the Applications, Properties and Processing Parameters of Dual Phase Steels."
○ Shen, F., and Zhou, K., 2018, "Investigation on Thermal Response in Fretting Sliding with the Consideration of Plastic Dissipation, Surface Roughness and Wear," Int. J. Mech. Sci., 148, pp. 94–102.
○ Hutchings, I. M., 2001, "Wear and Lubrication," K.H.J. Buschow, R.W. Cahn, M.C. Flemings, B. Ilschner, E.J. Kramer, S. Mahajan, and P.B.T.-E. of M.S. and T. Veyssière, eds., Elsevier, Oxford, pp. 9551–9556.
○ Mao, L. J., He, X., Cai, M. J., and Qian, L. Q., 2022, "Influence of Contact Load on the Dry Sliding Wear Performance of 7075 Aluminum Alloy," Exp. Tech.
○ Odabas, D., 2018, "Effects of Load and Speed on Wear Rate of Abrasive Wear for 2014 Al Alloy," IOP Conf. Ser. Mater. Sci. Eng., 295, p. 12008.
○ Bortoleto, E. M., Rovani, A. C., Seriacopi, V., Profito, F. J., Zachariadis, D. C., Machado, I. F., Sinatora, A., and Souza, R. M., 2013, "Experimental and Numerical Analysis of Dry Contact in the Pin on Disc Test," Wear, 301(1), pp. 19–26.
○ Raghavendra, C. R., Basavarajappa, S., and Sogalad, I., 2019, "Analysis of Temperature Field in Dry Sliding Wear Test on Pin-on-Disc," Heat Mass Transf., 55(5), pp. 1545–1552.
○ Murugesan, M., and Jung, D. W., 2019, "Johnson Cook Material and Failure Model Parameters Estimation of AISI-1045 Medium Carbon Steel for Metal Forming Applications," Mater. , 12(4).
○ Gåård, A., Hallbäck, N., Krakhmalev, P., and Bergström, J., 2010, "Temperature Effects on Adhesive Wear in Dry Sliding Contacts," Wear, 268(7), pp. 968–975.
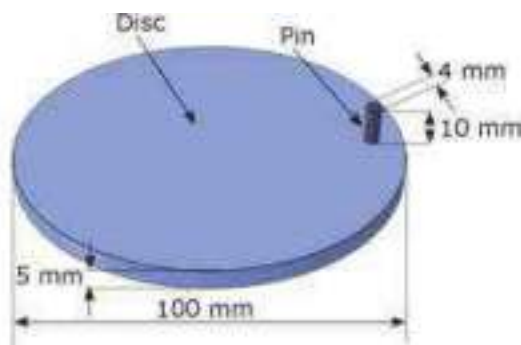
Supplementary Information

Fig. S1. Schematic of pin on disc tribotester.
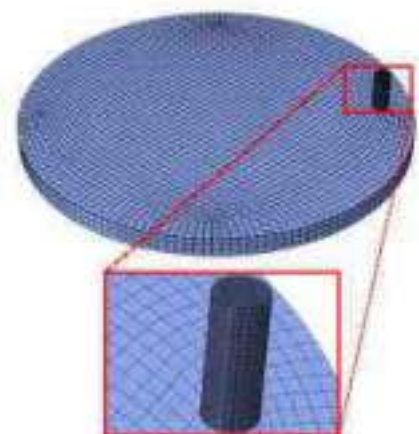
Fig. S2. Meshing of pin on disc tribotester with magnified view of pin.
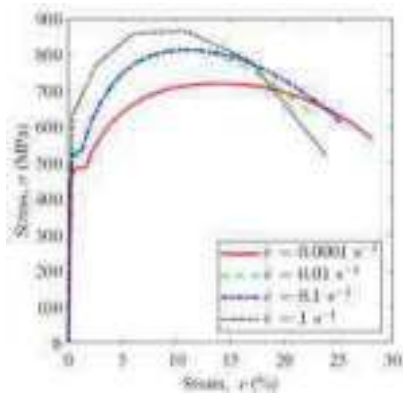
Fig. S3. Representative uniaxial tensile stress-strain curves at various strain rates.
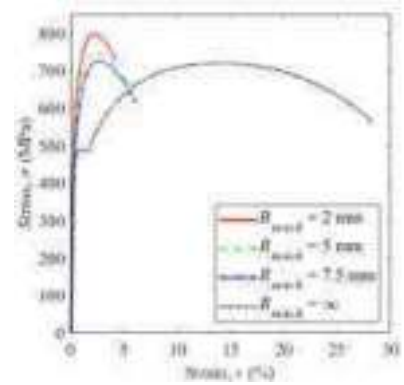
Fig. S4. Representative uniaxial tensile stress-strain curves at various notch radii.
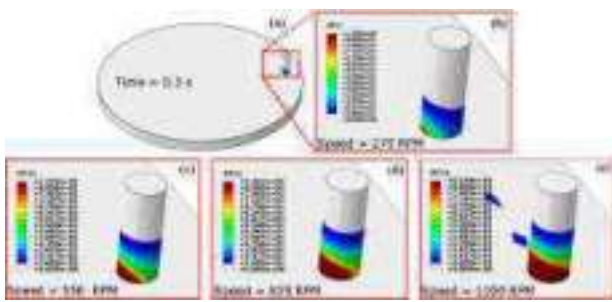
Fig. S5. Contour plots of temperature distribution of the pin and disc assembly at 0.3 s. Magnified view of the region squared in fig. (a) at (b) 275, (c) 550, (d) 825, and (e) 1100 RPM rotational speed.
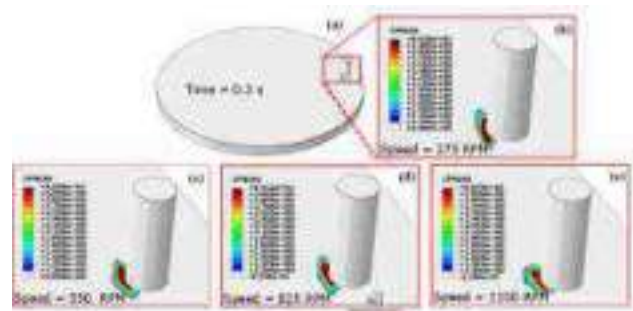
Fig. S6. Contour plots of pressure distribution of the pin and disc assembly at 0.3 s. Magnified view of the region squared in fig. (a) at (b) 275, (c) 550, (d) 825, and (e) 1100 RPM rotational speed

A water droplet-based triboelectric nanogenerator

Shalini[1], Jay Krishna Anand[3], Dhiman Mallick[2,1*], and Ankur Goswami[3,1*]

[1]School of Interdisciplinary Research Indian Institute of Technology Delhi, India [2]Department of Electrical Engineering Indian Institute of Technology Delhi, India

[3]Department of Material Science and Engineering Indian Institute of Technology Delhi, India

Keywords: Electrets, Hydrophilic, Hydrophobic, Electrowetting Droplet, Contact Angle, Electric double layer (EDL)

Abstract

Energy harvesting and sensing from water droplet motion have been proposed through numerous works in recent years. One of them is a water-polymer interface, which can be utilized to harvest energy as well as sensing using the principle of contact electrification and varying capacitance between the water droplets and the dielectric layer. Various water motion-based transducers allow efficient energy generation but require an external electric field. Additionally, the system is limited by the unstable and low density of surface charges. Herein, we propose an efficient electret-based electricity generator that generates electricity when a water droplet moves through a hydrophilic channel. The device is passive in nature as it does not require any external voltage source or additional process which gravely limits the use of passive water droplet-based transducers. Electrets were created on the hydrophobic surface by injecting a uniform charge through the corona discharge method, which results in a high negative charge density of 1.5 mC/m2. By utilizing the dedicated patterned pre-charged surface, an instantaneous voltage of 4.0 V at a current of 0.8 μA was obtained. These values correspond to a power density above 3.2 mW/m2 and a power conversion efficiency of up to 10.7 % from the water droplet's kinetic energy. Our electret-based energy harvester shows excellent stability and durability of surface charge and degradation of sporadic testing for 140 days. This approach is not only applicable for energy harvesting from water droplets but also opens avenues for various sensors such as chemical sensors.

Introduction

INTRODUCTION

The energy crisis and the global warming threats have become urgent and challenging which have compelled humankind to explore various alternate sustainable energy sources, which are freely available in the environment. Ambient vibrations are ubiquitous and wide band in nature, which can be used as a potential source for energy harvesting[1]. The concept of mechanical energy harvesting is unique, and it can be accomplished by various mechanisms such as electrostatic, piezoelectric, and triboelectric. In all these mechanisms, the generated current output is of two types one is real current and the other one is displacement current[2]. The former depends on the motion of free charges with the function of time, and the latter depends on the summation of the time- varying electric field of the free charges and the dielectric polarization.

On the other hand, the energy harvesting based on the electrostatic effect can be illustrated using a capacitive model as shown in Figure 1©, in which the current is only a conduction mechanism for electrical charge transport. Based on the capacitive model output current can be expressed as, where Q is the stored charge in the capacitor, the first term introduces current with the change in applied voltage, and the second term shows current with the variation in capacitance.

$$I = \frac{dQ}{dt} = C\frac{dV}{dt} + V\frac{dC}{dt}$$

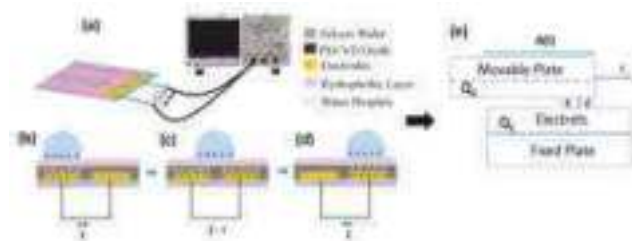Figure 1 (a) Schematic of the device (b) The water droplet started to overlap with the first electrode, therefore, charge transferred from the first electrode to the second electrode due to the formation of an electric double layer at the water polymer interface. (c) The water droplet was located in between the electrodes (d) the Droplet started to overlap with the second electrode. (c) Capacitive model.

The dielectric material shows permanent polarization because of its asymmetrical molecular structure. When the surface of the dielectric makes a contact with water droplets, a thin electric double layer (EDL) forms at the dielectric water interface as shown in Figures (b), (c) and (d). The electrostatic charge on the dielectric surface attracts the opposite ions of the water droplets[3]. This phenomenon related to EDL can be studied through the energy conversion method. In recent years, many promising results have been obtained using the EDL method. Furthermore, contact electrification between the water and polymer shows that the EDL method is capable of converting mechanical energy into electricity. On the other hand, the water droplet and polymer operating mechanisms can be explained through the variable capacitor model. The water on the hydrophobic film acts as an induction medium to attract opposite charges on the metal electrodes[4]. The interfacial capacitance is proportional to the overlap area from the water droplets as per equation (2).

$$Q = CV = \frac{sA}{d}V \qquad (2)$$

It is known that CYTOP or fluorinated polymers and superhydrophobic surfaces induce negative charges when the water droplet slides down, whereas the droplet acquires a positive charge. When droplets start to move over the polymer surface, electric double layer forms at the interface. Since hydrophobic surfaces have a negative charge in water, thereby image charge is formed spontaneously at the water-polymer

interface due to the absorbance of hydroxyl ions at the juncture[5].

Experimental Work

A targeted device design was proposed and fabricated wherein hydrophilic channels were made which are surrounded by hydrophobic boundaries as shown in Figure 2 (e). Water droplet gets confined on the hydrophilic channel by the hydrophobic boundaries and is able to roll over back and forth on the surface at tiny periodic vibration. Before the device fabrication, several material properties were optimized such as the wettability of the CYTOP film, its thickness, thermal stability, and chemical durability. Surface potential, surface charge and wettability of CYTOP were determined using various characterization such as Kelvin Probe Microscopy (KPFM), and contact angle measurements respectively. Other than this COMSOL, simulation was performed to do a theoretical study of surface potential using electrostatic physics as shown in Figures (a), (b) and ©.Figure 2: 2-D electric potential graph when water droplet in on pre-charged polymer film b) When water droplet is at mid of the polymer and grounded electrode c) water droplet are placed on the grounded electrode (d) Thickness measurement of CYTOP film using AFM (e) droplet morphology simulation taking dependent variables such as contact angle and channel width The efficiency of the droplet-based devices depends on the motion of droplets through hydrophilic channels without being hindered by the non-wetted hydrophobic surface.
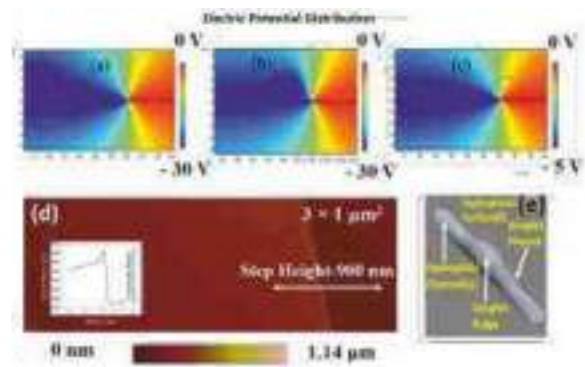
Therefore, some theoretical study was carried out to explore important parameters such as channel width, water droplet volume, contact angle (CA), contact angle hysteresis (CAH), etc. theoretical study was carried out by designing and simulating the device structure using the Surface Evolver 2.7 software tool [].

After analyzing the simulated results, it was observed that 800 µm is the optimum hydrophilic channel width surrounded by hydrophobic boundaries that can be used to confine the water droplet which can roll over on the surface under feeble periodic vibration as shown in Figure (e).
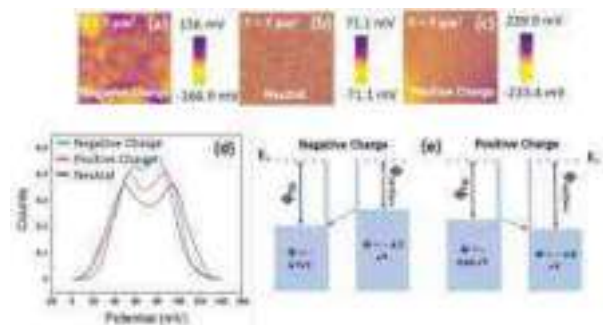
Figure 3: Surface potential mapping using KPFM after (a) injecting negative charge (b) no charge (c) injecting positive charge. (d) Surface potential distribution (e) fermi-level shift.

Hence, channel fabrication was performed by taking the advantage of the simulated results. Therefore, water droplet morphology was explored taking different channel widths. Later, the same simulation was carried out where SiO2 and CYTOP were used as hydrophilic and hydrophobic materials, which made similar contact angles of the water droplet. Further, Kelvin probe force microscopy (KPFM) was performed to explore the charge trapping ability of the hydrophobic material where electrets are to be made in the future. CYTOP is the material used to fabricate electrets, which is a commercially available hydrophobic material consisting of C-F bonds, having a high voltage breakdown of around 130 V/µm. EFM results are shown in Figures 3 (a) and (b) respectively, where charges are stored at the nanoscale using AFM contact mode. Later, EFM was performed to map the surface potential over the distance. Charge decay over the CYTOP surface was analyzed and observed the negative charges are more prevalent and stable than the positive charges, possibly due to CYTOP tribo-negative behaviors.

Results And Discussion

Later, an electrets-based electricity nanogenerator was tested using different ions of water droplets, and the results were found to be promising. Using de-ionized water 1.5 V was achieved, however, with pH4, pH11, and some ionic concentrations the generated voltage was

1.2 V, 4 V, and 3.5 V respectively as shown in Figure 4 (d). The output voltage was increased as the pH of water droplets was introduced over the pre-charged polymer surface or droplets of different pH impact the electret-based polymer surface. In this way, a pre-charged hydrophobic surface can be used as a pH sensor. Preliminary work was done to verify the concept and the idea. Hence, the idea to generate electricity using water droplets over the hydrophobic surface was explored successfully. This idea also opens avenues to develop sensors that can be used in the detection of water contamination, purification, etc.
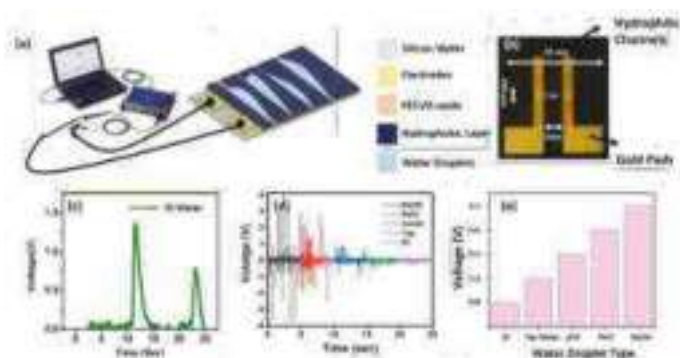

Figure 4: Water droplets with 50 µL volume were ejected by the micropipette when the droplet moves through hydrophilic channels voltage induced due to induction at the interface of dielectric and water (a) Schematic of droplet device (b) fabricated device © 1.5 V induced when pure DI water used (d) Voltage generation using different pH water (e) Increased generated voltage as water pH increases.

Conclusion

We have demonstrated that the droplet-based energy-harvesting device successfully generates enough electricity, which can turn on a LED light in real-time. Through water motion vibrations such as flowing and pressing there can be enough voltage or current to charge any wearable application like wristwatch batteries. The design of the droplet-based energy harvester device was a simple structure that involves only a dielectric layer as hydrophilic channels surrounded by the hydrophobic surface on the electrodes. This simple structure has the advantage for the process as well as for manufacturing cost that is most attractive of all of the advantages of droplet- based vibrational-based energy harvesters in comparison with others. In this study, we mainly considered the relationship between the area of overlap and variable capacitance and droplet morphology, but the amount of electricity generated depends on several factors, such as the dielectric constant of the dielectric layer, flow

speed, and the structure of the device that will be considered in upcoming research. Droplet-based energy harvesting technology can be applied toward not only various kinds of natural water droplet motion concepts, such as rain droplets, but also wastewater.

Acknowledgement

References

○ A. Goswami, S. Gowda, A. Tripathy, D. Roy, V. Bharadwaja, and P. Sen, "Low resistance liquid motion for energy harvesting," in 2015 28th IEEE International Conference on Micro Electro Mechanical Systems (MEMS), 2015, pp. 527-530.

○ F. Zhan et al., "Electron Transfer as a Liquid Droplet Contacting a Polymer Surface," ACS Nano, vol. 14, no. 12, pp. 17565-17573, 2020/12/22 2020.

○ L. E. Helseth, "A water droplet-powered sensor based on charge transfer to a flow- through front surface electrode," Nano Energy, vol. 73, p. 104809, 2020/07/01/ 2020.

○ Shalini et al., "Energy Harvesting From Water Droplet Motion Confined On A Hydrophobic-Hydrophilic Stripped Surface," in 2022 IEEE 35th International Conference on Micro Electro Mechanical Systems Conference (MEMS), 2022, pp. 943-946.

○ X. Li et al., "Spontaneous charging affects the motion of sliding drops," Nature Physics, vol. 18, no. 6, pp. 713- 719, 2022/06/01 2022.

○ R. Lipowsky, "Morphological wetting transitions at chemically structured surfaces," Current Opinion in Colloid & Interface Science, vol. 6, no. 1, pp. 40-48, 2001/02/01/ 2001.

An anisotropic bio-tribological performance of symmetrically micro-textured stainless steel 316L under simulated body fluid

Suryank Dwivedi[1,*], Amit Rai Dixit[1], Alok Kumar Das[1]

[1] Department of Mechanical Engineering, Indian Institute of Technology, Dhanbad, India.
*Corresponding author Email: suryankdwivedi11@gmail.com

Keywords: Micro-textures, Bio-Tribology, Lubrication, Friction and Wear.

Abstract

This work aims to study the anisotropic bio-tribological performance of symmetrically micro-textured stainless steel 316L under simulated body fluid. The topographical and morphological outcomes show that the flat end 300μm sized micro-grooves were fabricated periodically with different areal densities. Further, in-vitro bio-tribology analysis with hip-joint prosthesis condition is carried out, and results indicate that center distance, textured depth, and orientation play an important role in determining friction and wear performance. Friction and wear depth values increased for the parallel direction and decreased in the perpendicular direction, dictating anisotropic bio-tribological performance. Further, the effect of texture depth and center distance is analyzed, and details of the study are described in this manuscript.

Introduction

In the current scenario, the fabrication of textured surfaces has gained interest in improving surface functionality. It covers wide applications in surface engineering and biomedical fields. For medical implants, surface characteristics play an essential role in understanding wetting, biological, and tribological performances. Moreover, the fabrication of textured surfaces depends on the fabrication routes, nature of the material, feature's shape, and geometrical parameters [1].

The bio-tribological behavior can significantly affect surface functionality, leading to the prosthesis life cycle. During the relative motion of the contacting pair, i.e., bone and implants, an implant-tissue integration may occur, which needs to improve for the long service life of implants. It may differ with the age group, working environment, type of joints, and implant orientation. Past studies show that micro/Nanopatterning can enhance surface functionalization, i.e., bio-tribology. The literature shows that dimples and grooves with flat and conical ends or a combination of grooves and dimples are the most adopted micro features. These textures show an improved bio-tribological behavior under dry and lubricated wear tests [2,3]. However, the open literature has not reported the direction-dependent bio-tribological analysis under an in-vitro state.

Therefore, a biomedical grade stainless steel 316L was used to produce the micro-textured implant surfaces in the present case. A high-speed micro-milling machine was utilized to fabricate flat-end groove-shaped microtextures. A topographical, morphological, and bio-tribological characterization were done to study the effect of geometrical parameters and their orientation on the bio-tribological performance.

Experimental Details

The samples were fabricated using the commercially available stainless steel 316L (SS 316L) plate of 3mm. The plate was cut in the dimension of 20x20x3 mm3 through wire electric discharge machining (WEDM) and then ultrasonically cleaned and clamped in the fixtures to restrict any degree of freedom during the machining. Before the machining, samples were flattened using the 3mm two flute flat end mill micro-milling tool to achieve an area surface roughness of 50±5 nm, which is in the range of the roughness value of commercial implants. Further, linear groove textures were machined using the 3-axis high precision milling center using a pre-defined tool path with an accuracy of ±1μm. The experimental parameters such as pitch (p), width (w), depth (t), and diagonal (d) are 450 μm, 600 μm, and 750 μm, and 300 μm, 10 μm, 20 μm, and 30 μm, respectively. After machining three-dimensional (3D) surface profiles, two-dimensional (2D) and surface roughness values were measured from a roughness profile of the textured geometry through a 3D optical profilometer (Model: New View 9000, Make: Zygo, USA). Furthermore, the anisotropic bio-tribological performance of textured surfaces was evaluated using a reciprocating ball-on-plate universal tribometer (Model: MFT 5000, Make: Rtec Instruments, USA). During the wear test, in-vitro hip-joint prosthesis condition was maintained, and SS316L/SS316 sliding pairs were utilized. A normal Hertzian contact pressure was maintained, i.e.,10N load for 5 mins. The sliding frequency was set to 3 Hz, and the test was done

under simulated body fluid at 37 °C. The wear tracks were captured using the 3D profilometer to understand the wear mechanism.

Results And Discussion

A high-speed micro-milling center with the 3-axis CNC stage was adopted to fabricate the linear groove textures. Pre-designed CNC codes were used to create micro-grooves with different areal densities. The 3D topographical images and their cross-sectional profiles were captured and depicted in Fig. 1. The outcomes show groove textures formed at the center distance of 450 μm, 600 μm, and 750 μm, respectively, and at different depths, i.e., 10, 20, and 30, respectively. The geometrical parameters dictate that the micro-textures were formed within the error limit of 1%, and no such deviations are observed in the geometrical parameters. Further, the average surface roughness (Ra) for the textured surfaces is evaluated to understand the nature of the micro texturing. The results dictate that the textures with 10 μm depth have Ra values of 5.55 to 8.04 μm, which comes in the range of (1 μm < Ra < 10 μm). Moreover, for the texture depth of 30 μm, the Ra values vary from 12.15 μm to 13.19 μm. The results dictate that the roughness increases by increasing the center distance and texture depth. The outcomes depict that micromachining allows for the control of surface roughness at the macro and micro-roughness levels. The macro-roughness (Ra>10 μm) ensures a permanent connection between the implant and the bone and long-term mechanical stability, promoting periimplantitis and ion release. Micro-roughness (Ra > 1 − 10 μm) increases the contact area between the implant and the bone, reducing peri-implant inflammation and ion release risk. It also influences the bone tissue response to the implant surface [4]. Moreover, past studies dictated that rough surfaces will help in the increased wettability, which significantly increases the proliferation and differentiation in the early stage of bone formation [5,6].
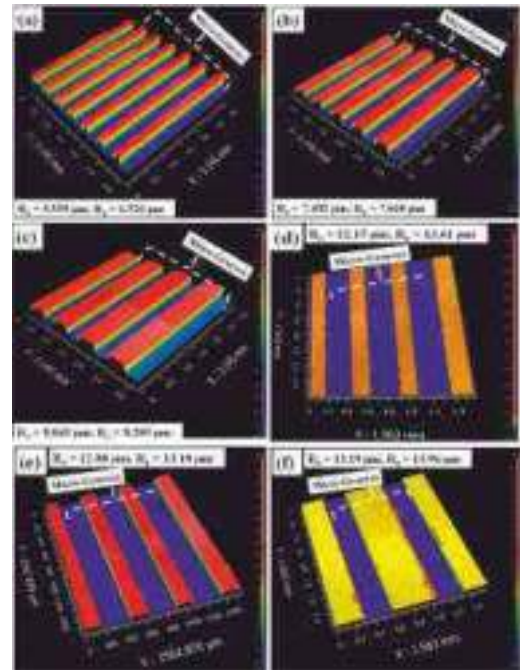
Further, the fabrication of joint prostheses seeks a detailed analysis of the bio-tribological behavior. The friction and wear are necessary to quantify the in-vitro state using the simulated body fluid. Therefore, the frictional characteristics are measured in terms of coefficient of friction (COF) and wear depth values. The bio-tribological analysis was done in all the samples along the parallel and perpendicular to the groove textures and tabulated in Fig. 2 (a-f). The average COF value in the parallel direction with CD of (a,b) 450 μm, (c,d) 600 μm, and (e,f) 750 μm at texture depth of 10 μm, 20 μm, and 30 μm, are in the range of 0.36 to 0.32, 0.34 to 0.35, and 0.38 to 0.34, respectively. The COF results show that the friction coefficient decreases while increasing the texture depth due to the increased roughness, i.e., texture depth. Similarly, in perpendicular direction with CD of (a,b) 450 μm, (c,d) 600 μm, and (e,f) 750 μm at texture depth of 10 μm, 20 μm, and 30 μm, are in the range of 0.28 to 0.26, 0.3 to 0.34, and 0.34 to 0.33, respectively. From the results, the authors can conclude that the groove textures present anisotropic bio-tribological characteristics. Thus, the texture's orientation can play an important role in reducing friction to improve the service life of implants under a physiological environment.

Furthermore, the wear tracks were captured in parallel and perpendicular directions for the CD of 750 μm at 10 μm, 20 μm, and 30 μm texture depth using the 3D optical profilometer. The 3D

Fig. 1(a-f). The 3D surface topography of groove textures with CD of (a to c) 450 μm at (a) 10 μm, (b) 20 μm, and (c) 30 μm, respectively, and with CD of (d to f) 750 μm at (d) 10 μm, (e) 20 μm, and (f) 30 μm, respectively.
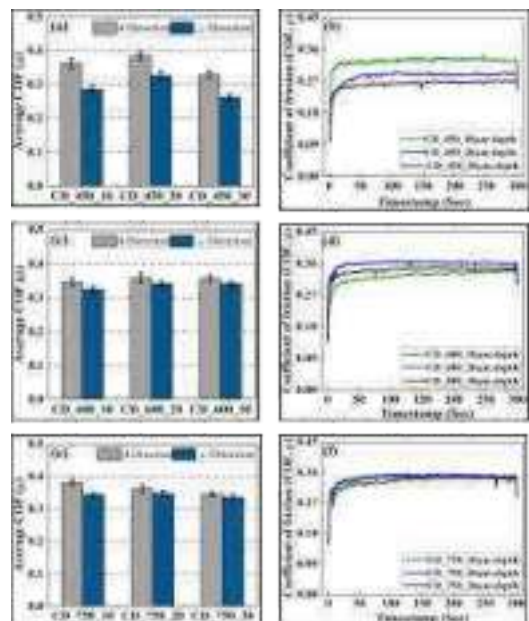

Fig. 2(a-f). The average COF and COF vs. Time graph for textured in parallel and perpendicular orientation.

wear tracks and their cross-sectional profiles were taken as per the ASTM standard G133-05 and tabulated in Fig. 3(a-h). The cross-sectional profile of each wear track was taken in at least five places, and the average wear depth was taken in this study. Fig. 3(a-d) corresponds to the CD of 450 μm with 30 μm texture depth in parallel and perpendicular directions. Similarly, Fig. 3(e-h) represents the 3D wear track for the CD of 750 μm with 30 μm textured depth in parallel and perpendicular directions. The results show that the wear depth loss is less in the perpendicular direction, which is in line with COF values. In the perpendicular direction, the contact area is less compared to the parallel direction, which leads to more wear loss. The wear depth for both samples is less than 10 μm, which dictates that the groove texture can withstand Hertzian contact pressure and can be used as an implant surface.

Conclusions

A groove textured surface was fabricated using three-axis high-speed micro-milling machine. The topographical, friction, and wear analysis were done to understand the bio-tribological behavior. The following conclusions are drawn:

1). A micro-scale texturing through high-speed micro-milling can be utilized to produce textured bio-metallic implant surfaces with a controlled micro-roughness scale range within the error limit of 1%.

2). An anisotropic bio-tribological characteristics are observed with the significant improvement in COF values along the perpendicular to the groove, which gives the idea about the orientation of the implant surfaces.

3). The 3D and cross-sectional profiles illustrated that loss in wear depth is more along the parallel direction, which is in line with the COF values.

Fig. 3(a-h). The 3D wear tracks and cross-sectional profiles for CD of (a-d) 450 µm and (e-h) 750 µm at 30 µm depth in (a, c, e, and g) parallel and (b, d, f, and h) perpendicular direction.

References

○ Pratap, T., & Patra, K. (2018). Direction dependent dynamic wetting of semi-hemispherical end micro-groove textured Ti-6Al-4V surface. Surface and Coatings Technology, 356, 138-149.

○ Jain, A., & Bajpai, V. (2019). Mechanical micro-texturing and characterization on Ti6Al4V for the improvement of surface properties. Surface and Coatings Technology, 380, 125087.

○ Ghosh, S., Choudhury, D., Roy, T., Mamat, A. B., Masjuki, H. H., & Pingguan-Murphy, B. (2015). Tribological investigation of diamond-like carbon coated micro-dimpled surface under bovine serum and osteoarthritis oriented synovial fluid. Science and technology of advanced materials.

○ Arkusz, K., Pasik, K., Halinski, A., & Halinski, A. (2021). Surface analysis of ureteral stent before and after implantation in the bodies of child patients. Urolithiasis, 49(1), 83-92.

○ Dwivedi, S., Dixit, A. R., & Das, A. K. (2022). Wetting behavior of selective laser melted (SLM) bio-medical grade stainless steel 316L. Materials Today: Proceedings, 56, 46-50.

○ Dwivedi, S., Dixit, A. R., Das, A. K., & Adamczuk, K. (2022). Additive texturing of metallic implant surfaces for improved wetting and biotribological performance. Journal of Materials Research and Technology, 20, 2650-2667.
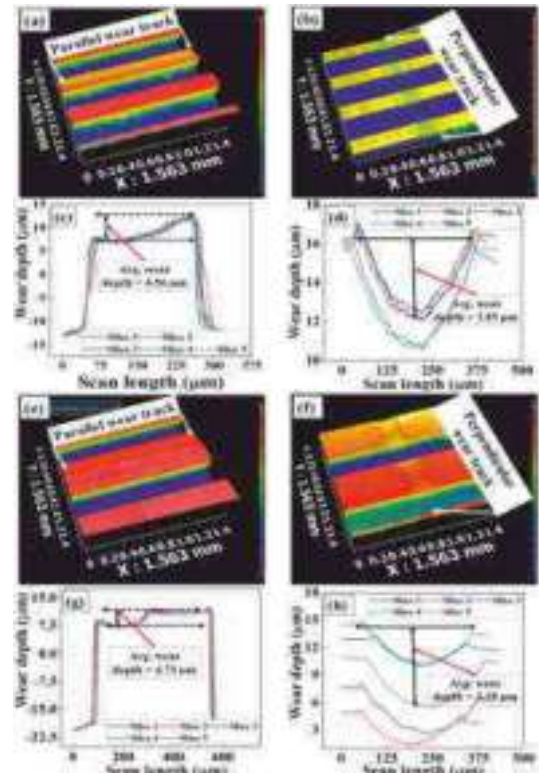
Investigation on the tribological characteristics of 3D printed bionic textured surface

Manupratapsingh Hirendrasingh Parmar, and Skylab P Bhore
Rotor Dynamics and Diagnostic Lab, Mechanical Engineering Department, Motilal Nehru National Institute of
Technology Allahabad, Prayagraj-211004, Uttar Pradesh
Email: skylabpbhore@mnnit.ac.in

Abstract

The nature inspired surface features have abundant potential in many applications. The researchers have studied the snake skin characteristics and explored the features of low friction coefficient. The use of bionic texture in safety razors shown significant friction reduction . The use of bionic texture in journal bearing is found to be effective as compare to plane bearing. The texture creation on the surface is achieved by different techniques such as laser, chemical etching, micro machining etc. In this paper, 3D printer is used to create the texture. The investigation on the tribological characteristics of the 3D printed surfaces is presented.

The texture samples are made using FDM (Fused Deposition Modeling) 3D printer. The material like Nylon, PLA, ABS are used. The pin on disc experiment is performed. The friction coefficient, temperature, load capacity for different operating condition are measured. The comparison of textured and nontextured surface using tribological characteristics is presented. The result shows that the textured surface reduces the friction. The wear of the textured sample is less than the nontextured sample. The quality of 3D printed texture is interesting and more research is in progress.

Introduction

In this modifying world, numerous benefits are provided by advances in industrial automation, however these are also related to the energy problem and environmental concerns. In practically all electromechanical systems, material losses caused by tribological behaviour of neighbouring parts are inevitable, and the tribological characteristics of contact surfaces have a direct impact on load-carrying capacity, efficiency, and service life. [7] . One such solution to this grave concern is the surface texturing. It is a very effective way to reduce the coefficient of friction, according to research done between 1999 and 2022.These textured are   nature inspired and very effective[5]. "Biomimetics" refers to biologically inspired design, adaption, or derivation from nature. imitation of biology or nature is meant. [1]. Snakes and various other reptiles have undergone major modifications over time, and these adaptations have enabled them to endure severe environments. One such noticeable alteration is in the texture of their skin.

The surface morphologies of snakes[9,2,3,4], fish [10], and other creatures were recently seen and investigated by bionics researchers, who discovered that these surface morphologies typically exhibited strong desorption, anti-adhesion, and wear resistance qualities [11].

When these textures are modified and mechanical components are designed using them as an inspiration, amazing benefits have been shown in terms of low coefficient of friction[5] and good wear resistant ability. Different methods to translate biological solutions to the technology world have been developed since bioinspiration should not simply rely on replicating nature. The biological solution carrying the outcome of a protracted evolutionary adaptation process must be preserved with extreme care. [8].

This study uses additive manufacturing with the Ultimaker 2 plus 3D printer because of its adaptability in making parts with complex designs in layer by layer approach. The varied textures that are inspired by various creatures are made. Additionally, we examine these samples using the Pin on Disk Wear and Friction Monitor to see if they can alter the coefficient of friction and wear for unlubricated contacts.

Understanding the design characteristics of the created texture and its overall optimization is the major goal of this article. The effects of creating various nature-inspired engraved surfaces with certain pattern, such as Hexagonal, round, Square and Diamond, were demonstrated using different materials such as PLA(Poly Lactic Acid), ABS, and Nylon. In order to compare the data and determine which of the textured samples reported the lowest coefficient of friction with the lowest wear and corresponding loading capacity, these samples were compared with the untextured sample under certain loading and speed (RPM) circumstances.Various crucial factors such the Aspect ratio of the pattern, pattern depth and the over all dimensions of the repeating pattern will also be discussed after comparing all the results for various parameters.

Investigating this is extremely intriguing since, unlike the Pin on Disk test, where the pin and disc are typically made of metal, this test uses an interface of polymer and metal. The use of such polymers with metallic parts to enhance tribological properties and performance now has a wide range of potential applications.

2. Methodology

The below figure show the methodology followed in the experimental investigation of various bionic textures.
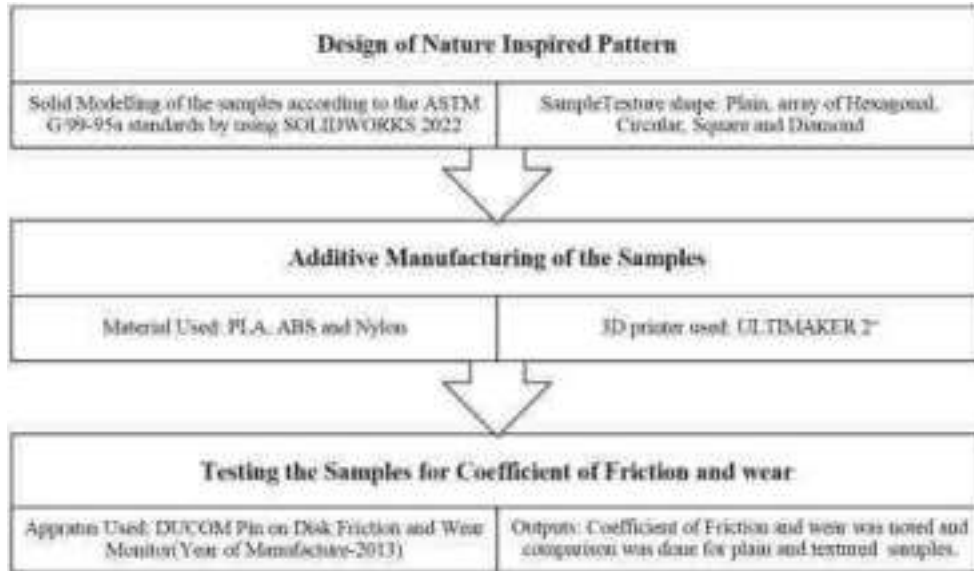
Fig.1- Work Flow Steps

2.1 Design of Nature Inspired Patterns

According to the ASTM G 99-95a[12] and G- F732[13] standards the sample was selected. Round cylindrical pin with pin diameter as 10 mm and length 60mm was fabricated. To save material and time, a screw and holder arrangement was made. This assembly helps to change the patter type quickly by just changing the screw with different pattern on it and screwing it with the holder to perform the test on Pin on Disk Friction and wear Monitor.

Fig.2-Solid Modeling of the Samples

SOLIDWORKS 2022 solid modeling software was used to make the 3D model of the sample Pin which was used to conduct the Friction and wer test. IT is deliberately made in two parts, a holder having 55mm length, 10mm diameter and internal metric threads of depth 10mm with pitch 1.5mm. The screw on the other hand has the total length 15mm with head thickness of 5mm with external metric threads of 1.5mm pitch extending 10mm length.

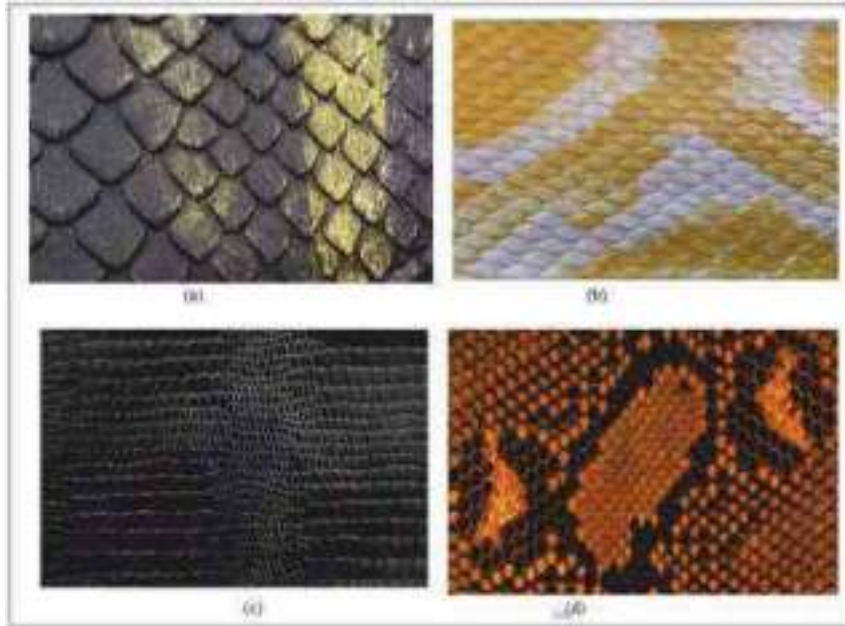Fig. 3 - Different Patters engraved in a array on the screw face

*Fig.4 [14] Different textures observed in various snakes
and inspiration taken .(a) Hexagon; (b) Diamond; (c) Square; (d) Circular*

From Fig. 3, different patterns were created on the screw face, each covering an area of around 78.5mm2 , having roughly the same texture aspect ratio with texture depth of 1mm . The Diamond patter(i) has a small diagonal of 0.40 mm and a long diagonal of around 0.50 mm. The sides of Hexagonal Pattern(ii) are around 0.5mm. In addition, the side length of each square in the square pattern (iv) is 0.5mm, and the circular pattern (iii) has a diameter of approximately 0.5mm. Each screw having a particular pattern is designed and further manufactured by using the 3D printer in batches for conducting the experiment.

2.2 Additive Manufacturing of the Samples

Once the 3D modeling of the samples is done, we use the additive manufacturing technique to manufacture the textured and untextured samples in batches. The solid model prepared in the SOLIDWORKS 2022 was saved in the STL file format and then by using the Ultimaker Cura software slicing is done for a particular batch of samples and is finally prepared to be 3D printed,the file is saved in G code format. In Cura software a stimulation of the 3D printing being done can be observed with an approximate printing time needed. Further this G code file is loaded in the memory card of the Ultimaker 2+ 3D printer and the additive manufacturing is done.
Specifications of the Ultimaker 2+ are:

Table 1- Specifications of UltimaKer 2⁺

1.	Layer Resolution	Up to 20 micron (0.02mm)
2.	Build Volume	230 x 225 x 205 mm
3.	Speed	30 - 300 mm/sec
4.	Print Surface	Heated bed, 20 - 100 C
5.	Nozzle Temperature	180 - 260 C
6.	Nozzle Diameter	0.25, 0.4, 0.6, 0.8mm
7.	Filament Diameter	2.85mm
8.	Supported Filaments Printing Software	Cura

Fig.5- Ultimaker 2+ 3D printer

103
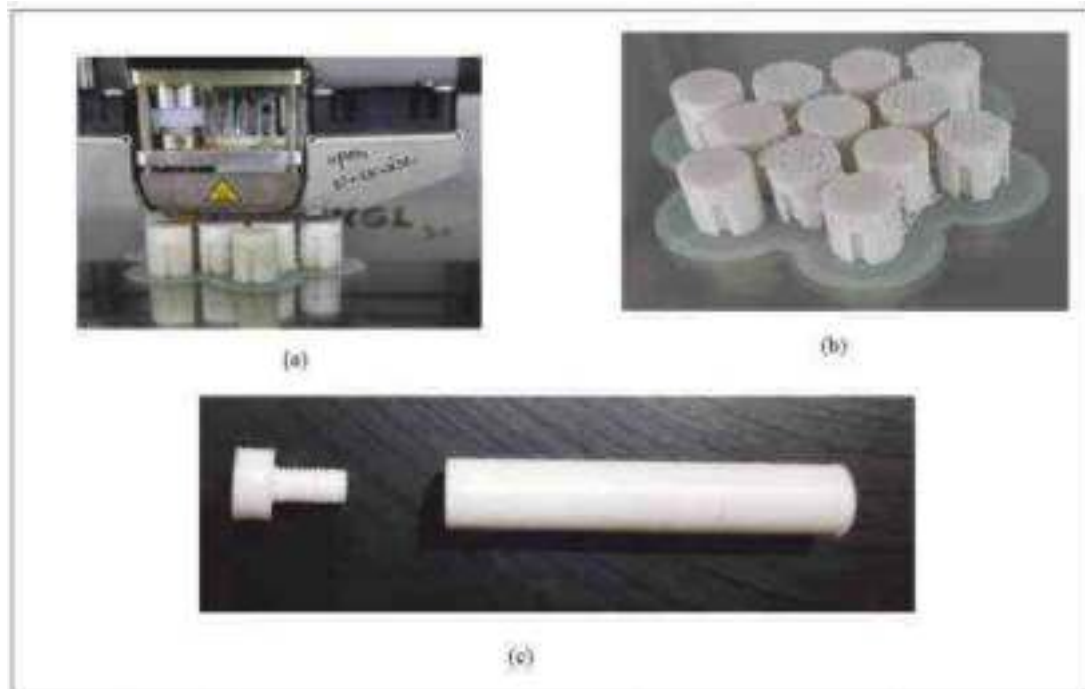
Fig.6- (a) Samples being 3D printed. (b) Printed Samples (untextured and textured); (c) Final Sample Pin

In the initial part of the research, PLA material was used to prepare the nature inspired textured samples. Plain samples were also made to compare the results with the different textured patterns and conclude some results. Nozzle diameter of 0.25mm was used with 0.06mm layer thickness and 100% infill for all the samples. The nozzle temperature was about 195 0C with built plate temperature of 600C.

2.3 Testing the Samples for Coefficient of Friction and wear

Pin on Disk Friction and wear monitor(Manufacturer- DUCOM,2013) was used to perform the friction and wear testing. Firstly according to the ASTM G99 standard for Pin on Disk apparatus the the specimens were cleaned properly by using a non chlorinated, non film forming cleaning agent, Acetone. After than each specimen textured and untextured was weighed to the nearest of 0.0001g by using the DENVER Instrument's weight balance.

Fig. 6 – (a) Pin on disk friction and wear monitor(Manufacturer- DUCOM,2013); (b) PLA Sample inserted in the holder ; (c) Pin on disk friction and wear monitor control interface ; (d) Outputs obtained on monitor.

The pin so prepared (Assembly of Holder and Screw) is securely inserted in the holder so that the pin is perpendicular to the disk when in contact to maintain proper contact conditions.

Initially different loads were applied to check the load bearing capacity of the PLA material. The main concern of this study was to determine the coefficient of friction and wear. Thus any type of melting is undesirable. The following table shows the results so obtained by varying the loading conditions. By performing experiment various times for untextured samples initially.

The two conclusion was drawn, Firstly when the loading condition was beyond 0.5 kg such as 1 kg, 2kg upto 3kg, the PLA samples showed a sign of melting with a strong smell of it. Secondly the texture depth is 1mm so when initially the samples were being tested ,the time interval of 600 sec was noted as per machine manual for the acceptable untextured sample with loading as 0.5 kg established before. This sample also showed a wear of surface up to 1mm in depth which is not desirable as after this the texture will be worn out completely and analysis can't be done with respect to the plain sample. Thus time interval of 550 sec is accepted for the analysis of textured samples to sustain the texture and match the time with plain samples so that a comparative analysis can be done by changing various textures.

Therefore the final input conditions for the Pin on Disk apparatus for each sample (textured and untextured) were taken as:

Table 2- Input Parameters for Pin on Disk Friction and wear Monitor

Applied Load(kg)	0.5
Pin Diameter(mm)	10
Wear track Diameter(mm)	100
Speed (RPM)	1000
Time (sec)	550

2.4 Results and Discussions for PLA sample with metal (Steel) Disk.
Table 3- Comparative analysis of the various textured samples with the plain sample

Table 3- Comparative analysis of the various textured samples with the plain sample

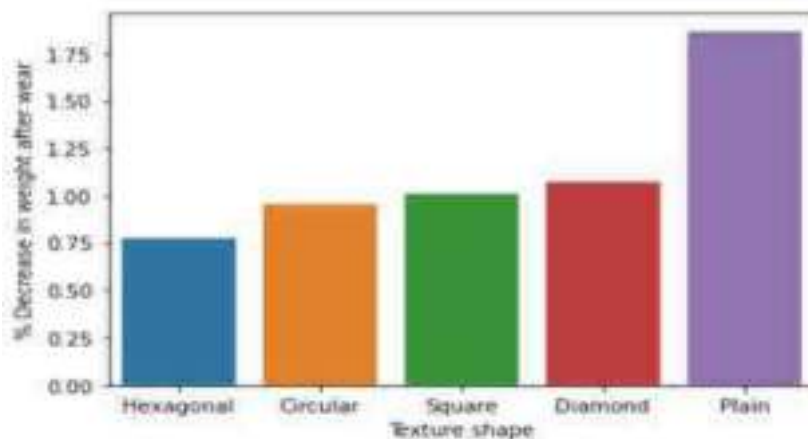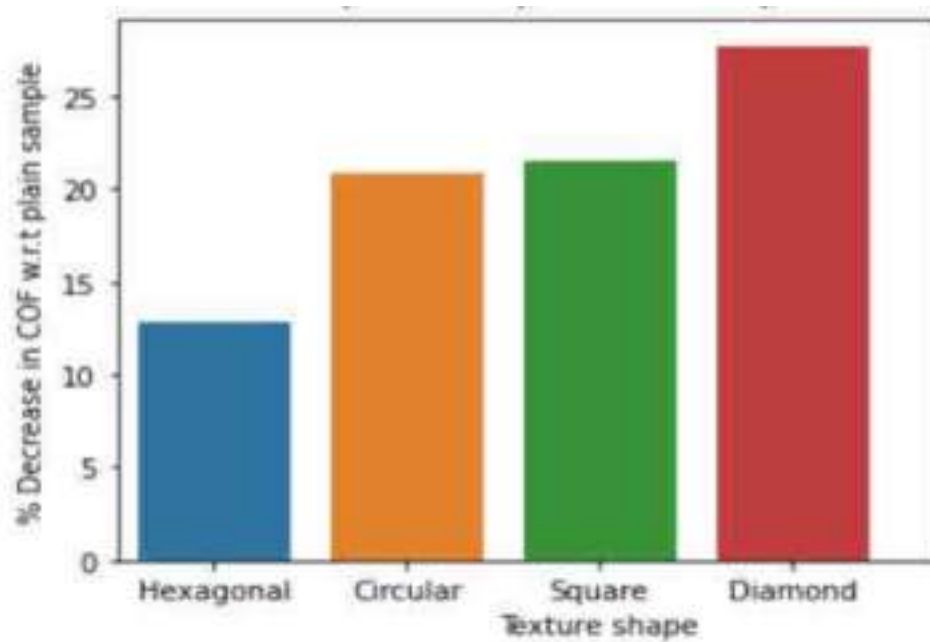| Sample No.	Texture shape	Weight before wear(g)	weight after wear(g)	% Decrease in weight after wear	COF	% Decrease in COF w.r.t plain sample
1	Hexagonal	0.6092	0.6045	0.77	0.28	12.77
2	Circular	0.6575	0.6512	0.958	0.254	20.87
3	Square	0.6646	0.6579	1.008	0.252	21.49
4	Diamond	0.6644	0.6573	1.068	0.232	27.72
5	Plain	0.6314	0.6196	1.868	0.321	NA

Fig.7- Percentage decrease in weight after wear

Fig.8 – Percentage decrease in COF with respect to plain sample

The experiment was successfully done for PLA samples with various textures. The objective parameters such as the coefficient of friction(COF) and wear was observed. Further a comparative analysis was done with respect to the plain sample with same input and environmental conditions and the results were recorded in tabulated and graphical fashion. The texture depth was 1mm for all the texture shapes and wear the texture was still visible and various conclusions can be drawn out and comments can be done on the % Decrease in COF with respect to plain sample and % Decrease in weight after wear for respective textures. For same input loading and speed parameters, the diamond texture showed excellent reduction in coefficient of friction which is nearly about 27.72% very prominent from Fig.8. On the other hand the there was no significant change observed in the weight of the samples after the wear however among themselves, the hexagonal texture showed the least percentage change in weight (0.77%).Also the wear of the untextured sample(Plain) was the highest which can be seen in Fig.7.

Conclusion

The experiment was successfully conducted and the following observations were made:

- It is observed that providing texture to the surface in contact (PLA to steel wear disk) subjected to some dynamic conditions, the overall coefficient of friction was reduced when compared with samples with no texture(Plain). Maximum reduction in COF was found in diamond texture among all which is 27.72%.
- This is quite different to the traditional concept which is to reduce friction between rubbing or sliding surfaces, they are made smooth to reduce the friction resistance and adhesion but based on the experimental investigation, providing textures can reduce the coefficient of friction to a significant percentage.
- The wear rate can also be predicted, wear rate for the same time frame can be drawn out and can be concluded that engraved textured samples can reduce the wear rate as well. But further the possibilities are yet to be studied to find the various effects of changing the texture depth and spacing within for formulating a global optimization.
- PLA material showed great results with steel wear disk but there is a great possibility for further testing having the wear disk and sample pin of same material and different materials can be tested can some useful results can be drawn out.

References

○ Bharat Bhushan,2009, Biomimetics: lessons from nature – an overview, Phil. Trans. R. Soc. A (2009) 367, 1445–1486

○ Martina J. Baum , Lars Heepe and Stanislav N. Gorb, 2014, Friction behavior of a microstructured polymer surface inspired by snake skin, Beilstein J. Nanotechnol. 2014, 5, 83–97.

○ Martina J. Baum, Lars Heepe, Elena Fadeeva and Stanislav N. Gorb, 2014, Dry friction of microstructured polymer surfaces inspired by snake skin, Beilstein J. Nanotechnol. 2014, 5, 1091–1103.

○ P Cuervo, D A López, J P Cano, J C Sánchez, S Rudas, H Estupiñán, A Toro1 and H A Abdel-Aal, 2016, Development of low friction snake-inspired deterministic textured surfaces, Surf. Topogr.: Metrol. Prop. 4 (2016) 024013.

○ Tsipenyuk A, Varenberg M., 2014, Use of biomimetic hexagonal surface texture in friction against lubricated skin, J. R. Soc. Interface 11: 20140113.

○ Kairi Furukawa, Masayuki Ochiai, Hiromu Hashimoto, Shinpei Kotani,2020,Bearing characteristic of journal bearing applied biomimetics, Tribology International 150 (2020) 106345.

○ Chao Zhao, Risheng Long, Yimin Zhang, Yibing Wang, Yueyong Wang, 2022,

○ Influence of characteristic parameters on the tribological properties of vein-bionic textured cylindrical roller thrust bearings

○ Fratzl P and Weinkamer R 2007 Nature's hierarchical materials Prog. Mater. Sci. 52 1263

○ Abdel-Aal, H.A.; El Mansori, M.; Zahouani, H. A Comparative Study of Frictional Response of Shed Snakeskin and Human Skin.Wear 2017, 376, 281–294, doi:10.1016/j.wear.2016.12.055.

○ Quan, S.; Yong, G.; Jun, G.; Liu, X.; Jin, Y.; Yang, S. Effect of Fish Scale Texture on Friction Performance for Reciprocating Pair with High Velocity. Ind. Lubr. Tribol. 2020, 72, 497–502, doi:10.1108/ilt-09-2019-0398.

○ Geraldi, N.R.; Dodd, L.E.; Xu, B.B.; Wood, D.; Wells, G.G.; McHale, G.; Newton, M.I. Bioinspired Nanoparticle Spray-Coating for Superhydrophobic Flexible Materials with Oil/Water Separation Capabilities. Bioinspir. Biomim. 2018, 13, doi:10.1088/1748-3190/aaa1c1.

○ Designation: G 99 – 95a (Reapproved 2000)e1, Standard Test Method for Wear Testing with a Pin-on-Disk Apparatus, www.astm.org , ASTM International 100 Barr Harbor Drive, West Conshohocken, PA 19428-2959, United States.

○ Designation: F 732 – 00, Standard Test Method for Wear Testing of Polymeric Materials Used in Total Joint Prostheses, www.astm.org , ASTM International, 100 Barr Harbor Drive, PO Box C700, West Conshohocken, PA 19428-2959, United States.

○ https://unsplash.com/s/photos/snake-skin.

Minimizing The Scratch Damage of Silica Glasses Via In Situ Deposition of Graphene Oxide Tribofilms

Sourav Sahoo[1*], Om P. Khatri[2], N. M. Anoop Krishnan[3,4], Nitya N. Gosvami[1]

[1]Department of Materials Science and Engineering, Indian Institute of Technology Delhi, India
[2]CSIR⸺Indian Institute of Petroleum, Mohkampur, Dehradun, India
[3]Department of Civil Engineering, Indian Institute of Technology Delhi, India
[4]Yardi School of Artificial Intelligence, Indian Institute of Technology Delhi, India
*Corresponding author Email: sourav.sahoo@mse.iitd.ac.in

Abstract

Glasses have become an indispensable part of daily life, although their brittleness makes them highly susceptible to surface-level damages like scratches, abrasions, and chipping during their processing and usage [1]. Such damages later act as the proverbial "Achilles' heel" by acting as the sites of crack growth, leading to catastrophic brittle fracture of the glass component [2], [3]. Herein, we demonstrate the enhanced resistance of silica glasses to scratch damages through lubrication with an in situ generated tribofilm of graphene oxide (GO) from its aqueous dispersion. Such lubricious tribofilms are observed to profoundly reduce the frictional forces, and hence, the sliding-induced tensile stresses that promote the formation of the conventional partial Hertzian cone cracks. The localized deposition of dense GO tribofilms within the scratched regions is confirmed by Micro-Raman spectroscopy analysis. Furthermore, the AFM analysis of the tracks reveals the sub-micron thickness and low-shear disposition of the GO tribofilms. The optical micrographs display distinctive differences in the crack density and severity of sliding with and without the GO tribofilms. To explain the observed differences in scratch damages, we theoretically analyze the role of friction in determining the tensile stresses generated behind the sliding contact. Finally, to study the driving force behind the fracture and wear events, we derive the energetics of the scratch damage, which qualitatively attributes the generation of fracture surface to the mechanical energy dissipated during scratching. The results provide new insights into the minimized scratch-induced surface damage of glasses in the presence of dispersion-derived tribofilms.

Introduction

The ubiquitous use of glasses in various applications, such as display screens of electronic equipment, automobile windscreens, and optical lenses, primarily relies on their excellent optical transparency [1]. However, their service life is marred by scratch-induced micro damages originating during their processing or application that ultimately affects the bulk mechanical strength of the glass component [4], [5]. The root cause of such surface-level deformations is the contact stresses between the glass and rigid counter surfaces, such as dust/abrasive particles, which pave the way for micro-cracks under sliding interactions. A viable way to limit the friction-induced tensile stresses while scratching is to deposit lubricious coating over the glass surfaces that can prevent the nucleation of cracks in the wake of sliding contact.

Among a wide gamut of materials studied for anti-friction and anti-wear lubricant additives, two-dimensional layered nanomaterials, such as graphene and MXenes, have attracted special attention owing to their remarkable mechanical strength, high conductivity, enhanced surface area, and lower interlayer shear strength [6]–[10]. The mechanism of lubrication in those nanomaterials involves the deposition of an interfacial tribochemical film, known as 'tribofilm,' over the friction faces, which imparts favorable friction and wear characteristics to the tribological pairs. However, since graphene is chemically inert to disperse uniformly in water and hydrocarbon-based solvents, its functionalization is necessary to tackle this limitation [11]–[13].

Graphene oxide (GO) is reported to possess excellent aqueous dispersion stability due to the carbon-oxygen functional groups, which hinders the $\pi - \pi$ interactions between the sheets [14]. This character, along with their superior nanoscale tribological performance, make them a preferable candidate for water-based lubricant additives. This study demonstrates a significant reduction in the severity of contact damage in glasses by the in situ deposition of a lubricious and surface-bound tribofilm of GO from its aqueous dispersion. The scratch damage, i.e., fracture and wear, on a fused silica glass against a spherical sapphire probe is analyzed under liquid conditions. The results provide further insights into the effect of dispersed GO sheets in controlling friction and wear-related damages during the scratching of glasses.

Experimental Details

The fused silica glass plates were scratched against spherical sapphire (Al2O3) probes (∅ 10 mm) in reciprocating scratch mode. Sapphire probes were chosen due to their excellent mechanical strength and chemical inertness in the aqueous environment. The aqueous GO dispersion (1 mg/mL), having a lateral sheet size of about 1 μm, was used as the liquid medium for the scratch tests. For a control experiment, the same test was repeated with deionized (DI) water as the medium to contrast the added effect of dispersed GO sheets in modulating the severity of scratching.

The reciprocating scratch tests of fused silica glass were carried out on a universal tribometer (MFT-5000, Rtec Instruments) with a customized liquid cell setup over a localized surface, as shown in Fig. 1. The scratch experiments were carried out at room temperature and ambient humidity with three different normal loads of 7, 10, and 15 N, with a scratching speed of 1 mm/s and a stroke length of 1.5 mm. To ensure proper shearing action throughout the track, the stroke length was optimized to be around 7–10 times the contact circle diameter at all loads applied in this study. The total scratching time was kept as 25 min, and to ensure repeatability, at least three scratch experiments were conducted for each combination of load and the liquid medium.

Results & Discussion

Friction of Silica Glass against the Sapphire Probe:

To study the scratch damage, the reciprocating scratch experiments on glass substrates were conducted in DI water and GO dispersion. Figure 2 shows the coefficient of friction (COF) plot of silica glass against the sapphire probe as a function of the sliding time in both DI water and aqueous GO dispersion. The COF in DI water is observed to increase steadily and attains a stable value of about 0.55 during the initial 200 s, while in aqueous GO dispersion, the COF significantly reduces to about 0.1 during the initial 300 s. The transient behavior of COF during the first ∼200 s is attributed to the run-in phase.

The thickness of the fluid film, calculated with the Hamrock-Dowson formula, results in sub-nanometer values with the λ parameter being significantly lower than 1 (boundary lubrication regime) in the case of both liquids. However, the 80% smaller value of COF observed in GO dispersion compared to DI water suggested the deposition of GO sheets to form a lubricious tribofilm which is absent in the case of DI water although operating under boundary lubrication regime. Moreover, the low COF is observed to be consistent, implying the formation of a stable, surface-bound tribofilm providing the continuous lubricating effect.

Characterization of the GO-Derived Tribofilm:

Micro-Raman spectroscopic measurements were conducted to confirm the deposition of the GO-derived tribofilm on the glass surface. Figure 3(a) shows the micro-Raman spectra obtained at a region within the scratch track. The prominent intensity of the characteristic D and G bands at 1360 and 1600 cm−1, respectively, provides evidence of a surface-bound GO tribofilm that lubricates the sliding contact and protects the glass surface from severe damage. The ID/IG ratio of GO is ∼0.74, which corresponds to a multilayer morphology of the deposited GO sheets. Figure 3(b) and (c) show the
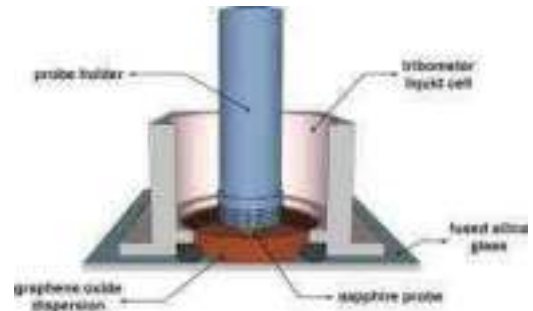

Figure 1: Schematic representation of the tribometer experimental setup designed for reciprocating scratch tests on the fused silica glass surface in a liquid environment.
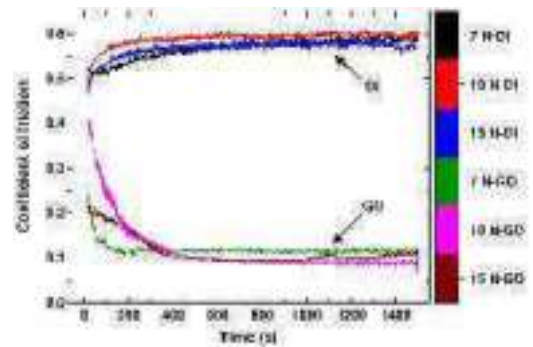

Figure 2: Coefficient of friction with respect to time for different reciprocating scratch test conditions on the fused silica glass substrate with the sapphire probe in DI water and GO dispersion.
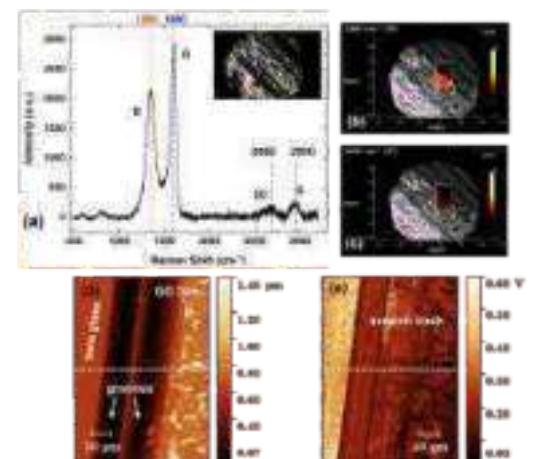

Figure 3: (a) Micro-Raman spectra of a region inside the scratch track showing the characteristic D and G peaks, (b,c) intensity maps of the 1360 cm–1 (D) and 1600 cm–1 (G) peak signals, (d) AFM topographical image showing the GO film inside the wear track, and (e) AFM friction map of the same region of the wear track showing the frictional contrast.

intensity map of the 1360 cm–1 (D) and 1600 cm–1 (G) peak signals, respectively. The absence of signals from the surrounding region demonstrates the highly localized deposition of the tribofilm within the scratch track.

The AFM topographical and frictional variation across the left edge of the track is shown in Fig. 3(d) and (e). The bare glass represents the non-scratched portion of the silica glass surface adjacent to the scratch track. The elevated topography inside the track indicates a continuous GO-derived film depositing over the scratched region. The low-shear disposition of the film is also confirmed by the friction map obtained simultaneously during the imaging, where the contrast in the signals between the bare non-scratched (left) and the scratched (right) regions is distinctly observed. The lower magnitude of frictional signals inside the wear track spatially correlates well with the deposited GO-derived tribofilm. On qualitatively comparing the average value of the frictional signals within the GO film region (0.058 V) and the bare glass substrate (0.310 V), about 80% reduction in the lateral signal is observed inside the lubricated track, which is in excellent agreement with the COF data from the tribometer. This further highlights that the low interfacial shear strength between the layers of the deposited GO tribofilm contributed to reducing the frictional (shear) stresses at the sliding contact.

Surface Damage Evolution during Scratching:

To visually demonstrate the reduction in scratch damage by the GO tribofilm, the scratch tracks were analyzed using optical micrography. Figure 4 shows a representative micrograph of the silica glass substrate after subjecting to reciprocating scratch tests in aqueous GO dispersion and DI water environments. The difference between the density of surface cracks and the severity of sliding (scratch track width, wear grooves, etc.) is strikingly apparent between the two cases at a similar normal load. In GO-mediated sliding, fewer partial Hertzian cone cracks are observed, along with visibly reduced micro-wear signified by the absence of continuous pits. However, on the other hand, sliding under DI water at similar loads produces deeper micro-scratches and a higher density of surface cracks, resulting in crack interaction and causing micro-wear events, evident in the form of continuous pits observed within the DI track.

Figure 4: A representative optical micrograph (10×) of the reciprocating scratch tracks on fused silica glass under (a) GO and (b) DI showing the differences in the severity of sliding and density of partial cone cracks along the track.

Conclusions

In conclusion, it is demonstrated that the GO sheets dispersed in the aqueous medium deposits as a lubricious tribofilm on the glass surface under tribological stresses. This thin and lubricious GO tribofilm, as confirmed by micro-Raman spectroscopy and AFM analysis, is observed to remain stable throughout the course of sliding. It is demonstrated that the tribofilm not only reduces the friction by about 80% but also minimizes the surface damage of glasses occurring as cracks and wear compared to the scratching performed in DI water. In other words, both friction and the wear behavior of glasses could be significantly improved by incorporating these GO sheets suspended in water. Overall, it is shown that the GO films can deposit in situ during the scratching of glass surfaces through a hitherto unknown tribofilm generation mechanism. These tribological films on glass surfaces can therefore be effective in enhancing the scratch resistance of glasses by reducing the interfacial friction and contact-induced damage in glasses.

❍ References
❍ A. K. Varshneya and J. C. Mauro, Fundamentals of Inorganic Glasses, 3rd Edition. Elsevier, 2019. doi: 10.1016/C2017-0-04281-7.
❍ J. Cheng et al., "Effect of scratches on the damage characteristics of fused silica optics under extremely-high impact load," International Journal of Mechanical Sciences, vol. 219, p. 107099, Apr. 2022, doi: 10.1016/j.ijmecsci.2022.107099.
❍ B. P. Rodrigues, T. To, M. M. Smedskjaer, and L. Wondraczek, "Mechanical Properties of Oxide Glasses," Reviews in Mineralogy and Geochemistry, vol. 87, no. 1, pp. 229–281, May 2022, doi: 10.2138/rmg.2022.87.06.
❍ S. Kasimuthumaniyan, N. N. Gosvami, and N. M. A. Krishnan, "Towards understanding the scratchability in functional glasses," Ceramics International, 2021, doi: https://doi.org/10.1016/j.ceramint.2021.04.233.
❍ P. Bandyopadhyay, A. Dey, A. K. Mandal, N. Dey, and A. K. Mukhopadhyay, "New observations on scratch deformations of soda lime silica glass," Journal of Non-Crystalline Solids, vol. 358, no. 16, pp. 1897–1907, Aug. 2012, doi: 10.1016/j.jnoncrysol.2012.05.041.
❍ D. Berman, A. Erdemir, and A. V. Sumant, "Reduced wear and friction enabled by graphene layers on sliding steel surfaces in dry nitrogen," Carbon, vol. 59, pp. 167–175, 2013, doi: https://doi.org/10.1016/j.carbon.2013.03.006.
❍ D. Berman, A. Erdemir, and A. V. Sumant, "Few layer graphene to reduce wear and friction on sliding steel surfaces," Carbon, vol. 54, pp. 454–459, Apr. 2013, doi: 10.1016/j.carbon.2012.11.061.
❍ S.-W. Liu et al., "Robust microscale superlubricity under high contact pressure enabled by graphene-coated microsphere," Nature Communications, vol. 8, 2017, doi: 10.1038/ncomms14029.

Understanding The Load Dependency of Vickers Hardness Value of Glasses Using Machine Learning Technique

Sajid Mannan[1*], Nitya Nand Gosvami[2], N. M. Anoop Krishnan[1,3]

[1]Department of Civil Engineering, Indian Institute of Technology Delhi, India
[2]Department of Materials Science and Engineering, Indian Institute of Technology Delhi, India
[3]Yardi School of Artificial Intelligence, Indian Institute of Technology Delhi, India
*Corresponding author Email: cez218288@civil.iitd.ac.in

Abstract

Machine Learning has become a popular tool in various fields and has largely advanced in recent years. In this study, we developed a machine learning model for predicting the Vickers hardness of oxide glasses from their compositions and load values. Further, we performed SHAP analysis to interpret the model output and identify each composition's contribution toward the output value. We have trained two plain ML models, one with load and the other without load, to see their effect on the hardness value of oxide glasses. We have observed that with load, the predictions are more accurate than without load, which signifies that the load plays an essential role in controlling the hardness. However, the plain ML model cannot capture the hardness-load dependency. Thus, we developed a Physics Informed Neural Network (PINN) model to capture load and composition dependency more rationally. We have observed that PINN is able to capture the load dependency behaviour of oxide glasses which was not the case in the previous plain ML model. Results show that the hardness value decreases with increasing load for every composition, which is in agreement with the previous studies.

Introduction

Glasses have become an indispensable part of daily life. It has provided many life-changing products over the past millennia to improve the quality of human living through various applications, viz., automobile windshields, window glasses, smartphone/computer protective screens, bioactive glasses and nuclear waste immobilization [1],[2]. However, the wider applicability of glasses is limited due to their inherent brittle nature, poor fracture and scratch-resistance. Glass surfaces are often exposed to dust particles that may act as potential abrasives, thereby inducing scratches deteriorating the mechanical and optical properties causing premature failure. Earlier it was believed that glasses are brittle and do not exhibit any plasticity, but recent studies showed contrary results wherein experiments at lower length scales proved that glasses possess plasticity [3], [4]. This plastic behaviour originates from the stress concentration generated due to sharp contact loading, causing permanent deformation in glasses. One of the ways to quantify the material's resistance to plastic deformation is by measuring its hardness. However, hardness is not a material property and exhibits significant variation depending on the measurement methods, length scale and ambient conditions. Thus, in this work, we attempt to understand the load dependency of hardness using a machine learning data-driven approach. In addition, we trained the PINN model in which we informed neural networks with an empirical relation of load with hardness.

Methodology

The dataset comprising comprehensive glass compositions and property sources, along with relevant references, is collected from the International Glass Database (INTERGLAD V7.0). However, the data corresponding to hardness value is significantly less (approx. 2840), which further diminished after data processing and left with 2096 glass compositions. To create a large dataset, we manually collected 1229 data points from literature combined with the INTERGLAD to make our model more robust and reliable. Further, we trained different machine learning models such as plain neural networks and PINN. Finally, SHAP analysis was performed to understand the model output and identify each composition's contribution toward the hardness. The workflow of the methodology followed is summarized in Fig.1.
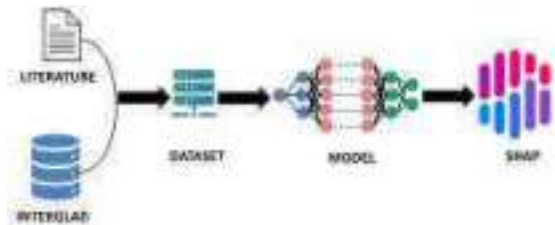

Figure 1: Workflow diagram

Results & Discussion

Figure 2 indicates the experimental and predicted values of hardness with load and without load on train and test datasets. The R^2 score for training and test are (0.88 and 0.87) and (0.92 and 0.89), respectively. Note the R^2 score values found to be more promising in the case of the model considering load instead without load implies a good correlation between experimental and predicted values. It is essential to highlight that the test dataset was kept hidden and only used the best model obtained after hyperparameter tuning. Although the developed ML model worked fine and predicted the hardness with reasonable accuracy, it did not capture the load dependency of hardness. It has been observed that hardness decreases with increasing load and gets almost constant at higher load is termed as Indentation Size Effect (ISE)[5][6], but this was not observed in the predicted plot shown, as shown in Fig. 4(A). To address this, we developed a PINN model, where we trained the model for multiple loads with the same compositions for a different family of glass. Since, here, we have already passed information to our model in the form of an analytical equation, our model learns the trend accordingly, and it is apparent from Fig. 4(B) that it captures the trend of load-hardness dependency.

Figure 3 indicates the PINN model's measured and predicted hardness values on train datasets. The R^2 score for training and test are (0.979 and 0.948) respectively. It is clear from the R^2 score that the PINN model works better than our previous plain ML model. The learning curve with epoch in Fig. 3(B) is plotted for training and test datasets to see the model performance. Here one epoch is considered when full data is passed through the neural network during the training phase, and there is no batching in data. To see the model performance, we have also plotted the predicted hardness vs actual hardness of soda-lime-borate glass for multiple loads in Fig. 4 from both the plain and PINN models. It is clear from Fig. 4(A) that our plain model is not able to capture the trend, although Fig. 4(B) shows that the PINN model successfully captures the load dependency of hardness, i.e., ISE.

Note that although models capture the composition-property details, interpretability is too complex as these are black box models and do not have a clear picture of the network learned during training since we have multiple hidden layers and nodes, which makes their structure more complex, eventually learning a large number of parameters for optimal results. To address this challenge, recent studies have tried to understand the composition-property relationship with various known theories such as Partial Dependence Plot (PDP) and SHapley Additive exPlanations (SHAP). Here we mainly focus on the SHAP explanation as it was found to be a good explainable theory for many features and the contribution of each feature to the output value.

Figure 4 indicates the violin plot of SHAP. It has been observed that high values of selenium (Se) and sodium (Na) negatively impact the hardness value, i.e., as we increase their concentration, the absolute hardness value of glass decreases. The color of points represents normalized weight percentage of features, with pink and blue representing the higher and lower value, respectively. The
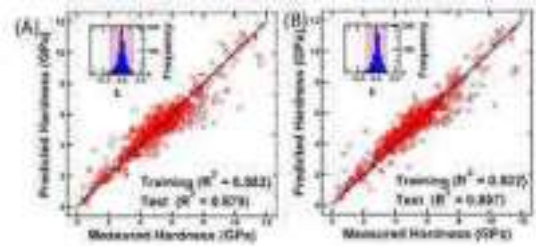
Figure 2: Predicted values of (A) Hardness without Load and (B) Hardness with Load of oxide glasses using optimized plain ML models. A histogram of errors is plotted in the inset where the shaded region represents the 90% confidence interval.

Figure 3: (A) Predicted vs Measured Hardness using PINN model (B) Learning curve of the PINN with epoch in logarithmic scale.

Figure 4: (A) Hardness vs Load using plain ML model (B) Hardness vs Load using PINN model.

Figure 5 SHAP values for Hardness, the color of points in represents the magnitude of the weight% of oxide in the glasses.

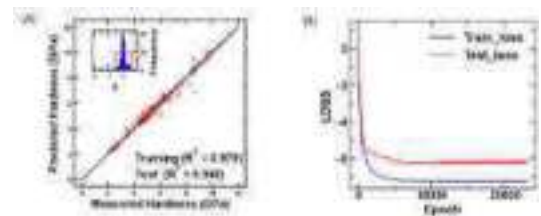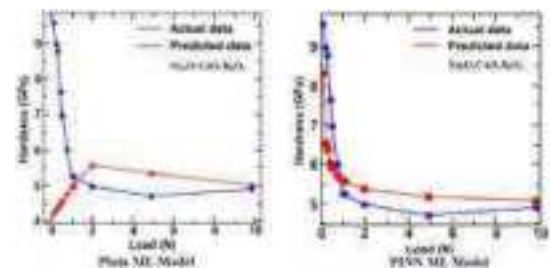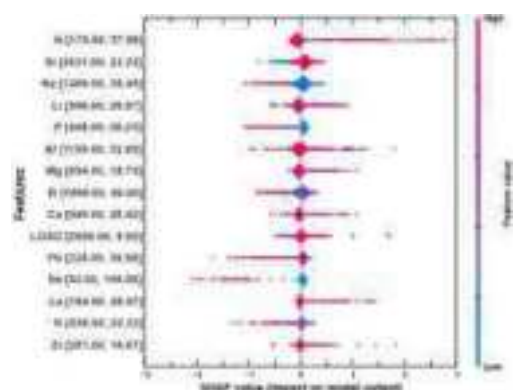directionality of the feature's impact on the prediction from this plot; for example, nitrogen (N), silicon (Si), magnesium (Mg), and lanthanum (La) oxides have high mean absolute SHAP values and will increase as their weight percentage increases. However, the oxides of selenium (Se) and sodium (Na) have higher mean absolute SHAP values, but it will decrease as their weight percentage increases. This suggests that the higher values of nitrogen (N), silicon (Si), magnesium (Mg), and lanthanum (La) increase the value of prediction output.

Conclusions

Altogether, we have shown that despite the complex nature of the ML model, it can be remarkably understood and interpreted from the SHAP plot. We have demonstrated how the input features of the model influence the output property value (i.e., hardness) in the case of glass using the SHAP algorithm. Interestingly, nitrogen (N) plays a significant role in improving the hardness value of glass. However, it is present in very few samples as nitrogen oxides are generally unstable; thus, it found only in chalcogenide glasses. In addition, the model predicted that oxides of silica (Si), magnesium (Mg), boron (B), and calcium (Ca) play a significant role in improving the hardness value. Also, we have observed that load plays a significant role in controlling the hardness value of glass. Furthermore, we have shown the load dependency of hardness using the PINN model. It has been observed that the hardness value decreases with increasing the load value and getting almost constant at a higher load, which is found in agreement with previous studies.

References

○ R. R and J. Kaewkhao, "Glass material and their advanced applications," KnE Social Sciences, Jul. 2019, doi: 10.18502/kss.v3i18.4769.

○ M. I. Ojovan and W. E. Lee, "Glassy Wasteforms for Nuclear Waste Immobilization," METALLURGICAL AND MATERIALS TRANSACTIONS A, p. 15.

○ E. W. Taylor, "Plastic Deformation of Optical Glass," Nature, vol. 163, no. 4139, Art. no. 4139, Feb. 1949, doi: 10.1038/163323a0.

○ F. M. Ernsberger, "Role of Densification in Deformation of Glasses Under Point Loading," Journal of the American Ceramic Society, vol. 51, no. 10, pp. 545–547, 1968, doi: 10.1111/j.1151-2916.1968.tb13318.x.

○ M. M. Smedskjaer, "Indentation size effect and the plastic compressibility of glass," Appl. Phys. Lett., vol. 104, no. 25, p. 251906, Jun. 2014, doi: 10.1063/1.4885337.

○ A. S. Hakeem, J. Grins, and S. Esmaeilzadeh, "La-Si-O-N glasses: Part II: Vickers hardness and refractive index," Journal of the European Ceramic Society, vol. 27, no. 16, pp. 4783–4787, Jan. 2007, doi: 10.1016/j.jeurceramsoc.2007.04.003.

Comparative study of nanoscale wear behavior of graphite in DI water vs. polyalphaolefin oil

Jitendra Soni[1*], Nitya Nand Gosvami[1]

[1]Department of Materials Science and Engineering, Indian Institute of Technology Delhi,
Hauz Khas, New Delhi, India 110016
*Corresponding Author: msz218016@mse.iitd.ac.in

Abstract

Two-dimensional graphene material is an effective atomically-thin solid lubricant with excellent mechanical strength. However, its lubricating property is influenced in the presence of surrounding medium where the interaction between the molecules and graphene layers may exhibit complex friction and wear behavior. In the current work, the friction and wear characteristics of graphite were compared in the presence of two different mediums: DI water and non-polar solvent as Polyalphaolefin (PAO4) oil at step edge and interior step-free regions at nanoscale level. The experiments conducted using an atomic force microscope (AFM) in different regions revealed that PAO4 provided significantly better wear resistance to the graphene layers near the surface of graphite than water in both step edge and interior step-free regions. The critical load required to cause wear in the presence of PAO4 was more than six times the load required to cause wear in the presence of water at step edge region. PAO4 offered wear resistance in the interior region of graphene at 4000 nN load even for about 200 sliding cycles with no trace of wear. This study essentially provides safety operational limits of loads for tribological applications of graphene for various small scale engineering applications.

Introduction

Micro- and nanoscale devices suffer from notable issues of typical surface phenomena such as friction and wear, which challenge the effective lubrication of sliding interface at the small scales [1]. Graphene, possessing an extremely high mechanical strength [2] and remarkable capability to reduce friction with a single atomic layer [3], emerges to be an ideal solution to subdue the complications [4]. However, graphene is extremely sensitive to the surrounding environment which affects its lubrication longevity and friction-reduction performance [5]. Several studies have demonstrated that the wear of graphene commences at the step edge where dangling bonds are in abundance, in contrast, graphene flakes are quite resilient in the interior regions when scratched by a diamond probe [6]. When immersed in liquids such as water, oil or ionic liquids, the interaction between the liquid molecules and the carbon atoms of graphene has directly shown to influence the complex friction behavior by developing a structure of solvent molecules that passivates the dangling bonds at step edge and interior regions which improve the friction and wear resistance of graphene [7]. In this respect, a recent study also displayed the unique behavior of higher wear strength at step edge in humid conditions than in dry cases due to saturation of dangling bonds by atmospheric water molecules [8].

The interaction of liquid molecules with graphene layers is very intriguing to understand how the surrounding environment can ease resistance to shear and reduce wear. A load-dependent study on graphene in a non-polar solvent systematically presented the effect of organization of ordered molecular layers at the graphene surfaces [9], however, a detailed investigation of wear phenomena remains unexplored. Hence, in the current study, we investigated the wear behavior of few layered graphene in DI water and a non-polar solvent, i.e., PAO4 oil using AFM at room temperature. The anti-wear performance of graphene layers was examined in the step edge as well as interior regions. This research aims to further contribute to an overall understanding of different liquid-graphene interactions at the interface affecting the friction and wear of graphene which is essential for engineering effective small-scale devices.

Experimental Section

To study the wear behavior of multilayer graphene, freshly-cleaved highly oriented pyrolytic graphite (HOPG) was immersed in DI water or PAO4 at room temperature (20–25 ℃) using an AFM (Drive AFM, Nanosurf, Switzerland). The nanoscale friction and wear measurements were carried with diamond-like-carbon (DLC) coated sharp AFM probes (spring constant: 3 N/m, Multi75DLC, Budget-sensors, Bulgaria) in the interior as well as step edge regions of graphene. Friction and wear were analyzed on the graphitic surface by scanning the probe over the experimental region of scan area $1 \mu m \times 1 \mu m$ with scan speed of ($50 \mu m/s$) while gradually increasing the normal load until wear in the experimental region occurred or it reached to the maximum limit permitted by the AFM system.

Result And Discussion

3.1 Topography and friction images of graphite immersed in liquid

AFM topography and friction images are displayed in Figure 1 where (a) and (c) represent the topographic images of graphite in water and PAO4, respectively, and (b) and (d) represent the friction maps in water and PAO4 oil, respectively. The contrast in the brightness in topographic images separates graphene layers at different steps and the dark lines in friction images depict the sudden change in friction at the step edges during scanning.

3.2   Friction and wear behavior of graphite in DI water

Figure 2(a) and (b) demonstrate the friction behavior of graphite in DI water at different regions and AFM topography of wear occurred at the interior region with wear profile shown in inset, respectively. The friction forces were observed to increase with the increase in normal load. Repeated experiments conducted in various regions reflected that wear occurred in the interior regions (data represented by green dots in Figure 2(a)) at about 90% higher critical loads than at step edge regions (data represented by blue dots in Figure 2(a)). With the commence of wear at the critical loads showed the drastic increase in friction values in interior region due to infiltration of wear particle of graphene during the scanning, however, there was no significant increase in friction values due to wear in step edge regions. The wear of graphene layers occurred at much lower loads at step edge region than in interior region due to the dangling bonds at the edges. Moreover, the steps experienced comparatively higher shear stresses than the interior region in the experimental region which led to the commencing of wear at the steps.

3.3 Friction and wear behavior of graphite in PAO4 oil

The friction and wear behavior of graphite were investigated in the presence of PAO4 oil. The friction force values obtained were of the order similar to that obtained in water medium. Due to the presence of step edges, friction force was relatively higher due to obstruction in the scanning path than in interior regions. In comparison to DI water as surrounding medium, graphene layers with step edges underwent wear at relatively higher critical loads of ~2000nN as illustrated in Figure 3. In contrast, there was no trace of wear at the interior regions even at higher loads of 4000 nN (which appeared as the maximum limit of load to be allowed by the AFM system) when the experimental region was scanned for 200 sliding cycles. These outcomes suggested that graphene layers were quite resilient when PAO4 oil was used as a lubricating medium for applications at loads below 2000 nN irrespective of the type of region. The wear resistance of graphene in the presence of PAO4 oil could be due to protective boundary layers of strongly adsorbed PAO4 molecules than water molecules at the vicinity of surface and step edges, however, they are yet to be determined by quasi-static force separation curves in this study.

Figure 1 (a) AFM topography of graphite in DI water (b) Friction image of graphite in DI water (c) AFM topography of graphite in PAO4 oil (d) Friction image of graphite in PAO4 oil
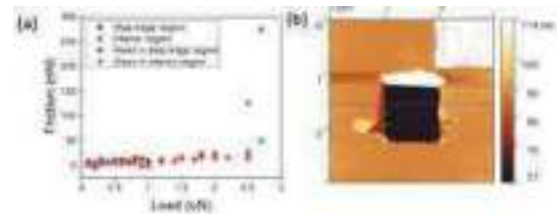
Figure 2(a) Friction data at various load in step edge and interior regions (b) AFM topography of the wear at interior region (wear profile shown in inset)
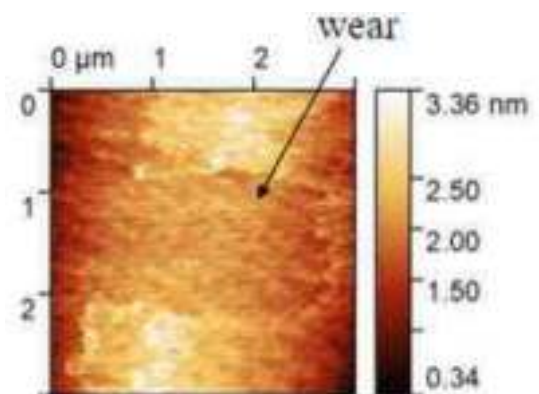
Figure 3. AFM topography of wear at step edge region in PAO4 oil

Conclusions

The interaction of liquid with graphite surface greatly impacts the wear behavior of graphene layers near the surface under different loads which becomes very crucial for small scale tribological applications. The current study investigated that there was no significant effect of surrounding medium on friction behavior of graphene; however, wear resistance of graphene was greatly affected by the lubricating medium. The critical load for wear to occur in the
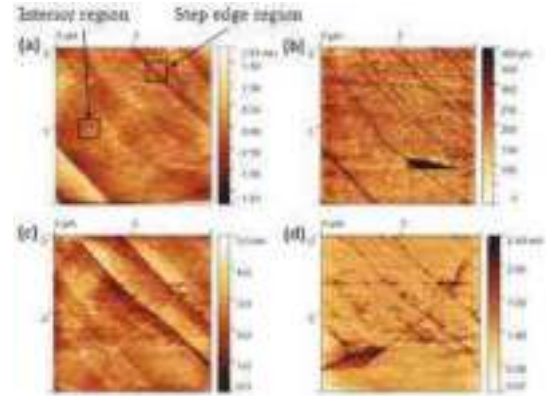
presence of PAO4 oil was about 90% higher than that required in water when step edge regions are considered. Nevertheless, PAO4 oil offered great wear resistance to the graphene layers below 2000 nN of loads. The regions with no steps exhibited excellent wear resistance in PAO4 oil even when the region was scanned at 4000 nN load for about 200 sliding cycles.

References

- Mate CM. Tribology on the Small Scale. Oxford University Press; 2007. https://doi.org/10.1093/acprof:oso/9780198526780.001.0001.
- Lee C, Wei X, Kysar JW, Hone J. Measurement of the Elastic Properties and Intrinsic Strength of Monolayer Graphene. Science (1979) 2008;321:385–8. https://doi.org/10.1126/science.1157996.
- Lee C, Li Q, Kalb W, Liu X-Z, Berger H, Carpick RW, et al. Frictional Characteristics of Atomically Thin Sheets. Science (1979) 2010;328:76–80. https://doi.org/10.1126/science.1184167.
- Berman D, Erdemir A, Sumant A v. Graphene: a new emerging lubricant. Materials Today 2014;17:31–42. https://doi.org/10.1016/j.mattod.2013.12.003.
- Bhowmick S, Banerji A, Alpas AT. Role of humidity in reducing sliding friction of multilayered graphene. Carbon N Y 2015;87:374–84. https://doi.org/10.1016/j.carbon.2015.01.053.
- Kim K-S, Lee H-J, Lee C, Lee S-K, Jang H, Ahn J-H, et al. Chemical Vapor Deposition-Grown Graphene: The Thinnest Solid Lubricant. ACS Nano 2011;5:5107–14. https://doi.org/10.1021/nn2011865.
- Tocci G, Joly L, Michaelides A. Friction of Water on Graphene and Hexagonal Boron Nitride from Ab Initio Methods: Very Different Slippage Despite Very Similar Interface Structures. Nano Lett 2014;14:6872–7. https://doi.org/10.1021/nl502837d.
- Qi Y, Liu J, Dong Y, Feng X-Q, Li Q. Impacts of environments on nanoscale wear behavior of graphene: Edge passivation vs. substrate pinning. Carbon N Y 2018;139:59–66. https://doi.org/10.1016/j.carbon.2018.06.029.
- Baboukani BS, Pitkar A, Ye Z, Nalam PC. Load-Dependent Friction Hysteresis for Graphitic Surfaces in n-Hexadecane. Adv Mater Interfaces 2022:2201249. https://doi.org/10.1002/admi.202201249.

Study Of Piezo-viscous Polar Lubricated Multirecessed Conical Hybrid Journal Bearing

Arvind K. Rajput[1][*] and Vishal Singh[2]

[1][*]Assistant Professor, Department of Mechanical Engineering, Indian Institute of Technology, Jammu, India
[2]Research Scholar, Department of Mechanical Engineering, Indian Institute of Technology, Jammu, India
*Corresponding author Email: arvind.mechei@gmail.com

Keywords: Conical Journal, FEM, Piezo-viscosity, Couple-stress, Piezo-polar Lubrication

Abstract

Conical bearings offers several advantages over conventional cylindrical journal/thrust bearings such as support to radial and axial loading, compact size. It offers the key advantage of clearance adjustability compared to other bearing configurations. Due to these advantages, conical journal bearings offers versatile, robust and compact operation[1,2]. Moreover, the role of lubricant becomes crucial in the operation of bearing. To modify the rheological behaviour of lubricating oil, different additives are blended with the lubricating oil such as viscosity modifiers, corrosion inhibitors, antioxidants etc. It has been reported that the presence of long chain additive molecules such as Viscosity Index (VI) improver polymers in lubricating oil results in increase of load carrying capacity with reduction in friction coefficient[3–5]. These lubricants can be modelled as polar (couple-stress) fluids.

Additionally, due to high build up pressures, the lubricant within journal bearing clearance undergoes substantial agitations and leads to pressure-viscosity interactions. These interactions severely affects the viscosity of lubricating oil and it becomes essential to consider the pressure-viscosity dependency as piezo-viscous nature of lubricant[6,7].
The present study investigates the effect of piezo-viscous polar lubrication on the performance of multirecessed conical hybrid journal bearing. A modified form of Reynold's equation governing the flow of piezo-viscous polar lubrication within the clearance space of journal bearing is solved by FE analysis. Based on the FE analysis, a MATLAB code is developed to compute the bearing pressure field and its performance characteristics. The computed results indicates a significant enhancement in bearing performance characteristics with piezo-viscous polar lubricant.

Introduction

With a rapid growth on industrial development, there is need of robust, reliable and compact design of bearing system. While supporting the external loads in two different directions simultaneously (radial and axial), conical journal bearings fulfills the need of compact design. Moreover, it provides the advantage of clearance adjustability during assembly. That's why the researchers focused their valuable attentions in the domain of conical journal bearings. In 1974, Stout and Rowe [1] presented the key design parameters of conical hydrostatic journal bearing. Since then a number of studies examined the performance of conical journal bearing in conjunction with the effects of semi-cone angle [2], non-Newtonian lubrication [3], inertia and temperature dependent viscosity [4], wear [5], surface modifications [6], porosity [7] etc.

Moreover, the role of lubrication becomes critical for the improvement of bearing performance. To enhance the performance of the lubricant, various types of additives are blended in base oil. Consequently the nature of oil shifted from Newtonian to non-Newtonian. Literature studies reported that presence of long chain polymer additives in lubricating oil improves the bearing performance characteristics to a significant extent. This type of lubricant can be modeled as a couple-stress lubricant and may be studied using couple-stress theory developed by Stokes [8]. Furthermore, at higher pressures, the lubricant undergoes huge agitations and leads to pressure-viscosity interactions. These pressure-viscosity interactions enhances the effective viscosity of lubricant which can be analyzed as piezo-viscous lubricant. The piezo-viscous lubricant improves bearing performance characteristics to minor extent [6,9,10]. However, it must be considered for the accurate prediction of bearing performance characteristics.

Additionally, at high pressure conditions, the couple-stress lubricant may exhibit pressure dependent viscosity which can be idealized as piezo-viscous polar lubricant. Both piezo-viscosity and couple-stresses improves bearing performance characteristics simultaneously. It becomes needful to consider the combined effects of piezo-viscosity and couples-stresses as the piezo-viscous nature affects the polar nature of the lubricant. A very few studies investigated the influence of piezo viscous polar lubrication on the performance of journal bearing [11,12]. A rigorous

survey of available literature reveals that no study analyzed the influence of piezo-polar lubrication on the performance of multirecessed conical hybrid journal bearing compensated with CFV restrictor. The results of the study are expected to be beneficial for the research community.

Analysis

Figure 1 depicts a schematic diagram of four pocket conical hybrid journal bearing system. The flow of piezo-polar lubricant in clearance space of conical bearing is governed by the modified Reynold's equation which yields in non-dimensional form as follows:

$$\frac{1}{\beta^2 \sin^2 \gamma} \frac{\partial}{\partial \alpha} \left(\frac{\Psi}{12\bar{\mu}} \frac{\partial \bar{p}}{\partial \alpha} \right) + \frac{1}{\beta} \frac{\partial}{\partial \beta} \left(\frac{\bar{p}\Psi}{12\bar{\mu}} \frac{\partial \bar{p}}{\partial \beta} \right) = \frac{\Omega}{2} \frac{\partial \bar{h}}{\partial \alpha} + \frac{\partial \bar{h}}{\partial \bar{t}}$$

Where, (Ψ) is piezo- polar function

The oil film thickness in a conical journal bearing yields as follows:

$$\bar{h} = \left(1 - \bar{X}_j \cos \alpha - \bar{Z}_j \sin \alpha \right) \cos \gamma + \bar{Y}_j \sin \gamma$$

To determine the unknown pressure field, the fluid film domain is discretized by using four noded quadrilateral isoparametric element. The finite element formulation of equation (1) is obtained by using Galerkin's technique. FEM formulation yields to the following algebraic equation in matrix form:

$$[F]_e [\bar{p}]_e = [\bar{Q}]_e + \bar{\Omega}[\bar{R}_H]_e + \bar{\dot{X}}_j[\bar{R}_{X_j}]_e + \bar{\dot{Z}}_j[\bar{R}_{Z_j}]_e + \bar{\dot{Y}}_j[\bar{R}_{Y_j}]_e$$

Figure 1: Schematic of multirecessed conical hybrid journal bearing system

Performance Characteristics

The radial load carrying capacity of a conical bearing is expressed as:

$$\bar{F}_R = \overline{\int p dA_R} = \int_{-\lambda}^{\lambda} \int_{0}^{2\pi} \bar{p} \cos \gamma d\alpha d\beta$$

It can be further resolved in X and Z directions as follows:

$$\bar{F}_x = \int_{-\lambda}^{\lambda} \int_{0}^{2\pi} \bar{p} \cos \alpha \cos \gamma d\alpha d\beta \quad ; \quad \bar{F}_z = \int_{-\lambda}^{\lambda} \int_{0}^{2\pi} \bar{p} \sin \alpha \cos \gamma d\alpha d\beta$$

Also, the axial load carrying capacity can be computed as:

$$\bar{F}_y = \overline{\int p dA_y} = \int_{-\lambda}^{\lambda} \int_{0}^{2\pi} \bar{p} \sin \gamma d\alpha d\beta$$

Where , area components in axial direction and radial direction respectively.
The oil film stiffness and damping coefficients are expressed as:

$$\bar{S}_{ij} = -\frac{\partial \bar{F}_i}{\partial \bar{q}_j}; \qquad (6) \qquad \bar{C}_{ij} = -\frac{\partial \bar{F}_i}{\partial \dot{\bar{q}}_j};$$

Where, $\bar{F}_i$ = Generalised force $(i = x, z, y)$

$\bar{q}_j = \bar{X}_j, \bar{Z}_j, \bar{Y}_j$ (Journal centre displacement)

$\dot{\bar{q}}_j = \dot{\bar{X}}_j, \dot{\bar{Z}}_j, \dot{\bar{Y}}_j$ (Journal centre velocity)

Validation Of The Fe Model

Based on the FE analysis, a MATLAB program is developed for the computation of bearing performance characteristics of multirecessed conical hybrid journal bearing. For the validation of developed MATLAB program, the computed results are compared with published literature results. Figure 2 clearly shows a good agreement in between present and published results and indicates the authenticity of the developed model.

Results And Discussion

To simulate the realistic performance of the bearing system, a judicious selection of the geometric and operating parameters of multirecessed conical hybrid journal bearing is made. The
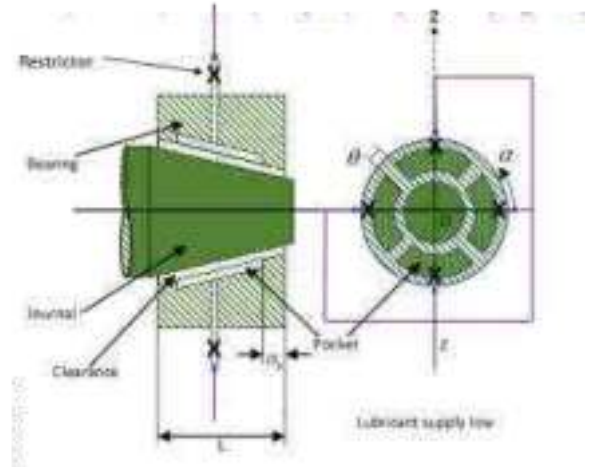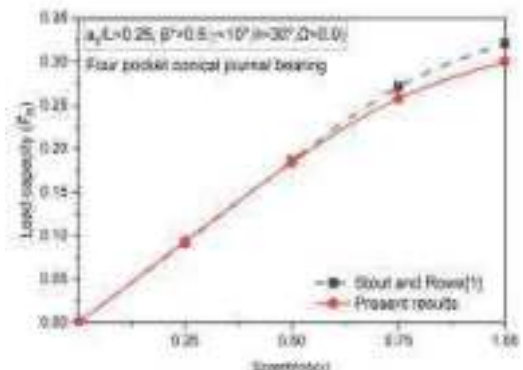

Figure 2: Variation of load capacity ($\bar{F}_0$) versus eccentricity (e) for validation of multirecessed conical hybrid bearing system

characteristics parameters of the bearing system are plotted against the variation of external load ($_0W$). The variation of $_{max}p$ versus is depicted in the Figure 3. It may be observed that the value of increases with an increase in .

For semi-cone angle (γ) =$_{oo}$10/20, there is a significant hike in the value of $_{max}p$ in the order of (7.12-8.10)/(8.82-10.03)%, (28.27-40.42)/(32.99-44.63)% and (37.63-52.25)/(45.32-59.87)% for piezo-viscous, couple stress and piezo-viscous-polar lubricant respectively vis-à-vis Newtonian lubricant. Furthermore, the bearing with higher semi-cone angle () =$_o$20 results in a substantial hike in the value of in the order of 11.50-16.26%, 12.88-17.73%, 14.64-18.70% and 16.18-20.25% for Newtonian, for piezo-viscous, couple stress and piezo-viscous-polar lubricant respectively vis-à-vis bearing with semi-cone angle (γ) =$_o$10. The rise in for piezo-polar lubricant may be attributed to the combined effects of pressure dependent viscosity and polar nature of lubricant.

Figure 3: Variation of $_{max}p$ versus $_0W$

Conclusions

The study investigates the influence of piezo-polar lubrication and semi-cone angle on the performance of multirecessed conical hybrid bearing system compensated with CFV restrictor. The numerically simulated results indicate that the piezo-viscous polar lubricant offers a significant rise in the performance of the conical journal bearing in terms of characteristics parameters $_{max}p$, $_{min}h$, $_{ij}S$ and $_{ij}C$ etc. It may be due to combined effects of pressure dependent viscosity and polar nature of lubricant. Further higher semi-cone angle results in higher value of, and.
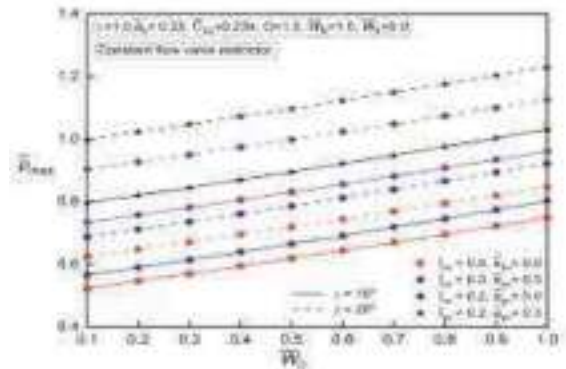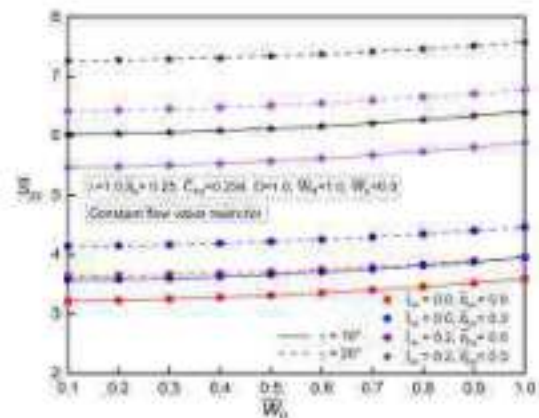

Figure 4: Variation of $_{zz}S$ versus $_0W$

References

○ Stout KJ, Rowe WB. Externally pressurized bearings — design for manufacture Part 1 — journal bearing selection. Tribology. 1974;7:98–106.

○ Srinivasan K, Prabhu BS. Steady state characteristics of conical hybrid bearings. Wear. 1983;89:57–67.

○ Kumar D, Chandra P, Sinha P. Ferrofluid lubrication of externally pressurized circular plates and conical bearings. Int J Eng Sci. 1993;31:593–604.

○ Chandra P, Sinha P, Saxena S. Effect of lubricant inertia in externally pressurized conical bearings with temperature dependent viscosity. Acta Mech. 1994;106:157–71.

○ Sharma SC, Phalle VM, Jain SC. Performance analysis of a multirecess capillary compensated conical hydrostatic journal bearing. Tribol Int. 2011;44:617–26.

○ Kumar A, Sharma SC. Optimal Parameters of Grooved Conical Hybrid Journal Bearing With Shear Thinning and Piezo-viscous Lubricant Behavior. J Tribol [Internet]. 2019 [cited 2022 Mar 9];141. Available from: https://doi.org/10.1115/1.4043507

○ Singh A, Sharma SC. Behaviour of conical porous hybrid journal bearing operated with MHD lubricant considering influence of surface irregularities. Tribol Int. 2022;174:107730.

○ Stokes VK. Couple Stresses in Fluids. Phys Fluids. American Institute of Physics; 1966;9:1709–15.

○ Jain SC, Sinhasan R. Performance of flexible shell journal bearings with variable viscosity lubricants. Tribol Int. 1983;16:331–9.

○ Chandrawat HN, Sinhasan R. A study of a two-lobe journal bearing considering elastohydrodynamic effects. Wear. 1988;127:161–77.

○ Jaya Chandra Reddy G, Eswara Reddy C, Rama Krishna Prasad K. Effect of viscosity variation on the squeeze film performance of a narrow hydrodynamic journal bearing operating with couple stress fluids. Proc Inst Mech Eng Part J J Eng Tribol. IMECHE; 2008;222:141–50.

○ Lahmar M, Bou-Saïd B. Nonlinear Dynamic Response of an Unbalanced Flexible Rotor Supported by Elastic Bearings Lubricated with Piezo-Viscous Polar Fluids. Lubricants. Multidisciplinary Digital Publishing Institute; 2015;3:281–310.

On The Superior Wear Resistance and Adhesion Strength of Compositonally Modulated Ni-W Multilayer Coatings

Lavakumar Bathini[1,2*], M.J.N.V Prasad[2] and Nitin P Wasekar[1]

[1]International Advanced Research Centre for Powder Metallurgy and New Materials (ARCI), India
[2]Depatment of Metallurgical Engineering and Materials Science, India
*Corresponding author Email: lavakumarbathini@gmail.com

Keywords: Tribology, Microstructure, Electrodeposition, Gradient

Abstract

Electrodeposited Ni-W alloy coatings have been recognized as the potential replacements for the conventional hard chrome coatings [1]. However, presence of tensile residual stresses in the Ni-W coatings generated during the electrodeposition has restricted their industrial deployment [2]. As a result, the electrodeposited nanocrystalline Ni-W coatings often suffer from cracking and delamination during the tribological loading. Furthermore, the presence of a sharp microstructural gradient at the substrate-coating interface leads to poor adhesion owing to the strain incompatibility and often results in brittle failure under bending [3]. In the present study, a facile approach of compositionally modulated multilayers has been adapted to circumvent the aforementioned problems. The Ni-W multilayer coatings with alternative soft (~2.6 GPa) and hard (~8.5 GPa) layers have been developed with layer thickness spanning from 2500 nm to 50 nm. The microstructure and therefore the hardness of individual layers are tailored by tuning the W-content. The deposited Ni-W multilayers have demonstrated substantially lower residual stresses compared with their homogeneous counterpart while retaining the high hardness. The optimized multilayer coatings have shown superior wear resistance and adhesion strength. The improved adhesion and tribological properties are rationalized through strain delocalization and enhanced thermal properties of multilayer coatings.

Introduction

Experimental Details

Owing to the mild grain boundary segregating nature of W in Ni during electrodeposition, the grain size of the Ni-W coatings can be tailored by tuning the W-content [6]. In the present study, the W-content is tuned by applying the short intermediate anodic pulses. Since the W is relatively active element, the intermediate anodic pulses strip the W from the deposited coating. The pulse parameters for depositing the high-W (~ 15 at%) and low-W (~ 1 at%) coatings have been optimized by systematic study. Using the programmable recipe feature in the DPR-20-50-200 pulse power generator (Dynatronix, USA), multilayer coatings with alternate layers of high and low-W content were deposited by switching between the predefined parameters. The tribological behavior of the developed multilayers coatings is evaluated and compared with their homogeneous counterparts using the ball-on-disc configuration in accordance with the ASTM-G99 standard. Furthermore, using the three-point bend test, the adhesion strength of the multilayers coatings is evaluated.

Results & Discussion

The multilayer coatings with varying layer thickness (λ) ranging from 2.5 to 0.05 μm were deposited by adjusting the recipe duration. The cross-sectional SEM image in backscattered electron (BSE) mode for the Ni-W multilayer coating with λ ~2 μm is shown Figure.1 (left hand side). The bright layer is high-W layer while the dark layer is of low-W content. The cross sectional EBSD analysis of the multilayer coatings is shown in right side of Figure. 1. As expected, the compositional modulation across the layers has resulted in the concurrent microstructural modulation (coarse and fine grain size for low-W and high-W layers, respectively). Hardness of multilayer coatings has increased with decrease in the layer thickness demonstrating the Hall-Petch type of behavior. Furthermore, the multilayer coatings have demonstrated substantially lower residual stresses compared to the homogeneous hard Ni-W coating. Figure. 2 shows the wear rate and coefficient of friction (inset) of homogeneous and multilayer coatings. The Ni-W multilayer coating with λ ~0.1 μm (indicated as ML0.1) has shown superior wear resistance and lower friction coefficient compared to the homogeneous counterparts. Presence of tensile residual stresses exaggerates the severity of contact stresses during the sliding and leads to sub-surface cracking and delamination. Higher hardness and lower residual stresses of the multilayer coating have led to its superior wear performance. It is well known that the toughness along with the strength play an important role in improving the wear resistance of the coatings. A mere improvement in the hardness renders the brittleness and consequent failure of the coatings at higher loads. Since, the multilayers are composed of alternate hard and soft Ni-W layers, we expect the toughness of these multilayers to be higher than the homogeneous hard Ni-W coating which might have assisted in the improvement of tribological properties.

The post-mortem analysis of the wear tracks and corresponding debris revealed the supporting evidences for the above claims and depicted the plausible failure modes during the sliding wear. The wear track of homogeneous Ni-15W coating has depicted the cracks probably originating due to the residual tensile stresses present in the coating. While, the Ni-W multilayer coating has shown smooth and crack-free wear track.

Furthermore, we have observed a relatively higher oxidation on the wear tracks of homogeneous coatings compared to the multilayers. During the sliding contact, almost all the frictional energy is believed to convert into heat. This heat, except at very low speeds, leads to an appreciable temperature raise. Despite their pivotal role, thermal properties of materials are often overlooked in explaining the tribological behavior. To understand the frictional heating behavior of the Ni-W coatings, the electrical resistivity of the coatings was measured using the four-probe technique. Later, by applying the Wiedemann-Franz law, the electrical resistivity is converted to the thermal conductivity and thermal diffusivity. A thorough analysis has revealed that the thermal diffusivity of the multilayer coatings is superior compared to the hard homogeneous Ni-W therefore less severe wear track oxidation.
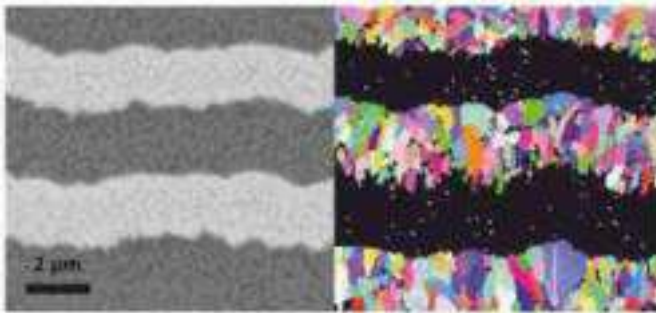

Figure 1: The SEM back scattered electron (BSE) image of Ni-W multilayer coating (right side) along with the EBSD analysis.
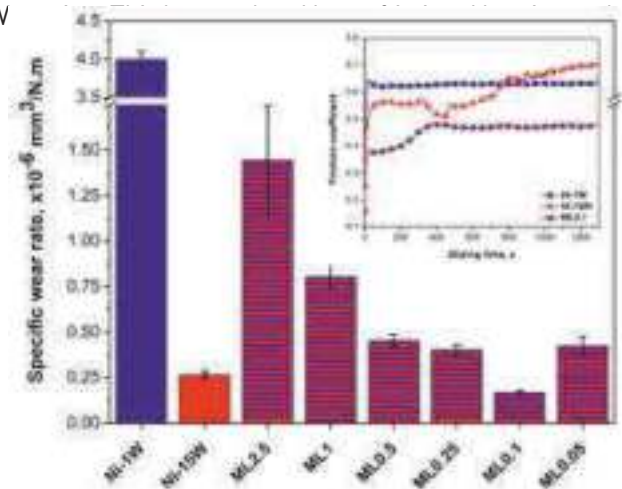

Figure 1: Siding wear performance comparison of homogeneous and multilayer coatings. Inset shows the friction coefficient comparison.

Conclusions

In conclusion, by exploiting the advantage of reverse/anodic pulsed current, Ni-W multilayer coatings comprised of alternate soft and hard Ni-W layers with layer thickness (λ) ranging from ~2.5 μm to 0.05 μm have been deposited from a single electrodeposition bath. The multilayer coatings have shown a substantial reduction in the residual stresses. The multilayering architecture has allowed to deposit hard coatings with lower residual stresses. Despite the similar hardness, Ni-W multilayer coating (λ ~0.1 μm) has demonstrated superior wear resistance compared to the homogeneous Ni-W coating containing higher amounts of W (15 at%). The enhanced wear resistance of multilayer coating is attributed to both lower residual stresses and relatively higher thermal diffusivity. The multilayer coating has shown lower friction coefficient due to the presence of thin adherent oxide film.

References
- ⭕ N.P. Wasekar, G. Sundararajan / Wear 342-343 (2015) 340–348
- ⭕ T.D. Ziebell, C.A. Schuh / Journal of Materials Research, (2012), 1271-1284, 27(9)
- ⭕ Y. Lin et al. / Materials Science & Engineering A 844 (2022) 143170
- ⭕ E. Ma and T. Zhu / Materials Today (2017), 323-331, 20(6)
- ⭕ L Bathini et al. / Surface & Coatings Technology 445 (2022) 128728
- ⭕ A.J. Detor, C.A. Schuh / Acta Materialia 55 (2007) 371–379

Influence of Processing Condition and Post-spray Heat Treatment on The Tribological Performance of High Velocity Air-fuel Sprayed Cr3c2-25nicr Coatings

Rahul Jude Alroy1,2, Kamaraj2, G. Sivakumar1*

1Centre for Engineered Coatings, International Advanced Research Centre for Powder Metallurgy and New Materials (ARCI), Hyderabad - 500 005, Telangana, India
2Department of Metallurgical and Materials Engineering, Indian Institute of Technology, Madras-600036, Tamil Nadu, India
*Corresponding author E-mail: gsivakumar@arci.res.in

Abstract

The superior wear performance offered by thermal sprayed Cr3C2-25NiCr coatings enables the usage of such coatings in a wide range of industrial applications. High-velocity thermal spraying with an optimal combination of feedstock particle size and combustion mode would commonly deposit a dense Cr3C2-25NiCr coating microstructure with improved adhesion and fewer phase degradation, thus offering better wear resistance. The post-heat treatment of as-deposit coatings initiates the precipitation of small-sized carbides and splat-splat sintering, resulting in improved wear performance. Therefore the choice of feedstock particle size, combustion mode and post-heat treatment conditions significantly influence the coating microstructure, properties and, consequently, the wear performance. The study comprehensively compares the sliding wear behavior (ball-on-disc) of high velocity air-fuel (HVAF) and oxygen augmented air-fuel (HVAF(O)) sprayed fine and coarse Cr3C2-25NiCr coatings through as-deposited coating microstructure, phases present and mechanical properties. Additionally, a post-heat treatment of as-deposited coatings was performed to improve the wear performance prior to the wear testing. The effect of particle size, combustion mode and post-heat treatment on sliding wear behavior of Cr3C2-25NiCr coating were comprehensively investigated through post-wear analysis. The study effectively consolidates an optimal combination of processing and post-heat treatment condition for improved wear performance of HVAF sprayed Cr3C2-25NiCr coatings, which would be highly beneficial to industries.

Introduction

Thermal spraying of Cr3C2-NiCr on industrial parts could mitigate erosion-corrosion wear and extend component lifetime [1,2]. As a result, thermal sprayed Cr3C2-NiCr could be used in a wide range of industrial applications where wear and corrosion coexist. A high-velocity thermal spray process deposits a denser Cr3C2-NiCr coating with superior properties, effectively mitigating wear or corrosion-related degradation [3].

Cr3C2-NiCr coatings contain many metastable and supersaturated phases despite being sprayed at high velocity [4]. The post-heat treatment of thermal sprayed Cr3C2-NiCr assisted the supersaturated or metastable phase in growing towards equilibrium, resulting in variation in microstructural features, coating properties, and performance [5]. In this study, fine and coarse Cr3C2-NiCr particles were sprayed through HVAF and HVAF(O) modes. Our previous study [6] evaluated the structure-property correlation of these coatings for improved erosion resistance. In this study, these coating specimens were taken for heat treatment studies and the variation in microstructural features, phases and mechanical properties were studied through ball-on-disc wear testing.

Experimental Details

Sample code	Spraying mode	Powder Comp.	Particle size (µm)	Carbide grain Size µm	Heat treatment
CCL.1	HVAF		10-30	5	—
CCL.2	HVAF(O)			5	—
CCH.1	HVAF		15-45	5	—
CCH.2	HVAF	Cr3C2-NiCr		5	—
HTL.1	HVAF		10-30	5	At 800°C, inert condition for 1 hour
HTL.2	HVAF(O)			5	
HTH.1	HVAF		15-45	5	
HTH.2	HVAF			5	

Table 1: Summary of specimen coding, spraying mode, powder details and heat treatment used for the study

HVAF spraying was done through a kermetico C7 spray gun. A grit-blasted SS 304 10 x 10 x 4 cm test coupon was selected for coating deposition and further analysis. The post-heat treatment of specimens was done in a tubular furnace at 800ºC for 1hr.

The microstructural features of powder, as-sprayed, heat-treated coating and worn-out coating surfaces were analyzed by FE-SEM (make: Zeiss Gemini). All the specimens were mounted, sectioned and polished to an acceptable level before SEM analysis.

Ball-on-disc (ASTM G99) wear test was performed using an MFT-5000, R-tech universal tribometer. Alumina ball was used as the counterpart, with a load of 40N, wear track of Φ6mm and a relative sliding speed of 0.2 m/s.

Results & Discussion

Agglomerated and sintered Cr3C2-NiCr with two different particle size ranges (10-30 & 15-45) were sprayed through HVAF and HVAF(O). The detailed microstructure and phase analysis of the coating was evaluated in the previous studies [6]. As-sprayed coatings were taken to heat treatment, which initiated the precipitation of carbide-binder interacted regions in as-sprayed coatings. The as-sprayed and heat-treated cross-sectional microstructure of Cr3C2-NiCr coatings are shown in Fig. (1) and (2). CCL.1 coatings exhibited a uniform distribution of carbides around the binder phase (see Fig. 1(a)), whereas CCL.2 showed mid-grey contrast carbide-binder interacted regions (see Fig. 1(c).

The varied combination of particle size-combustion mode attributed to such distinct as-deposited coating microstructure (blue arrows indicated carbide-binder interacted regions and black arrows indicated porosity). The heat treatment induced precipitation of small-sized carbides, as shown in Fig. 1 (b), (d), Fig. 2 (b) and (d). The availability of carbide-binder interacted regions in as-sprayed coatings governed the precipitation. As a result, a uniform distribution of precipitates was identified in CCL.2 but not in other conditions (precipitate-free regions are shown in red arrows).
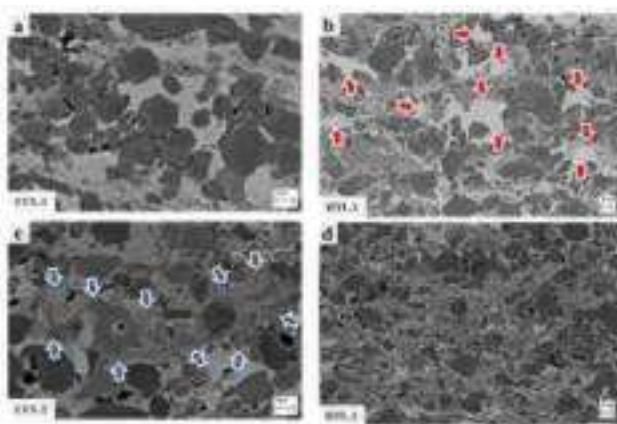

Fig. 1: Cross-sectional SEM image of as-sprayed (a, c) and heat-treated (b, d) CCL.1 and CCL.2 coatings
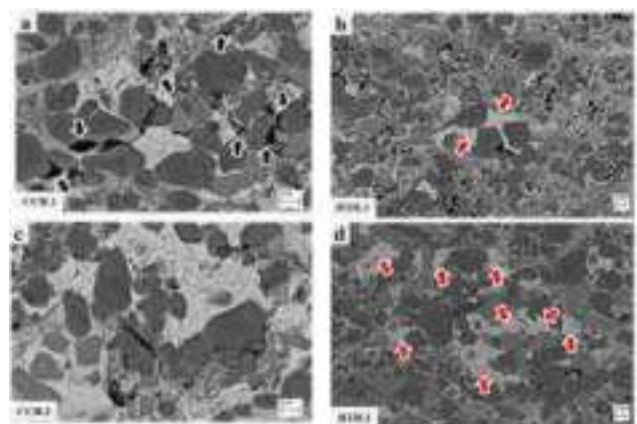
Fig. 2: Cross-sectional SEM image of as-sprayed (a, c) and heat-treated (b, d) CCH.1 and CCH.2 coatings

The friction coefficient (COF) vs. sliding distance for as-deposited and heat-treated coatings are shown in Fig. 3. Interestingly, the COF values varied for coatings with different processing conditions and heat treatment. CCL.2 and CCH.1 displayed the highest COF compared to the CCL.1 and CCH.2 coatings. The heat-treated coatings displayed lower COF than their respective as-deposited coatings. The specific wear rate for each condition was formulated based on the volume of material removed and shown as a comparison graph in Fig.4. The wear rate followed the trend of COF. As a result, the highest wear rate was displayed by CCH.1, followed by CCL.2, CCL.1 and CCH.2. Overall, heat treatment improved the wear performance of Cr3C2-NiCr coatings. Microstructural evaluation of worn-out specimens was done to decipher the wear mechanism associated with each condition, as shown in Fig. (5) and (6).
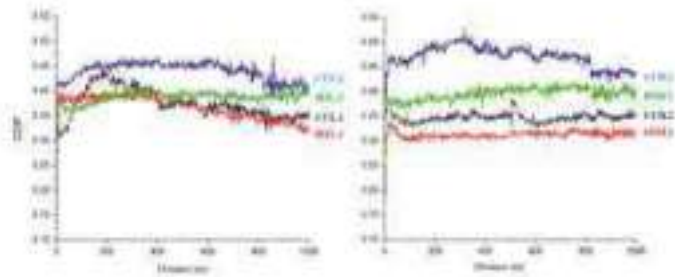
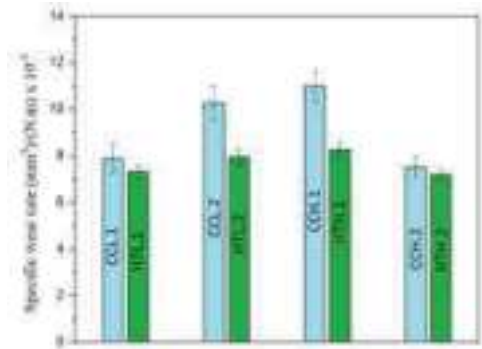*Figure 3: Summary of COF vs. sliding distance for all the specimens*

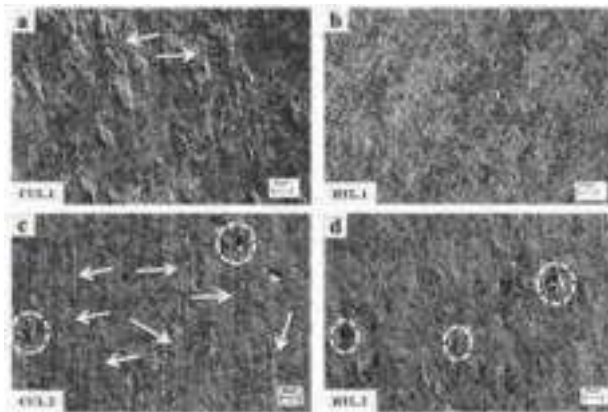*Figure 4: Summary of specific wear rate for all the specimens*

Figure 5: Wear track SEM image of as-deposited (a, c) and heat-treated (b, d) CCL.1 and CCL.2 coatings (arrows indicates abrasive grooves and circle indicates pull-outs)

Fig. 6: Wear track SEM image of as-deposited (a, c) and heat-treated (b, d) CCL.1 and CCL.2 coatings (arrows indicates abrasive grooves and circle indicates pull-outs)
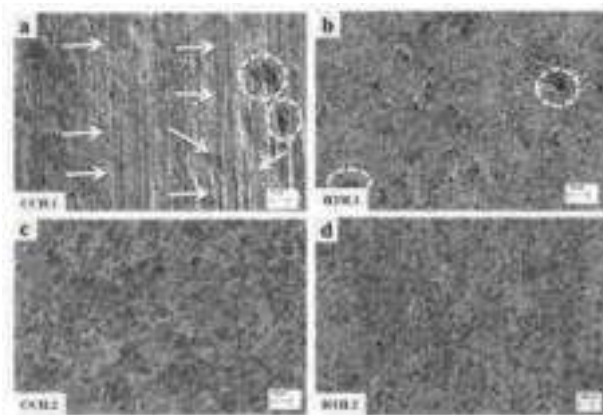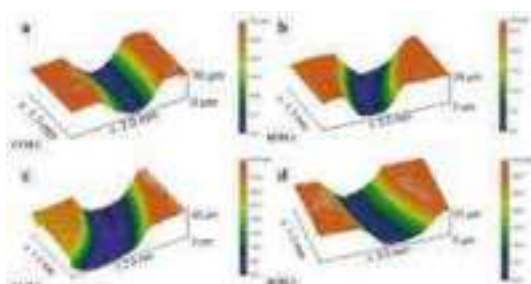

Figure 7: 3-D topography of as-deposited (a, c) and heat-treated (b, d) CCH.1 and CCH.2 coatings

s inferred from Fig. 5 (c) and (d), many abrasive grooves and pull-outs were identified on CCL.2 and HTL.2 worn-out surfaces. Besides, CCL.1 displayed only a few impressions of abrasive grooves and instances of carbide pull-out were not identified. The higher heat flux offered in CCL.2 resulted in a higher degree of carbide melting, interaction with the binder phase and supersaturation of the binder phase. Supersaturated regions lower the impact strength of coatings and inter-splat adhesion. Under sliding wear, such weak zones detach quickly and initiate three-body abrasion, which augments the COF and wear rate of the CCL.2 coatings. The proper choice of particle size-combustion mode ensured deposition of CCL.1 coatings with improved adhesion. As a result, carbide pull-outs were not identified (see Fig. 1(a)) under sliding wear, which reduced the COF and wear rate of CCL.1 coatings. Heat treatment improved the splat-splat bonding of coating and the overall hardness through small-sized carbide precipitation. Both contributed to lowering the COF and wear rate of heat-treated coatings.

The wear track of CCH.1 (see Fig. 6(a)) exhibited a significant number of abrasive grooves and carbide pull-out impressions, which corroborated the higher COF and wear rate values displayed by the coatings. On the other side, abrasive grooves were not identified on the wear track of CCH.2 (see Fig. 6(c)), which exhibited the lowest COF and wear rate among all other coatings. The improved intersplat adhesion and lower porosity of CCH.2 are attributed to the superior wear performance. In CCH.1, the particles were not subjected to a sufficient degree of heating and acceleration, resulting in poor adhesion and higher porosity. Upon heat treatment of CCH.1 coatings, a significant improvement in wear resistance were identified (see graph in Fig. 4), which is associated with the improvement in splat-splat adhesion.

3-D profiles of the wear track of the as-deposited and heat-treated CCH.1 and CCH.2 coatings are shown in Fig. 7. As inferred, CCH.1 exhibited a wear track width and depth of 1284 μm and 42 μm, respectively, which was in agreement with the augmented COF and wear rate values shown by the CCH.1 coatings. The best-

performing CCH.2 coatings displayed a track width and depth of $1019 \mu m$ and $28 \mu m$, respectively. Heat treatment lowered the wear track depth and width, corroborating the improved wear performance offered by heat-treated coatings. The improved adhesion and hardness of coatings offered by heat treatment resulted in a better counter surface against high-load sliding wear.

Conclusions

The sliding wear behavior of as-deposited and heat-treated Cr3C2-NiCr coatings was evaluated to emphasize the role of HVAF processing conditions and secondary heat treatment in the wear performance of coatings. The significant findings drawn from the study can be summarized as

- The correct choice of powder particle size-combustion mode deposits coating with preferable microstructure, resulting in superior wear performance.
- Under sliding wear, coatings with improved splat adhesion offer lower COF, wear rate and, thereby, excellent wear performance
- Heat-treatment induced small-sized carbide precipitation and splat-splat sintering improves the wear resistance of Cr3C2-NiCr coatings

References

- O. Berghaus, The 2016 Thermal Spray Roadmap, 25 (2016) 1376–1440. https://doi.org/10.1007/s11666-016-0473-x.
- L.M. Berger, Application of hardmetals as thermal spray coatings, Int. J. Refract. Met. Hard Mater. 49 (2015) 350–364. https://doi.org/10.1016/j.ijrmhm.2014.09.029.
- P. Vuoristo, Thermal Spray Coating Processes, Elsevier, 2014. https://doi.org/10.1016/B978-0-08-096532-1.00407-6.
- V. Matikainen, G. Bolelli, H. Koivuluoto, M. Honkanen, M. Vippola, L. Lusvarghi, P. Vuoristo, A Study of Cr3C2-Based HVOF- and HVAF-Sprayed Coatings: Microstructure and Carbide Retention, J. Therm. Spray Technol. 26 (2017) 1239–1256. https://doi.org/10.1007/s11666-017-0578-x.
- C. Lorenzana, J. Delgado, J. Sanchez, Role of heat treatments in the improvement of the sliding wear properties of Cr 3 C 2 – NiCr coatings, 157 (2002) 207–213.
- R. Jude, M. Kamaraj, G. Sivakumar, HVAF vs oxygenated HVAF spraying: Fundamental understanding to optimize Cr 3 C 2 -NiCr coatings for elevated temperature erosion resistant applications, J. Mater. Process. Tech. 309 (2022) 117735. https://doi.org/10.1016/j.jmatprotec.2022.117735.

Investigation of tribological behavior on additively manufactured bone plate polished through Hybrid-Electrochemical Magnetorheological (H-ECMR) finishing process

Atul Singh Rajput, Manas Das, and Sajan Kapil

Department of Mechanical Engineering, Indian Institue of Technology Guwahati, India
Corresponding author Email: manasdas@iitg.ac.in

Abstract

Additive Manufacturing (AM) or 3D printing provides the benefits of individualizing the implant per patient requirements. However, the major limitation associated with additively manufactured implants is poor surface quality. Hence, Hybrid-Electrochemical Magnetorheological (H-ECMR) polishing is an advanced surface finishing process that utilizes the rheological properties of the Magnetorheological (MR) fluid to enhance the surface quality of the workpiece without hampering its surface topography. Bone plates are essential for providing mechanical support during the healing of bone fractures by adapting to the biochemical environment. Bone plates are fabricated through Selective Laser Melting (SLM), and their surface quality is further enhanced through the MFAF process. Pin-on-Disc (PoD) study is performed on the polished surface of the bone plate to analyze its wear resistance. The surface topography of the bone plate is analyzed through Scanning Electron Microscope (SEM) before and after finishing, and a uniform surface is achieved on the polished surface. Apart from the average surface roughness (Ra), other roughness parameters like skewness (Rsk) and kurtosis (Rku) are also analyzed to study the characteristics of surface irregularities on the polished surface.

Introduction

Hybrid-Electrochemical Magnetorheological (H-ECMR) polishing is an advanced finishing process developed to improve the surface quality of additively manufactured biomedical implants to improve their functionality. The developed process combines the synergic action of the electrochemical reaction and mechanical abrasion to produce a uniform surface roughness value in the range of a few nanometers. The bone plate is used as the support material during the healing of broken bones. Additive Manufacturing (AM) or 3D printing provides the benefits of individualizing the implant per patient requirements [1]. Selective Laser Melting (SLM) is a layer-by-layer manufacturing method that uses laser to melt down the powder to fabricate the final product [2]. However, the surface quality of the Selective laser-printed bone plates is very poor, requiring a post-processing method to improve its surface quality [3]. In the present study, the H-ECMR finishing operation is bone plate fabricated with selective laser melting. Different surface roughness parameters, including average surface roughness (Ra), skewness (Rsk), and kurtosis (Rku), are analyzed on the surface of the bone plate with the assistance of the optical profilometer.

Experimental Details

The selective laser melting fabricates the bone plate made of SS316L. Furthermore, the bone plate is fixed in the bed of the 5-axis computer numerical controlled milling machine. The indigenously developed electromagnet-based polishing tool is retrofitted with the 5-axis CNC milling machine to enable surface finishing operation, as shown in Fig. 1. The electromagnet-based polishing tool is developed to provide a magnetic field to stiffen the MR fluid during the surface finishing operation, which is further used as the polishing media.
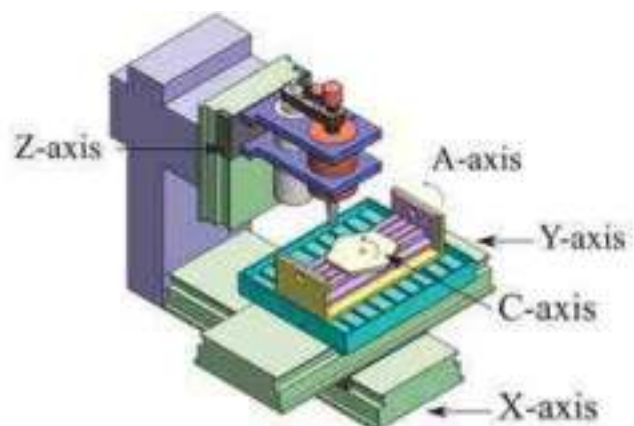

Figure 1: Computer-aided model of the developed Hybrid Electrochemical Magnetorheological (H-ECMR) finishing process

The different constituents of the MR fluid during the polishing are Carbonyl Iron particles (CIPs), diamond, magnesium chloride, ethylene glycol, distilled water, and glycerol in the volume ratio of 0.4, 0.07, 0.16, 0.06, 0.22, and 0.08 respectively [4]. However, the milling operation is performed on the SLM fabricated bone plate before the H-ECMR finishing process to reduce the workpiece's average surface roughness in the sub-micron range. It is due to the reason that the H-ECMR finishing process only works when the initial surface roughness value is less than 1 micrometer. Furthermore, the dry pin-on-disc experiment is performed on bone plates before and after the polishing to evaluate the change in the wear resistance of the biomaterial [5].

Results & Discussion

The H-ECMR finishing process is performed on the selective laser melted workpiece to improve its surface quality. The initial value of the average surface roughness (Ra) is 8.96 μm, as shown in Fig. 2(a). The average surface roughness value (Ra) is reduced to 0.96 μm after the milling operation, as shown in Fig. 2(b). Moreover, after performing the H-ECMR finishing process, a mirror-like polished surface is achieved on the bone plate with the value of average surface roughness (Ra) in the range of nanometers (i.e., 36 nm). The value of skewness (Rsk) and kurtosis (Rku) on the polished are -1.2 and 2.36, respectively, representing the flat with a lower number than the valleys on the polished surface. However, the skewness and kurtosis values on the SLM fabricated part is 3.6 and 6.3, respectively, representing that the pointed peaks with a higher number than the valleys are produced on the surface fabricated through SLM. The negative skewness and kurtosis value less than 3 have lower chances of wear out of the surface during their tribological contact.
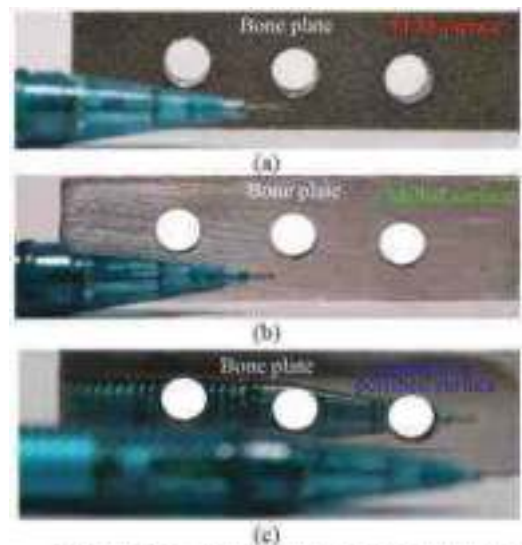

Figure 2: Bone plate surface (a) before milling, (b) after milling, and (c) after polishing

The H-ECMR finishing process utilizes the rheological characteristics of the Magnetorheological (MR) fluid to enhance the surface quality of the workpiece. The external magnetic field helps to indent the abrasive particle into the workpiece. Moreover, the polishing tool's feed and rotational motion help remove the indented material from the workpiece. The combined force action helps reduce surface irregularities and produces a mirror-like polished surface.

The dry pin-on-disc experiment performs the wear test on all three surfaces. Herein the pin is made of the SS316L, and the disc is made of Ultra High Molecular Weight Polyethylene (UHMWPE). The interacting surface of the pin with the disc is milled, followed by the H-ECMRF finishing process. The wear rate was observed for the SLM fabricated surface and milled surface. Polished surfaces are $9.86 \times 10-5$ mm3/min, $1.06 \times 10-5$ mm3/min, and $0.471.06 \times 10-5$ mm3/min, respectively, as shown in Fig. 3. The surface roughness in the range of the nanometer after the H-ECMRF finishing process is the primal reason for the significant reduction in the wear rate of the polished surface. Furthermore, the improved value of the kurtosis and skewness also suggest the same trends for the wear rate of the biomaterial.
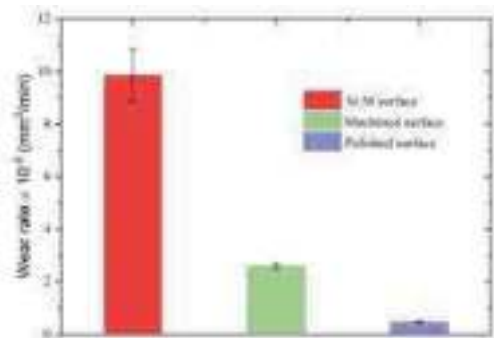
Figure 3: Wear rate on the SLM fabricated surface, milled surface, and polished surface

Conclusions

The current work focuses on the surface enhancement of the bone plate made of SS316L fabricated with Selective Laser Melting (SLM) assistance. The Hybrid-Electrochemical Magnetorheological (H-ECMR) finishing process enhances the bone plate's surface quality and improves functionality. The key finding of the present work is summarized below.

- The H-ECMR finishing process can produce uniform mirror-liked polished surfaces on the biomaterial.
- The average surface roughness (Ra) value on the SLM fabricated surface, milled surface, and polished surface is 8.96 μm, 0.96 μm, and 36 nm, respectively.
- The value of skewness (Rsk) and kurtosis (Rku) on the polished are -1.2 and 2.36, respectively, representing the

flat with a lower number than the valleys on the polished surface.

◯ The wear rate observed for the SLM fabricated surface, milled surface, and polished surfaces are 9.86×10-5 mm3/min, 1.06×10-5 mm3/min, and 0.471.06×10-5 mm3/min.

References

◯ L. Ostrovska et al., "Biological evaluation of ultra-fine titanium with improved mechanical strength for dental implant engineering," J. Mater. Sci., vol. 51, no. 6, pp. 3097–3110, 2016, doi: 10.1007/s10853-015-9619-3.

◯ W. W. Wits, S. Carmignato, F. Zanini, and T. H. J. Vaneker, "Porosity testing methods for the quality assessment of selective laser melted parts," CIRP Ann., vol. 65, no. 1, pp. 201–204, Jan. 2016, doi: 10.1016/J.CIRP.2016.04.054.

◯ I. Yadroitsev, P. Bertrand, and I. Smurov, "Parametric analysis of the selective laser melting process," Appl. Surf. Sci., vol. 253, no. 19, pp. 8064–8069, Jul. 2007, doi: 10.1016/J.APSUSC.2007.02.088.

◯ A. S. Rajput, M. Das, and S. Kapil, "Investigations on a hybrid chemo-magnetorheological finishing process for freeform surface quality enhancement," J. Manuf. Process., vol. 81, pp. 522–536, Sep. 2022, doi: 10.1016/J.JMAPRO.2022.07.015.

◯ A. S. Rajput, M. Das, and S. Kapil, "Characterization of wear resistance and corrosion during magnetorheological fluid assisted finishing (MFAF) of Ti-6Al-4V and duplex stainless steel for enhanced biocompatibility:," https://doi.org/10.1177/09544089221107990, Jun. 2022, doi: 10.1177/09544089221107990.

Influence of Young's Modulus on The Adhesive Interaction Between an Elastic Body and a Rigid Half-space

Rojin Mathews, T.R. Sreesastha Ram and Jayadeep U.B.
Department of Mechanical Engineering, National Institute of Technology Calicut, Kerala– 673601, India
Email:- rojinmathews89@gmail.com

Keywords: Adhesion, van der Waals force, Finite element method, Body force formulation, Young's modulus

Abstract

We have used the finite element method to analyse the adhesive contact interaction between an elastic object and rigid half-space. The adhesive force is incorporated as a body force, derived from the Lennard-Jones potential. This framework can be used to analyse the adhesive contact between elastic asperity with a semi-infinite rigid body. We have studied the variation of adhesive force with changes in values of Young's modulus. The analysis results match well with the analytical models.

Introduction

Introduction
Adhesion is the attraction between dissimilar molecules and cohesion is the attraction between similar molecules. Hence, adhesion results in an attraction or sticking between solid surfaces or particles, thus necessitating a normal force to separate them [1].

Adhesion between atoms or molecules of solids can be due to various reasons like capillary force, electrostatic force, hydrophobic force etc. Adhesion due to van der Waals (vdW) forces, which has the origin in the electrical dipoles, will always be present between atoms or molecules. Therefore, adhesion due to vdW force has special significance [2].

In the present work, numerical simulation is carried out to study the adhesive interaction of elastic asperity with a semi-infinite rigid body, using Abaqus FE software. We have studied the influence of the change in values of Young's modulus on adhesive interactions between a cubic asperity and a rigid half-space. In presence of adhesion, the elastic cube experiences a mechanical instability called jump-to-contact, which is significantly influenced by the variations in Young's modulus.

Computational Modeling
The magnitude of body force due to adhesion at a point in the elastic body near a rigid half-space is a function of the distance between the point and the half-space, while the direction is normal to the surface of the half-space [3]. The interaction force per unit volume at any point in the elastic body can be obtained by integrating the volumetric potential over the half-space and taking the gradient with respect to the distance from the half-space [4].

We can obtain the body force of interactions between two objects by assuming that the Lennard-Jones potential represents the potential of interaction between two atoms in interacting solids:

$$V = -\frac{C}{r^6} + \frac{D}{r^n} \qquad (1)$$

where C and D are material constants, and r is the separation between the interacting atoms. The index 'n' in the repulsive interaction is traditionally chosen as 12 for computational reasons.

The potential of interaction between two volume elements is obtained by adding the potential of interaction between all pairs of constituent atoms (pairwise addition):

$$V_{vol} = \left(-\frac{C}{r^6} + \frac{D}{r^n}\right)\beta_1\beta_2\,d\Omega_1\,d\Omega_2 \qquad (2)$$

where β_1 and β_2 are the number densities of atoms in the interacting volume elements ($d\Omega_1$ and $d\Omega_2$). Taking the gradient of the volumetric potential with the separation, magnitude of the force between two volume elements can be calculated.

$$f_{int} = -\frac{\partial V_{rel}}{\partial r} = \left(-\frac{6C}{r^7} + \frac{nD}{r^{n-1}}\right)\beta_1\beta_2 d\Omega_1 d\Omega_2 \quad (3)$$

By using the Hamaker constant, $A_H = \pi^2 C\beta_1\beta_2$ [5] and repulsion constant $A_R = \pi^2 D\beta_1\beta_2$ [6], we get

$$f_{int} = \left(-\frac{6A_H}{\pi^2 r^7} + \frac{nA_R}{\pi^2 r^{n-1}}\right)d\Omega_1 d\Omega_2 \quad (4)$$

maker constant can be calculated using dielectric constant of the material. The interaction force per unit volume at any point in the elastic body can be obtained by integration of the volumetric potential over the half-space and taking the gradient with respect to the distance from the half-space [7].

$$f_{int} = -\frac{\pi C\beta_1\beta_2}{2r^4} + \frac{\pi D\beta_1\beta_2}{5r^{10}} \quad (5) \qquad f_A = -\frac{A_H}{2\pi r^4} \quad (6)$$

The second term in the above expression represents the short-ranged repulsion between atoms, which we have incorporated using the contact elements in FEM. Utilizing the Hamaker constant, the first term of the above equation (attractive term), the body force representing the attractive adhesion force, can be written as which we use as the body force acting the elastic object, due to the presence of the rigid half-space.

Finite Element Model
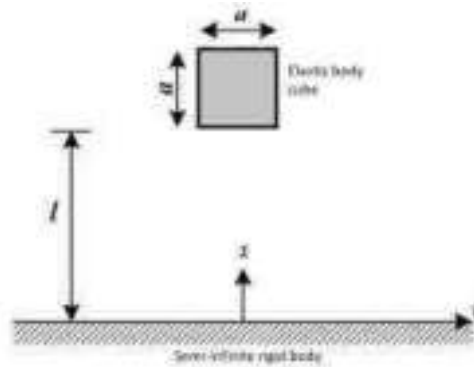
Fig. 1: Schematic representation of an elastic cubic contact geometry to the semi-infinite rigid body.

Elastic adhesive contact of cubic asperity of varying Young's modulus (40 GPa, 70 GPa, 100 GPa, 150 GPa, 200 GPa) with a plane surface of the semi-infinite rigid body is analyzed with the FE adhesive contact model. Finite element mesh for the asperity is constructed with 20-node quadratic brick elements, and the surface of the rigid body was modelled as a rigid plane. FE analysis is performed between an elastic body with rigid half-space by introducing an adhesive interaction contact model [3].

Analyses are conducted with a commercial FE code Abaqus for the case where the asperity initially separated from the rigid plane approaches the plane.

Results & Discussion

Total force of adhesion, obtained as the reaction force on the cubical asperity, varies with the change in separation with the rigid half-space. Therefore, the location of asperity is characterized using the parameter l, which is the gap between the bottom of cube and the plane surface, initially before getting modified by the interaction force.

The cubical asperity is brought in the negative z-direction to the surface of the rigid half-space (approach). On reaching near half-space, the asperity experiences an attractive force, the magnitude of which increases with the reduction in separation.
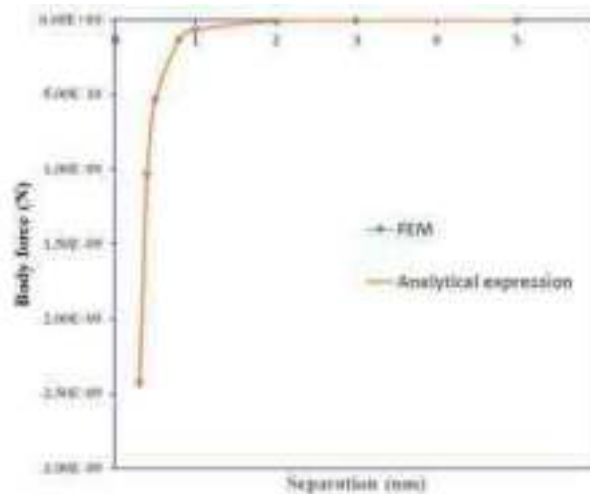

Fig. 2: Comparison of body force over separation by FE method and analytical expression.

Figure 2 shows the FE analysis of the interaction between an elastic body and a semi-infinite rigid half-space with a body force formulation utilizing the Hamaker constant compared with the analytical expression [8]. The typical value of the Hamaker constant is taken as $5*10^{-20}$ J. The FE analysis curve shows a similar trend in results as the magnitude of attraction increases with the approach. From the above figure, it is clear that the FE analysis results agree well with the analytical expressions.
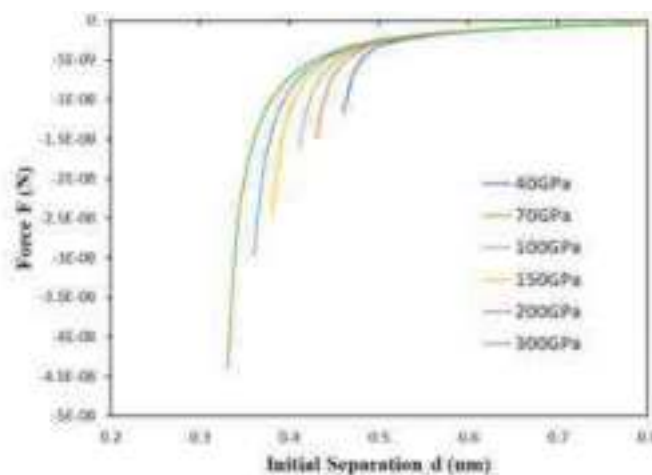
Fig.3: Variation of the adhesion force acting on the cube as a function of separation with half-space for different Young's modulus.

Figure 3 shows the variation of the adhesion force with the separation. The force is plotted against the separation between deformable cube with rigid half space for different values of Young's modulus. When the Young's modulus value increases from 40GPa to 300GPa, the force from the analysis is higher for lower value of E for the same initial separation. The reduction in value of Young's modulus, corresponding to a reduction in stiffness, result in larger deformations. When the initial separation is the same, the deformation of the cube brings it closer to the half-space, thereby increasing the adhesion force.

The force curves are significantly influenced by the difference in Young's modulus, E. The stiffer cube has less deformation than the cube with the lower value of Young's modulus. Therefore, the changes in separation due to deformation are small for the stiffer cube in the presence of interaction force, which causes a significant difference in the occurrence of the jump to contact instability for different Young's modulus.

When a deformable body is close to a rigid half-space, mechanical instability is induced by adhesion when the effective stiffness of the body becomes lesser than the gradient of adhesion force with separation (jump-to-contact instability) [9]. All the curves in Fig. 3 ends at the jump-to-contact instability. For a stiffer material with less deformation, the jump-to-contact instability occurs at smaller separation than the softer material. Therefore, a cube with a lower Young's modulus value comes in contact with half-space at earlier separation due to jump-to-contact instability.

Conclusions

The contact problem of a cubic asperity with the plane surface of a rigid half-space is addressed using a finite element (FE) technique for studying adhesive interactions. In the presence of adhesive force, the reaction force between the surface of the semi-infinite rigid body and the cubic asperity varies. The asperity feels an attracting force when it is close to the surface, and as it approaches the half-space closer, the force magnitude increases. Variations of the adhesion force acting on the cube with the separation for different Young's modulus were also considered to understand adhesive contact problems better.

Mechanical instability is caused by adhesion when a deformable body is brought close to a rigid half-space. It occurs when the effective stiffness of the body is smaller than the gradient of adhesion force with separation, known as the jump-to-contact instability occurs at lesser separation for a stiffer material than a softer material. As a result, due to jump-to-contact instability, a cube with a lower Young's modulus value makes contact with half-space at an earlier separation.

In this work, we discussed the adhesive interaction between a cubic asperity and rigid half-space, which offers significant computational simplification. We can extend this study for asperities of different shapes with varying Young's modulus, and a more realistic scenario wherein the interaction is between two deformable bodies.

References

⭕ F. L. Leite, C. C. Bueno, A. L. da Róz, E. C. Ziemath, and O. N. Oliveira, "Theoretical models for surface forces and adhesion and their measurement using atomic force microscopy," Int J Mol Sci, vol. 13, no. 10, pp. 12773–12856, 2012, doi: 10.3390/ijms131012773.

⭕ Hans-Jürgen Butt and Michael Kappl, Surface and Interfacial Forces, First Edition. Wiley-VCH, 2010. doi: 10.1002/9783527629411.

⭕ S. S. Cho and S. Park, "Finite element modeling of adhesive contact using molecular potential," Tribol Int, vol. 37, no. 9, pp. 763–769, Sep. 2004, doi: 10.1016/j.triboint.2004.04.007.

⭕ R. A. Sauer and S. Li, "An atomic interaction-based continuum model for adhesive contact mechanics," Finite Elements in Analysis and Design, vol. 43, no. 5, pp. 384–396, Mar. 2007, doi: 10.1016/j.finel.2006.11.009.

⭕ Hamaker H.C., "The London-van der Waals attraction between spherical particles," Physica, vol. 4, no. 10, pp. 1058–1072, 1937.

⭕ U. B. Jayadeep, M. S. Bobji, and C. S. Jog, "A body-force formulation for analyzing adhesive interactions with special considerations for handling symmetry," Finite Elements in Analysis and Design, vol. 117–118, pp. 1–10, Sep. 2016, doi: 10.1016/j.finel.2016.04.001.

⭕ Jayadeep U B, "continuum modeling of adhesive interactions based on interatomic potentials," Indian Institute of Science, Bangalore, 2014.

⭕ V. Adrian Parsegian, Van der Waals forces: A handbook for biologists, chemists, engineers, and physicists. Cambridge University Press, 2005. doi: 10.1017/CBO9780511614606.

⭕ Hendrik Holscher, Encyclopedia of Nanotechnology. Springer Netherlands, 2012. doi: 10.1007/978-90-481-9751-4.

Advances and Trends in Industrial Lubrication

Jeevan T.P.[1]* and Divya H.V.[2]

[1,2] Department of Mechanical Engineering, Malnad College of Engineering, Hassan, Karnataka, India.
*Corresponding author Email: jeevantpmce@gmail.com

Keywords: Lubrication, friction, wear, metal working and metal forming

Abstract

Lubrication is critical in machines and equipment with moving parts, yet with so many factors to consider, it can quickly become overwhelming. One of the most crucial factors in maintaining the health and effectiveness of a machine is proper lubrication, which enables continuous machine operation. The ideal lubricant minimizes solid-to-solid contact and eliminates all friction levels that might restrict movement and cause wear. This article is intended to highlight lubrication trends in manufacturing industries. The aim is to provide a general overview of lubrication and its recent research advances and trends in industry.

Introduction

Ever since the emergence of synovial fluid, that lubricates the joints and bursae of vertebrate animals, nature has provided lubrication. To lubricate sledges for carrying game or lumber and boulders for building, prehistoric humans used mud and reeds. The original wagons axles were greased with animal fat, which was widely used till the petroleum industry was established in the 19th century, when crude oil replaced animal fat as the primary source of lubricants [1, 2]. All through the advancement of a wide range of products intended for the lubricating requirements of the vehicle, the airplane, the diesel locomotive, the turbojet, and power machinery of every sort, the natural lubricating capacity of crude oil has continuously increased.

Since the beginning of the industrial revolution, around the time of the steam engine's development, the dynamics of the lubrication sector are currently progressing at a rate and intensity that have not been witnessed.

In many ways, the methods and products developed during that time still have a strong hold on the history of lubrication. This is demonstrated by the many lubricants that are utilised as well as the goods, equipment, and methods that are used with them. Nevertheless, evolutionary and maybe revolutionary transformation is under way [3].

The market for lubricants is anticipated to develop at a compound annual growth rate (CAGR) of less than 2% throughout the forecast period, from a size of over 35 million tonnes in 2020. (2021-2026). The market for industrial lubricants is anticipated to grow from USD 62.8 billion in 2019 to USD 73.3 billion in 2024, at a CAGR of 3.1%. Enormous industrial expansion in Asia-Pacific and the Middle East & Africa, together with an increase in process automation across most sectors, are the two main factors driving the market. (Market Research Report, published in 2021 by Mordor Intelligence and Markets Research Pvt. Ltd.)

Lubrication: Functions, Regimes and Methods
Lubrication is primarily used to lessen wear and heat between surfaces in contact that are moving relative to one another. Even though wear and heat cannot be absolutely avoided, they can be significantly decreased to low or tolerable levels. Decrease in the coefficient of friction between the contacting surfaces to lessen the impacts of heat and wear, which are both influenced by friction. In addition to reducing oxidation and preventing rust, lubrication is used to convey mechanical power in hydraulic fluid power applications, provide insulation in transformer applications, and seal against dust, dirt, and water.
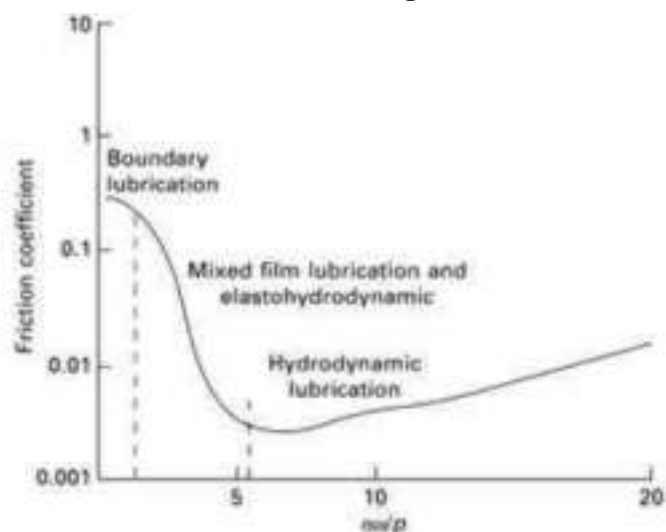

Fig. 1 Stribeck curve [4]

The type of lubrication film that is produced under operating circumstances and is based on the amount of contact between surfaces is described by lubrication regimes. The Stribeck Curve, which links friction with sliding speed, lubricant viscosity, and normal load, describes lubrication regimes. Stribeck (Stachowiak and Batchelor, 2001) showed that the coefficient of friction is inversely related to the pressure applied to the contact surfaces and directly proportional to the viscosity of the lubricant and the difference in speed between the contact surfaces. The Stribeck curve, or the friction coefficient against the bearing number, is depicted in Figure 1 as follows: $\mu\omega/p$ (lubricant viscosity (μ), speed (ω) and contact pressure (p). Based on the Stribeck diagram, there are three regimes of lubrication: hydrodynamic lubrication, mixed lubrication, and boundary lubrication.

The appropriateness of the lubricant and lubrication technique have a significant impact on the lifespan of machine parts. Over the years, several lubrications system types have been created and developed based on the unique needs of machines and various industrial sectors. The numerous types of lubricating methods are displayed in Table 1.

Table 1 Methods of lubrication

Method of Lubrication	Suitability
Bath Lubrication	Suitable for low/medium speed
Drip Lubrication	Applicable at relatively high speed and up to medium load.
Splash Lubrication	Usable up to relatively high speed
Forced circulation Lubrication	High speeds and high temperature conditions.
Jet Lubrication	High speed and heavy load.
Minimum Quantity Lubrication (MQL)	Suitable for Machining processes
Air-Oil Lubrication	Suitable for large machines in heavy industry and machine tools

Trends Of Lubrication

In Metal Forming

Metal forming lubricants are unique; liquids can be used for room temperature applications, but solid lubricants or multi-phase lubricants are common. Lubricants are expensive, challenging to apply uniformly, difficult to remove and often an environmental impossibility to discard. In later processes like painting or adhesive bonding, they cause issues. To manage surface quality, lessen tool wear, and limit power consumption, lubricants are essential.

Environmentally friendly lubrication systems have been pursued if there have been lubricants, but this has become a special focus recently. This is challenging mainly as applied to boundary additives and their unique chemistries [5].

By using strip drawing and deep drawing experiments, the performance of three bio-lubricants (cottonseed, karanja, and jatropha oils) is assessed. In terms of resultant friction coefficient, drawability, and thinning at low normal pressure, all three bio-lubricants outperform mineral-oil-based lubricants. It is discovered that cottonseed oil performs better than the other two bio-lubricants. However, when normal pressure increased, the lubricating effectiveness of biolubricants drastically declined. This issue may be solved by using extreme pressure additives. [6].

Wickowski et al. suggested switching to lubricants based on vegetable oils and boric acid in place of traditional mineral/synthetic lubricants. In production as well as laboratory strip drawing and cupping tests, the lubricants' efficacy was evaluated. Reduced frictional resistance and galling protection are achieved extremely well by using an oil-based lubricant with a boric acid component [7].

Owing to the difficulties in employing traditional lubricants for high-temperature (HT) applications, materials with self-lubricating ability are becoming more common in metal forming and power generation industries. There has been a lot of research done on HT self-lubrication utilizing alkaline-earth fluorides like CaF_2 or BaF_2. In recent years, interest in new classes of HT solid lubricants has grown significantly. Although their tribological characteristics are poor at room temperature, MAX phases like Ti_3SiC_2 and Ti_2AlC might minimise wear and friction at high temperatures. [8].

IN METAL CUTTING

The science of metal cutting has advanced dramatically in the last one hundred years. In the 1940s, Merchant established a research group at the Cincinnati Milacron company that made significant contributions to a fundamental understanding of machining mechanics.

Tool wear for materials that are difficult to manufacture, such nickel-based alloys, is a particular problem. The traditional cooling and lubricating method in these situations is oil emulsion and water-based cutting fluids. However, the need for alternative machining techniques is being driven by the environmental and health risks connected with the use of these fluids. Cryogenic machining, cold air, vegetable oils, and dry machining with ceramic cutters are a few examples of these techniques. Cryogenic fluids are a tempting cooling alternative among these techniques, and they have attracted a lot of attention in the literature[9, 10].

The need for micro-scale goods and components has grown quickly in recent years, especially in the areas of electronics, communications, optics, avionics, medicine, and vehicles. Micro-engines, tiny-reactors, micro heat exchangers, medical implants, drug delivery systems, and diagnostic tools are a few examples of typical uses for these goods [11]. These goods are often made with micro- and sub-micrometer components. Numerous engineering investigations have focused on establishing micro- and nanomachining technologies in reply to this requirement. This recent development demands a new micro-manufacturing platform that creates new machining techniques for micro and nanocomponents in addition to integrating various fabrication methods. The micro-manufacturing platform should also be able to create various materials with high throughput and at a reasonable price[12].

Conclusions

The field of tribology has seen enormous development in the past two decades, and this is especially true for tribology applied to industrial processes. An essential understanding of the differences between manufacturing and machine element tribology has been developed and applied to improve the robustness of manufacturing processes. Friction rules are complex, and lubricant is necessary for process viability but often a desired level of friction must be preserved. The area of tribology with the fastest recent growth is superlubricity. It will mark a significant turning point in the evolution of technology. It significantly minimises wear and friction-induced noise in addition to reducing the friction coefficient by many orders of magnitude. As a result, more tribologists are working on superlubricity. Superlubricity has advanced significantly in both solid and liquid forms.

References

- Jeevan, T.P. and S.R. Jayaram, Tribological Properties and Machining Performance of Vegetable Oil Based Metal Working Fluids—A Review. Modern Mechanical Engineering, 2018. 8(1): p. 42-65.
- Khakimov, F.S., N.S. Mukhtorov, and O.S. Maksumova, Environmentally friendly synthesis route of terpolymers derived from alkyl acrylates and their performance as additives for liquid hydrocarbon products. Journal of Polymer Research, 2020. 27(10): p. 1-15.
- Scott, R., The practical handbook of machinery lubrication. 2012: Noria Corporation.
- Yan, Y., Tribology and tribo-corrosion testing and analysis of metallic biomaterials, in Metals for Biomedical Devices. 2010, Elsevier. p. 178-201.
- Bay, N., et al., Environmentally benign tribo-systems for metal forming. CIRP annals, 2010. 59(2): p. 760-780.
- Prakash, V. and D.R. Kumar, Performance evaluation of bio-lubricants in strip drawing and deep drawing of an aluminium alloy. Advances in Materials and Processing Technologies, 2020: p. 1-14.
- Więckowski, W., J. Adamus, and M. Dyner, Sheet metal forming using environmentally benign lubricant. Archives of Civil and Mechanical Engineering, 2020. 20(2): p. 1-12.
- Torres, H., M. Rodríguez Ripoll, and B. Prakash, Tribological behaviour of self-lubricating materials at high temperatures. International Materials Reviews, 2018. 63(5): p. 309-340.
- Pu, Z., et al., Enhanced surface integrity of AZ31B Mg alloy by cryogenic machining towards improved functional performance of machined components. International journal of machine tools and manufacture, 2012. 56: p. 17-27.
- Kaynak, Y., et al., Tool-wear analysis in cryogenic machining of NiTi shape memory alloys: A comparison of tool-wear performance with dry and MQL machining. Wear, 2013. 306(1-2): p. 51-63.
- Crichton, M.L., et al., Characterising the material properties at the interface between skin and a skin vaccination microprojection device. Acta biomaterialia, 2016. 36: p. 186-194.
- Gao, S. and H. Huang, Recent advances in micro-and nano-machining technologies. Frontiers of Mechanical Engineering, 2017. 12(1): p. 18-32.

Exploring the tribological performance of lubricants containing polymer functionalized silica nanoparticles

Syed Junaid[1*], Lukkumanul Hakkim1, Leena Nebhani[1], Nitya Nand Gosvami[1]

[1]Department of Materials Science and Engineering, Indian Institute of Technology Delhi, Hauz Khas, New Delhi, India 110016
*Corresponding author Email: Syed.Junaid@mse.iitd.ac.in

Keywords: Tribology, Wear, Silica, Nanoparticles, Lubricant additive

Abstract

Silica nanoparticles are extensively being studied as an additive to lubricants in order to replace environmentally harmful sulfur, phosphorus & ash containing conventional lubricant additives. This work uses functionalized silica synthesized with a varied length of polymeric chains grafted on its surface as an additive in polyalphaolefin 4 (PAO 4). Reciprocating sliding wear tests under lubricated conditions are carried out with AISI 52100 steel spherical ball against EN31 steel flat coupon.

The formulated lubricants are examined to understand the influence of functionalization and length of grafted polymeric chains on their dispersion stability. Base oil containing 0.5 wt.% spray dried control silica nanoparticles and 0.5 wt.% Oleic acid, which acts as a dispersant, formed transparent, uniform dispersion and exhibited excellent tribological properties with a reduction in Coefficient of friction (COF) value by ~ 52% and a reduction in absolute wear volume by ~14% compared with a neat base oil (PAO 4). Advanced characterization techniques like FE-SEM with EDS mapping, EPMA, and lateral force microscopy analysis using AFM are performed to examine the tribofilm formation on worn surfaces. Detailed analysis using these techniques is carried out to understand further the underlying mechanisms that induce COF reduction and thereby improve energy transfer efficiency.

Introduction

Various Engineering applications require lubrication between sliding components to minimize energy transfer inefficiency, reliability issues, and material losses due to friction and wear. Most recent estimates amount to economic losses of 1.0-1.5% of the GDP of industrialized nations [1]. Various additives are mixed with the base lubricants for lubricating sliding contacts to minimize friction and wear. Nanoparticles (NPs) of metals and metal oxides are attractive substitutes when incorporated as additives in base lubricants. They have shown excellent mechanical and tribological properties where significant friction and wear reduction can be achieved [2,3]. When NPs are dispersed in lubricants, they may form robust protective coatings, also referred to as "tribofilms", as they form at the rubbing interface, providing significant wear resistance. The film can also self-lubricate depending upon the choice of nanoparticles and their encapsulation, which can allow tuning of the shear strength of the sliding contact. In addition to protective tribofilm formation, various studies suggest that NPs provide excellent tribological properties via other mechanisms, including mending and rolling [4]. However, one major issue with the use of NPs is their high tendency to undergo aggregation in non-polar oils, for example, synthetic lubricating base oil polyalphaolefin (PAO), because of the significant difference in chemical composition between the oil and NPs and the high van der Waals attractive forces between NPs [5]. Recent studies show that silica particles with surface functionalization are one of the best NPs for tribological applications as they are environmentally friendly and are cost effective [6].

Therefore, in the present work, we have investigated the tribological performance and dispersion stability of the non-polar synthetic lubricant PAO4 by adding polymer functionalized silica nanoparticles of different particle sizes and grafted polymeric chain lengths.

Experimental Details

Materials
This work used six types of silica NPs with varied polymeric chains. Namely, PS grafted USHER silica (Ls01), Control Stöber silica (LS02), Octyl functionalized Stöber silica (LS03), Control RHA silica (LS04), PS grafter RHA silica

(LS05), Octadecyl functionalized RHA silica (LS06). These silica NPs were dispersed in synthetic Poly-alpha olefin (PAO) base oil. The PAO4 base oil used in the present work was Durasyn 164 PAO4 (Total, France). The kinematic viscosities of this PAO are 17.6 cSt and 4.0 cSt at 40 and 100 °C, respectively, and its pour point is −69 °C. 0.5 wt.% of each type of synthesized silica was added to the base oil along with 0.5 wt.% of Oleic acid (OA) and Ultrasonicated using Bath sonication for a duration of 2 hours. OA was added as a dispersant as it improves the dispersion stability of the formulated lubricants.

Tribological Testing

Ball-on-flat reciprocating wear tests were performed using R-Tec MFT5000 universal tribometer with a customized liquid cell set up to study the effect of adding functionalized silica nanoparticles to the PAO4 base oil on tribological performance. AISI 52100 steel ball with a 10 mm diameter was used as a stationary contact surface, and EN31 steel with the same composition was used as a reciprocating counter surface. A sliding stroke of 1.5 mm and an oscillation frequency of 2 Hz were used, and all tribological tests were repeated three times to ensure the repeatability of the data obtained. Each test was performed for a duration of 30 minutes. A piezoelectric load cell recorded the friction force in situ, and the coefficient of friction (COF) was obtained by dividing the friction force by the load. After the tribological testing, the EN31 steel flat containing the wear scars was cleaned by ultrasonication using hexane to remove residual oil from the sample. Further sonication using ethanol was carried out to remove loose particles of surface debris. Wear volume measurements were carried out using an optical surface profilometer embedded with the universal tribometer (MFT 5000, R-Tec, USA). The surface of the wear scars was further analyzed using FESEM−EDS (JEOL-JSM-7800F) and EPMA (EPMA-1720 HT, Shimadzu, Japan). These techniques are used for characterizing the worn surface by high-resolution imaging and elemental mapping of the wear scars to identify the deposition of functionalized silica tribofilm/patches on the surface. An atomic force microscope (Drive AFM, Nanosurf, Switzerland) is used for topography imaging and friction contrast analysis.

Results & Discussion

Characterization of functionalized Silica

Dispersion stability of the formulated lubricants containing silica nanoparticles of different sizes was studied. LS01, LS02 and LS03 lubricant samples contain commercially available silica nanoparticles with particle sizes ranging from 200-600 nm. Lubricants LS04, LS05 & LS06 contain in-house synthesized silica nanoparticles with particle sizes below 100 nm. LS04 has fine silica nanoparticles with a particle size of approximately 20-25 nm. Figure 1. (b) Shows the TEM micrograph of LS04 silica nanoparticles, and (a) shows the X-ray diffraction spectra of the silica dispersed in the LS04 sample. The characteristic peak at a 2theta value of 23 degrees signifies the presence of nano SiO2 particles [7]. LS01, LS02, LS03 & LS05 formed milky white dispersion after sonication, and the lubricant stability ranged between 10-12 hours, whereas LS04 and LS06 formed transparent uniform dispersions without any visual trace of agglomeration even after 14 days. Polystyrene chains are grafted on the surface of LS01 and LS05 NPs to improve their dispersion with the non-polar synthetic base oil PAO4. However, the precursor used for their synthesis differs, and the considerable difference in particle size affects the dispersion stability. Similarly, the LS02 and LS04 samples were synthesized using the same method without any surface modification. However, the difference in precursor material and silica particle size resulted in different times of nanoparticle particle segregation.
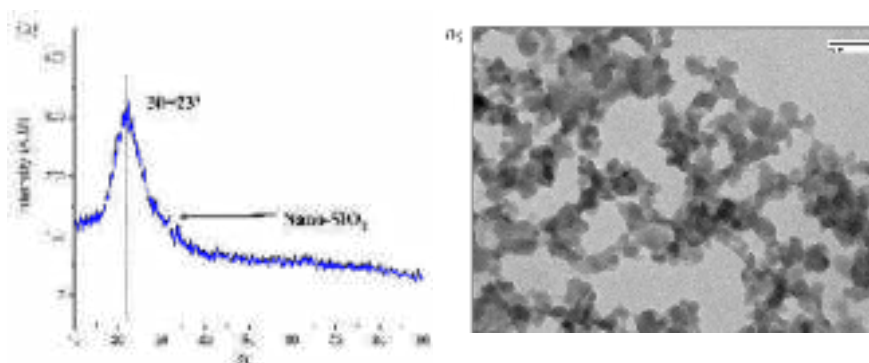

Figure 1: (a) X-ray diffraction (XRD) spectra of LS04 silica nanoparticles. (b) TEM micrograph of LS04 silica nanoparticles.

Friction and wear study

The coefficient of friction (COF) vs time plot is shown in figure 2. Each test was repeated three times, and an average curve of three repetitions is reported. It is evident from the figure that under similar reciprocating wear conditions, neat base oil exhibits an average COF value of > 0.2, which is higher than all the other lubricant samples containing functionalized silica as an additive, i.e., LS01-LS06.

In association with the friction data, the wear volumes of the scars were calculated analytically using an optical surface profilometer. Figure 3 shows the improvement in wear resistance characteristics of lubricants containing silica nanoparticles compared to the neat base oil.
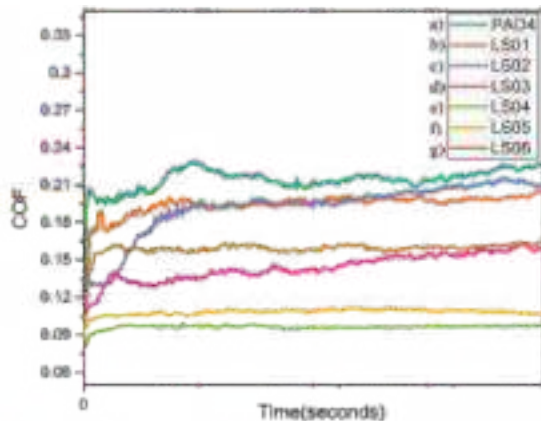

Figure 2: Co-efficient of friction vs time plot of Silica nanoparticles additive-based lubricant with concentrations of a) Base oil PAO4, b) LS01, c) LS02, d) LS03, e) LS04, f) LS05, g) Ls06.
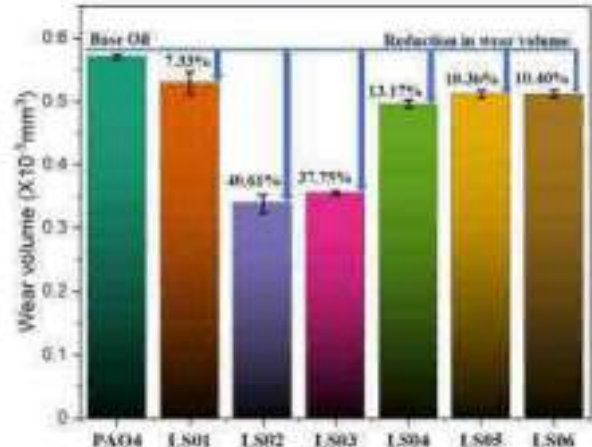

Figure 3: Wear volume comparison plot showing the reduction in wear volume by silica additive-based lubricants in relative percentage terms with respect to the neat base oil.

It can be observed that though the COF value for LS02 and LS03 samples is higher, they exhibit higher wear resistance by wear reduction of 40.61% and 37.75%, respectively. This is attributed to the particle size and the precursor of synthesis. Polymer grafting also plays a crucial role here. As the particle size is 200 nm-600 nm and synthesized from a softer precursor material, LS02 & LS03 samples show better wear resistance. But the dispersion stability and coefficient of friction reduction are far better for the LS04 sample. COF value is reduced from >0.2 to < 0.085 by adding LS04 silica nanoparticles to the base oil PAO4.

The formation of low friction tribofilms/patches on the worn surface is the reason behind the reduction in COF value when functionalized silica-based lubricants. This is confirmed by the surface characterization of the wear scars using FESEM, EPMA and AFM. As Figure 4 shows the uniform deposition of silicon at the center of the wear track and oxygen in the overall wear scar after the tribotest using LS04, it can be concluded that the silica nanoparticles are acting as an interface between the steel-steel contact surfaces and hinder the damage of sliding surfaces by forming a protective layer at the interface.

Conclusions

In conclusion, the tribological performance of synthetic lubricants containing functionalized silica nanoparticles as additives with different particle sizes was investigated. A tremendous decrease in coefficient of friction and a considerable increase in wear resistance was obtained by the nominal addition of silica as an additive to the base oil. Correlation between the frictional properties and the type of precursor used for the synthesis of Silica nanoparticles has been established. LS04 sample containing spray dried control RHA silica nanoparticles with particle size < 25 nm showed excellent tribological properties and dispersion stability owing to their size, shape and precursor for synthesis compared with other varieties of silica dispersed lubricants.
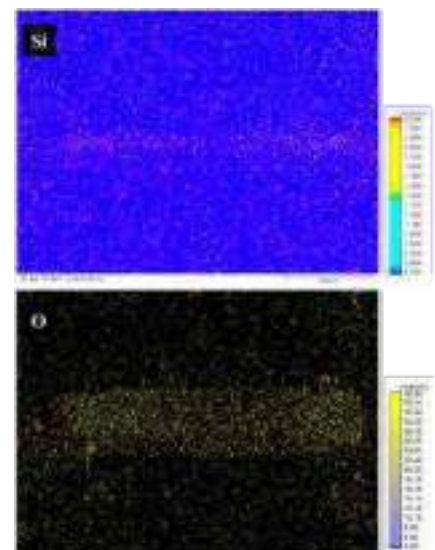

Figure 4: Elemental mapping of Si and O on the wear track after reciprocating wear test using LS04 lubricant sample using EPMA.

References

○ Holmberg K, Andersson P, Erdemir A. Global energy consumption due to friction in passenger cars. Tribol Int. 2012; 47:221–234.

○ Dai W, Kheireddin B, Gao H, Liang H. Roles of nanoparticles in oil lubrication. Tribol Int. 2016; 102:88–98.

○ Lahouij I, Vacher B, Martin J-M, Dassenoy F. IF-MoS2 based lubricants: influence of size, shape, and crystal structure. Wea 2012;296(1–2):558–567.

○ Shenoy B, Binu K, Pai R, Rao D, Pai RS. Effect of nanoparticles additives on the performance of an externally adjustable fluid film bearin Tribol Int. 2012;45(1):38–42.

○ Martin, J. M.; Ohmae, N. Nanolubricants; John Wiley & Sons: Chichester, 2008.

○ Bryan T. Seymour, Wenxin Fu, Roger A. E. Wright, Huimin Luo, Jun Qu, Sheng Dai, and Bin Zhao ACS Applied Materials & Interface 2018 10 (17), 15129-15139.

○ Sun, Jinfeng et al. "Effect of Nano-SiO2 on the Early Hydration of Alite-Sulphoaluminate Cement." Nanomaterials (Basel, Switzerland vol. 7,5 102. 3 May. 2017, doi:10.3390/nano7050102

Design and Fabrication of a Multi-station Biotribometer Based on Astm Standard F732

Jaswant Kumar Hirwani* and Sujeet Kumar Sinha

Department of Mechanical Engineering, Indian Institute of Technology Delhi, India
*Corresponding author Email: jaswant.hirwani@gmail.com

Abstract

Cross-shear motion and protein containing liquids are the two essential factors that affect the wear life of implants. Therefore, the current pin on the disc device is designed to produce a multi-directional sliding motion. A calibration test was conducted with a standard UHMWPE pin and CoCrMo disc under diluted bovine serum lubrication with a protein concentration of 20 mg/ml. For contact stress of 2 MPa and sliding velocity of 20.73 mm/s, the average specific wear rate of UHMWPE was $2.8 \times 10\text{-}6$ mm3/Nm, which is clinically relevant. Abrasion and burnishing were dominant wear mechanisms, and some locations had protuberances, possibly due to the early degradation of protein or the plastic deformation of UHMWPE. Meaningful and clinically relevant information from this device makes it acceptable for biotribological applications.

Introduction

The hip and knee are the major load-bearing joints that require implantation in severe osteoarthritis or accidental damage. There is always a great demand for wear screening devices to develop new implant materials or find fundamental insights about tribological phenomena. Devices developed in the past based on the cross-shear principle claim to reproduce clinically relevant wear rate and wear mechanism [1–3]. These devices are costly due to complex motion and loading arrangements. Also, the scarcity of available devices and more extended testing periods of 5-7 weeks makes it difficult to progress the research in this field. Therefore this work focuses on developing and calibrating a novel prosthetic biotribometer with an easy loading mechanism, cross-shear sliding arrangement, provision for different motion control, and non-reactive lubricant containers.

Description of Device
Figure 1 shows the schematic of the design features. The device has three rotational motors attached to the top plate of the machine. The linear actuators are attached to the cantilever, just below the rotational unit. The lubricant container is also mounted on top of this linear stage. The far end of the cantilever is used for deadweight loading. The device was built based on the requirements mentioned in ASTM F732. The device can simulate the wear of both hip and knee joints. For knee simulation, linear reciprocation is needed with a stress level of 3.54 MPa and a speed of 50 mm/s. For hip joints, these values may vary between 2-10 MPa and 12.5-75 mm/s with cross-shear motion. Other capabilities of the device are provided in Table 1.

Experimental Details
Compression molded UHMWPE pin and polished CoCrMo disc were selected for wear testing. The protein concentration of serum was 20 mg/ml. The stress and sliding velocity were selected as 2 MPa and 20.73 mm/s. The pin rotation was fixed at 60 rpm to change its orientation against the sliding disc. The total test period was 96 hours which resulted in 4.417 km. The lubricant change interval was 48 hours. The weight measurements were taken with a precision balance of 0.01 mg least count.
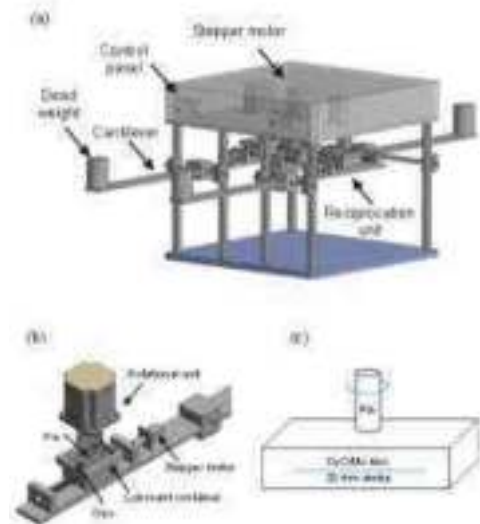
Figure 1: Schematic view of prosthetic biotribometer developed at IIT Delhi. (a) C ompete assembly (b) Visualization of pin and disc arrangements with lubricant container (c) Pin and disc motion with stoke length used in this experiment.

Table 1. Comparison of ASTM F732 requirements and our device.

ASTM F732 parameters	Requirement	Our device capability
Knee or Hip type	both	both
Knee, cross-shear	zero	yes
Hip, cross-shear	yes	yes
Stress level	2-10 MPa	2-5 MPa
Sliding Velocity	12.5 to 75 mm/s	5 to 50 mm/s
Sliding distance per wear cycle	25 to 150 mm	yes
Bovine serum container	yes	yes
Pin shape	Flat-ended cylindrical pin	yes
Cycle Counter	yes	yes
Metal shape	flat	flat

RESULTS & DISCUSSION
Figure 2 shows the specific wear rate of all the individual samples, average values, and previously published data. The average wear rate of UHMWPE was found to be $2.8 \times 10{-6}$ mm3/Nm, which is in the range of the data reported elsewhere [4,5]. Figure 3 shows the worn surface morphologies. Abrasion and burnishing were found to be the significant surface characteristics. Few locations had protuberances due to the plastic flow of UHMWPE.
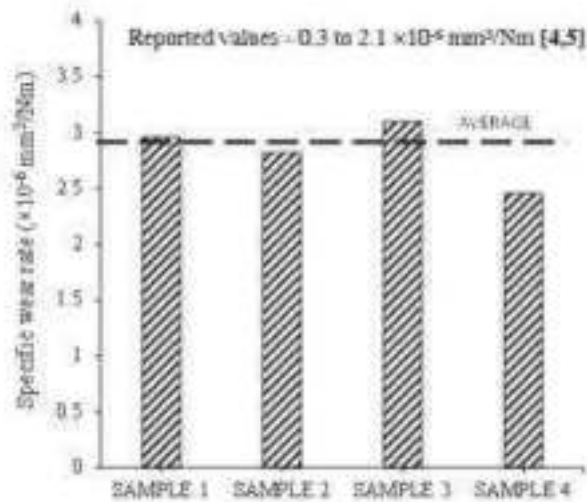

Figure 2 Specific wear rate obtained from the developed machine under serum lubrication condition against CoCrMo disc. Previously reported values are also given for comparison.
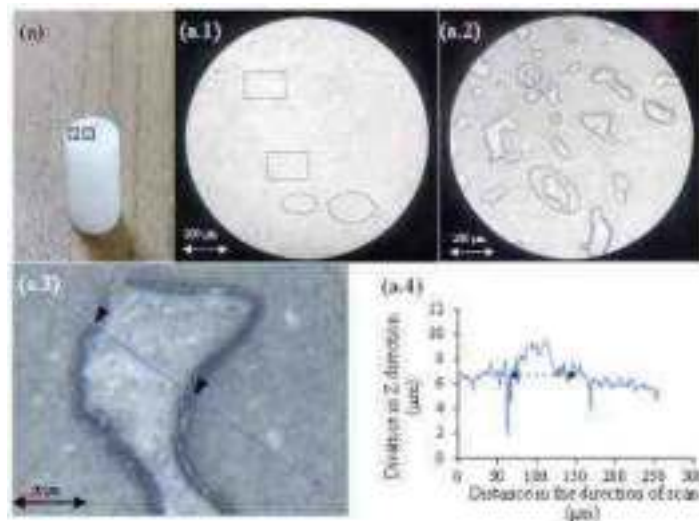

Figure 3. Worn surface analysis using an optical microscope for (a) UHMWPE pin and (a.1) Shows a small portion of worn UHMWPE surface with abrasive wear and burnishing features represented by square and elliptical regions, respectively. (a.2) Shows protuberances on UHMWPE worn surface which resulted from plastic deformation (a.3) Shows the magnified view of the protuberance, and (a.4) corresponding wear profile shows protruded structure.

Conclusions

A biotribometer has been successfully developed for the wear simulation of hip/knee implant materials according to the criteria mentioned in ASTM F732. Specific wear rate and surface morphologies obtained from the devices were clinically relevant and in line with the previously published data. Therefore this device can be further utilized for implant wear simulation.

Acknowledgement

References

- Hunt BJ, Joyce TJ. A tribological assessment of Ultra High Molecular Weight Polyethylene types GUR 1020 and GUR 1050 for orthopedic applications. Lubricants. 2016, 4(3).
- Saikko V. A hip wear simulator with 100 test stations. Proc Inst Mech Eng Part H J Eng Med. 2005, 219(5):309.
- Turell M, Wang A, Bellare A. Quantification of the effect of cross-path motion on the wear rate of ultra-high molecular weight polyethylene. Wear. 2003, 255(7–12):1034.
- Sawae, Y. Wear of UHMWPE for Joint Prosthesis. In Handbook of Polymer Tribology, 2018, pp. 81-109.
- Joyce, T. Biopolymer tribology. In Handbook of Polymer Tribology, 2018, pp. 111-152.

Sponsors

Platinum Sponsor

IndianOil

Gold Sponsors

nanosurf

Rtec instruments

MAGNUM engineers
Science | Tribology | Innovation

OPTIMOL INSTRUMENTS

SKF

Bharat Petroleum
energising lives

Silver Sponsors

Balmerol LUBRICANTS

Indian Additives limited

Exhibitors and Business Meet Partners

INDUSTRON

PCS Instruments
LEADERS IN TRIBOLOGY TEST EQUIPMENT

ACE INSTRUMENTS

ORBIT
Research Associates

DUCOM
MATERIAL CHARACTERIZATION SYSTEMS

Anton Paar

AGARAM
Customer-Centric

Other Supporting Companies/Organizations

TTRF contributes to tribology's future.
TTRF
TAIHO KOGYO TRIBOLOGY RESEARCH FOUNDATION

iNSERB INDIA

DRDO
DEFENCE R&D ORGANISATION
MINISTRY OF DEFENCE

MINIMAC
Systems pvt. ltd.
(An ISO 9001 : 2015 company)